

APPLIED COMPUTATIONAL ELECTROMAGNETICS SOCIETY JOURNAL

**Special Issue on Emerging Devices and
Antennas for 5G/6G Applications**

Guest Editors:

Yongjin Zhou, Shanghai University

Lei Zhao, China University of Mining and Technology

Kai-Da Xu, Xi'an Jiaotong University

Yan Zhang, Southeast University

Xi Gao, Guangxi University of Science and Technology

July 2021

Vol. 36 No. 7

ISSN 1054-4887

The ACES Journal is abstracted in INSPEC, in Engineering Index, DTIC, Science Citation Index Expanded, the Research Alert, and to Current Contents/Engineering, Computing & Technology.

The illustrations on the front cover have been obtained from the research groups at the Department of Electrical Engineering, The University of Mississippi.

THE APPLIED COMPUTATIONAL ELECTROMAGNETICS SOCIETY

<http://aces-society.org>

EDITORS-IN-CHIEF

Atef Elsherbeni

Colorado School of Mines, EE Dept.
Golden, CO 80401, USA

Sami Barmada

University of Pisa, ESE Dept.
56122 Pisa, Italy

ASSOCIATE EDITORS

Mohammed Hadi

Kuwait University, EE Dept.
Safat, Kuwait

Alistair Duffy

De Montfort University
Leicester, UK

Wenxing Li

Harbin Engineering University
Harbin 150001, China

Maokun Li

Tsinghua University
Beijing 100084, China

Mauro Parise

University Campus Bio-Medico of Rome
00128 Rome, Italy

Yingsong Li

Harbin Engineering University
Harbin 150001, China

Riyadh Mansoor

Al-Muthanna University
Samawa, Al-Muthanna, Iraq

Lijun Jiang

University of Hong Kong, EEE Dept.
Hong, Kong

Shinichiro Ohnuki

Nihon University
Tokyo, Japan

Kubilay Sertel

The Ohio State University
Columbus, OH 43210, USA

Antonio Musolino

University of Pisa
56126 Pisa, Italy

Abdul A. Arkadan

Colorado School of Mines, EE Dept.
Golden, CO 80401, USA

Salvatore Campione

Sandia National Laboratories
Albuquerque, NM 87185, USA

Wei-Chung Weng

National Chi Nan University, EE Dept.
Puli, Nantou 54561, Taiwan

Alessandro Formisano

Seconda Università di Napoli
81031 CE, Italy

Piotr Gas

AGH University of Science and Technology
30-059 Krakow, Poland

Long Li

Xidian University
Shaanxa, 710071, China

Steve J. Weiss

US Army Research Laboratory
Adelphi Laboratory Center (RDRL-SER-M)
Adelphi, MD 20783, USA

Jiming Song

Iowa State University, ECE Dept.
Ames, IA 50011, USA

Maokun Li

Tsinghua University, EE Dept.
Beijing 100084, China

Atif Shamim

King Abdullah University of Science and Technology (KAUST)
Thuwal 23955, Saudi Arabia

Marco Arjona López

La Laguna Institute of Technology
Torreon, Coahuila 27266, Mexico

Paolo Mezzanotte

University of Perugia
I-06125 Perugia, Italy

Luca Di Rienzo

Politecnico di Milano
20133 Milano, Italy

Lei Zhao

Jiangsu Normal University
Jiangsu 221116, China

Sima Noghianian

Commscope
Sunnyvale, CA 94089, USA

Qiang Ren

Beihang University
Beijing 100191, China

Nunzia Fontana

University of Pisa
56122 Pisa, Italy

Stefano Selleri

DINFO – University of Florence
50139 Florence, Italy

Amedeo Capozzoli

Univerita di Napoli Federico II, DIETI
I-80125 Napoli, Italy

Yu Mao Wu

Fudan University
Shanghai 200433, China

EDITORIAL ASSISTANTS

Matthew J. Inman

University of Mississippi, EE Dept.
University, MS 38677, USA

Shanell Lopez

Colorado School of Mines, EE Dept.
Golden, CO 80401, USA

EMERITUS EDITORS-IN-CHIEF

Duncan C. Baker

EE Dept. U. of Pretoria
0002 Pretoria, South Africa

Allen Glisson

University of Mississippi, EE Dept.
University, MS 38677, USA

Ahmed Kishk

Concordia University, ECS Dept.
Montreal, QC H3G 1M8, Canada

Robert M. Bevensee

Box 812
Alamo, CA 94507-0516, USA

Ozlem Kilic

Catholic University of America
Washington, DC 20064, USA

David E. Stein

USAF Scientific Advisory Board
Washington, DC 20330, USA

EMERITUS ASSOCIATE EDITORS

Yasushi Kanai

Niigata Inst. of Technology
Kashiwazaki, Japan

Alexander Yakovlev

University of Mississippi, EE Dept.
University, MS 38677, USA

Levent Gurel

Bilkent University
Ankara, Turkey

Mohamed Abouzahra

MIT Lincoln Laboratory
Lexington, MA, USA

Ozlem Kilic

Catholic University of America
Washington, DC 20064, USA

Erdem Topsakal

Mississippi State University, EE Dept.
Mississippi State, MS 39762, USA

Sami Barmada

University of Pisa, ESE Dept.
56122 Pisa, Italy

Fan Yang

Tsinghua University, EE Dept.
Beijing 100084, China

Rocco Rizzo

University of Pisa
56123 Pisa, Italy

William O'Keefe Coburn

US Army Research Laboratory
Adelphi, MD 20783, USA

EMERITUS EDITORIAL ASSISTANTS

Khaled ElMaghoub

Trimble Navigation/MIT
Boston, MA 02125, USA

Kyle Patel

Colorado School of Mines, EE Dept.
Golden, CO 80401, USA

Christina Bonnington

University of Mississippi, EE Dept.
University, MS 38677, USA

Anne Graham

University of Mississippi, EE Dept.
University, MS 38677, USA

Madison Le

Colorado School of Mines, EE Dept.
Golden, CO 80401, USA

Allison Tanner

Colorado School of Mines, EE Dept.
Golden, CO 80401, USA

Mohamed Al Sharkawy

Arab Academy for Science and Technology, ECE Dept.
Alexandria, Egypt

JULY 2021 REVIEWERS

Guan-Yu Chen
Eduard Costa
Xi Gao
Peng Huang
Ashutosh Kedar
Venkata Kishore Kothapudi
Haotian Li
Long Li
Weijia Li
Yin Li
Yingsong Li
Ding-Bing Lin
Weifeng Lin
Siti Harwani Md Yusoff
Mohammd Pourbagher

Neethu S.
Neetu Sehrawat
Stefano Selleri
Abhishek Sharma
Sellakkutti Suganthi
Yu-Ming Wu
Yang Xiong
Kai Da Xu
Xuexia Yang
Wenhua Yu
HongLin Zhang
Runren Zhang
Yan Zhang
Yong Jin Zhou

THE APPLIED COMPUTATIONAL ELECTROMAGNETICS SOCIETY JOURNAL

Vol. 36 No. 7

July 2021

SPECIAL ISSUE ON EMERGING DEVICES AND ANTENNAS FOR 5G/6G APPLICATIONS

A Dual-Band and Low-Cost Microstrip Patch Antenna for 5G Mobile Communications Fatih Kaburcuk, Gurkan Kalinay, Yiming Chen, Atef Z. Elsherbeni, and Veysel Demir	824
Vortex Beam Optimization Design of Concentric Uniform Circular Array Antenna with Improved Array Factor Qiang Feng, Yifeng Lin, Yushan Zheng, and Long Li	830
An Adaptive Sparse Array Beamforming Algorithm Based on Approximate L_0 -norm and Logarithmic Cost Haixu Wang and YingSong Li	838
Reflectarray Resonant Element based on a Dielectric Resonator Antenna for 5G Applications Nur Fazreen Sallehuddin, Mohd Haizal Jamaluddin, Muhammad Ramlee Kamarudin, and Muhammad Hashim Dahri	844
A Highly Efficient Dual-Band Transmitarray Antenna Using Cross and Square Rings Elements Yongliang Zhang, Xiuzhu Lv, Jiaxuan Han, Shuai Bao, Yao Cai, and Zhao Wu	852
Dual-polarized Fixed-frequency Beam Scanning Leaky-wave Antenna for 5G Communication Hao Xiang Li and Yong Jin Zhou	858
Miniaturized Wideband Bandpass Filter based on Capacitor-loaded One-eighth Wavelength Coupled Line Jin Shi, Jiancheng Dong, Kai Xu, and Lingyan Zhang	865
A Wideband and Wide Scanning Tightly Coupled Dipole Array with Meta-Surface Wide-Angle Impedance Matching Yuan Ye, Zhao Yu Huang, Yun Jiang, Li-an Bian, Chang Zhu, Jing Jian Huang, and Nai Chang Yuan	872
Train-mounted Broadband Monopole Antenna for 5G Communication Hao Xiang Li, Lu Xu, Feng Qian, and Yong Jin Zhou	879
Single-Chip Two Antennas for MM-Wave Self-Powering and Implantable Biomedical Devices Dalia Elsheakh, Somaya Kayed, and Heba Shawkey	885

A Low-Profile and Beam-tilted Continuous Transverse Stub Array Antenna at W-band Demiao Chu, Yujun Xiong, and Ping Li	894
Design of W-band PIN Diode SPDT Switch with Low Loss Yun Jiang, Yuan Ye, Daotong Li, Zhaoyu Huang, Chao Wang, Jingjian Huang, and Naichang Yuan	901
Robust Adaptive Beamforming based on Automatic Variable Loading in Array Antenna Bin Yang, Wenxing Li, Yuanyuan Li, and Yunlong Mao	908
Ultra-wideband Transmissive Linear Polarization Device Based on Graphene Liwei Guo, Simin Li, Xing Jiang, Xin Liao, and Lin Peng	914
High-Q Active Microwave Sensor Based on Microstrip Complementary Split-Ring Resonator (MCSRR) Structure for Dielectric Characterization Hong-Yi Gan, Wen-Sheng Zhao, Da-Wei Wang, Jing Wang, Qi Liu, and Gaofeng Wang	922
Fast Analysis of Broadband Electromagnetic Scattering Characteristics of Electrically Large Targets using Precorrected Fast Fourier Transform Algorithm based on Near Field Matrix Interpolation Method Wei Bin Kong, Xiao Fang Yang, Feng Zhou, Jia Ye Xie, Chuan Jie Chen, Na Li, and Wen Wen Yang	928
A Compact High Gain Multiband Bowtie Slot Antenna with Miniaturized Triangular Shaped Metallic Ground Plane Zaheer A. Dayo, Qunsheng Cao, Yi Wang, Permanand Soothar, Imran A. Khoso, Gulab Shah, and Muhammad Aamir	935

A Dual-Band and Low-Cost Microstrip Patch Antenna for 5G Mobile Communications

Fatih Kaburcuk¹, Gurkan Kalinay², Yiming Chen³, Atef Z. Elsherbeni³, and Veysel Demir⁴

¹Department of Electrical-Electronics Engineering
Sivas Cumhuriyet University, Sivas, 58140, Turkey
fkaburcuk@cumhuriyet.edu.tr

²Department of Electrical-Electronics Engineering
Erzurum Technical University, Erzurum, 25050, Turkey
gurkan.kalinay@erzurum.edu.tr

³Department of Electrical Engineering
Colorado School of Mines, Golden, CO 80401, USA
yimingchen@mymail.mines.edu, aelsherb@mines.edu

⁴Department of Electrical Engineering
Northern Illinois University, Dekalb, IL 60115, USA
vdemir@niu.edu

Abstract — This paper investigates the numerical and experimental analysis of a low-cost and dual-band microstrip patch antenna for the fifth generation (5G) mobile communications. The numerical analysis of the proposed antenna is performed using the computational electromagnetic simulator (CEMS) software which is based on the finite-difference time-domain (FDTD) and CST software which is based on the finite integration technique (FIT). The performance of the proposed antenna designed and fabricated on a low-cost FR-4 substrate is verified with the simulated and measured results. The antenna operates at dual frequency bands which are 24 and 28 GHz. The antenna maximum gain values are 3.20 dBi and 3.99 dBi in the x - y plane at 24 and 28 GHz, respectively. The proposed antenna provides almost omni-directional patterns suitable for 5G mobile communication devices.

Index Terms — 5G antenna, dual-band antenna, low-cost antenna.

I. INTRODUCTION

The developments in the mobile communications industry have been increasing day by day due to the increasing use of wireless and mobile devices. Therefore, mobile communication technology [1] developed from the first generation (1G) to the fourth generation (4G) has become unable to meet the demands of the user today. The fifth generation (5G) technology [2], which can provide higher data rate, wider bandwidth, larger

capacity, and lower latency than 4G, has been developed to meet user demands. Thus, low-cost, lightweight, and low-profile antennas which have high performance over a wide bandwidth and are operated at licensed frequency bands are needed for 5G mobile communications. The 5G frequency bands [3-4] above 6 GHz announced by the Federal Communication Commission (FCC) [5] are licensed in the USA as 24.25-24.45 GHz, 24.75-25.25 GHz, 27.5-28.35 GHz, 37-37.6 GHz, and 37-38.6 GHz.

Some of the major differences between the 5G mobile communication technology and all previous technologies are to use the antennas operating at higher frequencies where it is easier to obtain wider bandwidth and to use efficient and high-performance antennas. Therefore, antenna design is one of the most important parts of 5G communication technology. The most common antenna type is the microstrip patch antenna, which is widely used due to its low-cost, small size, and light weight.

The antenna design for 5G communication brings new challenges to researchers. One of the challenges in antenna design for 5G mobile technology is the fabrication of small size antenna on a low-cost substrate such as FR-4, because it is too lossy especially at high frequencies. However, FR-4 is a common PCB fabrication material, the most cost effective, easy to find, and maintaining robust mechanical as well electrical characteristics. Therefore, this substrate provides significant cost saving to manufacturing companies for antennas. At higher frequency, it makes difficult to

design the antenna because of its reduced size, inaccuracy in the connector modelling, soldering issue between the connector pin and feeding line, and other inaccuracy of the fabrication capabilities.

In the literature, many microstrip antennas operating at 5G frequencies above 6 GHz [6–15] are proposed and characterized by their compactness, small geometric dimensions, antenna bandwidth, and gain. Most of these were not fabricated, not measured, just designed on a substrate having a low dielectric constant, ultra-low loss tangent, and high cost. However, the antenna proposed in this paper is designed and fabricated on a low-cost and lossy FR-4 substrate. Although the antenna is fabricated on a low cost and lossy substrate, the gain patterns and their maximum values of the antenna are at least as suitable as the antennas in the literature for 5G mobile communications.

II. ANTENNA DESIGN PARAMETERS

The geometry of the proposed antenna is shown in Fig. 1 and its dimensions are given in Table 1. The antenna is designed and printed on both sides of a low-cost FR-4 substrate with a relative permittivity of 4.4, thickness of 1.6 mm, and loss tangent of 0.025. The overall size of the antenna is 25 mm × 20 mm × 1.6 mm. There are two radiating patches on the front side of the substrate and a partial ground plane on the back side of the substrate. The numerical analysis of the antenna is performed using the computational electromagnetic simulator (CEMS) software [16] which is based on the finite-difference time-domain (FDTD) method [17] and on CST software [18] to verify their simulation consistency before fabrication and testing. The fabricated prototype of the antenna is shown in Fig. 2. The configuration of the simulation platform is Intel® Core™ i7-4790 CPU, 32 GB Random-Access Memory (RAM), and NVIDIA RTX 2070 Super GPU operating on Windows 10 system.

Table 1: Dimension of the proposed antenna

	F ₁	F ₂	F ₃	F ₄	P ₁	P ₂	G
Length (mm)	5	2	1	1.2	4.7	2.3	13.2
Width (mm)	2	0.8	0.4	0.4	7.4	3	25

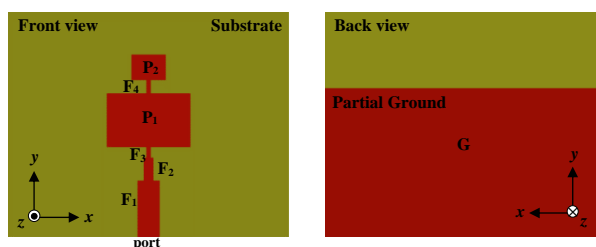


Fig. 1. Front and back views of the proposed antenna.

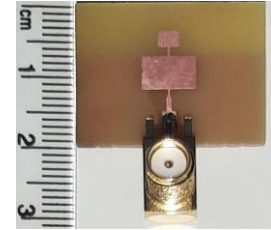


Fig. 2. Fabricated prototype of the proposed antenna.

A. CEMS simulation parameters

In CEMS simulation the problem space is composed of cubic cells and the choice of the cell size determines the accuracy of the solutions. In order to satisfy the numerical stability [17], the cell size should be less than $\lambda_{\min}/20$, where λ_{\min} is the wavelength of the highest frequency in the problem space. Therefore, in this work, the cell size of the problem in all directions is set to 0.1 mm which is less than $\lambda_{\min}/20$. The problem space is terminated by 10 layers of convolutional perfectly matched layer [19] with 15 cell layers of air buffer. The total number of cells in the problem space is 4,950,000. The simulation shows reasonable convergence after 8000 time-steps with the GPU computing capability of almost 2 billion cells per second (MCPS) execution. The resulting total simulation time of this antenna is 19.8 seconds in CEMS running on the GPU specified in Section II.

B. CST simulation parameters

Commercial electromagnetic software CST is used to verify the accuracy of the simulation based on CEMS package. To keep consistency as much as possible, time-domain solver is also selected in CST, while unlike the FDTD method applied by CEMS, FIT is processed as the simulation method in CST. As for the working space, there are 365,040 total adaptive cells, in which the cell sizes are $\lambda_{\min}/15$ for the maximum and $\lambda_{\min}/20$ for the minimum. It should be pointed out that CST simulation of this antenna is computed on CPU due to the GPU limitation in CST educational license. All the other settings and the dimensions are kept the same as those in CEMS and the total simulation time was 163 seconds. The performance of this design based on CST and CEMS will be illustrated in the following section.

III. NUMERICAL AND EXPERIMENTAL RESULTS

A. Input reflection coefficient and radiation pattern

The simulated and measured input reflection coefficients (S_{11}) of the dual-band antenna are shown in Fig. 3 with good agreement at operation frequencies of 24 and 28 GHz. There are some acceptable differences between the measured and simulated results. The reasons

of these differences might be due to poor soldering for the SMA connector, fabrication tolerance, losses on the SMA connector and coaxial cable, etc. The simulated gain patterns on the three plane cuts (x - y , x - z , and y - z) of the antenna at 24 and 28 GHz are shown in Fig. 4. The gain patterns in the x - y and x - z planes of the antenna are almost omni-directional. The omni-directionality of the antenna in the x - y plane at 24 and 28 GHz is 68.6% and 45%, respectively, for a gain difference of 6 dBi. The omni-directionality of the antenna in the x - z plane at 24 and 28 GHz is 81.9% and 85.8%, respectively. The performance parameters of the simulated and measured antenna are given in Table 2.

B. Effect of patches and ground plane

The antenna is composed of two patches: the smaller one (P_2) and the larger one (P_1). In order to show the effects of the sizes of the two radiating patches and the ground plane on the antenna performance, the proposed dual-band patch antenna is optimized in three different scenarios. First only P_1 is optimized (Case 1); then P_1 and P_2 are the optimization parameters with full ground plane (Case 2) and finally only P_2 is optimized (Case 3). The geometries of the three cases are presented in Fig. 5. Figure 6 shows the S_{11} of the antennas obtained using CEMS for these cases. The performance parameters of the antennas for the three cases are given in Table 3. The simulated results show that the proposed antenna provides good impedance matching, bandwidth, and better or comparable gain over the resonance frequencies of 24 and 28 GHz compared to other cases.

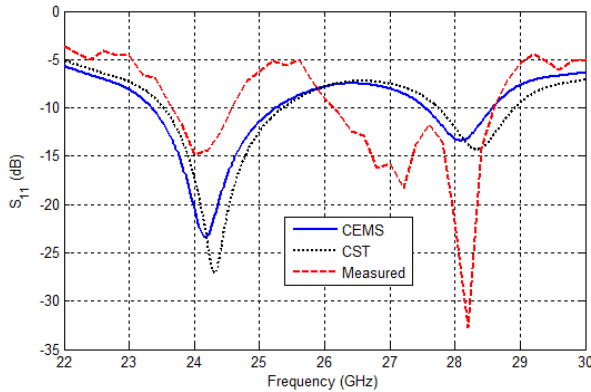


Fig. 3. Simulated and measured S_{11} of the antenna.

Table 2: Performance parameters of the proposed antenna

	Resonance Freq. (GHz)	S_{11} (dB)	Freq. Range (GHz)	Bandwidth (MHz)	Gain (dBi)
CEMS	24.16	-23.4	23.36-25.26	1900	3.20
	28.1	-13.4	27.56-28.57	1010	3.99
CST	24.31	-27.12	23.54-25.36	1820	3.53
	28.34	-14.33	27.75-28.91	1160	3.86
Measured	24	-14.86	23.7-24.6	900	-
	28.2	-32.72	26.2-28.5	2300	-

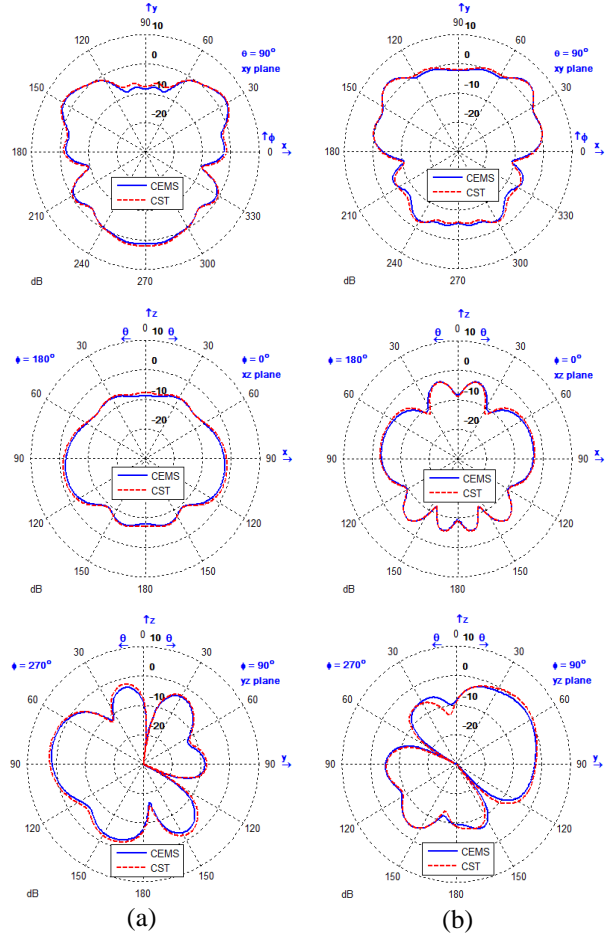


Fig. 4. Gain patterns of the antenna on the three plane cuts at (a) 24 GHz and (b) 28 GHz.

Table 3: Performance parameters of different configurations of the antennas

	Resonance Freq. (GHz)	S_{11} (dB)	Freq. Range (GHz)	Bandwidth (MHz)	Gain (dBi)
Case 1	24.12	-27.97	23.36-25.20	1840	2.11
	28.06	-11.61	27.50-28.46	960	4.02
Case 2	23.98	-19.27	23.10-24.86	1760	2.49
	27.20	-14.71	26.52-27.96	1440	2.85
Case 3	21.36	-20.72	20.22-23.24	3020	0.66
	26.26	-15.24	25.64-26.84	1200	0.74

C. Substrate thickness effects

By increasing and decreasing the thickness (h) of the FR-4 substrate, the antenna performance is investigated. The S_{11} of the antennas on the thickness of 0.8, 1.6, and 2.4 mm FR-4 substrate is shown in Fig. 7. The performance parameters of the simulated antennas are given in Table 4. The results in the table show that the thickness of substrate has a significant impact on the resonance frequencies, bandwidth, and gain. The antenna on the 0.8 mm substrate has a wider bandwidth than the proposed antenna, but its maximum gain values are lower than the proposed antenna. In addition, it is

seen from Fig. 7 that the antenna on the 2.4 mm substrate has an S_{11} value above -10 dB in the specified frequency bands.

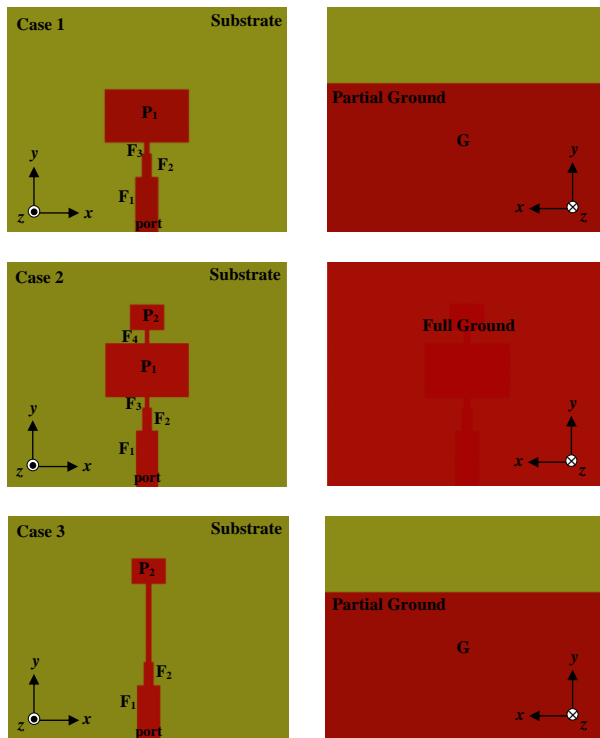


Fig. 5. Geometry of the antennas for three different cases.

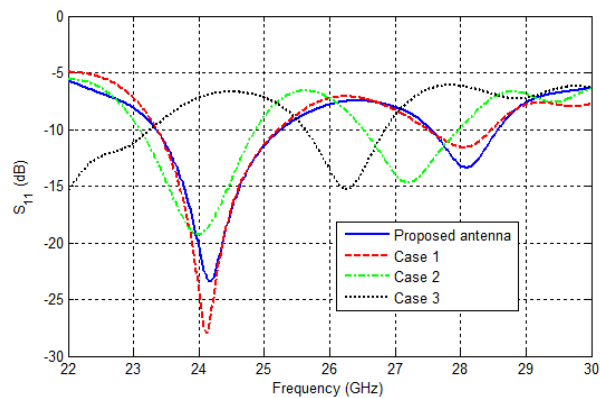


Fig. 6. Simulated S_{11} of the antennas for three different cases.

Table 4: Performance parameters of the antenna on different thickness of substrate

Thickness (mm)	Resonance Freq. (GHz)	S_{11} (dB)	Freq. Range (GHz)	Bandwidth (MHz)	Gain (dBi)
0.8	23.94	-17.76	22.54-25.74	3200	2.48
	27.22	-21.37	25.74-28.18	2440	0.55
1.6	24.16	-23.4	23.36-25.26	1900	3.20
	28.1	-13.4	27.56-28.57	1010	3.99

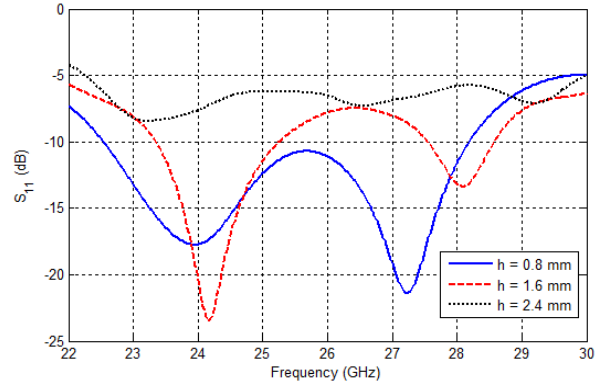


Fig. 7. Simulated S_{11} of the proposed antenna on the thickness of 0.8, 1.6, and 2.4 mm FR-4 substrate.

VI. CONCLUSION

Numerical and experimental analysis of the proposed microstrip patch antenna on a low-cost FR-4 substrate are presented for 5G mobile communications. The numerical analysis of the antenna is performed using CEMS software which is based on FDTD method and on CST software. The simulated and measured input reflection coefficients of the antenna are in good agreement at 24 and 28 GHz. The maximum gain values are 3.20 dBi and 3.99 dBi at 24 and 28 GHz, respectively. The proposed antenna has good performance in a small form factor which makes it a good candidate for 5G handheld devices.

REFERENCES

- [1] P. Gupta, "Evolution of mobile generations: 1G to 5G", *International Journal for Technological Research in Engineering*, vol. 1, pp. 152-157, 2013.
- [2] J. G. Andrews, S. Buzzi, W. Choi, S. V. Hanly, A. E. Lozano, A. C. K. Soong, and J. C. Zhang, "What will 5G be?," in *IEEE Journal on Selected Areas in Communications*, vol. 32, no. 6, pp. 1065-1082, June 2014.
- [3] <https://www.qualcomm.com/media/documents/files/spectrum-for-4g-and-5g.pdf>
- [4] https://www.5gamerica.org/wp-content/uploads/2019/07/5G_Americas_Spectrum_Recommendations_for_the_U.S_Final.pdf
- [5] <https://www.fcc.gov/5G>
- [6] O. M. Haraz, M. M. M. Ali, S. Alshebeili, and A. Sebak, "Design of a 28/38 GHz dual-band printed slot antenna for the future 5G mobile communication networks," *2015 IEEE International Symposium on Antennas and Propagation & USNC/URSI National Radio Science Meeting*, pp. 1532-1533, 2015.
- [7] N. Ojaroudiparchin, M. Shen, and G. F. Pedersen, "A 28 GHz FR-4 compatible phased array antenna

- for 5G mobile phone applications,” *2015 International Symposium on Antennas and Propagation (ISAP)*, pp. 1-4, 2015.
- [8] G. Gampala and C. J. Reddy, “Design of millimeter wave antenna arrays for 5G cellular applications using FEKO,” in *2016 IEEE/ACES International Conference on Wireless Information Technology and Systems (ICWITS) and Applied Computational Electromagnetics (ACES)*, pp. 1-2, Mar. 2016.
- [9] D. Alvarez Outerelo, A. V. Alejos, M. Garcia Sanchez, and M. Vera Isasa, “Microstrip antenna for 5G broadband communications: Overview of design issues,” *2015 IEEE International Symposium on Antennas and Propagation & USNC/URSI National Radio Science Meeting*, pp. 2443-2444, 2015.
- [10] Y. Jandi, F. Gharnati, and A. Oulad Said, “Design of a compact dual bands patch antenna for 5G applications,” *2017 International Conference on Wireless Technologies, Embedded and Intelligent Systems (WITS)*, pp. 1-4, 2017.
- [11] S. X. Ta, H. Choo, and I. Park, “Broadband printed-dipole antenna and its arrays for 5G applications,” in *IEEE Antennas and Wireless Propagation Letters*, vol. 16, pp. 2183-2186, 2017.
- [12] A. F. Kaeib, N. M. Shebani, and A. R. Zarek, “Design and analysis of a slotted microstrip antenna for 5G communication networks at 28 GHz,” *2019 19th International Conference on Sciences and Techniques of Automatic Control and Computer Engineering (STA)*, pp. 648-653, 2019.
- [13] B. Hicdurmaz and Ö. F. Gumus, “Design and analysis of 28 GHz microstrip patch antenna for different type FR-4 claddings,” *Uludag University Journal of the Faculty of Engineering*, vol. 24, no. 2, 2019.
- [14] P. M. Teresa and G. Umamaheswari, “Compact slotted microstrip antenna for 5G applications operating at 28 GHz,” *IETE Journal of Research*, pp. 1-8, 2020.
- [15] R. Przesmycki, M. Bugaj, and L. Nowosielski, “Broadband microstrip antenna for 5G wireless systems operating at 28 GHz,” *Electronics*, vol. 10, no. 1, 2021.
- [16] V. Demir and A. Z. Elsherbeni, “Computational electromagnetic simulator,” Software Package version 4, veysdemir@gmail.com, Apr. 2021.
- [17] A. Z. Elsherbeni and V. Demir, *The Finite-Difference Time-Domain Method for Electromagnetics with MATLAB Simulations*, second edition, ACES Series on Computational Electromagnetics and Engineering, SciTech Publishing, an Imprint of IET, Edison, NJ, 2016.
- [18] CST Microwave Studio, ver. 2008, Computer Simulation Technology, Framingham, MA, 2008.
- [19] M. Kuzuoglu and R. Mittra, “Frequency dependence of the constitutive parameters of causal perfectly matched anisotropic absorbers,” *IEEE Microwave Guided Wave Letters*, vol. 6, no. 12, pp. 447-449, 1996.



Fatih Kaburcuk received both the M.Sc. and Ph.D. degrees from Syracuse University, Syracuse, NY, USA, in 2011 and 2014, respectively, all in Electrical Engineering. During his graduate studies, he worked as a Research Assistant with Syracuse University and PPC-Belden Inc. in

Liverpool, NY, USA. He worked as a Visiting Research Scholar at the Department of Electrical Engineering, Colorado School of Mines, Golden, CO, USA in 2014. He joined the Erzurum Technical University in 2015 and served as an Assistant Professor until 2019. Currently, Kaburcuk has been serving as an Associate Professor with the Department of Electrical-Electronics Engineering, Sivas Cumhuriyet University, Turkey. His research interest includes numerical methods in electromagnetics, biological effect of electromagnetic radiation, and finite-difference time-domain analysis of antennas and RF devices.



Gurkan Kalinay received the B.S. degree from the Department of Electrical-Electronics Engineering, Erzurum Technical University, Erzurum, Turkey, in 2018. He is currently pursuing his M.Sc. degree at Erzurum Technical University. During his graduate studies, he works as a Research Assistant with Erzurum Technical University. His main research interests are in design of antennas and RF devices.



Yiming Chen was born in Henan, China, in 1993. He received the B.S. degree from the Department of Electronic and Electrical Engineering, Northeast Agricultural University, Harbin, China, in 2016 and the M.S. degree in the Department of Electrical Engineering, China University of Mining and Technology, Xuzhou, China, in 2019. Now he is pursuing the Ph.D. degree at the Department of Electrical Engineering, Colorado School of Mines, Colorado, USA. His main research interests are in metasurface and antennas for RFID applications.



Atef Z. Elsherbeni received two honor B.Sc. degrees in Electronics and Communications, in Applied Physics, and a M.Eng. degree in Electrical Engineering, all from Cairo University, Egypt, in 1976, 1979, and 1982, respectively, and a Ph.D. degree in Electrical Engineering from Manitoba University, Winnipeg, Manitoba, Canada, in 1987. He started his engineering career as a part time Software and System Design Engineer from March 1980 to December 1982 at the Automated Data System Center, Cairo, Egypt. Elsherbeni joined the faculty at the University of Mississippi in 1987 as an Assistant Professor of Electrical Engineering. He advanced to the ranks of Associate Professor and Professor in 1991 and 1997, respectively, and became the Associate Dean for Research and Graduate Programs from 2009 to 2013. He then joined the EECS Department at Colorado School of Mines in August 2013 as the Dobelman Distinguished Professor. He was appointed the Interim Department Head for EECS department from 2015 to 2016 and became the EE Department Head from 2016 to 2018. He spent a sabbatical term in 1996 at the EE Department, University of California at Los Angeles (UCLA) and was a visiting Professor at Magdeburg University in Germany and at Tampere University of Technology in Finland during the summers of 2005 and 2007, respectively. In 2009 he was selected as Finland Distinguished Professor by the Academy of Finland and TEKES. Elsherbeni is the Editor-in-Chief for ACES Journal, a past Associate Editor to Radio Science Journal, a past Chair of the Engineering and Physics Division of Mississippi Academy of Science, a past Chair of Educational Activity Committee for IEEE Region 3 Section, and the general Chair for the 2014 APS-URSI Symposium, the president of ACES Society from 2013 to 2015, and the IEEE Antennas and Propagation Society (APS) Distinguished Lecturer for 2020-2023. Elsherbeni is a Fellow member of IEEE and ACES.



Veysel Demir is an Associate Professor at the Department of Electrical Engineering at Northern Illinois University. He received his Bachelor of Science degree in Electrical Engineering from Middle East Technical University, Ankara, Turkey, in 1997. He studied at Syracuse University, New York, where he received both a Master of Science and Doctor of Philosophy degrees in Electrical Engineering in 2002 and 2004, respectively. During his graduate studies, he worked as a Research Assistant for Sonnet Software, Inc., Liverpool, New York. He worked as a visiting Research Scholar in the Department of Electrical Engineering at the University of Mississippi from 2004 to 2007. He joined Northern Illinois University in August 2007 and served as an Assistant Professor until August 2014. He has been serving as an Associate Professor since then.

Vortex Beam Optimization Design of Concentric Uniform Circular Array Antenna with Improved Array Factor

Qiang Feng, Yifeng Lin, Yushan Zheng, and Long Li*

Key Laboratory of High Speed Circuit Design and EMC of Ministry of Education
School of Electronic Engineering
Xidian University, Xi'an, 710071, China
*lilong@mail.xidian.edu.cn

Abstract — In this paper, an improved array factor of the concentric uniform circular array (CUCA) antenna is proposed for the orbital angular momentum (OAM) vortex beam optimization design. From the perspective of the radiation pattern's power conservation principle, a correction factor is introduced to the conventional array factor of CUCA. Then, based on the improved array factor, by adjusting the rings' radii parameters of the CUCA, we optimize the vortex beam's sidelobe level through the generic algorithm (GA). Two different CUCA antenna model are calculated as examples to further illustrate the effectiveness of the improved array factor. Subsequently, an electromagnetic simulation model of two rings CUCA antenna is built at C band for generating low sidelobe vortex beam carrying OAM mode. The electromagnetic simulation model of the designed CUCA antenna is also fabricated and measured. The corresponding antenna far-field vortex beam radiation pattern and near-field vortex wave electric field distributions are measured. The simulation results and the measurement results are in good agreement. The proposed designs of antenna and OAM vortex beam regulation are expected to be used for 5G and 6G communications applications.

Index Terms — Concentric uniform circular array (CUCA), Generic algorithm (GA), orbital angular momentum (OAM), sidelobe suppression, uniform circular array (UCA), vortex beam.

I. INTRODUCTION

It has been many years since the concept of the orbital angular momentum (OAM) was presented [1]. In 2007, the OAM was introduced in radio domain through the uniform circular array (UCA) antenna [2], and then it was systematically researched [3]. The OAM was considered to be applied in communication and radar field [4-7], although there were still some controversies about it [8-12]. At the same time, many kinds of OAM vortex wave antennas were developed [13]. The array antenna especially UCA antenna [4, 7] and metasurface

antenna [14-17] are comparatively more widely used.

Since the UCA antennas were researched systematically, it was widely researched in wireless communication [4, 18, 19] and radar imaging [7, 20]. However, there are still many important problems needed to be solved [4, 11], and one of them is the vortex beam optimization design, such as the sidelobe suppression. It seems that a few publications consider this issue. In the communication domain, it was referred in [4] that the high peak intensity sidelobe of the vortex beam caused the power dissipation, but no better solutions were presented. In the radar domain, the CUCA antenna [7, 20] were used for vortex beam alignment and sidelobe suppression. In [7], the multiple OAM modes vortex beams' mainlobe alignments were realized by changing the different rings' radii of the CUCA. For different types of single OAM mode vortex beam, in [20], the vortex beam sidelobe suppression and beam collimation were achieved simultaneously through controlling the excitation amplitude of the CUCA with the fixed array radiuses.

Nevertheless, we find some drawbacks that were not evidently noticed in the previous related researches when they design and simulate the UCA antenna models. We note that the UCA array factor used in the traditional design process is inaccurate especially in the CUCA design, which is virtually an approximation. In this paper, we introduce a correction factor (CF) to improve this deficiency. The improved CUCA array factor is utilized in our vortex beam optimization design. Then, through the generic algorithm (GA) optimization about the radius settings of the CUCA, the low sidelobe vortex beam can be realized. The rest parts of this paper are organized as follows. In Section II, the CUCA model is reanalyzed and the correction factor (CF) for the CUCA antenna array factor is presented. Then, it is the specific optimization process and the related analysis through the GA. In Section III, an electromagnetic full-wave simulation model of a two rings CUCA antenna is optimized, designed, and built, based on the improved array factor, and the corresponding vortex beam

radiation pattern analysis are carried out. Finally, we fabricated the designed two rings CUCA antenna. The corresponding far-field and near-field measurement are finished. Section IV is the conclusion.

II. CONCENTRIC UNIFORM CIRCULAR ARRAY (CUCA) ANTENNA MODEL AND THE GA OPTIMIZATION DESIGN

In this part, the CUCA model's array factors are reanalyzed, and the correction factor (CF) is introduced for improving the accuracy of the CUCA's array factor. Then, based on the improved array factor, a corresponding new fitness function for GA is derived for vortex beam sidelobe suppression optimization design. By optimizing the radius parameters of the CUCA, the best radius parameters are obtained. The corresponding design and optimization processes are also presented in detail.

A. CUCA antenna model re-describe

A general CUCA antenna model is shown in Fig. 1, and the array factor of the single UCA can be written as [3, 21],

$$\begin{aligned} AF_i(\mathbf{r}) &= \sum_{n=0}^{N-1} \frac{1}{|\mathbf{r} - \mathbf{r}_n|} e^{jk|\mathbf{r} - \mathbf{r}_n|} e^{j\ell\varphi_n} \\ &\approx \frac{e^{jkr}}{r} \sum_{n=0}^{N-1} e^{-j(k\hat{\mathbf{r}} \cdot \mathbf{r}_n - \ell\varphi_n)} \\ &\approx N_i j^{-\ell} \frac{e^{jkr}}{r} e^{j\ell\varphi} J_\ell(ka \sin \theta) \end{aligned} \quad (1)$$

where $\varphi_n = 2\pi n / N$ is the azimuth angle of the n_{th} array element of the UCA, and ℓ is the OAM mode number. The array factor of the CUCA is,

$$AF_c(\mathbf{r}) = \sum_{i=1}^m N_i j^{-\ell} \frac{e^{jkr}}{r} e^{j\ell\varphi} J_\ell(ka_i \sin \theta), \quad (2)$$

where i means the i_{th} ring of the CUCA. Noting that there are some approximations in the formula derivation process: the far-field approximation of $|\mathbf{r} - \mathbf{r}_n| \approx r - \hat{\mathbf{r}} \cdot \mathbf{r}_n$ for phase approximation, and $|\mathbf{r} - \mathbf{r}_n| \approx r$ for amplitude approximation. Simultaneously, note that there is also another approximation which is very important that could be ignored, i.e., the Bessel function in (1) is actually obtained when N is large enough. However, if N is not large enough, this approximation will no longer be hold. This problem is not obvious in the single ring UCA design, but it will affect the accuracy of the CUCA's vortex beam design.

We introduce a correction factor (CF) to correct this inaccuracy based on the principle of power conservation. The approximate $AF(\mathbf{r})$ in (1) includes the item $J_\ell(ka \sin \theta)$ whose parameter a will lead to the shape stretch or squeeze of this Bessel function, $J_\ell(ka \sin \theta)$,

with its peak value remained unchanged, which is unreasonable compared with the actual UCA antenna radiation. As researched in [3], when the radius of the UCA changes, the obtained radiation pattern gain will also change, i.e., as the UCA radius increases, the gain of the vortex beam also increases. Thus, in order to solve the problem of this inconsistency, we add a correction factor (CF) into the $AF(\mathbf{r})$. The CF is defined as,

$$\begin{aligned} CF(i) &= \sqrt{1/P_i} \\ &= \sqrt{1 / \left\{ \frac{1}{N_i} \int_0^{90} AF_i^2(\theta) d\theta \right\}}, \end{aligned} \quad (3)$$

where P_i is the normalized power which excludes the influence of N_i , the array elements number of the single ring UCA. Considering the symmetry and calculation concise, only quarter space of the radiation pattern, i.e., the angle range from 0 degree to 90 degree, are calculated. Thus, the corrected array factor of the i_{th} ring UCA could be,

$$AF'_i(\mathbf{r}) = AF_i(\mathbf{r}) \cdot CF(i). \quad (4)$$

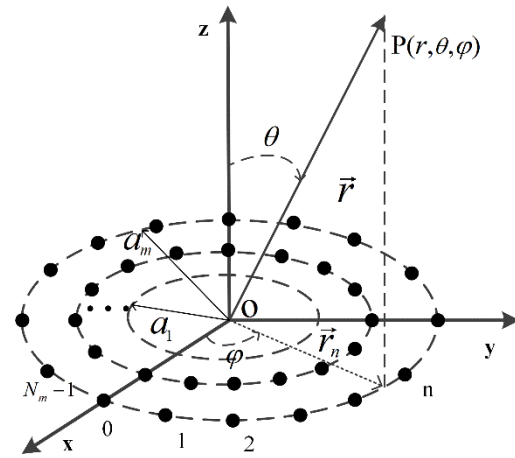


Fig. 1. The CUCA model. It is composed by several rings UCA with different radii, a_i . The array element number of each UCA is N_i , $i=1,2,\dots,m$, and m is the ring number of the CUCA.

Then the corresponding array factors of an eight elements UCA antenna model under different radius parameters are calculated. Note that the working frequency is 4.25 Hz with working wavelength of $\lambda = 0.07$ m, and the order of the Bessel function is $\ell = 1$ which corresponds to the OAM mode number $\ell = 1$. As shown in Fig. 2, the normalized array factor change curves versus different UCA radii are compared together under the condition whether the CFs are added. As shown in Fig. 2 (a), when the UCA's radius changes, its array factor curve is stretched or squeezed while holding the same peak value. From the perspective of power

conservation, this is unreasonable. Thus, as shown in Fig. 2 (b), the CFs are used. As the UCA's radius changes, the array factor curve's peak value adjusts correspondingly. For example, when the UCA's radius decreases, its radiation pattern will be stretched, and thus the corresponding peak value will turn to be decreased. We remark that the array factor curves calculated with the CFs turn to be more reasonable and more close to the real radiation pattern.

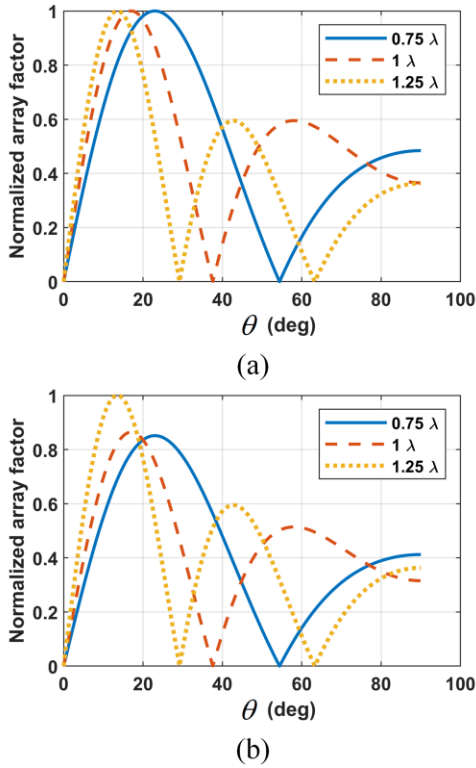


Fig. 2. The normalized array factor change curves under different UCA radiuses, (a) without CF and (b) with CF. Three different UCA radiuses are used here, 0.75λ , 1λ , and 1.25λ .

B. GA optimization design and two calculation examples

In this subsection, based on the improved array factor of the CUCA, the array optimization design for vortex beam's sidelobe suppression through the GA is performed. We describe the corresponding optimization problem and optimization process in detail. Then, two different CUCA antenna models are calculated as the examples to further illustrate the effectiveness of the improved array factor with the correction factor (CF).

The array factor of the CUCA can be rewritten as,

$$\begin{aligned} AF_c(\mathbf{r}) &= \sum_{i=1}^m \{N_m j^{-i} \frac{e^{jkr}}{r} e^{j\ell\varphi} J_\ell(ka_i \sin\theta)\} \cdot CF(i) \\ &= \sum_{i=1}^m AF_i(\theta) \cdot CF(i) \end{aligned} \quad (5)$$

The fitness function of the GA can be expressed as,

$$f(\mathbf{a}) = P_{side} / P, \quad (6)$$

where $\mathbf{a} = (a_1, a_2, \dots, a_i)$, P_{side} is the power level of the sidelobe, and P is the peak power level of the CUCA's array factor. Thus, the corresponding optimization problem turns to be as follows,

$$\min f(\mathbf{a}) \quad \text{s.t.} \quad \begin{cases} \mathbf{A}\mathbf{a} \leq \mathbf{b}, \\ lb_i \leq a_i \leq ub_i \end{cases} \quad (7)$$

\mathbf{A} is the corresponding coefficient matrix used for restricting the radii of the CUCA's rings. $\mathbf{a} = (a_1, a_2, \dots, a_i)^T$ is the vector constituted by the radii of the different rings of the CUCA, in which expression $(*)^T$ means the matrix transpose. \mathbf{b} is the corresponding coefficient vector. $\mathbf{lb} = (lb_1, lb_2, \dots, lb_i)$ and $\mathbf{ub} = (ub_1, ub_2, \dots, ub_i)$ are the low boundary and up boundary constraints of the different rings's radii of the CUCA. All these optimization parameters, including matrix \mathbf{A} , vector \mathbf{b} , low boundary \mathbf{lb} , and up boundary \mathbf{ub} , are decided by the specific CUCA configurations.

Then, we calculate two examples: one example is a two rings CUCA model, and the other example is a three rings CUCA model. In both these two calculation examples, three different situations are compared, the CUCA's array factor calculated with the CF, the CUCA's array factor calculated without the CF, and the exact array factor calculation using pattern multiplication, i.e., exact calculation. We calculated the two rings CUCA antenna model and three rings CUCA antenna model respectively as follows. Note that the rings' radius parameters are optimized through the GA, and the optimized array factor with the CF is adopted here. The corresponding GA optimize processes are mainly realized by the optimization tool in MATLAB. The main related parameters configurations about the GA are listed in Table 1, and the other related optimization parameters are default. Note that for the Mutation function and Crossover function, the default options 'Constraint dependent' was adopted in the 'optimtool' of MATLAB.

Table 1: The relevant parameters settings of GA in MATLAB

Population Size	Optimization Variable Number	Crossover Fraction	Mutation Function	Crossover Function	Stopping Criteria	
					Generations	Function Tolerance
50	2 or 3	0.8	'Constraint dependent'	'Constraint dependent'	Optimization variable number \times 100	10^{-6}

For three rings CUCA antenna model, it has 8 array elements, 14 array elements and 20 array elements for each ring. The boundary constraints adopted here in the GA optimization are set as,

$$\mathbf{A} = \begin{bmatrix} 1 & -1 & 0 \\ 0 & 1 & -1 \end{bmatrix}, \mathbf{b} = \begin{bmatrix} -0.025 \\ -0.025 \end{bmatrix},$$

$$\mathbf{lb} = (0.045, 0.07, 0.095), \quad (8)$$

$$\mathbf{ub} = (0.12, 0.12, 0.14).$$

Note that the length unit used here is meter and the working frequency is 4.25 GHz with working wavelength of 0.07 m. For the two rings CUCA antenna model with 8 elements and 14 elements, its boundary constraints adopted in the GA optimization are set as,

$$\mathbf{A} = \begin{bmatrix} 1 & -1 \end{bmatrix}, \mathbf{b} = [-0.025],$$

$$\mathbf{lb} = (0.045, 0.07), \quad (9)$$

$$\mathbf{ub} = (0.12, 0.12).$$

Note that all these parameters are selected based on the given CUCA antenna model's configurations, which considers the factors such as the interval space between the array elements, the interval space between the different UCA rings, and the amount of the array elements of the CUCA.

After performing the GA optimization, we obtain the optimized radius parameters of the CUCA models as follows. For the two rings CUCA model, we select the optimized radiuses parameters as 45 mm and 86 mm. The calculated array factor curves under three different situations are compared together in Fig. 3 (a). For the three rings CUCA model, its optimized radiuses of the three rings are 47.2 mm, 71.2 mm, and 112.3 mm respectively. The calculated array factor curves are compared in Fig. 3 (b) as follows. From these two calculation examples, it is obvious that the array factor curve calculated with adding the CF is closer to the exact calculation results. For the calculated array factor with CF, although there are still some inconsistencies, its main radiation pattern parameters, such as the mainlobe's beam width, and the sidelobe's zero positions, are more consistent with the array factor calculated under the exact calculation.

Noting that the CUCA model used in this paper is an ideal antenna model, and we mainly solve this problem from a pure mathematical perspective. Although only the array factor of the antenna array is considered, however, it usually has an important weight

in antenna array design. In practical antenna design and optimization design process, the array antenna design theory must be followed.

For example, in this paper, N is the array element number of each UCA. From a pure mathematical perspective, N is arbitrary, however, in practical antenna design process, the actual antenna size limit, as well as the array antenna elements' interval distance and their mutual coupling constraints, all these factors will restrict the number of N . In practical optimization design, the applicable range of N is usually determined by the actual antenna array model. Moreover, for the GA optimization, the selection of the boundary constraints is also important, different boundary constraints selection could lead to different optimization results.

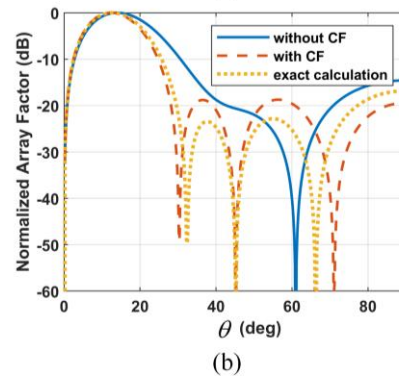
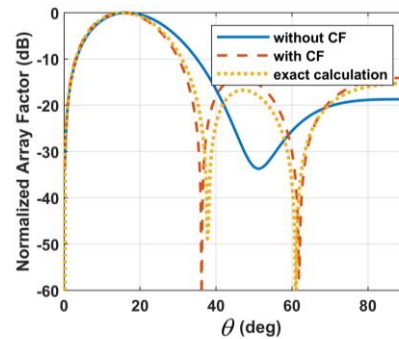


Fig. 3. Comparison about the calculated array factors of two rings CUCA and three rings CUCA under these three different situations, without the correction factor (CF), with the correction factor (CF), and exact calculation. (a) The two rings CUCA antenna model; (b) the three rings CUCA antenna model.

III. ARRAY ANTENNA SIMULATION AND MEASUREMENT

In this part, the electromagnetic (EM) simulation models of the CUCA antenna with the optimized rings' radii is built through EM simulation software ANSYS HFSS to realize low sidelobe vortex beam design with OAM mode number $\ell = 1$ at center frequency 4.25 GHz. Two other antenna array models are also built as references: One model is a single ring UCA antenna, and the other model is a double rings CUCA antenna whose ring radiuses are different from the optimized radius parameters values. Finally, the optimized CUCA antenna is fabricated, and it is measured in both far-field and near-field environment.

A. Array antenna simulation

Considering the electromagnetic simulation model construction and the ease of the prototype fabrication and measurement, we optimized another two rings CUCA antenna model with eight elements for each rings. Adopting the GA optimization process mentioned above, based on the improved array factor of the CUCA, finally, we select a group optimized radius parameters, 54 mm and 98 mm, as our design parameters for the simulated EM simulation model of the two rings CUCA antenna.

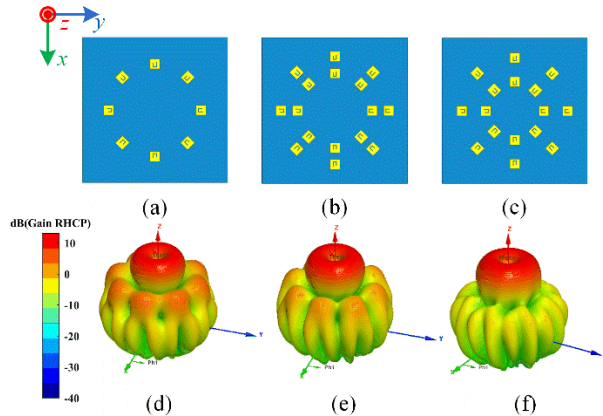


Fig. 4. The size of the array are all same with $260 \text{ mm} \times 260 \text{ mm} \times 2 \text{ mm}$, and the substrate used here is F4B whose $\epsilon_r = 2.65$. (a) The single ring UCA whose radius is 86 mm; (b) the double rings CUCA, $a_1 = 69 \text{ mm}$, and $a_2 = 100 \text{ mm}$; (c) the optimized CUCA, $a_1 = 54 \text{ mm}$, and $a_2 = 99 \text{ mm}$; (d)-(f) the simulated 3D radiation patterns.

Together with the other two reference array antenna model, these three different EM simulation models are shown in Figs. 4 (a)-(c), whose 3D far-field radiation patterns are shown in Figs. 4 (d)-(f). What needs to be mentioned here is that a center feeding right hand circular polarization (RHCP) antenna is used as the array

element to simplify the later feeding network design, because an optional excitation phase of the array element can be easily realized by centrally rotating the certain angle of the antenna element [22, 23]. But for brevity, it is not exhibited here in detail. In Fig. 5, the 2D radiation gain pattern of these three different array antenna models are compared together. The optimization array with sidelobe suppression has slightly larger gain than the other two models' gain. The optimized CUCA antenna does work, whose sidelobe level is obviously better than the other two reference models, and it obtains nearly -15 dB vortex sidelobe level.

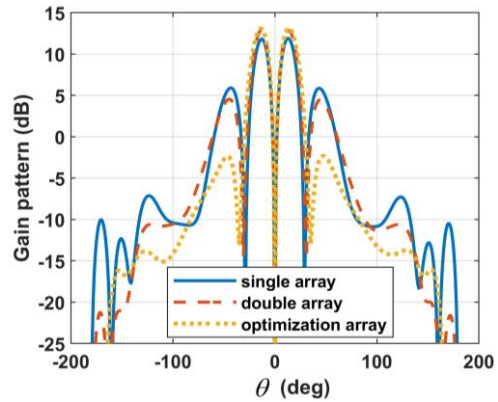


Fig. 5. The 2D radiation gain pattern comparisons between the three different CUCA antenna models. The exact maximum gain values of the single array, double array, and optimization array are 11.8 dB, 12.8 dB, and 13.1 dB respectively.

B. Array antenna measurement

The fabricated prototype corresponding to the CUCA model in Fig. 4 (c) is shown in Fig. 6. A 16 ways power divider module is used for antenna array feeding, which was connected to the antenna array by the same RF cables with same length. Before the actual test in the microwave anechoic chamber, the S11 of the prototype antenna is measured as shown in Fig. 7, which satisfies the general engineering requirements.

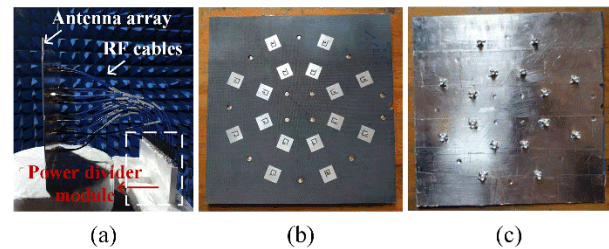


Fig. 6. (a) The whole prototype of the antenna array with the feeding network. The size of the array prototype is $260 \text{ mm} \times 260 \text{ mm} \times 2 \text{ mm}$. (b) Top side view, and (c) bottom side view.

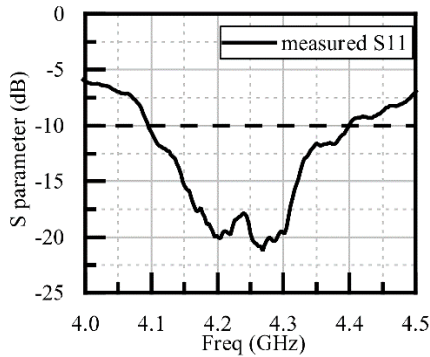


Fig. 7. The measured S_{11} of the prototype antenna.

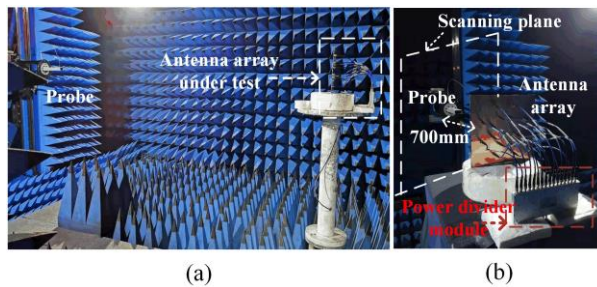


Fig. 8. (a) The far-field measurement environment. (b) The near-field measurement environment, and the distance between the measurement probe and the antenna array is 700 mm, the scanning plan is 800 mm \times 800 mm with sample period of 16 mm leading to 51 \times 51 sampling grid.

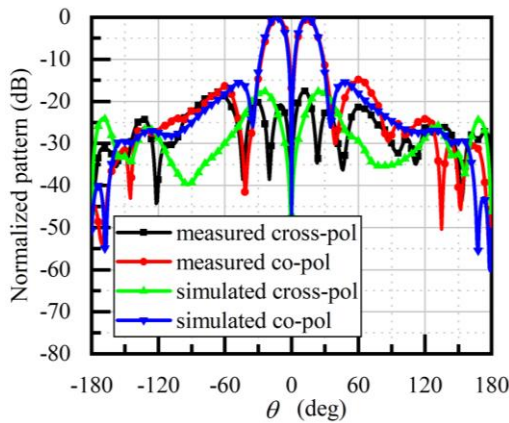


Fig. 9. The 2D radiation pattern comparisons between the simulated results and the measured results.

The far-field and near-field measurement environment are shown in Figs. 8 (a) and (b) respectively. In Fig. 9, the simulated 2D radiation pattern and the measured results are compared together, which are consistent. It can be seen that a nearly -15 dB sidelobe level is realized. Finally, the vortex beam electric field

distributions are measured and they are compared with the simulation results as shown in Fig. 10, which are consistent well. From Figs. 10 (a) and (b), it is obvious that the typical ‘doughnut’ shape electric field distribution and spiral phase distribution are obtained, and the circular polarization OAM vortex wave carrying OAM mode number $\ell = 1$ is realized. In Fig. 11, it performs a further OAM mode purity analysis [24] about the measured vortex electric field, in which the principal OAM mode component of OAM mode number $\ell = 1$ is obviously higher than the other modes about 18 dB.

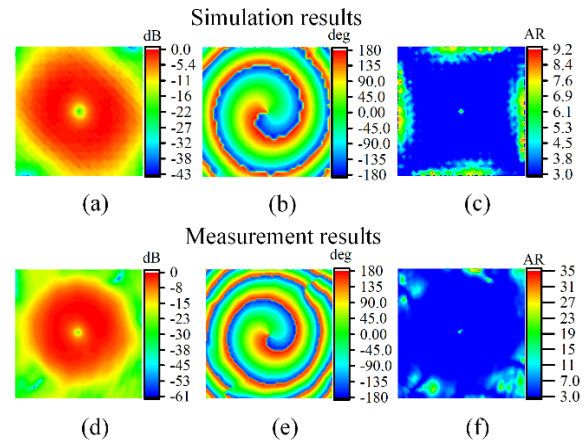


Fig. 10. The simulated and the measured vortex electric field distributions. The simulated observation plane has same size as the measurement, and the distance between the observation plane and the array is same as the measurement situation. (a) Intensity distribution, (b) phase distribution, (c) axial ratio (AR) distribution. The areas with dark blue color means that the value of the AR is less than 3dB, and (d)-(f) is the measurement results.

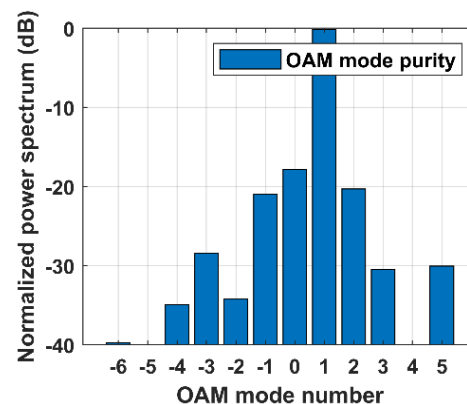


Fig. 11. The calculated OAM mode purity of the measurement vortex electric field, and the normalized OAM mode power means the power of different OAM modes that are normalized by the total received OAM mode power.

IV. CONCLUSION

To summarize, considering the inaccuracies about the approximate array factor calculation of the CUCA antenna, we introduced a correction factor to improve it from the viewpoint of the antenna's radiation pattern power conservation. The corresponding illustrations and the calculation examples were also provided in detail. In order to realize the vortex beam optimization design such as the sidelobe suppression, the GA was adopted to optimize the CUCA's radius parameters. Relevant EM simulation model were built, fabricated and measured. The corresponding far-field and near-field antenna measurements were carried out in microwave anechoic chamber, which showed that the optimized low sidelobe vortex beam was realized. Not limited to the sidelobe suppression, this design method about the vortex beam optimization design, could be applied in the wireless communication field and radar field in the future.

ACKNOWLEDGMENT

This work is supported by National Key R&D Program of China.

REFERENCES

- [1] A. M. Yao and M. J. Padgett, "Orbital angular momentum: Origins, behavior and applications," *Advances in Optics and Photonics*, vol. 3, no. 2, pp. 161-204, 2011.
- [2] B. Thide, H. Then, J. Sjöholm, K. Palmer, J. Bergman, T. D. Carozzi, Y. N. Istomin, N. H. Ibragimov, and R. Khamitova, "Utilization of photon orbital angular momentum in the low-frequency radio domain," *Phys. Rev. Lett.*, vol. 99, no. 8, pp. 087701, Aug. 24, 2007.
- [3] S. M. Mohammadi, L. K. S. Daldorff, J. E. S. Bergman, R. L. Karlsson, B. Thide, K. Forozesh, T. D. Carozzi, and B. Isham, "Orbital angular momentum in radio—A system study," *IEEE Transactions on Antennas and Propagation*, vol. 58, no. 2, pp. 565-572, 2010.
- [4] D. Lee, H. Sasaki, H. Fukumoto, K. Hiraga, and T. Nakagawa, "Orbital angular momentum (OAM) multiplexing: an enabler of a new era of wireless communications," *IEICE Transactions on Communications*, vol. E100.B, no. 7, pp. 1044-1063, 2017.
- [5] A. Trichili, K.-H. Park, M. Zghal, B. S. Ooi, and M.-S. Alouini, "Communicating using spatial mode multiplexing: Potentials, challenges, and perspectives," *IEEE Communications Surveys & Tutorials*, vol. 21, no. 4, pp. 3175-3203, 2019.
- [6] G. Guo, W. Hu, and X. Du, "Electromagnetic vortex based radar target imaging," (in Chinese), *Journal of National University of Defense Technology*, vol. 6, pp. 71-76, 2013.
- [7] T. Yuan, H. Wang, Y. Qin, and Y. Cheng, "Electromagnetic vortex imaging using uniform concentric circular arrays," *IEEE Antennas and Wireless Propagation Letters*, vol. 15, pp. 1024-1027, 2016.
- [8] O. Edfors and A. J. Johansson, "Is orbital angular momentum (OAM) based radio communication an unexploited area?," *IEEE Transactions on Antennas and Propagation*, vol. 60, no. 2, pp. 1126-1131, 2012.
- [9] M. Tamagnone, C. Craeye, and J. Perruisseau-Carrier, "Comment on 'Encoding many channels on the same frequency through radio vorticity: first experimental test'," *New Journal of Physics*, vol. 14, no. 11, 2012.
- [10] F. Tamburini, B. Thidé, E. Mari, A. Sponselli, A. Bianchini, and F. Romanato, "Reply to comment on 'Encoding many channels on the same frequency through radio vorticity: First experimental test'," *New Journal of Physics*, vol. 14, no. 11, 2012.
- [11] M. Oldoni, F. Spinello, E. Mari, G. Parisi, C. G. Someda, F. Tamburini, F. Romanato, R. A. Ravanelli, P. Coassini, and B. Thide, "Space-division demultiplexing in orbital-angular-momentum-based MIMO radio systems," *IEEE Transactions on Antennas and Propagation*, vol. 63, no. 10, pp. 4582-4587, 2015.
- [12] M. Andersson, E. Berglind, and G. Björk, "Orbital angular momentum modes do not increase the channel capacity in communication links," *New Journal of Physics*, vol. 17, no. 4, 2015.
- [13] Z. Guo, Y. Wang, Q. Zheng, C. Yin, Y. Yang, and Y. Gong, "Advances of research on antenna technology of vortex electromagnetic waves," (in Chinese), *Journal of Radars*, vol. 8, no. 5, pp. 631-655, Sep. 2019.
- [14] J. Q. Han, L. Li, H. Yi, and Y. Shi, "1-bit digital orbital angular momentum vortex beam generator based on a coding reflective metasurface," *Optical Materials Express*, vol. 8, no. 11, pp. 3470-3478, 2018.
- [15] J. Q. Han, L. Li, H. Yi, and W. M. Xue, "Versatile orbital angular momentum vortex beam generator based on reconfigurable reflective metasurface," *Japanese Journal of Applied Physics*, vol. 57, no. 12, 2018.
- [16] F. Bi, Z. Ba, and X. Wang, "Metasurface-based broadband orbital angular momentum generator in millimeter wave region," *Opt Express*, vol. 26, no. 20, pp. 25693-25705, 2018.
- [17] R. Xie, G. Zhai, X. Wang, D. Zhang, L. Si, H. Zhang, and J. Ding, "High-efficiency ultrathin dual-wavelength pancharatnam-berry metasurfaces with complete independent phase control," *Advanced Optical Materials*, vol. 7, no. 20, p. 1900594, 2019.
- [18] R. Chen, H. Xu, M. Moretti, and J. Li, "Beam

- steering for the misalignment in UCA-based OAM communication systems," *IEEE Wireless Communications Letters*, vol. 7, no. 4, pp. 582-585, 2018.
- [19] R. Chen, H. Zhou, M. Moretti, X. Wang, and J. Li, "Orbital angular momentum saves: Generation, detection, and emerging applications," *IEEE Communications Surveys & Tutorials*, vol. 22, no. 2, pp. 840-868, 2020.
- [20] Y. Qin, K. Liu, Y. Cheng, X. Li, H. Wang, and Y. Gao, "Sidelobe suppression and beam collimation in the generation of vortex electromagnetic waves for radar imaging," *IEEE Antennas and Wireless Propagation Letters*, vol. 16, pp. 1289-1292, 2017.
- [21] T. Yuan, Y. Cheng, H. Wang, and Y. Qin, "Mode characteristics of vortical radio wave generated by circular phased array: Theoretical and experimental results," *IEEE Transactions on Antennas and Propagation*, vol. 65, no. 2, pp. 688-695, 2017.
- [22] L. Li and X. Zhou, "Mechanically reconfigurable single-arm spiral antenna array for generation of broadband circularly polarized orbital angular momentum vortex waves," *Sci. Rep.*, vol. 8, no. 1, p. 5128, 2018.
- [23] J. Liang, Z. L. Jing, Q. Feng, Y. S. Zheng, and L. Li, "Synthesis and measurement of a circular-polarized deflection OAM vortex beam with sidelobe suppression array," *IEEE Access*, vol. 8, pp. 89143-89151, 2020.
- [24] Q. Feng, J. Liang, and L. Li, "Variable scale aperture sampling reception method for multiple orbital angular momentum modes vortex wave," *IEEE Access*, vol. 7, pp. 158847-158857, 2019.

An Adaptive Sparse Array Beamforming Algorithm Based on Approximate L_0 -norm and Logarithmic Cost

Haixu Wang and YingSong Li*

College of Information and Communication Engineering
Harbin Engineering University, Harbin, 150001, China

*liyingsong@ieee.org

Abstract — This paper introduces a constrained normalized adaptive sparse array beamforming algorithm based on approximate L_0 -norm and logarithmic cost (L0-CNLMLS). The proposed algorithm can control the sparsity of the array by introducing an approximate function of L_0 -norm. In addition, the introduction of logarithmic cost improves the stability of the algorithm as well as the convergence rate of the algorithm. The sparsity of the array can be controlled when adjusting related parameter in the proposed algorithm. Simulation results show the better performance of L0-CNLMLS compared with some conventional algorithms.

Index Terms — Approximate L_0 -norm, constrained adaptive beamforming, logarithmic cost function, sparse sensor arrays.

I. INTRODUCTION

The sparse antenna signal processing technology has a wide application in modern signal processing. In practical applications, the communication system may be restricted by conditions such as energy, which may require the system to reduce the number of equipment. The sparse array signal processing technology is proposed to address this problem. In recent years, a main method of sparse array technology is to use sparse algorithms which can achieve the same performance and use less actual elements. Aiming at the application of beamforming, a sparse adaptive beamforming algorithm is proposed.

The adaptive digital beamforming technology is widely used due to its good characteristics. The early classic beamforming algorithm is the linearly constrained minimum-variance (LCMV) algorithm proposed in [1], which can form the ideal beam in the case of fixed interference signals and desired signals. Subsequently, people successfully achieve the adaptive realization of LCMV algorithm which called constrained normalized least mean square (CNLMS) algorithm [2]. These adaptive beamforming algorithms can solve the optimization problem for any desired signal and interference direction.

With the introduction of compressed sensing

technology in [3] and the corresponding algorithms in [4-5], people start relative study about sparse adaptive algorithms. The zero attracting LMS algorithm generates a zero attractor according to a combination of L_1 -norm penalty and the quadratic LMS cost function in the iteration. A series of related algorithms [6-7] provide an idea to study sparse adaptive algorithms.

Based on the ability of these previously mentioned algorithms to induce sparsity, we can expand these methods' application by introducing linear constraints. Inspired by the sparse adaptive algorithm [8-10], for beamforming applications, the L_1 -norm CNLMS algorithm proposed in [11] and its weighted version successfully introduce L_1 -norm penalty into beamforming algorithm. However, it has a disadvantage that the sparsity cannot be adjusted. In addition, many beamforming algorithms based on the adaptive algorithm LMS have been proposed and applied to various aspects of signal processing for specific conditions [12-13]. In this paper, we propose an adaptive sparse array beamforming algorithm based on approximate L_0 -norm and logarithmic cost (L0-CNLMLS). The proposed algorithm can control the sparsity of array as well as improve the stability.

In compressed sensing theory, the sparse signal reconstruction ability of L_0 -norm is much better than L_1 -norm. However, due to the non-convex nature of L_0 -norm and the optimization problem of L_0 -norm is NP-hard problem, most algorithms use L_1 -norm to solve the problem of sparse signal reconstruction. In recent years, more and more approximate methods for the L_0 -norm have been proposed and widely used. In the algorithm proposed in this paper, an approximate function of L_0 -norm is used for calculation and derivation. Using the steepest descent iteration method, the update expression is successfully obtained. Besides this, a novel of new convergence factor is used and makes the algorithm get a better convergence rate.

In addition, we introduce a kind of logarithmic cost function [14] based on the original algorithm. When the algorithm uses a logarithmic cost function, its convergence rate can be better than that of the classical algorithm like LMS. The logarithmic cost function

makes the algorithm compromise between convergence speed and steady-state performance. In the case of ensuring a certain convergence speed, the stability of the algorithm is also improved. Furthermore, the introduction of a logarithmic cost function does not add too much computational complexity.

II. THE PROPOSED L0-CNLMLS ALGORITHM

In this section, the derivation steps of L0-CNLMLS is shown in detail. Since the logarithmic cost shows good characteristics for the disturbance on the error, we add the logarithmic cost function into the mean square error. Then the linearly constrained minimization problem can be expressed as follows:

$$\min_{\mathbf{w}} E \left[|e_k|^2 - \frac{1}{\alpha} \log(1 + \alpha e_k^2) \right] \text{ s.t. } \begin{cases} \mathbf{C}^H \mathbf{w}_k = z \\ \|\mathbf{w}_k\|_0 = p \end{cases}, \quad (1)$$

where e_k and \mathbf{w}_k is iteration error and the vector of coefficients in the algorithm. \mathbf{C} is an $N \times L$ constraint matrix which contains the array orientation information and z is the corresponding constraint vector containing L (number of constraints) elements. p is the parameter of L_0 -norm to adjust the sparsity of the algorithm.

Considering that L_0 -norm minimization is a Non-Polynomial (NP) hard problem, an approximate function is carried out to simplify the complexity of computation. A popular approximation is the Geman-McClure function, the expression can be written as:

$$F_\beta(x) = 1 - \frac{1}{1 + \beta|x|}. \quad (2)$$

The derivative form of the Geman-McClure function which will be used in the following derivation is given by:

$$f_\beta(x) = \frac{\beta \text{sign}(x)}{(1 + \beta|x|)^2}, \quad (3)$$

where $\text{sign}(x)$ denotes the basic signum function. By employing the Lagrange multiplier λ , the constraints can be included into the objective function. And then we can get the cost function with L_0 -norm penalty as follows:

$$J(\mathbf{w}) = E \left[|e_k|^2 - \frac{1}{\alpha} \log(1 + \alpha e_k^2) \right] - \lambda_1^H (z - \mathbf{C}^H \mathbf{w}) - \lambda_2 (p - \|\mathbf{w}_k\|_0). \quad (4)$$

According to the steepest descent method, the solution for $J(\mathbf{w})$ can be given as:

$$\mathbf{w}(n+1) = \mathbf{w}(n) - \frac{\mu_0}{2} \hat{\nabla}_{\mathbf{w}} J(\mathbf{w}). \quad (5)$$

Symbol $\hat{\nabla}$ denotes the gradient operator and μ_0 is a fixed value which controls the misadjustment. Differentiate and calculate the cost function which contains L_0 -norm penalty, the gradient vector can be

obtained as (6):

$$\hat{\nabla}_{\mathbf{w}} J(\mathbf{w}) = -2g(e_k^*) \mathbf{x}_k + \mathbf{C} \lambda_1 + \lambda_2 f_\beta(\mathbf{w}), \quad (6)$$

where function $g(e_k^*) = \frac{\alpha(e_k^*)^3}{1 + \alpha(e_k^*)^2}$. Using the prior

knowledge $\mathbf{C}^H \mathbf{w}_k = z$, we can get the solution of Lagrangian multiplier λ_1 giving by:

$$\lambda_1 = (\mathbf{C}^H \mathbf{C})^{-1} \mathbf{C}^H (2g(e_k^*) \mathbf{x}_k - \lambda_2 f_\beta(\mathbf{w})). \quad (7)$$

The value \mathbf{x}_k denotes the input signal vector in the k^{th} iteration. By defining the L_0 -norm error function as $e_{L_0}(k) = p - f_\beta^H(\mathbf{w}_k) \mathbf{w}_k$ and rearranging the terms of formula, the solution of λ_2 can be obtained as follows:

$$\lambda_2 = \frac{1}{N} \left[-\frac{2}{\mu} e_{L_0}(k) + f_\beta^H(\mathbf{w}_k) (2g(e_k^*) \mathbf{x}_k - \mathbf{C} \lambda_1) \right], \quad (8)$$

where $N = f_\beta^H(x) f_\beta(x)$. After organizing the formulas, the solutions for λ_2 and λ_1 can be obtained. The final update equation of L0-CNLMLS algorithm can be expressed as follows:

$$\mathbf{w}_{k+1} = \mathbf{w}_k + \mu_k \frac{\alpha(e_k^*)^3}{1 + \alpha(e_k^*)^2} \mathbf{Q} + \mathbf{f}_{L_0}(k), \quad (9)$$

where

$$\begin{cases} \mathbf{P} = \mathbf{I}_{N \times N} - \mathbf{C} (\mathbf{C}^H \mathbf{C})^{-1} \mathbf{C}^H, \\ a = f_\beta^H(\mathbf{w}_k) \mathbf{P} \mathbf{x}_k, \\ b = f_\beta^H(\mathbf{w}_k) \mathbf{P} f_\beta(\mathbf{w}_k), \\ \mathbf{Q} = \mathbf{P} \left(\mathbf{x}_k - \frac{a f_\beta(\mathbf{w}_k)}{b} \right), \\ \mathbf{f}_{L_0}(k) = (p - f_\beta^H(\mathbf{w}_k) \mathbf{w}_k) \left(\frac{\mathbf{P} f_\beta(\mathbf{w}_k)}{b} \right), \\ \mu_k = \frac{\mu_0 (e_k - \mathbf{f}_{L_0}^H(k) \mathbf{x}_k)}{e_k \mathbf{Q}^H \mathbf{x}_k + \gamma}. \end{cases} \quad (10)$$

The variable μ_k is a new convergence factor carried out to minimize the instantaneous posteriori squared error at instant k [15]. Bases on the above derivation process, we can get:

$$\frac{\partial [e_{ap}(k) e_{ap}^*(k)]}{\partial \mu_k^*} = 0, \quad (11)$$

where $e_{ap}(k) = e_k (1 - \mu_k \mathbf{x}_k^H \mathbf{Q}) - \mathbf{f}_{L_0}(k) \mathbf{x}_k$. According to the prior knowledge and solve the above formula (11), we can get the expression of the new convergence factor:

$$\mu_k = \frac{\mu_0 [e_k - \mathbf{f}_{L_0}^H(k) \mathbf{x}_k]}{e_k \mathbf{Q}^H \mathbf{x}_k + \gamma}. \quad (12)$$

The parameter γ is a small positive constant to ensure the correctness of the calculation. By replacing μ_0 with μ_k , the above final iterative formula can be obtained.

III. SIMULATION RESULTS

In this section, several simulations are carried out to show the better performance of the proposed L0-CNLMLS algorithm. Simulation results and comparisons of L0-CNLMLS with similar algorithms (shrinkage L1-norm constrained LMS algorithm (SL1-CLMS) [16], L0-norm feature LMS (L0-F-LMS) [17] and L0-CNLMS) are illustrated to demonstrate the improvement of the proposed algorithm. Interferers and the signal of interest (SOI) used in the experiments are narrowband QPSK signals. The experiments are conducted under two different sparsities.

In the first simulation the parameter of the approximate L_0 -norm function is set to be 15 and the parameter α is set to be 2. The initial adaptation step size of L0-CNLMLS and L0-CNLMS is fixed at 0.004 and 0.003, respectively. For L0-F-LMS, the adaptation step size is set to be 5×10^{-9} . The sparse parameter p is 0.3. The iteration number is 6000 in this simulation.

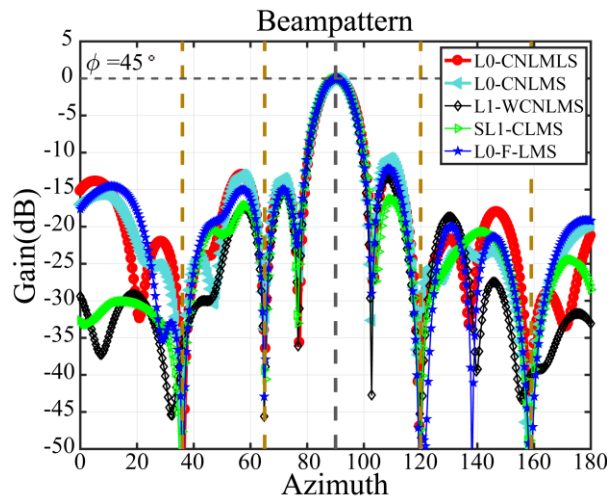


Fig. 1. Beampatterns for L0-CNLMLS algorithm and similar algorithms.

Figure 1 shows the beampatterns for L0-CNLMLS algorithm and some other algorithms. Results show that the proposed algorithm and the other algorithms all can form main lobe and nulls. In the terms of side lobe, the average height of the five algorithms is almost the same.

Figure 2 shows the thinned triangular array and the change of coefficient vector for L_0 -norm to L0-CNLMLS algorithm and the other two algorithms which use L_0 -norm. The array used in the simulations is a triangular array considered as the sensor for P-band

signals which has particularly advantage in satellite detection. The triangular array contains 117 array elements. The white points represent the array elements which are closed while the black points denote normal working antenna arrays. From the L_0 -norm in Fig. 2, the L0-CNLMLS algorithm converges after 5000 iterations. It is found that the L0-CNLMLS algorithm converges faster than the L0-CNLMS algorithm and L0-F-LMS algorithm.

According to the numbers of the points, the sparsity of the array can be calculated as 30.7% which is very close to the preset sparse parameter value of 30%. The L0-CNLMS algorithm and L0-F-LMS algorithm achieve a sparsity of 31.6%. It is obvious that the L0-CNLMLS algorithm can control the sparsity much better than the other algorithms under the same conditions.

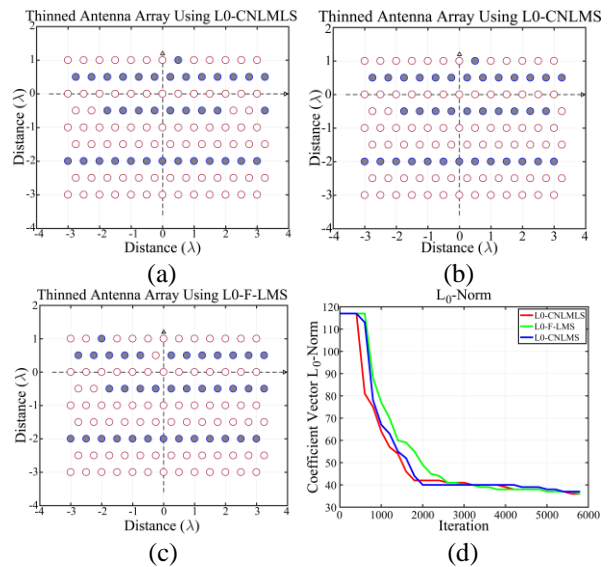


Fig. 2. Thinned triangular array for the L0-CNLMLS and other two algorithms: (a) L0-CNLMLS; (b) L0-CNLMS; (c) L0-F-LMS; (d) convergence of the used algorithms.

In experiment 2, the sparse parameter p set to be 0.7 with the other parameters unchanged. Figure 3 and Fig. 4 show the respective beampatterns and thinned triangular array of the proposed algorithm and other algorithms.

According to the thinned antenna array in Fig. 4, the sparsity of the array in this simulation can be obtained as 70.1%. For large sparse ratio, the L0-CNLMLS and L0-CNLMS are almost the same in the ability to control the sparsity of the array while the L0-F-LMS shows a worse performance by calculation. Simulation results prove that the sparsity of the array can be controlled by the adjustment of corresponding parameter.

Figure 4 (d) shows the L_0 -norm of the coefficient vector. The better convergence ability of proposed algorithm can be seen. The L0-CNLMLS algorithm converges after about 2300 iterations, the L0-CNLMS

and L0-F-LMS converged slight slowly. Table 1 shows the comparison of the two experiments. The proposed algorithm achieves sparsities of 30.7%, 70.1% which equal to the prescribed parameter p of 0.3, 0.7.

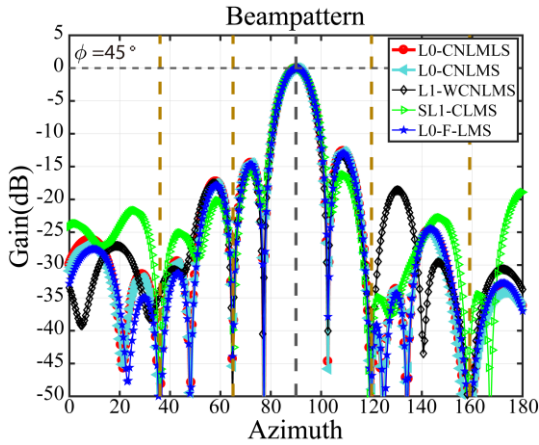


Fig. 3. Beampatterns for L0-CNLMLS algorithm and the other algorithms under large sparsity ratio.

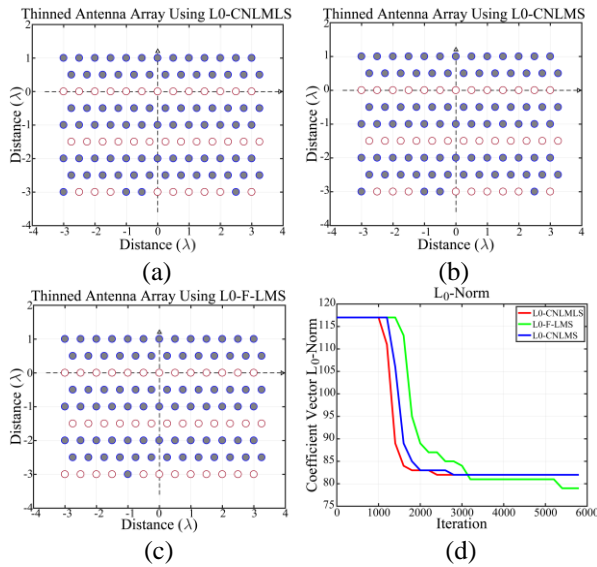


Fig. 4. Thinned triangular array in experiment 2: (a) using L0-CNLMLS; (b) L0-CNLMS; (c) L0-F-LMS; (d) convergence of the used algorithms with $p=0.7$.

Experiment	Parameter	Result
I	0.3	0.307
II	0.7	0.701

In addition, we found that the logarithmic cost can improve the stability of proposed algorithm. Figure 5 is two different results in simulation I. The L0-CNLMS achieves different sparsities of 31.6% and 32.4% under

the same parameters, while the L0-CNLMLS shows better stability in controlling the sparsity than L0-F-LMS algorithm. As for SL1-CLMS algorithm, the algorithm uses too much different array elements in different sparsities. Compared with algorithm using L_1 -norm, the L0-CNLMLS algorithm achieves the ability to precisely control the sparsity of the array. The logarithmic cost ensures a good agreement between the sparse parameter and simulation results, which shows the better performance of proposed algorithm.

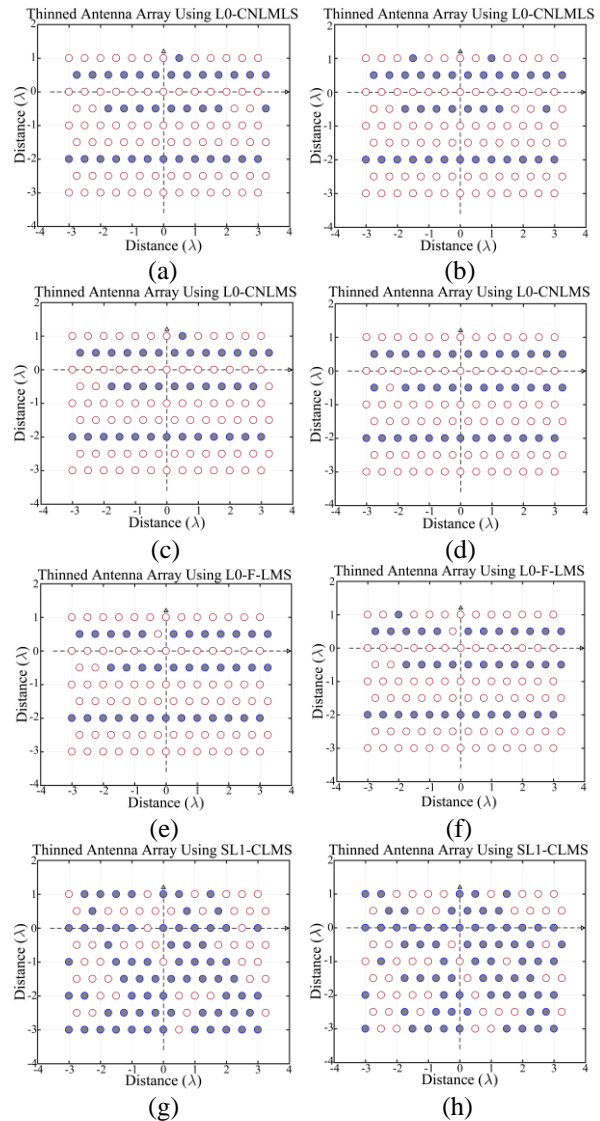


Fig. 5. Two different results in simulation I under same conditions. (a), (b) The antenna array thinned by L0-CNLMLS with sparsity of 30.7%. (c), (d) The antenna array thinned by L0-CNLMS with sparsity of 31.6%, 32.4%, respectively. (e), (f) The antenna array thinned by L0-F-LMS with sparsity of 30.7%, 31.6%, respectively. (g), (h) Different results of antenna array using SL1-CLMS.

IV. CONVERGENCE ANALYSIS

In this section, the convergence analysis of L0-CNLMLS is carried out. Defining the priori error in the k^{th} iteration as:

$$e_k = \mathbf{x}_k^H \mathbf{w}_o + \mathbf{n}_k - \mathbf{x}_k^H \mathbf{w}_k = \mathbf{n}_k - \mathbf{x}_k^H \Delta \mathbf{w}_k, \quad (13)$$

where $\Delta \mathbf{w}_k = \mathbf{w}_k - \mathbf{w}_o$, \mathbf{w}_o is considered as the optimal coefficient vector and \mathbf{n}_k denotes the noise in the k^{th} iteration. Defining $\varepsilon_k = \mathbf{Q}^H \mathbf{x}_k$, the final iteration equation of proposed algorithm can be written as:

$$\mathbf{w}_{k+1} = \mathbf{w}_k + \frac{\mu_0}{\varepsilon_k} \left[g(e_k) - \mathbf{f}_{L_0}^H(k) \mathbf{x}_k \right] \mathbf{Q} + \mathbf{f}_{L_0}(k). \quad (14)$$

Combining the element $\mathbf{f}_{L_0}(k)$ and inserting e_k into (14), the equation can be expressed as:

$$\mathbf{w}_{k+1} = \mathbf{w}_k + \left[\mathbf{I} - \frac{\mu_0}{\varepsilon_k} \mathbf{Q} \mathbf{x}_k^H \right] \mathbf{f}_{L_0}(k) + \frac{\mu_0}{\varepsilon_k} g(e_k^*) \mathbf{Q}. \quad (15)$$

When the algorithm is converged, the constraint conditions $\mathbf{f}_{L_0}^H(\mathbf{w}_k) \mathbf{w}_{k+1} = p$ should be satisfied. Defining $\mathbf{f}_{L_0}(\mathbf{w}_k) = \mathbf{f}_k$. According to equation (10), we can get:

$$\mathbf{f}_{L_0}(k) = \left(\mathbf{f}_k^H \mathbf{w}_o - \mathbf{f}_k^H \mathbf{w}_k \right) \left(\frac{\mathbf{P} \mathbf{f}_k}{b} \right) = -\mathbf{A} \Delta \mathbf{w}_k, \quad (16)$$

where $\mathbf{A} = \frac{\mathbf{P} \mathbf{f}_k \mathbf{f}_k^H}{b}$ is an idempotent matrix. The conclusion $\text{tr}[\mathbf{A}] = 1$ can be easily obtained shows that there is only one non-zero eigenvalue among all the eigenvalues of matrix \mathbf{A} . Therefore, the coefficient error form of (15) is:

$$\begin{aligned} \Delta \mathbf{w}_{k+1} &= \Delta \mathbf{w}_k + \left[\mathbf{I} - \frac{\mu_0}{\varepsilon_k} \mathbf{Q} \mathbf{x}_k^H \right] (-\mathbf{A} \Delta \mathbf{w}_k) \\ &+ \frac{\mu_0}{\varepsilon_k} g(e_k^*) \mathbf{Q} \\ &= \left[\mathbf{I} - \mu_0 \mathbf{B} \right] \Delta \mathbf{w}_k - \left[\mathbf{I} - \mu_0 g'(e_k^*) \mathbf{B} \right] \mathbf{A} \Delta \mathbf{w}_k \\ &+ \frac{\mu_0}{\varepsilon_k} g'(e_k^*) n_k^* \mathbf{Q} \end{aligned}, \quad (17)$$

where $\mathbf{B} = \frac{\mathbf{Q} \mathbf{x}_k^H}{\varepsilon_k}$ is also an idempotent matrix with a

non-zero eigenvalue of 1. From simulation results

$g'(e_k^*) = \frac{\alpha(e_k^*)^2}{1 + \alpha(e_k^*)^2}$ can be obtained as a constant very

close to 1. Then, take expectation on both sides of (17), we will have:

$$E[\Delta \mathbf{w}_{k+1}] = E\{[\mathbf{I} - \mu_0 \mathbf{B}][\mathbf{I} - \mathbf{A}]\Delta \mathbf{w}_k\} + E\left[\frac{\mu_0}{\varepsilon_k} n_k^* \mathbf{Q}\right]. \quad (18)$$

According to [15], $\Delta \mathbf{w}_k$ is statistic independence with n_k , \mathbf{x}_k and \mathbf{f}_k . Under the truth of the expectation of n_k is 0, (18) can be written as:

$$E[\Delta \mathbf{w}_{k+1}] = [\mathbf{I} - \mu_0 \mathbf{B}][\mathbf{I} - \mathbf{A}]E[\Delta \mathbf{w}_k] = [\mathbf{I} - \mu_0 \mathbf{B}][\mathbf{I} - \mathbf{A} - \mu_0 \mathbf{B} - \mu_0 \mathbf{A} \mathbf{B}]^k [\mathbf{I} - \mathbf{A}]E[\Delta \mathbf{w}_0]. \quad (19)$$

In the case of $\mathbf{A} \mathbf{B} = 0$, we can get the final convergence domain as:

$$0 < \mu_0 < 1. \quad (20)$$

Actually, the convergence domain is a little larger according to [14] because the introduction of logarithmic cost can influence convergence performance. The selection of step-size for L0-CNLMLS is always far below the upper bound to gain better performance in actual application.

V. CONCLUSION

In this paper, an adaptive sparse array beamforming algorithm based on approximate L_0 -norm and logarithmic cost (L0-CNLMLS) is proposed and analyzed. The L0-CNLMLS algorithm uses GMF function to be the approximate function of the L_0 -norm penalty and avoid the NP-hard problem. The introduction of L_0 -norm allows the algorithm to control the sparseness of the array. The use of logarithmic cost function improves stability while ensuring a certain convergence speed of the algorithm.

Simulation results show that the proposed algorithm exhibits better performance and convergence speed compared with some sparse beamforming algorithm in recent years under different sparsities. In addition, the L0-CNLMLS algorithm can control the sparsity of antenna array more precisely for small sparse ratio, so as to improve the stability performance. In the future, the algorithms in [18-21] will be considered to construct new sparsity beamforming algorithms.

REFERENCES

- [1] O. L. Frost, "An algorithm for linearly constrained adaptive array processing," in *Proceedings of the IEEE*, vol. 60, no. 8, pp. 926-935, Aug. 1972.
- [2] J. A. Apolinario, S. Werner, P. S. R. Diniz, and T. I. Laakso, "Constrained normalized adaptive filters for CDMA mobile communications," *9th European Signal Processing Conference (EUSIPCO 1998)*, Rhodes, pp. 1-4, 1998.
- [3] D. L. Donoho, "Compressed sensing," in *IEEE Transactions on Information Theory*, vol. 52, no. 4, pp. 1289-1306, Apr. 2006.
- [4] Y. Chen, Y. Gu, and A. O. Hero, "Sparse LMS for system identification," *2009 IEEE International Conference on Acoustics, Speech and Signal Processing*, Taipei, pp. 3125-3128, 2009.

- [5] R. Arablouei and K. Dogancay, "Reduced-complexity constrained recursive least-squares adaptive filtering algorithm," in *IEEE Transactions on Signal Processing*, vol. 60, no. 12, pp. 6687-6692, Dec. 2012.
- [6] S. Nunoo, U. A. K. Chude-Onokwo, R. Ngah, and Y. K. Zahedi, "Variable step-size l0-norm NLMS algorithm for sparse channel estimation," *2014 IEEE Asia Pacific Conference on Wireless and Mobile*, Bali, pp. 88-91, 2014.
- [7] R. L. Das and M. Chakraborty, "Sparse adaptive filters - An overview and some new results," *2012 IEEE International Symposium on Circuits and Systems (ISCAS)*, Seoul, pp. 2745-2748, 2012.
- [8] J. F. de Andrade, M. L. R. de Campos, and J. A. Apolinário, "An L1-constrained normalized lms algorithm and its application to thinned adaptive antenna arrays," *2013 IEEE International Conference on Acoustics, Speech and Signal Processing*, Vancouver, BC, pp. 3806-3810, 2013.
- [9] C. Paleologu, J. Benesty, and S. Ciochină, "An improved proportionate NLMS algorithm based on the l0 norm," *2010 IEEE International Conference on Acoustics, Speech and Signal Processing*, Dallas, TX, pp. 309-312, 2010.
- [10] J. Yang and G. E. Sobelman, "Sparse LMS with segment zero attractors for adaptive estimation of sparse signals," *2010 IEEE Asia Pacific Conference on Circuits and Systems*, Kuala Lumpur, pp. 422-425, 2010.
- [11] K. Shi and P. Shi, "Convergence analysis of sparse LMS algorithms with l1-norm penalty based on white input signal," *Signal Processing*, vol. 90, no.12, pp. 3289-3293, Dec. 2010.
- [12] M. V. S. Lima, T. N. Ferreira, W. A. Martins, and P. S. R. Diniz, "Sparsity-aware data-selective adaptive filters," *IEEE Transactions on Signal Processing*, vol. 62, no. 17, pp. 4557-4572, July 2014.
- [13] Y. Li, Z. Jiang, W. Shi, X. Han, and B. D. Chen, "Blocked maximum correntropy criterion algorithm for cluster-sparse system identification," *IEEE Transactions on Circuits and Systems II: Express Briefs*, vol. 66, no. 11, pp. 1915-1919, 2019.
- [14] M. O. Sayin, N. D. Vanli, and S. S. Kozat, "A novel family of adaptive filtering algorithms based on the logarithmic cost," in *IEEE Transactions on Signal Processing*, vol. 62, no. 17, pp. 4411-4424, Sept. 1, 2014.
- [15] P. S. R. Diniz, *Adaptive Filtering: Algorithms and Practical Implementation*. New York, USA: Springer, 2010.
- [16] H. Yazdanpanah, J. A. Apolinário, P. S. R. Diniz, and M. V. S. Lima, "l0-norm feature lms algorithms," *2018 IEEE Global Conference on Signal and Information Processing (GlobalSIP)*, Anaheim, CA, USA, pp. 311-315, 2018.
- [17] W. Shi, Y. Li, L. Zhao, and X. Liu, "Controllable sparse antenna array for adaptive beamforming," *IEEE Access*, vol. 7, no. 1, pp. 6412-6423, 2019.
- [18] T. Liang, Y. Li, W. Xue, Y. Li, and T. Jiang, "Performance and analysis of recursive constrained least lncosh algorithm under impulsive noises," *IEEE Transactions on Circuits and Systems II: Express Briefs*, 10.1109/TCSII.2020.3037877.
- [19] W. Shi, Y. Li, and B. Chen, "A separable maximum correntropy adaptive algorithm," *IEEE Transactions on Circuits and Systems II: Express Briefs*, vol. 67, no. 11, pp. 2797-2801, 2020.
- [20] Q. Wu, Y. Li, Y. Zakharov, W. Xue, and W. Shi, "A kernel affine projection-like algorithm in reproducing kernel hilbert space," *IEEE Transactions on Circuits and Systems II: Express Briefs*, vol. 67, no. 10, 2020.
- [21] X. Huang, Y. Li, Y. V. Zakharov, Y. Li, and B. Chen, "Affine-projection Lorentzian algorithm for vehicle hands-free echo cancellation," *IEEE Transactions on Vehicular Technology*, Accepted.

Reflectarray Resonant Element based on a Dielectric Resonator Antenna for 5G Applications

Nur Fazreen Sallehuddin¹, Mohd Haizal Jamaluddin¹, Muhammad Ramlee Kamarudin²,
and Muhammad Hashim Dahri²

¹Wireless Communication Centre, Universiti Teknologi Malaysia, Skudai, Johor 81310, Malaysia
fazreen83@yahoo.com, haizal@fke.utm.my

²Department of Electrical and Electronic Engineering
Universiti Tun Hussein Malaysia, Batu Pahat, Johor 86400, Malaysia
muhammadhashimdahri@yahoo.com, mramlee@uthm.edu.my

Abstract — The performance of a proposed cross hybrid dielectric resonator antenna (DRA) element for dual polarization configuration operating at 26 GHz for 5G applications is presented in this paper. The new cross hybrid DRA unit cell is introduced which combines a cross shape DRA with a bottom loading cross microstrip patch. This technique of a bottom loading cross microstrip patch is chosen as the tuning mechanism (varying the length of the microstrip to tune the phase) instead of changing the DRA dimensions because of their ease of implementation and fabrication. By doing so, high reflection phase range with low reflection loss performance can be obtained, which is essential for a high bandwidth and high gain reflectarray for 5G applications. The design and simulation have been done using commercial software of CST MWS. The reflection loss, reflection phase and slope variation were analyzed and compared. A metallic cross microstrip patch of varying length placed beneath the DRA to act as the phase shifter to tune the phase and give smooth variation in slope with a large phase range. The proposed cross hybrid DRA unit cell provides a high reflection phase range of 342° and 1.8 dB reflection loss. The computed results are compared with experimental results revealing reasonable agreement, thereby confirming the viability of the design.

Index Terms — DRA reflectarray, phase range, reflection loss, reflection phase, unit cell.

I. INTRODUCTION

Reflectarray antennas are the combination of some capabilities and some advantages between phased array antennas and parabolic reflectors [1,2]. It comprised of an array of element radiators illuminated by a feed antenna (usually a horn antenna). The feed antenna provides the feeding mechanism to the array, in order to eradicate the need for a complex and lossy corporate feed

network. Therefore, the losses in reflectarray antenna can be easily optimized due to its simple feeding mechanism. The feeding is located at the focal distance of the reflectarray. Usually, the focal distance is evaluated in focal-length-to-diameter (f/D) ratio. The distance of the reflectarray and the feed represented by f , while the longest dimension of the reflectarray represented by D [3,4]. The occurrence waves coming from the feeding are reradiated and scattered back with electrical phases that are required to form a planar wave front in the far-field distance towards the desired direction. One vital component of the reflectarray performance investigation is the unit cell elements have been designed and characterized accurately [5]. The unit cell element's dimensions are responsible to accurately predict the phase shift required for planar wavefront. The radiation patterns of the reflectarray antenna can only be estimated after the unit cell element and the full reflectarray has been fully characterized and designed. Reflection phase and reflection loss are two major important parameters to analyse the performance of reflectarrays unit element. The reflectarray unit element's reflection loss will have an impact on the gain of a full reflectarray antenna, whilst the reflection phase or phase range of the unit cell corresponds to the bandwidth of the reflectarray antenna [6]. A complete cycle of phase swing with 360° is normally considered adequate to design any size of reflectarray with a good performance [7].

Initially, microstrip unit elements are widely used to develop reflectarrays antenna due to their good criteria such as low profile, light weight, flatness, easy deployment in space, beam steering capability as well as their low manufacturing cost [8]. Nevertheless, the conductor loss of the microstrip reflectarray antenna becomes worse. The reflectarray antenna's competency at mmW frequencies of the microstrip unit cell also may drop markedly. Reflectarray made by dielectric resonator (DRA) that has small losses and large phase range is

presented to overcome this problem [9-11].

DRA has been investigated for designing various reflectarray antennas to obtain high reflection phase range, and small reflection loss by changing the length of the DRA or any other one of its geometrical parameters to present phase variations to the radiating unit cells [12]. But the fabrication process will be more complex when the reflectarray antenna made by different DRAs sizes. For that reason, the unit cells of DRA reflectarray also able to be combined alongside several strip elements like patches, slots as well strips. The purpose of that is to produce wide band reflectarray or specifically to expand the bandwidth and concurrently to ensure the easy fabrication [13-15]. As a consequence, a full reflection phase range with smooth variation in slope will be able to be produce practicably. However, a problem faced by a slot loaded DRA reflectarray was an electric field that can leak through the under-loading slot that may lead to a growing back lobe radiation problem. Meanwhile, the top-loaded microstrip patch DRA element has a risk of gain reduction due to misalignment between patch and DRA that may arise because the microstrip has to install by manual at the upper of the DRA surface. In another study, a transparent rectangular DRA reflectarray element with beneath-loaded strip have been proposed giving a phase range of 316° with reflection loss of less than 3 dB [16]. Another approach to enhance the reflectarray element's bandwidth with large reflection phase range is by implementing dual-polarized technique [17-19]. The option of the polarization be able to accomplish by using square shapes or rectangular shapes for linear polarization. Whereas circular polarization or dual polarization can be attained by using circular shapes or crossed shapes.

Inspired by the mentioned foregoing studies of the unit elements, the goal of this study is to introduce a new DRA reflectarray element with a microstrip patch incorporated underneath the DRA as a phase tuning mechanism for 5G applications. For the ease of fabrication purpose, the size of each DRA is always the same. The only change is made on the microstrip length (L_m). The focus has been given specifically on attaining large phase range which is greatly associated to the low reflection loss and substantial operational bandwidth performance. The aim is to design a DRA-based reflectarray element with low reflection loss, wide bandwidth and ease fabrication for 5G applications.

II. RESEARCH METHOD

In this work, the frequency band from 24 GHz to 28 GHz has been chosen for design specifications based on several 5G frequency bands that have been suggested in [20]. 26 GHz as a resonant frequency has been selected to design the reflectarray unit element.

The unit elements of the reflectarray nominated in

this paper made of DRA. The dielectric constant of the DRA is $\epsilon_r = 10$. The cross shaped DRA consists of two rectangular DRA (RDRA) with the same size. The cross microstrip patch on the other hands is formed by two identical rectangular patch elements. The resonant frequency, f_0 for the RDRA has been calculated by using the equation (1) that derived from the Dielectric Waveguide Model (DWM) [21]:

$$k_z \tan\left(\frac{k_z h}{2}\right) = \sqrt{(\epsilon_r - 1)k_0^2 - k_z^2}, \quad (1)$$

where k_0 is the free space wave number, h represents the width in the z -direction and k_z represents the wave propagation number in the z -direction.

The DRA width (W) has been set at 2.40 mm whilst the DRA length (L) has been set at 8.00 mm. The cross microstrip patch acts as a phase shifter to adjust the phase of the unit cell element. On the other hand, the microstrip length (L_m) is varied from 1.50 mm to 4.50 mm as the phase shifting mechanism while the width of microstrip patch (W_m) has been set at 1.50 mm. Table 1 summarizes the optimized unit cell design dimensions.

Table 1: Parameters of dielectric resonator reflectarray antenna unit element

Parameter	Value (mm)
L	8.0
W	2.4
H	2.2
L_m	Varies from 1.50 to 4.50
W_m	1.5

Figure 1 (a) shows the setup of waveguide simulation for the unit cell element. The proposed unit cell element is placed at one end (bottom) of the waveguide and the incident wave from the wave port is positioned from another end of the waveguide (top). The unit cell element is simulated with proper boundary conditions to imitate an infinite periodic structure. The top and bottom surfaces of the waveguide setup are interpreted to be perfect electric conductor (PEC) walls, whilst the other two side walls (left and right sides) are interpreted as perfect magnetic walls (PMC). The geometry of the unit cell which is the cross hybrid DRA is demonstrated in Fig. 1 (b). The unit element's substrate is made of a Rogers RT5880 with dielectric constant 2.2 and thickness 0.381 mm with its ground laminated on the back surface. This unit cell is a coalition of a cross shaped DRA and a cross shaped microstrip patch. The bottom loading patch was chosen as the tuning mechanism because it can be simply etched using the technology of standard printed circuit board (PCB). This method can provide high dimensioning accuracy and simplifies the tuning process. Moreover, it can also avoid misalignment problem and fabrication complexity

at once. The Fig. 1 (c) shows the fabricated cross hybrid DRA unit cell elements.

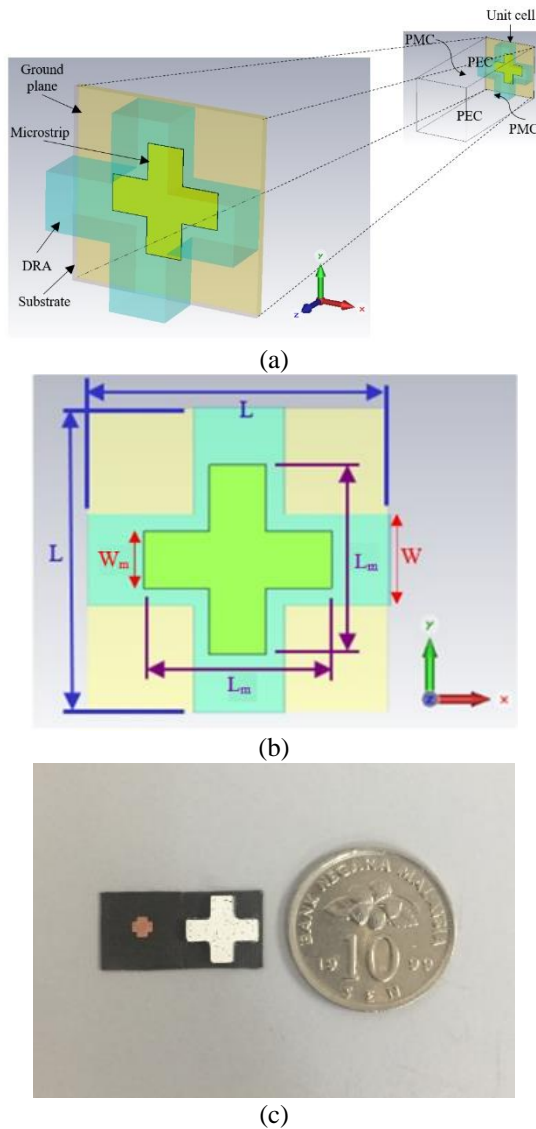


Fig. 1. (a) The simulation of unit element in periodic boundary condition and the zoom in for the proposed Cross hybrid DRA unit element geometry. (b) Top view of the proposed Cross hybrid DRA unit element. (c) Photograph of the fabricated Cross hybrid DRA unit element.

The overall measurement setup is shown in Fig. 2 (a), where the open ended waveguide is used to carry the parameter measurements of the unit cell elements. The unit cell under test is placed at one end and the other end is connected to WR-34 waveguide adapter. The reflection phase and reflection loss of the unit cell elements are measured using VNA (Vector Network Analyzer), which is connected to the waveguide using coaxial to waveguide adapter of WR-34 adapter as

shown in Fig. 2 (b). Two unit cell element reflectarray is fixed into the other aperture of the waveguide simulator as shown in Fig. 2 (c).

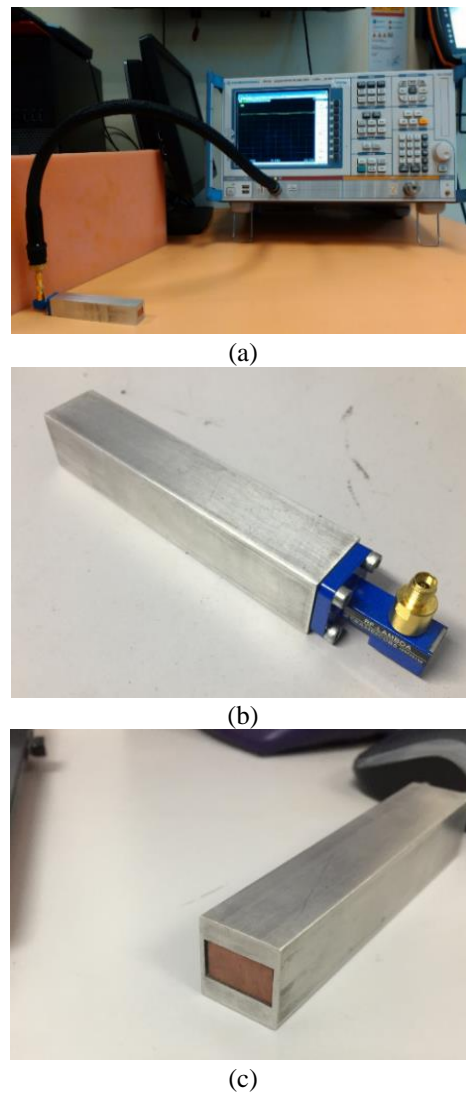


Fig. 2. (a) Scattering parameter measurements of measurement setup. (b) Coaxial to waveguide adapter WR-34 connected to waveguide. (c) Unit cell elements in waveguide aperture.

IV. RESULTS AND ANALYSIS

The proposed cross hybrid unit cell elements with microstrip patch dimensions underneath the DRA are constructed and validated as shown in Fig. 1 (c). The simulated and measured reflection phase and reflection loss of the cross hybrid DRA reflectarray elements are as presented in Fig. 3. The unit cell came with various cross microstrip lengths (L_m). The length is varied to tune the phase. Based on the results, it is found that 342° phase variations can be obtained at 26 GHz. The reflection loss is reasonably small at 1.8 dB.

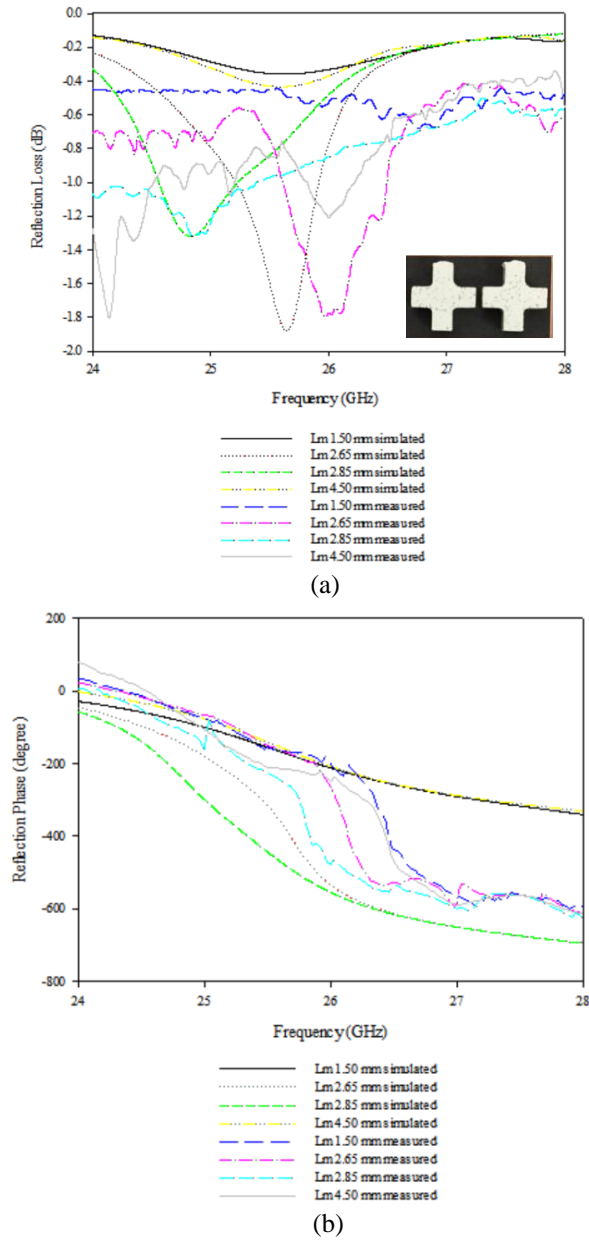


Fig. 3. (a) Simulated reflection loss and measured reflection loss of cross hybrid DRA unit cell, and (b) simulated reflection phase and measured reflection phase of cross hybrid DRA unit cell.

In order to show the advantage of the proposed cross hybrid DRA unit cell, the performance of the cross hybrid DRA unit cells is compared with similar size of full substrate unit cells which hold same DRA height and dielectric constant. This was done to confirm the function of the cross microstrip patch and the DRA in determining the resonant frequency and operating principle of the unit cell. The result comparisons are as shown in Fig. 3 and Fig. 4. The full substrate configuration is acquired by

extending the cross DRA size until the walls of the PEC and PMC unit cell's waveguide setup. The tuning mechanism of the full substrate unit cell is the same as the cross hybrid DRA. To further confirm the advantages of cross hybrid DRA reflectarray elements, a set of four full substrate unit cells has also been designed and fabricated at the same frequency.

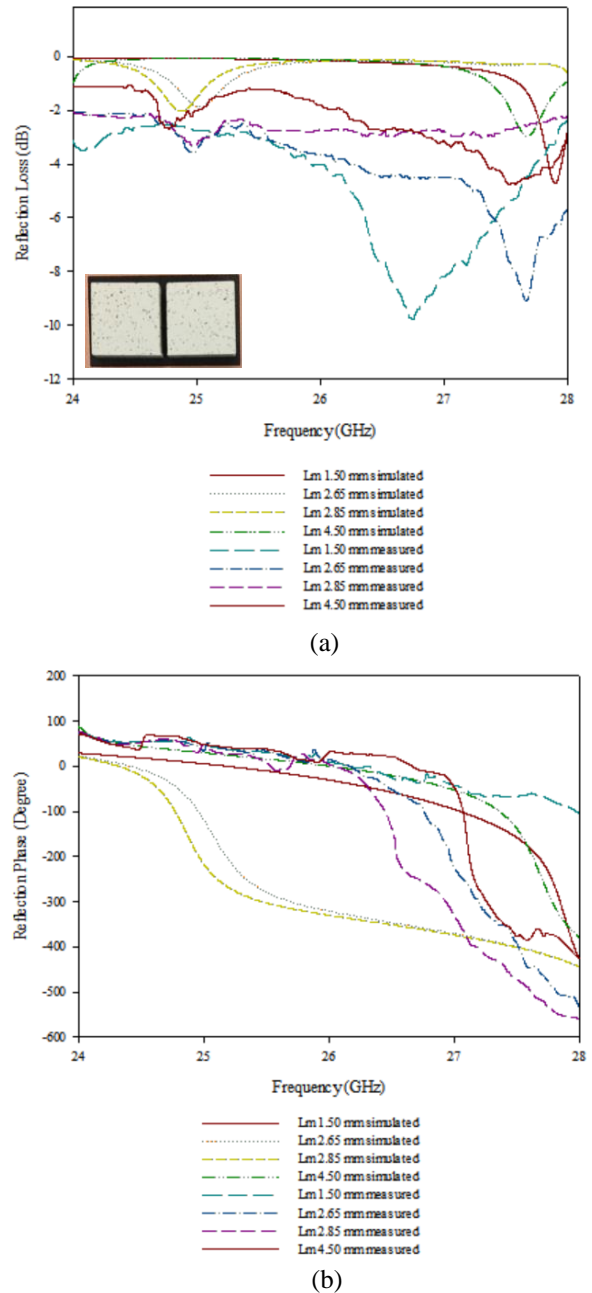


Fig. 4. (a) Simulated reflection loss and measured reflection loss of the full substrate DRA unit cell, and (b) reflection phase and measured reflection phase of the full substrate DRA unit cell.

Figure 3 (a) and Fig. 4 (a) depict the comparison between the reflection loss of the cross hybrid DRA elements and full substrate DRA elements. The hybrid DRA shows significantly lower reflection loss compared to full substrate DRA with difference of almost 5 dB between both. In term of phase range, the cross hybrid DRA produces 342° while full substrate DRA produces slightly lower range of 330° . This can be viewed in Fig. 3 (b) and Fig. 4 (b) respectively. It is proved by phase range results that cross hybrid DRA unit cell can provide wider bandwidth than full substrate unit cell. Because, the resonant frequency of cross DRA is already combined with the resonant frequency of the cross microstrip patch. Thus, higher phase range is achieved as compared to the full substrate structure. The wider phase range correlates with the enhancement of bandwidth performance of the cross hybrid DRA.

In summary, the reflection loss of cross hybrid DRA unit cells is much lower compared to full substrate DRA unit cells as shown in Fig. 5. A slightly frequency shift perceived between measured and simulated results. This may be caused by the adhesive glue used to bond the DRA and the substrate, which was not considered earlier in the simulation. The extra loss that clearly unavoidable at the measurement results is also closely related to the waveguide simulator, cable and connectors losses.

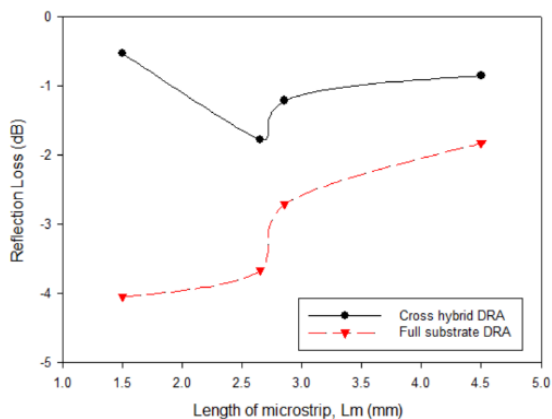


Fig. 5. Reflection loss of cross hybrid DRA unit cell and full substrate DRA unit cell at variable microstrip lengths (microstrip length as the tuning mechanism).

The bandwidth performance of the reflectarray unit element can be analyzed from the curves of the reflection loss. Figure 6 shows the reflection loss curves of cross hybrid DRA and full substrate DRA unit cells in frequency range between 24 GHz to 28 GHz. To clarify the bandwidth of the unit cell, it is determined by moving 10% above the maximum reflection loss value [22]. Table 2 tabulate the 10% bandwidth for the cross hybrid DRA and full substrate DRA. The table display the cross hybrid DRA unit cell element gives broader bandwidth of 498 MHz compared to full substrate DRA unit cell with narrower bandwidth of 122 MHz.

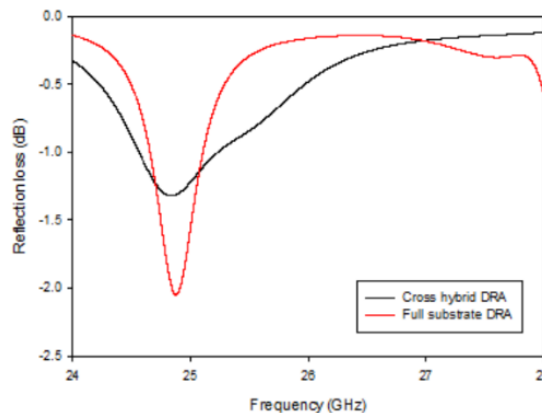


Fig. 6. Reflection loss curves of cross hybrid DRA unit cell and full substrate DRA unit cell in frequency range between 24 GHz to 28 GHz.

Table 2: 10% Bandwidth and reflection loss of unit cells

Unit Cell	10% Bandwidth (MHz)	Reflection Loss (dB)
Cross hybrid DRA	498	1.32
Full substrate DRA	122	2.05

Figure 7 shows that the phase variation curves for two different polarizations are almost identical. It proves that these unit cell elements provide dual polarization operation. It seems that, only one phase variation is illustrated in the graph, the other one being symmetric because of the symmetrical antenna design [1].

Finally, Table 3 summarized comparison between the proposed approach and previous works. The proposed cross hybrid DRA unit cell offers better bandwidth performance, reflection loss and simpler design compared with other DRA element based structures as listed in Table 3.

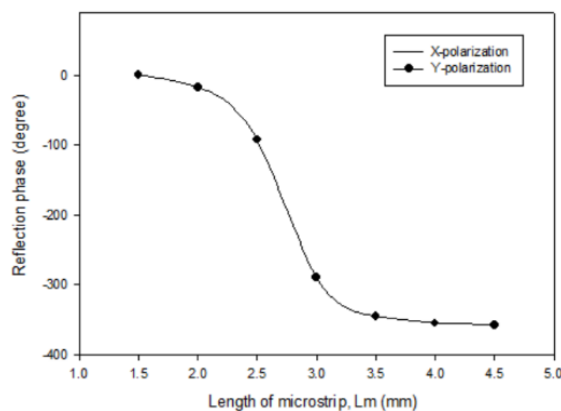
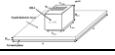
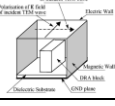
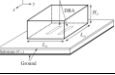
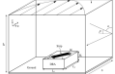
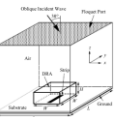
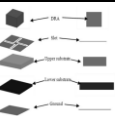
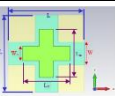


Fig. 7. Reflection phase versus microstrip length at x- and y-polarization directions of cross hybrid DRA unit cell.

Table 3: Comparison between the proposed approach and previous works

Ref.	Design	Freq. (GHz)	Unit Cell Reflection Loss (dB)	Unit Cell Phase Range (°)	Design Complexity
[9]		30	-	330	Mode-rate
[13]		30	-	360	High
[14]		7.5	Moderate	313	Low
[16]		6	Low	147	Mode-rate
[17]		6.5	High	316	Low
[18]		9.3	-	400	Low
Cross hybrid DRA		26	Low	346	Low

IV. CONCLUSION

A cross hybrid DRA unit cell with microstrip patch, which is placed underneath the DRA, aim for easy implementation and fabrication, has been proposed as a reflectarray element in order to realize the 5G requirements of wideband operation. The unit cell offers low reflection loss and a phase range of almost 360° at 26 GHz, which indicates wide bandwidth performance. The phase of each unit cell can be adjusted by varying the length of the cross microstrip. It was also demonstrated that the cross hybrid DRA structure exhibits better performance compared to the full substrate configuration. The further investigations on the use of proposed DRA unit cell element for high gain reflectarray operation is under progress.

ACKNOWLEDGMENT

This work is supported by the Universiti Teknologi Malaysia (UTM) and Ministry of Science Technology and Innovation (MOSTI) under Sciencefund Grant (Vote 4S134).

REFERENCES

- [1] J. Huang and J. A. Encinar, *Reflectarray Antennas*, John Wiley and Sons, Inc., Publication, 2007.
- [2] P. Nayeri, A. Z. Elsherbeni, and F. Yang, "The analogy between offset configurations of parabolic reflectors and reflectarrays," *Applied Computational Electromagnetics Society Journal*, vol. 32, no. 11, pp. 960-965, Nov. 2017.
- [3] M. H. Dahri, M. H. Jamaluddin, M. Inam, and M. R. Kamarudin, "A review of wideband reflectarray antennas for 5G communication systems," *IEEE Access*, vol. 6, no. 1, pp. 5973-5985, Aug. 2017.
- [4] B. Devireddy, A. Yu, F. Yang, and A. Z. Elsherbeni, "Gain and bandwidth limitations of reflectarrays," *Applied Computational Electromagnetics Society Journal*, vol. 26, no. 2, pp. 170-178, Feb. 2011.
- [5] M. H. Jamaluddin, R. Sauleau, X. Castel, R. Benzerger, and L. Le Coq, "Design, fabrication and characterization of a dielectric resonator antenna reflectarray in Ka-band," *Prog. Electromagn. Res. B*, vol. 25, no. 25, pp. 261-275, Sept. 2010.
- [6] J. Shaker, M. R. Chaharmir, and J. Ethier, *Reflectarray Antennas: Analysis, Design, Fabrication, and Measurement*. Artech House Publishers, 2013.
- [7] S. R. Lee, E. H. Lim, and F. L. Lo, "Broadband single-layer E-patch reflectarray," *Radioengineering*, vol. 26, no. 1, pp. 97-106, Apr. 2017.
- [8] S. Costanzo, F. Venneri, A. Borgia, and G. Di Massa, "A single-layer dual-band reflectarray cell for 5G communication systems," *Int. J. Antennas Propag.*, vol. 2019, pp. 8-11, Mar. 2019.
- [9] M. H. Jamaluddin, R. Gillard, R. Sauleau, L. Le Coq, X. Castel, R. Benzerger, and Th. Koleck, "A dielectric resonator antenna (DRA) reflectarray," *Proc. 39th Eur. Microw. Conf.*, vol. 6164, pp. 25-28, Oct. 2009.
- [10] N. F. Sallehuddin, M. H. Jamaluddin, M. R. Kamarudin, M. H. Dahri, and S. U. T. Anuar, "Dielectric resonator reflectarray antenna unit cells for 5G applications," *Int. J. Electr. Comput. Eng.*, vol. 8, no. 4, pp. 2531-2539, Aug. 2018.
- [11] B. Imaz-Lueje, D. R. Prado, M. Arrebola, and M. R. Pino, "Reflectarray antennas: A smart solution for new generation satellite mega-constellations in space communications," *Sci. Rep.*, vol. 10, no. 1, pp. 1-13, Dec. 2020.
- [12] S. H. Zainud-Deen, S. M. Gaber, A. M. Abd-Elhady, K. H. Awadalla, and A. A. Kishk, "Perforated dielectric resonator antenna reflectarray," *Applied Computational Electromagnetics Society Journal*, vol. 26, no. 10, pp. 848-855, Oct. 2011.
- [13] M. G. Keller, J. Shaker, A. Petosa, A. Ittipiboon, M. Cuhaci, and Y. M. M. Antar, "A Ka-band dielectric resonator antenna reflectarrays," *30th Eur. Microw. Conf.*, pp. 272-275, Oct. 2000.
- [14] S. Lee, E. Lim, and F. Lo, "DRA reflectarray unit elements with thin under-loading parallel slots," *Prog. Electromagn. Res. Symp.*, vol. 48, pp. 103-110, Mar. 2014.

- [15] C. Tienda, J. A. Encinar, M. Barba, and M. Arrebola, "Analysis, design and demonstration of a dual-reflectarray antenna in Ku-band for European coverage," *Applied Computational Electromagnetics Society Journal*, vol. 31, no. 5, pp. 498-508, May 2016.
- [16] E. Lim, H. Y. Wong, and F. L. Lo, "Rectangular DRA reflectarray with an inclined top-loading microstrip patch," *PIERS Proc. Guangzhou, China*, pp. 878-881, Aug. 25-28, 2014.
- [17] Y. Tan, E. Lim, and F. Lo, "Transparent DRA reflectarray with bottom-loading strip," *Prog. Electromagn. Res. C*, vol. 58, no. May, pp. 43-50, June 2015.
- [18] F. Ahmadi, K. Forooraghi, Z. Atlasbaf, and B. Virdee, "Dual linear-polarized dielectric resonator reflectarray antenna," *IEEE Antennas Wirel. Propag. Lett.*, vol. 12, pp. 635-638, Apr. 2013.
- [19] S. Costanzo, F. Venneri, A. Borgia, and G. Di Massa, "Dual-band dual-linear polarization reflectarray for mmwaves/5G applications," *IEEE Access*, vol. 8, pp. 78183-78192, Apr. 2020.
- [20] Final Acts WRC, "In World Radiocommunication Conference Geneva: International Telecommunication Union," *World Radiocommun. Conf.*, vol. 238, pp. 25-27, 2015.
- [21] B. Of, J. Sabburg, J. A. R. Ball, and N. H. Hancock, *Dielectric Resonator Antennas*. vol. 35, no. 3. England: Research Studies Press, 1997.
- [22] A. Kiyani and M. Y. Ismail, "Design and analysis of high performance reflectarray resonant elements," *Procedia Eng.*, vol. 53, pp. 248-254, 2013.



Nur Fazreen Sallehuddin received her Bachelor degree in Electrical Engineering (Hons.) (2006) and Master degree in Technic and Vocational Education (2014) from Universiti Tun Hussein Onn Malaysia (UTHM). Experienced as Integration Assistant Engineer and Quality Assurance Engineer for solar industry and automotive industry respectively from 2007-2011. Currently she is pursuing the Ph.D. degree in Electrical Engineering at Wireless Communication Centre, University Technology of Malaysia (UTM). Her research interests and areas include dielectric resonators and reflectarray antennas design in 5G applications and millimeter waves.



Mohd Haizal Jamaluddin received the bachelor's and master's degrees in Electrical Engineering from Universiti Teknologi Malaysia, Malaysia, in 2003 and 2006, respectively, and the Ph.D. degree in Signal Processing and Telecommunications from the Université de Rennes 1, France, in 2009, with a focus on microwave communication systems and specific antennas such as dielectric resonator and reflect array and dielectric dome antennas. He joined the Department of Electronic Engineering, Faculty of Electrical Engineering, Universiti Teknologi Malaysia, as a Tutor in 2003. He is currently an Associate Professor with the Wireless Communication Centre, Universiti Teknologi Malaysia (UTM). He was a Senior Lecturer at Wireless Communication Centre (WCC), Universiti Teknologi Malaysia (UTM) until December 2017. He has published more than 40 ISI/Scopus papers in reputed indexed journals and more than 40 conference proceedings.



Muhammad Ramlee Kamarudin (Senior Member IEEE 13', Member IEEE 08', Member IET 11') obtained his first degree from Universiti Teknologi Malaysia (UTM), Johor Bahru, Malaysia, with honours, majoring in Electrical and Telecommunication Engineering and graduated in 2003. He received the M.S. degree in Communication Engineering in 2004 from the University of Birmingham, Birmingham, UK, and later he obtained his Ph.D. degree in 2007 from the same University under the supervision of Professor Peter Hall. Kamarudin is currently working as a Senior Lecturer at the Centre for Electronic Warfare, Information and Cyber (EWIC), Cranfield Defence and Security, Cranfield University, UK. Prior to this appointment, he was an Associate Professor at Wireless Communication Centre (WCC), Universiti Teknologi Malaysia (UTM), Malaysia until May 2017. He holds a H-Index of 19 (SCOPUS) and more than 1350 citations (SCOPUS). He is an author of a book chapter of a book entitled Antennas and Propagation for Body-Centric Wireless Communications and has published more than 200 technical papers in journals and proceedings including IEEE Transaction on Antenna and Propagation (TAP), IEEE Antennas and Wireless Propagation Letter (AWPL), IEEE Antenna Magazine, IEEE Access, International Journal of Antennas and Propagation (IJAP), Progress in Electromagnetics Research (PIER), Microwave and Optical Technology

Letters (MOTL), and Electronics Letters. His research interests include antenna design for 5G, wireless on-body communications, in-body communications (implantable antenna), RF and microwave communication systems, and antenna diversity. Kamarudin is an IEEE Senior Member (SMIEEE), a Member of IET (MIET), an Executive Member of Antenna and Propagation (AP/MTT/EMC), Malaysia Chapter, and a Member of IEEE Antennas and Propagation Society, IEEE Communication Society, IEEE Microwave Theory and Techniques Society and IEEE Electromagnetic Compatibility Society.



Muhammad Hashim Dahri

received the B.E degree in Telecommunications from the Mehran University of Engineering and Technology (MUET), Pakistan, in 2010 and the Masters by Research degree in Electrical Engineering from Universiti Tun Hussein Onn Malaysia (UTHM) in 2014. He is currently pursuing the Ph.D. degree with the Wireless Communication Centre (WCC), Universiti Teknologi Malaysia (UTM). He has authored over 20 research papers in various indexed journals and conference proceedings. His research interests include reflectarray antennas, planar printed antennas and tunable materials for antenna design.

A Highly Efficient Dual-Band Transmitarray Antenna Using Cross and Square Rings Elements

Yongliang Zhang¹, Xiuzhu Lv², Jiaxuan Han², Shuai Bao², Yao Cai², and Zhao Wu^{3,*}

¹ Department of Transportation
Inner Mongolia University, Hohhot, 010021, China
namar@imu.edu.cn

² Department of Electronic Information Engineering
Inner Mongolia University, Hohhot, 010021, China
31856006@mail.imu.edu.cn, 297492812@qq.com, bstrive@163.com, 17644240882@163.com

³ School of Physics and Telecommunication Engineering
Yulin Normal University, Yulin, 537006, China
kianty@163.com

Abstract — In this paper, a highly efficient dual-band transmitarray antenna using cross and square rings elements is presented for X and Ku bands. The dual-band transmitarray is designed for downlink/uplink frequencies of Ku band satellite communications. The transmitarray element consists of four metal patches and two dielectric substrates. The metal patch is printed on both sides of the substrate. By optimizing the parameters, the transmitarray element can achieve a transmission phase coverage greater than 360° and work independently in both frequency bands. Then, a method to select the size of the element is proposed, so that all the elements in the array can realize the transmission phase of the two frequencies as much as possible. A 201-elements transmitarray antenna is fabricated and measured and the band ratio of the antenna is 1.13. The measured maximum gain at 11.5 GHz is 22.4 dB, corresponding to the aperture efficiency is 52.7%. The measured maximum gain at 13 GHz is 24.2 dB, corresponding to the aperture efficiency is 62.4%. The 1-dB gain bandwidths are 9.7% (10.8-11.9 GHz) at X band and 9% (12.6-13.8 GHz) at Ku band.

Index Terms — Dual-band antenna, highly efficient, transmitarray antenna.

I. INTRODUCTION

TAs the transmitting and receiving device of wireless communication system, antenna directly affects the performance of communication system [1-3]. Compared with parabolic antenna, planar array antenna uses horn antenna to feed, which avoids complex feeding network. It also has the characteristics of multi-frequency band, miniaturization, low profile and high gain.

Planar array antenna includes reflectarray antenna (RA) and transmitarray antenna (TA). Compared with the RA [4-6], the feed of the TA and the radiated electric field are not on the same side, which can completely eliminate the influence of feed occlusion on the antenna performance and has a huge advantage in realizing high-gain directional beam. Therefore, the research of transmitarray antenna has received more and more scholars' attention.

Although the research of transmitarray antenna is relatively mature, it still has the disadvantages of narrow bandwidth and low efficiency. Therefore, in order to meet the needs of communication system, it is necessary to develop dual-band transmitarray antenna. In [7], a triple-layer dual-band transmitarray antenna using orthogonal slots was proposed. The band ratio of the antenna was 1.46 and its 1-dB bandwidth was 7.5% and 4.28% at the center frequency of 12GHz and 17.5 GHz, respectively. In [8], a multilayer dual-band (20/30GHz) transmitarray antenna using cross dipole was reported. The aperture efficiency of the TA was 35% and 50%. However, the transmission phase of the TA was less than 360° . [9] presents a dual-band, dual-polarised metallic slot transmitarray antenna. The antenna does not contain dielectric substrate and consists of only three thin metallic layers. Due to the high transmission loss of the TA element, the aperture efficiency of the TA was only 34.0% and 37.2% at 11 GHz and 12.5 GHz, respectively. A dual-band transmitarray antenna using four-layer metallic slots was designed in [10]. The band ratio of the antenna was 1.5 and its aperture efficiency were 52% and 53% at the center frequencies of 12 GHz and 18 GHz, respectively.

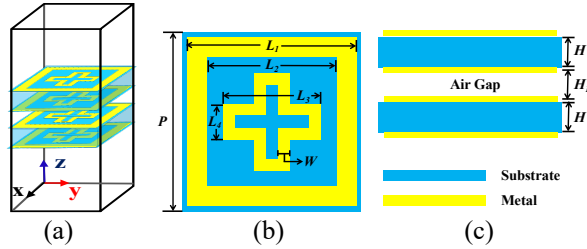


Fig. 1. Geometric model of the dual-band TA element: (a) three-dimensional plot, (b) top view, and (c) lateral view.

Table 1: Design parameters of the dual-band TA element

Parameter	Value
P	9mm
H	1.5mm
H_1	1.5mm
L_1	8.5mm
L_2	Vary
L_3	$L_2-1.6$ mm
L_4	1.8mm
W	0.6mm

The TA element of different frequency bands were placed in the same plane by special arrangement so that the transmitarray antenna could work in both frequency bands. However, this arrangement will be limited by the space, the design flexibility will be greatly reduced, and the coupling between high and low frequency TA elements is large. Other researches on dual-band transmitarray antenna were reported in [11-13].

In this work, an efficient dual-band transmitarray antenna using cross and square rings elements with low frequency separation is presented. In order to meet the requirements of satellite communication, the downlink and uplink frequency of the transmitarray antenna is 11.5/13 GHz, the band ratio of the antenna is 1.13. The chapters of the article are arranged as follows. Section I is the introduction of the transmitarray antenna. Section II is the structure and performance analysis of the TA element. In Section III, a method is proposed to select the element parameters so that all the elements in the array can phase compensate as much as possible in both frequency bands. The simulation and measurement results of the TA are also given in Section III. Finally, Section IV is the conclusion of this paper.

II. DUAL-BAND TA ELEMENT DESIGN

A. The TA element structure

The traditional dual-frequency TA is designed by arranging the element of different frequency bands in the same plane through reasonable space allocation, so that the TA could work independently in both frequency bands [11]. However, this design method is limited by space

and only applicable to antennas with large band ratio. The TA element proposed in this paper can use the same structure to work simultaneously in both frequency bands, which can avoid the problem of the arrangement of high and low frequency elements. The band ratio of the TA is only 1.13. The structure of the TA element is shown in Fig. 1. In order to achieve sufficient transmission phase range, the TA element consists of four patches and two dielectric substrates. The patches are printed on either side of the dielectric substrate. Each patch consists of a cross and a square ring. There is an air gap between the two dielectric substrates, the height of which is equal to the thickness of the dielectric substrates. The relative permittivity and loss tangent of the dielectric substrate are 3.5 and 0.0027, respectively.

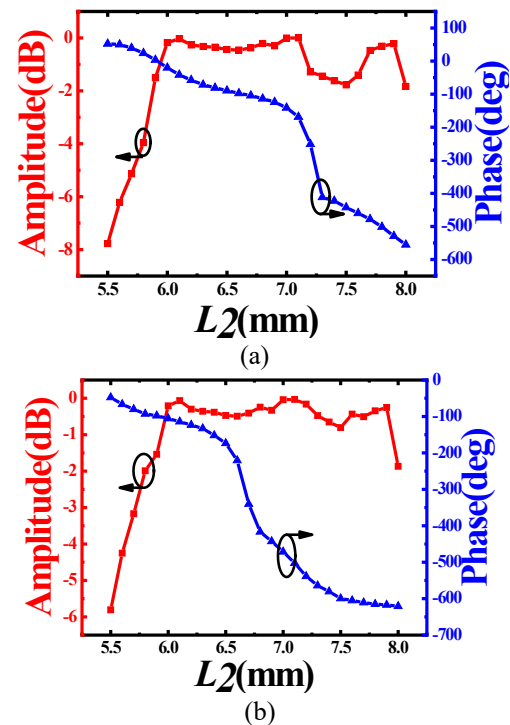


Fig. 2. The transmission amplitude and transmission phase versus L_2 : (a) Freq = 11.5 GHz and (b) Freq = 13 GHz.

In this design, high frequency electromagnetic simulation software Ansys HFSS is used to simulate and optimize the TA element. Master and slave boundary is selected to simulate planar periodic structural surfaces. In order to simplify the design and analysis while increasing the polarization stability of the TA element, the designed element adopts symmetrical structure in the X and Y directions. The peripheral size L_1 of the TA element is fixed, which can effectively suppress the phase error caused by coupling effect between the elements. By optimizing the size of the TA element, the transmission phase of the element is greater than 360° . The specific size

of the TA element is shown in Table 1. As shown in this table, the period P of the TA element is 9 mm ($0.346 \lambda_{\text{lower}}$ at 11.5 GHz and $0.391 \lambda_{\text{higher}}$). By using cross and square rings structures, there are eight adjustable parameters of the TA element. By optimizing a variety of adjustable parameters, the phase coverage of TA element can be greater than 360° and has a good oblique incidence performance. The period of the TA element are less than 0.5λ at both low and high frequencies, so the element has the advantage of high efficiency.

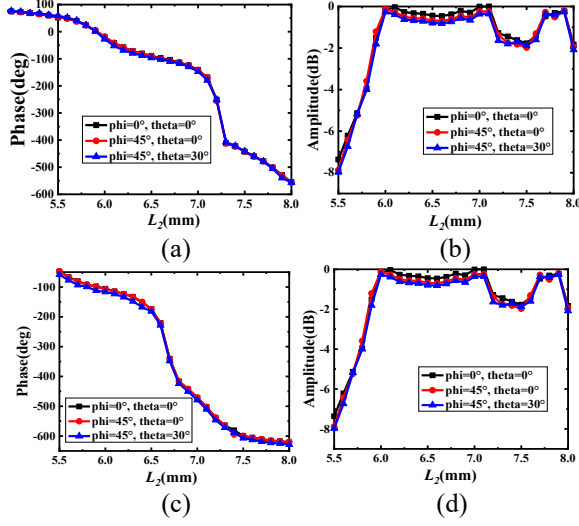


Fig. 3. Transmission coefficient versus L_2 at different oblique incidence angles: (a) transmission phase at 11.5 GHz, (b) transmission amplitude at 11.5 GHz, (c) transmission phase at 13 GHz, and (d) transmission amplitude at 13 GHz.

B. Transmission characteristic of the TA element

The transmission amplitude and transmission phase versus L_2 of the designed TA element in both frequency bands is shown in Fig. 2. As shown in this figure, the transmission phase of the TA element is greater than 360° in both frequency bands. At low frequency, when L_2 is greater than 6mm, the transmission amplitude of the element is always greater than -2dB. At high frequency, when L_2 is greater than 6mm and less than 7.9 mm, the transmission amplitude of the element is greater than -1 dB. This indicates that the TA element can be used in the design of dual-band transmitarray antenna. Since the area of the transmitarray is larger than a few wavelengths, most of the TA elements in the array are illuminated by oblique incident waves, the effect of oblique incidence should also be considered. φ is the angle between the incident wave and the X -axis, θ is the angle between the incident wave and the Z -axis. Figure 3 shows the transmission coefficient of the TA element at different incident angles. As can be seen from the figure, there is little difference between the transmission

phase and transmission amplitude of oblique incident waves (φ from 0° to 45° and θ from 0° to 30°) and normal incident wave. Therefore, all the TA elements in the transmitarray can be phase compensated using the transmission phase curve in Fig. 2.

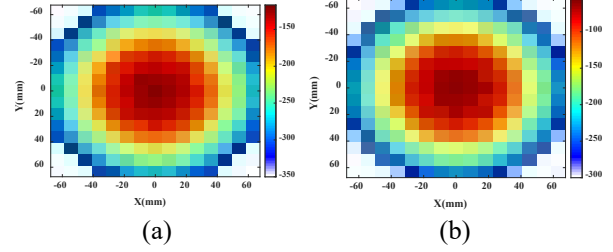


Fig. 4. Transmission phase distribution: (a) Freq = 11.5 GHz; (b) Freq = 13 GHz.

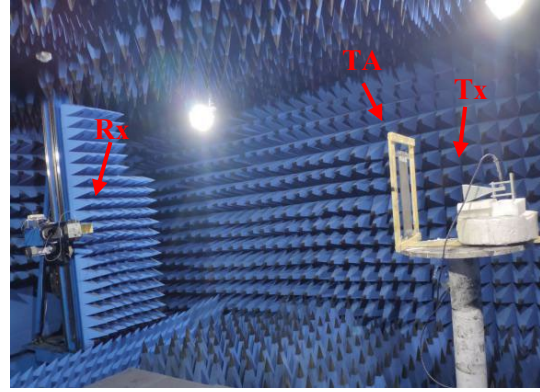


Fig. 5. Fabricated prototype under measurement in the anechoic chamber.

III. DUAL-BAND TRANSMITARRAY ANTENNA DESIGN AND MEASUREMENT

A. Design of dual-band transmitarray antenna

When the TA is in the transmission mode, the electromagnetic wave radiated by the feed horn irradiates to each TA element of the TA along different paths, and the difference of transmission path length leads to a certain wavelength difference between the feed horn and each TA element. Therefore, it is necessary to make corresponding phase compensation for each element in the TA, so as to realize the far-field in-phase superposition in the direction of the main beam. According to the transmitarray theory, the phase compensation value of each TA element can be calculated. In the obtained phase value, firstly select the TA element size that can meet the required transmission phase at both high and low frequencies. If it cannot be realized at the same time, the error coefficient of the TA element needs to be calculated according to equation (1):

$$e(m, n) = \sum_{i=l, h} |\Phi^{desired}(f_i)(m, n) - \Phi^{achieved}(f_i)(m, n)|. \quad (1)$$

In this equation, (m,n) is the position of the TA element; $\phi_{desired}(f_h)$ and $\phi_{desired}(f_l)$ are the transmission phases of high frequency and low frequency that can desired specific beam pointing; $\phi_{achieved}(f_h)$ and $\phi_{achieved}(f_l)$ are the transmission phases of high frequency and low frequency that the TA element can achieved through parameter scanning. The error coefficient of each TA element is calculated by equation (1), and the element size with the minimum error coefficient is selected to obtain the optimal element. Finally, the dual-band transmitarray antenna can obtain independent radiation pattern at both frequencies.

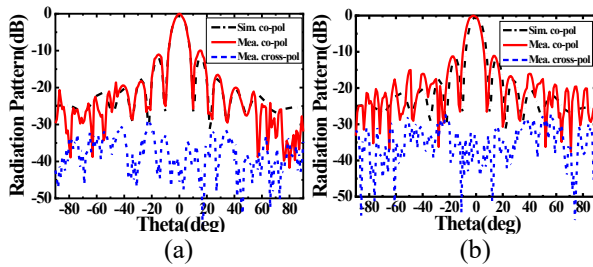


Fig. 6. The simulated and measured normalized radiation patterns at 11.5GHz: (a) E-plane and (b) H-plane.

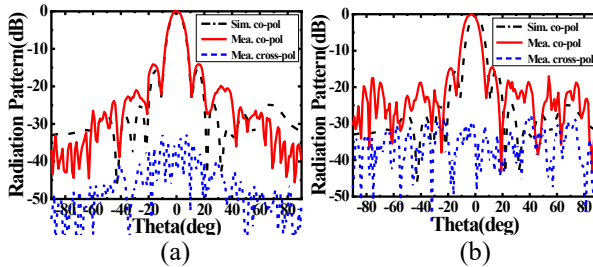


Fig. 7. The simulated and measured normalized radiation patterns at 13GHz: (a) E-plane and (b) H-plane.

In the design of transmitarray antenna, the number of TA elements also needs to be considered. The aperture efficiency of the array is calculated as follows:

$$\varepsilon_{ap} = \frac{G}{D_{max}}, \quad D_{max} = \frac{4\pi A}{\lambda}. \quad (2)$$

G is the measured gain, D_{max} is the maximum directivity, A is the area of the transmitarray, and λ is the wavelength in free-space. Therefore, the larger the number of elements, the greater the gain of the array, but the aperture efficiency of the array may be reduced. In this paper, a 201-element TA using the proposed TA element is proposed. The original array consisted of 15×15 cells, the corresponding aperture area is $135 \times 135 \text{mm}^2$. In order to improve the aperture efficiency of the transmitarray antenna, six TA elements were deleted in each of the four corners. The final aperture area of the transmitarray is 16281mm^2 . When the distance between the horn antenna and the transmitarray is optimal, all elements in the array

are irradiated uniformly by the horn antenna, changing the distance will result the decrease of the gain. The value of focal diameter ratio is generally 0.8-1.5, and the distance between the horn antenna and transmitarray is obtained through optimization. Through simulation and optimization, the distance between the horn antenna and transmitarray is $165 \text{mm} (6.35\lambda_{\text{lower}})$. The corresponding focal diameter ratio is 1.22. In the whole design of the transmitarray antenna, the focal diameter ratio is determined first, and then the appropriate feed horn is selected. When the focal diameter ratio is too large, the beam width of the feed horn needs to be narrower and the beam concentration degree should be higher, so as to ensure that most of the energy of the feed horn can be accepted by the transmitarray. Instead, a wide - beam feed antenna needs to be selected. The feed antenna is a wideband pyramidal horn antenna. The aperture size of the horn size is $84 \text{mm} \times 60 \text{mm}$. The working frequency range of the horn antenna is 6-18GHz. The operating frequency of the horn is 14.8dB at 11.5GHz and 15.6dB at 13GHz. By the calculation of the above theory, the phase distribution of the transmitarray at different frequencies is shown in Fig. 4. The corresponding dimension of the TA element can be obtained through the transmission phase curve in Fig. 2. By the calculation of equation (1), the dimensions of all TA elements can be obtained.

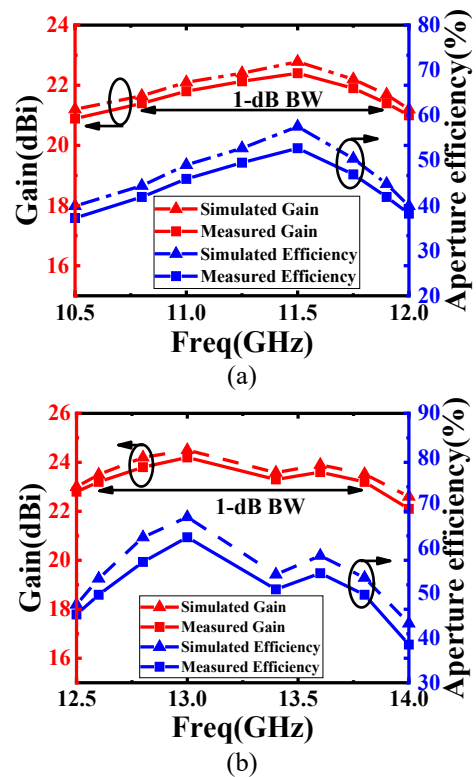


Fig. 8. The measured and simulated gain and aperture efficiency versus frequency: (a) X-band and (b) Ku-band.

B. Experimental results

The fabricated transmitarray antenna was measured in a microwave anechoic chamber, as shown in Fig. 5. TA is the transmitarray under test, Tx is the transmitting horn and Rx is the receiving horn. The normalized radiation patterns of the transmitarray antenna at 11.5 GHz are shown in Fig. 6. The normalized radiation patterns of the transmitarray antenna at 13 GHz are shown in Fig. 7. The measured gain is 0.38 dB lower than the simulation gain at 11.5 GHz. The measured gain is 0.3 dB lower than the simulation gain at 13 GHz. The differences between the measurement results and the simulation results are mainly due to the following points: first, the TA elements size are not as accurate as it should be in the manufacturing process; second, there are intrinsic noises in the anechoic chamber; third, the phase center of the horn antenna is unstable. The measured copolar boresight beams in the designed two bands are not pointed to the desired boresight is mainly caused by the instability of the dielectric substrate during experiment.

In Fig. 6, the cross-polarization of the E-plane and H-plane radiation patterns at 11.5 GHz are 28 dBi and 27 dBi, respectively. The sidelobe level of the E-plane and H-plane radiation patterns at 11.5 GHz are 10 dB and 11 dB, respectively. In Fig. 7, the cross-polarization of the E-plane and H-plane radiation patterns at 13 GHz are 32 dBi and 29 dBi, respectively. The sidelobe level of the E-plane and H-plane radiation patterns at 13 GHz are 14.1 dB and 14.5 dB, respectively. This indicates that the designed transmitarray antenna has good radiation performance. The measured and simulated gain and aperture efficiency versus frequency are shown in Fig. 8. The 1-dB gain bandwidths are 9.7% (10.8-11.9 GHz) at X band and 9% (12.6-13.8GHz) at Ku band. The measured aperture efficiencies in 11.5 GHz and 13 GHz are 52.7% and 62.4%, respectively. Table 2 compares the performance index of the designed TA with other TAs. It can be seen from the table that the designed TA has the characteristics of high efficiency and low band ratio.

Table 2: Comparison of the proposed TA with other TAs

Ref.	Freq. (GHz)	Gain (dB)	Aperture Efficiency (%)	Band Ratio	Total Element Number
[9]	11/12.5	23.74/24.45	38/34.6	1.13	196
[12]	12.5/14.25	31/31.8	45/41.3	1.14	-
[13]	20/30	24.6/27.2	36.0/29.0	1.50	1156
This work	11.5/13	22.4/24.2	52.7/62.4	1.13	201

IV. CONCLUSION

In this paper, a new transmitarray element was proposed for the design of dual-band transmitarray antenna. The transmitarray element structure includes four-layer cross and square rings. The simulation results show that the transmitarray element can reach 360° phase

coverage in both frequency bands and has good oblique incidence performance. To verify the validity of the transmitarray element. A 201-element transmitarray antenna using the proposed element was fabricated and measured. The measurement results have shown that the transmitarray antenna has good radiation performance. At 11.5 GHz, the measured gain and aperture efficiency were 22.4 dB and 52.7%, respectively. At 13GHz, the measured gain and aperture efficiency were 24.2 dB and 62.4%, respectively. The 1-dB bandwidth in X band and Ku band were 9.7% and 9%, respectively.

ACKNOWLEDGMENT

This work was supported by the National Natural Science Foundation of China (NSFC) under Project No. 61761032, Nature Science Foundation of Inner Mongolia under Contract No. 2019MS06006, Natural Science Foundation Youth Fund Project in Guangxi of China under No. 2018GXNSFBFA281124 and China Scholarship Fund.

REFERENCES

- [1] C. A. Balanis, "Antenna theory: Analysis and design," *IEEE Antennas & Propagation Society Newsletter*, vol. 24, no. 6, pp. 28-29, 2003.
- [2] K. D. Xu, H. Luyen, and N. Behdad, "A decoupling and matching network design for single- and dual-band two-element antenna arrays," *IEEE Transactions on Microwave Theory and Techniques*, vol. 68, no. 9, pp. 3986-3999, Sept. 2020.
- [3] K. D. Xu, J. Zhu, S. Liao, and Q. Xue, "Wideband patch antenna using multiple parasitic patches and its array application with mutual coupling reduction," *IEEE Access*, vol. 6, pp. 42497-42506, July 2018.
- [4] Q. Wang, Z. H. Shao, Y. J. Cheng, and P. K. Li, "Broadband low-cost reflectarray using modified double-square loop loaded by spiral stubs," *IEEE Transactions on Antennas and Propagation*, vol. 63, no. 9, pp. 4224-4229, Sept. 2015.
- [5] X. Xia, Q. Wu, H. Wang, C. Yu, and W. Hong, "Wideband millimeter-wave microstrip reflectarray using dual-resonance unit cells," *IEEE Antennas and Wireless Propagation Letters*, vol. 16, pp. 4-7, 2017.
- [6] Q. Gao, J. Wang, Y. Li, and Z. Li, "A multiresonant element for bandwidth enhancement of circularly polarized reflectarray antennas," in *IEEE Antennas and Wireless Propagation Letters*, vol. 17, no. 5, pp. 727-730, May 2018.
- [7] S. M. Gaber, H. Malhat, K. B. Awadalla, "Single feed dual-polarization dual-band transmitarray for satellite applications," *Radio Science Conference*, pp. 27-34, 2013.
- [8] M. R. Chaharmir, A. Ittipiboon, and J. Shaker, "Single-band and dual-band multilayer transmitarray

antennas,” *12th International Symposium on Antenna Technology and Applied Electromagnetics and Canadian Radio Sciences Conference*, pp. 1-4, 2006.

- [9] M. O. Bagheri, H. R. Hassani, B. Rahmati, and B. Rahmati, “Dual-band, dual-polarised metallic slot transmitarray antenna,” *Iet Microwaves Antennas & Propagation*, vol. 11, pp. 402-405, 2017.
- [10] R. Y. Wu, Y. B. Li, W. Wu, C. B. Shi, and T. J. Cui, “High-gain dual-band transmitarray,” *IEEE Transactions on Antennas and Propagation*, vol. 65, no. 7, pp. 3481-3488, July 2017.
- [11] H. Hasani, J. S. Silva, S. Capdevila, M. García-Vigueras, and J. R. Mosig, “Dual-band circularly polarized transmitarray antenna for satellite communications at (20, 30) GHz,” *IEEE Transactions on Antennas and Propagation*, vol. 67, no. 8, pp. 5325-5333, Aug. 2019.
- [12] A. Aziz, F. Yang, S. Xu, and M. Li, “An efficient dual-band orthogonally polarized transmitarray design using three-dipole elements,” *IEEE Antennas and Wireless Propagation Letters*, vol. 17, no. 2, pp. 319-322, Feb. 2018.
- [13] S. A. Matos, E. B. Lima, J. S. Silva, J. R. Costa, C. A. Fernandes, N. J. G. Fonseca, and J. R. Mosig, “High gain dual-band beam-steering transmit array for Satcom terminals at Ka-band,” *IEEE Transactions on Antennas and Propagation*, vol. 65, no. 7, pp. 3528-3539, July 2017.



Yongliang Zhang received the B.S. and Ph.D. degrees from Xidian University, Xi'an, China, in 2009 and 2014, respectively. He is currently with College of Transportation Inner Mongolia University, Hohhot, China.

His research interests include passive microwave/milli-meter wave device, filtering antenna, smart antennas, reconfigurable antennas, and frequency selective surfaces, electromagnetic compatibility, meta surface based antenna.



Xiuzhu Lv received bachelor degree in Communication Engineering from Inner Mongolia University of Science and Technology, Baotou, China, in 2018. From 2018, she pursued her Master degree in Inner Mongolia University. Her research interest are transmitarray antenna

and frequency selective surface.



Jiaxuan Han received the bachelor degrees of Electronic Information Engineering from the Henan Polytechnic University, Jiaozuo, China, in 2017. From 2019, he pursued master degree in Inner Mongolia University. His research interest include optimization algorithms for metasurface array, deep learning, and its applications in electromagnetic modeling.



Bao Shuai received bachelor degree from Shijiazhuang Tiedao University, Shijiazhuang, China in 2019. From 2019, he pursued his master degree in inner Mongolia University. His research interests include optimization algorithms for antenna, deep learning, and its applications in

electromagnetic modeling.



Yao Cai received bachelor degree from Northeast Electric Power University, Jilin, China, in 2019. From 2019, he pursued his Master degree in Inner Mongolia University. His research interests include electromagnetic metamaterial, reconfigurable antenna design and

applications.



Zhao Wu was born in Guangxi, China, in 1987. He received the B.E. degree in Electronic and Information Engineering and Ph.D. degree in Electromagnetic Fields and Microwave Technology from Xidian University, Xi'an, China, in 2011 and 2016, respectively. From

October 2016 to March 2017, he was with Huawei Technologies Co Ltd. Since April 2017, he has been working with College of Physics and Telecommunication Engineering as a Lecturer, Yulin Normal University. His research interests include metamaterials, novel antennas, reconfigurable antenna design and applications.

Dual-polarized Fixed-frequency Beam Scanning Leaky-wave Antenna for 5G Communication

Hao Xiang Li¹ and Yong Jin Zhou^{1,2,*}

¹Key Laboratory of Specialty Fiber Optics and Optical Access Networks
Shanghai University, Shanghai 200444, China

²State Key Laboratory of Millimeter Waves, Southeast University, Nanjing 210096, China
*yjzhou@shu.edu.cn

Abstract — A low profile and dual-polarized fixed-frequency beam scanning leaky wave antenna for 5G communication is presented, which is based on a corrugated microstrip line (CML) called spoof surface plasmons transmission line. The antenna radiates horizontally polarized electromagnetic wave and vertically polarized electromagnetic wave using two different periodic antennas elements. The fabricated antenna is measured and the results show that the operating frequency of the antenna is 3.4-3.7 GHz. The measured main beam angle scans from -9° to -30° . The measured gain is from 8.3 dB to 9.7 dB over the working band.

Index Terms —Spoof surface plasmons, 5G, dual-polarized, fixed-frequency

I. INTRODUCTION

The commercialization of the fifth generation mobile communication system (5G) puts forward many high performance requirements for the communication system [1]. As a crucial part of the communication system, the breakthrough of the antenna will obviously improve the performance of the whole communication system. The traditional beam scanning antenna usually uses frequency scanning mechanism or phase shifter to realize beam scanning, which will inevitably bring the problem of occupying wide-band spectral resources and complex feeding network structure, thus increasing the volume and cost of the whole system [2].

Leaky wave antennas (LWA) have advantages of high gain, frequency scanning features, and a simple feeding structure. The combination of metamaterials and traditional leaky wave antennas results in low profile, high gain, low cost leaky wave antennas, which emerged as potential candidates in modern wireless communication system [3,4]. The metamaterial leaky wave antennas can be divided into two kinds. One kind is based on the composite right-/left-handed (CRLH) transmission line and the other is based on the spoof

surface plasmons (SPs) [5,6]. By constructing CRLH transmission line design in the balance, researchers concluded that CRLH leaky wave antennas can overcome the open-stopband effects [7,8]. Different devices based on spoof SPs at millimeter wave and terahertz frequencies have been demonstrated [9-12]. The spoof SPs LWA can radiate spatial harmonics by introducing periodic modulations [13-17]. However, previous metamaterial leaky wave antennas occupy wide-band frequency resources in the frequency scanning process, hence most of the above metamaterial leaky wave antennas are generally designed for satellite communication (working at high frequency band) or radar detection to carry out large-angle scanning, which are not suitable for 5G communication system with relatively narrow operating bands [18,19]. Therefore, how to complete beam scanning metamaterial LWA at fixed-frequency is an important research area.

In recent years, researchers have achieved beam scanning metamaterial leaky-wave antennas at fixed frequencies by loading PIN-diodes or varactor diodes [20-24]. For example, single-polarized fixed-frequency beam scanning antennas based on spoof SPs have been proposed [20-21], respectively. However, these beam scanning antennas still are single-polarized, which does not meet the requirements of 5G communication system, since dual-polarized antenna in the communication system is necessary. Especially in 5G communication systems, large-scale antenna arrays are generally adopted, which requires the polarization diversity. Therefore, the study of dual-polarized fixed-frequency beam scanning antenna is important [25-26].

In this work, we propose a dual-polarized beam scanning antenna as shown in Fig. 1. The dispersion curve of the antenna unit is adjusted by loading a varactor diode to complete the beam scanning at a fixed-frequency. The working frequency band is located in 3.4-3.7 GHz for 5G communication. The maximum gain can reach 10 dB in the working frequency band, and the rotation angle at the 3.5 GHz is about 21° .

Compared with previous leaky wave antennas, the proposed antenna has the advantages of dual polarization, low profile and beam scanning at a fixed frequency.

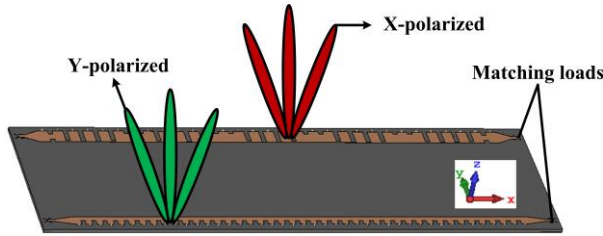


Fig. 1. A dual-polarized beam scanning LWA.

II. ANTENNA DESIGN

A. The design of X-polarized antenna

The X-polarized antenna structure with five modulation periods is shown in Fig. 2. The dimensions shown in Fig. 2 (a) are $od = 13$ mm, $op = 6od = 78$ mm, $w_1 = 0.6$ mm, $w_2 = 2.1$ mm, $h_4 = 15$ mm, $tl_1 = 0.7od$, and $tl_2 = 0.3od$. The groove depths are $h_1 = 3.137$ mm, $h_2 = 13.164$ mm, $h_3 = 14.51$ mm, respectively. The schematic of the LWA with sinusoidally modulated surface impedance is shown in Fig. 2 (b), which is composed of a corrugated metallic strip line, dielectric substrate and metallic ground, where the dielectric substrate is F4B with relative permittivity 3.5 and loss tangent 0.001. The thicknesses of dielectric substrate and the metal are 3 mm and 0.018 mm, respectively. The total length of the LWA is 440 mm.

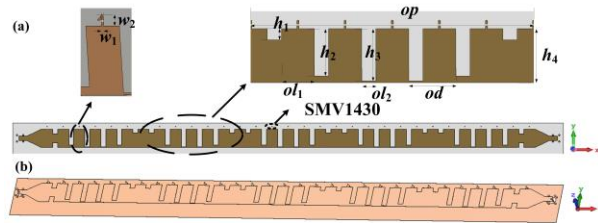


Fig. 2. (a) The details of X-polarized antenna, and (b) the perspective of X-polarized antenna (the dielectric substrate is transparent).

The radiation principle of X-polarized antenna with different grooves is that the surface impedance changes result in the formation of space radiation. The radiated electric field is always perpendicular to the groove [20]. Hence, the direction of its polarization is along the X-axis (X-polarized antenna).

According to the leaky-wave antenna theory, the surface impedance of the antenna is modulated periodically according to the sine function, as shown in

Equation (1),

$$Z_s(x) = jX_s [1 + M \cos(\frac{2\pi x}{p})], \quad (1)$$

where X_s , M , and p are the average surface reactance, modulation factor, and the modulation period, respectively.

From the Floquet theorem, the surface wave propagating on the impedance will excite infinite high-order spatial harmonics, as shown in Equation (2):

$$\beta_N p = \beta_0 + 2\pi n, \quad (2)$$

where β_0 is the phase constant of the fundamental space harmonic with $N = 0$ and β_N is the phase constant of N -order.

These higher spatial harmonics can be surface waves propagating along the surface or leakage waves radiating into free space. The mode of these high-order spatial harmonics mainly depends on the modulation period. The first negative harmonic mode is usually designed to generate the leaky-wave radiation, whose radiation angle can be calculated by Equation (3),

$$\theta \approx \sin^{-1}(\sqrt{1 + X'^2} - \frac{2\pi}{k_0 p}), \quad (3)$$

where $X' = X_s/\eta_0$ is the normalized average surface reactance and k_0 is the propagation constant of free space.

The simulated S-parameters and gain are obtained by using CST. The simulated dispersion curves of the antenna elements with different groove depths are shown in Fig. 3. From the dispersion curve, it can be seen when $h = 0$ mm (unmodulated spoof SPs transmission line), the slope of the dispersion curve is the speed of light and the greater the depth of the groove is, the lower the cut-off frequency is.

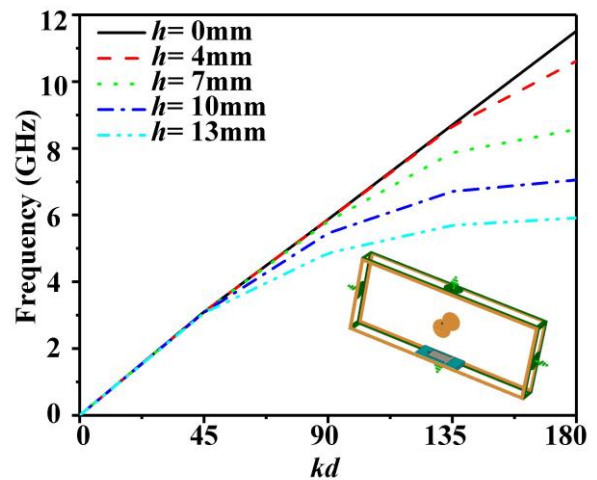


Fig. 3. The dispersion curves of the antenna elements with different groove depths.

The simulated S-parameters of the X-polarized antenna are shown in Fig. 4. It can be seen that the S_{11} is below -13 dB at 3.4-3.7 GHz, and the S_{21} is about -3 dB, which indicates that the antenna can work at 3.4-3.7 GHz.

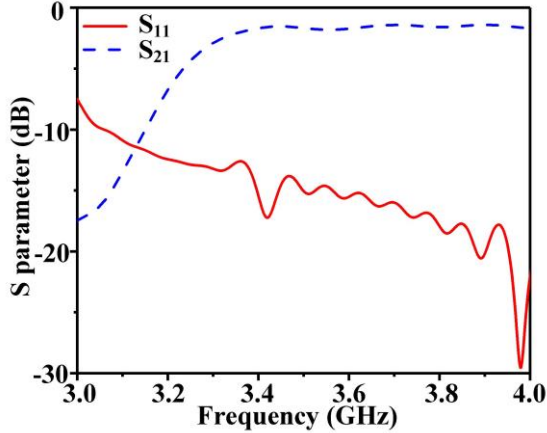


Fig. 4. The simulated S-parameters of X-polarized antenna with loaded capacitance of 0.88 pF.

The electric field of the X-polarized antenna is perpendicular to the groove. Hence, the direction of the polarization is along the X-axis [20]. The simulated far-field radiation pattern of the LWA is plotted in Fig. 5, which shows a narrow beam in E-plane (xoz plane) plane with low back lobes. The level of the cross polarization (Y polarization) is also low. By loading the SMV1430-040LF varactor diode, the X-polarized antenna can complete beam scanning at a fixed frequency.

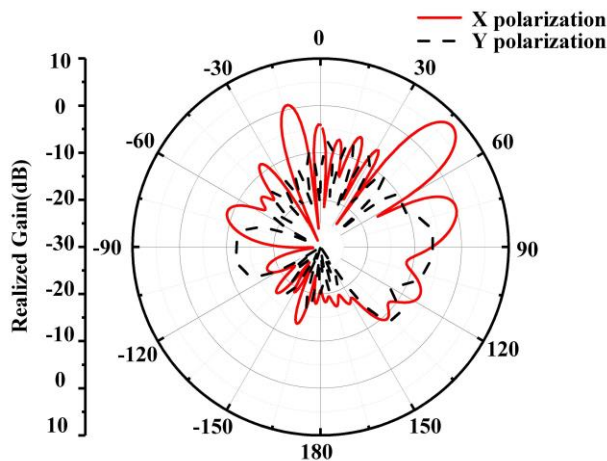


Fig. 5. Simulated far-field radiation pattern of the X-polarized antenna at 3.7 GHz with loaded capacitance of 0.88 pF.

B. The design of Y-polarized antenna

The radiation principle of the Y-polarized antenna is different from that of X-polarized antenna. By loading different capacitors periodically, the Y-polarized antenna radiates electromagnetic waves into space. The radiation principle of the antenna with same grooves is that the surface impedance changes due to different capacitances. So the electric field of the antenna is always along the loading capacitance [21]. It is along Y-axis direction (Y-polarized antenna). The Y-polarized antenna has seven modulation periods, as shown in Fig. 6. The geometric parameters shown in Fig. 6 (a) are $td = 9.2$ mm, $tp = 6td = 55.2$ mm, $h_s = 10$ mm, $tl_1 = 0.6td$, and $tl_2 = 0.4td$.

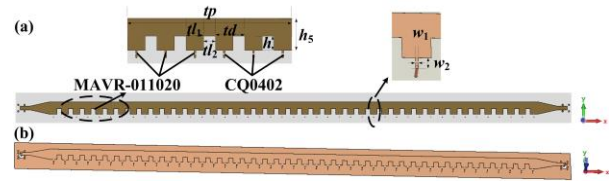


Fig. 6. (a) The details of Y-polarized antenna, and (b) the perspective view of the Y-polarized antenna.

The modulation period consists of six sub-wavelength units, and these sub-wavelength units loaded with three identical fixed capacitors and varactor diodes to periodically change the surface impedance. The surface impedance modulation principle of Y-polarized antenna can be equivalent to the triangular impedance modulation principle as shown in Equation (4):

$$Z_s(x) = \begin{cases} jX_s \left(1 + \frac{2M}{p}x - \frac{M}{2}\right) & \text{if } 0 \leq x \leq \frac{p}{2} \\ jX_s \left(1 - \frac{2M}{p}x + \frac{3M}{2}\right) & \text{if } \frac{p}{2} \leq x \leq p \end{cases}, \quad (4)$$

where X_s , M , and p are the average surface reactance, modulation factor and the modulation period, respectively. The surface impedance of the antenna unit is changed by periodically changing the capacitance, so the direction of electric field change is always perpendicular to the groove where the capacitance is loaded.

The simulation setting of one unit cell of the Y-polarized antenna is shown in Fig. 7 (a), where periodic boundary condition (PBC) is used in x direction and perfect electric conductor condition (PEC) is used in y direction. The Eigenmode Solver of the commercial software CST Microwave Studio is adopted. However, the lumped capacitor cannot be added in the Eigenmode Solver of CST Microwave Studio. Hence, an equivalent model is used to take place of the lumped capacitor in the simulations. The equivalent model consists of two metallic slabs spaced by a dielectric block. The

permittivity of the dielectric block can be calculated by $\epsilon_c = \epsilon_0 \cdot b_2 \cdot C / (a_1 \cdot a_2)$, in which C is the capacitance of the lumped capacitor, and a_1 , a_2 , and b_2 are the dimensions illustrated in Fig. 7 (a). The simulated dispersion curves of the unit with different capacitances are shown in Fig. 7 (b). We can predict the operation band of the antenna from the dispersion curve.

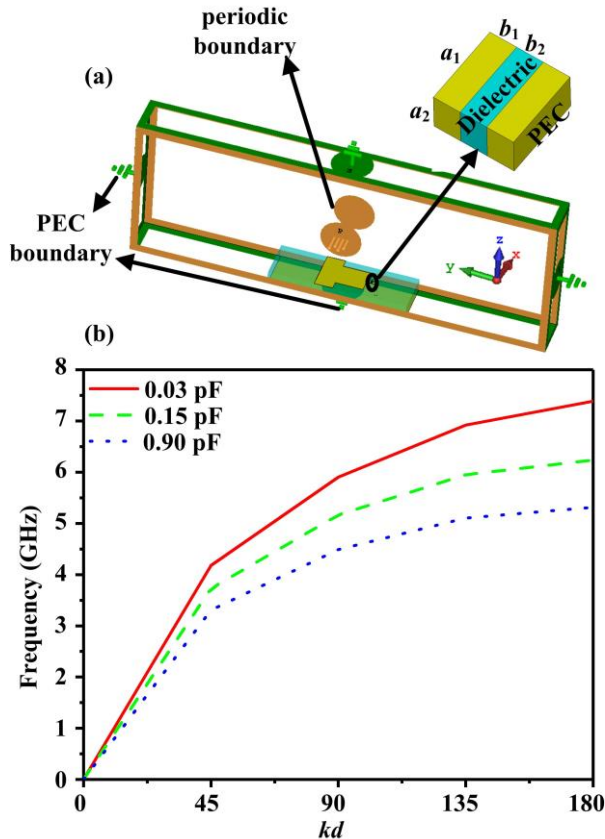


Fig. 7. (a) The details of simulation setting, and (b) the dispersion curves of the antenna elements loading different capacitors.

The simulated S-parameters of the Y-polarized antenna are shown in Fig. 8. It can be seen that the S_{11} is below -12 dB at 3.4-3.7 GHz, and the S_{21} is about -28 dB, which indicates that the antenna can effectively work at 3.4-3.7 GHz. Compared with Fig. 4, it can be seen that the S_{21} performs better in Fig. 8 for the Y-polarized antenna. That is because that the impedance changes caused by periodic loaded capacitors are more drastic than those caused by different groove depths, which leads to more leaky wave radiation energy of the Y-polarized antenna. Therefore, the S_{21} of the Y-polarized antenna performs better than that of the X-polarized antenna.

Furthermore, the simulated far-field radiation pattern of the LWA is plotted in Fig. 9, which shows a narrow

beam in E-plane (xoz plane) with low back lobes. The level of the X polarization is also low. By periodically loading the varactor diodes (MAVR-011020-1411) and the fixed capacitors (CQ0402BRNPO9BN1R1), the Y-polarized antenna completes beam scanning at a fixed frequency.

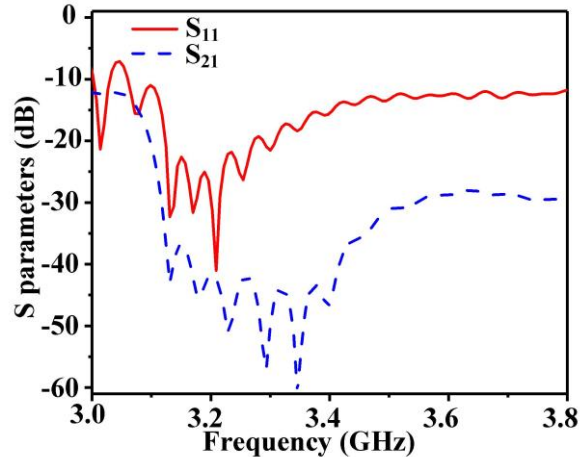


Fig. 8. The simulated S-parameters of Y-polarized antenna with loaded capacitance of 0.15 pF.

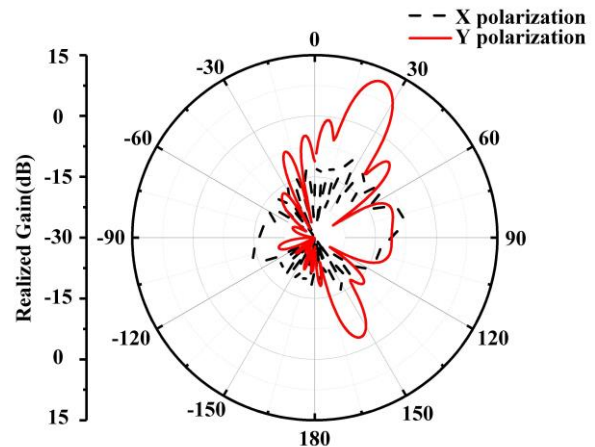


Fig. 9. The simulated far-field radiation pattern of the Y-polarized antenna at 3.7 GHz with loaded capacitance of 0.15 pF.

C. The design of dual-polarized antenna

We combine the X-polarized antenna and the Y-polarized antenna to form the dual-polarized antenna. The simulated isolation and far-field patterns of the dual-polarized antenna are shown in Fig. 10. As can be seen from Fig. 10 (a), the isolation degree of each port is less than -35 dB. From Fig. 10 (b), it can be seen that the beam scanning dual-polarized antenna has been achieved, where the X-polarized antenna and the Y-

polarized antenna are loaded with the capacitance of 0.7pF and 0.24pF, respectively.

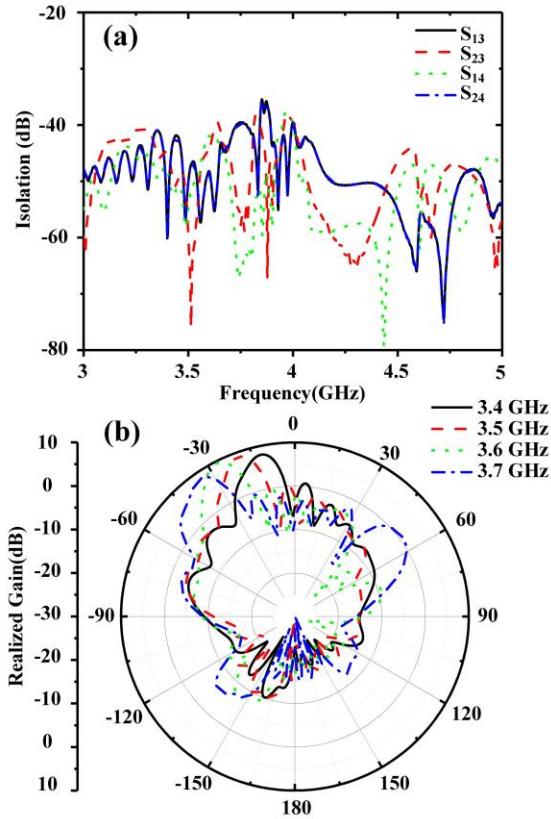


Fig. 10. (a) The isolation of the dual-polarized antenna, (b) Simulated synthesized far-field radiation pattern of the dual-polarized antenna.

III. RESULTS AND DISCUSSION

The fabricated antenna and its measurement environment are shown in Fig. 11. The dual-polarized antenna is shown in Fig. 11 (a). The final dimension of the dual-polarized antenna is 440 mm × 140 mm × 3 mm.

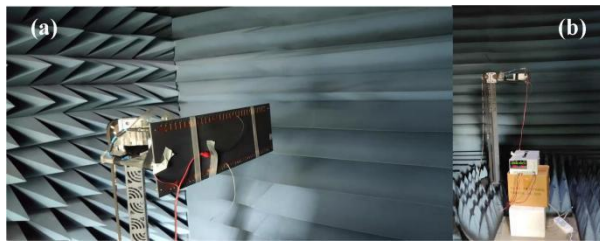


Fig. 11. (a) The sample of the fabricated antenna, and (b) the measurement environment.

The simulated and measured S-parameters are shown in Fig. 12. The higher the operating frequency of the active device is, the larger the influence of parasitic

parameters is. The measured S_{11} and S_{21} vary drastically from their simulated results, respectively. However, the trend of simulation result agrees well to that of measurement result. Both errors are caused by the inaccurate parasitic parameters of the varactor diodes and by machining and welding.

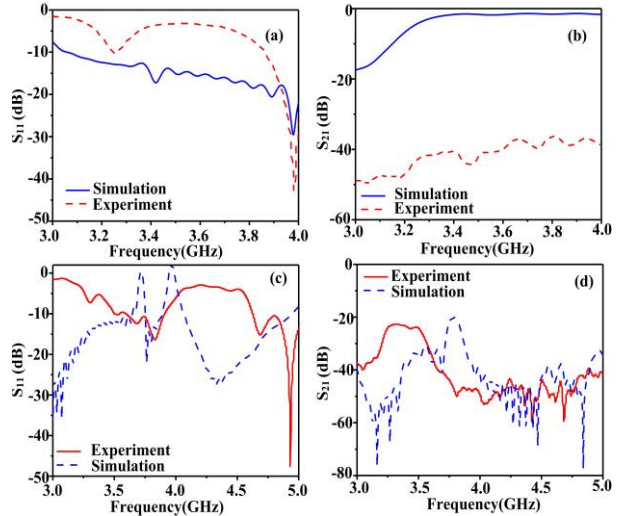


Fig. 12. The simulated and measured (a) S_{11} and (b) S_{21} of X-polarized antenna with loaded capacitance of 0.68 pF. The simulated and measured (c) S_{11} and (d) S_{21} of Y-polarized antenna with loaded capacitance of 0.15 pF.

The measured far-field radiation patterns of the dual-polarized antenna at 3.5 GHz with different voltages are shown in Fig. 13. It can be seen that when the voltage changes from 0 V to 5 V, the scanning angle is from -9° to -30° at 3.5 GHz.

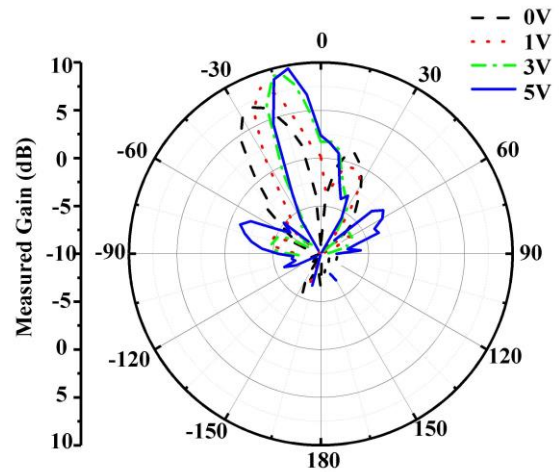


Fig. 13. The measured far-field radiation pattern of the dual-polarized antenna at 3.5 GHz with different voltages.

The simulated and measured gains of the dual-polarized antenna are shown in Fig. 14. It can be seen that the experimental results agree well with the simulation results. As the parasitic parameters of the varactor diode model are set to be typical values in simulation according to the datasheet, the actual values may be different in the lower frequency band, which results in that the actual gain at 3.3 GHz and 3.4 GHz is higher than the simulated gain.

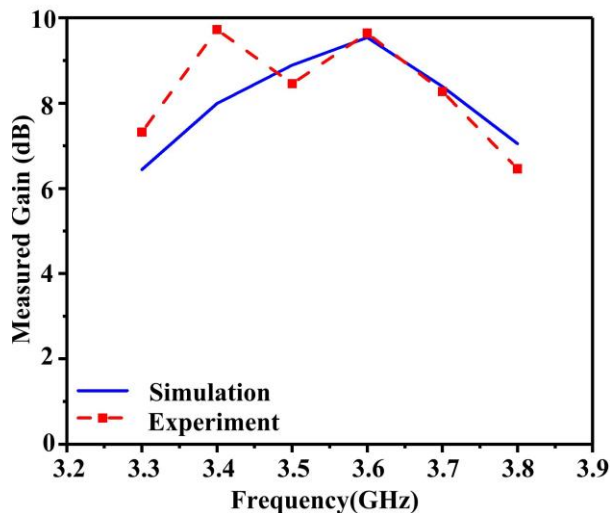


Fig. 14. The simulated and measured gain of the dual-polarized antenna.

IV. CONCLUSION

Here a dual-polarized high-gain fixed-frequency beam scanning antenna for 5G communication is proposed. By using the surface impedance modulation technology and loading the active devices, the dual-polarized antenna can achieve the fixed-frequency beam scanning at 3.4-3.7 GHz ($S_{11} < -10$ dB) for 5G communication systems.

ACKNOWLEDGMENT

This work was supported in part by the National Natural Science Foundation of China under Grant No. 61971469, and in part by Science and Technology Commission Shanghai Municipality (STCSM) under Grant No. 18ZR1413500, and in part by the Open Project Program of the State Key Laboratory of Millimeter Waves under Grant No. K202109.

REFERENCES

- [1] K. Kaur, S. Kumar, and A. Baliyan, "5G: A new era of wireless communication," *International Journal of Information Technology*, vol. 12, pp. 619-624, June 2020.
- [2] S. Rathod, K. Sreenivasulu, K. S. Beenamole, and K. P. Ray, "Evolutionary trends in transmit/receive module for active phased array radars," *Defence Science Journal*, vol. 68, pp. 553-559, 2018.
- [3] A. A. Oliner, "Leakage from higher modes on microstrip line with application to antennas," *Radio Science*, vol. 22, pp. 907-912, Nov. 1987.
- [4] D. R. Jackson and A. A. Oliner, "Leaky-wave antennas," in *Modern Antenna Handbook*, C. Balanis, Ed., New York, Nov. 2007.
- [5] K. D. Xu, S. Lu, Y. J. Guo, and Q. Chen, "High-order mode of spoof surface plasmon polaritons and its application in bandpass filters," *IEEE Transactions on Plasma Science*, vol. 49, pp. 269-275, Mar. 2021.
- [6] J. X. Li, J. W. Shi, K. D. Xu, Y. J. Guo, A. X. Zhang, and Q. Chen "Spoof surface plasmon polaritons developed from coplanar waveguides in microwave frequencies," *IEEE Photonics Technology Letters*, vol. 32, pp. 1431-1434, Oct. 2020.
- [7] A. Lai, T. Itoh, and C. Caloz, "Composite right/left-handed transmission line metamaterials," *IEEE Microwave Magazine*, vol. 5, pp. 34-50, Oct. 2004.
- [8] S. Rezaee and M. Memarian, "Analytical study of open-stop band suppression in leaky-wave antennas," *IEEE Antennas and Wireless Propagation Letters*, vol. 19, pp. 99, Jan. 2020.
- [9] K. D. Xu, Y. J. Guo, Q. Yang, Y. L. Zhang, X. J. Deng, A. X. Zhang, and Q. Chen, "On-chip GaAs-based spoof surface plasmon polaritons at millimeter-wave regime," *IEEE Photonics Technology Letters*, vol. 33, pp. 255-258, Jan. 2021.
- [10] Y. Li, J. Lin, H. Guo, W. Sun, S. Xiao, and L. Zhou, "A tunable metasurface with switchable functionalities: From perfect transparency to perfect absorption," *Advanced Optical Materials*, vol. 8, pp. 1901548, Jan. 2020.
- [11] S. Xiao, F. Zhong, H. Liu, S. Zhu, and J. Li, "Flexible coherent control of plasmonic spin-Hall effect," *Nature Communications*, vol. 6, pp. 1-7, Sep. 2015.
- [12] B. Yang, T. Liu, H. Guo, S. Xiao, and L. Zhou, "High-performance meta-devices based on multi-layer meta-atoms: interplay between the number of layers and phase coverage," *Science Bulletin*, vol. 64, pp. 823-835, May 2019.
- [13] G. S. Kong, H. F. Ma, B. G. Cai, and T. J. Cui, "Continuous leaky-wave scanning using periodically modulated spoof plasmonic waveguide," *Scientific Reports*, vol. 6, pp. 1-9, July 2016.
- [14] X. Liu, B. Chen, J. Zhang, "Frequency scanning planar antenna based on spoof surface plasmon polariton," *IEEE Antennas and Wireless Propagation Letters*, vol. 16, pp. 165-168, May 2016.
- [15] H. Chen, H. Ma, Y. Li, J. Wang, Y. Han, and M. Yan, "Wideband frequency scanning SSPP planar antenna based on transmissive phase gradient

- metasurface,” *IEEE Antennas and Wireless Propagation Letters*, vol. 17, pp. 463-467, Jan. 2018.
- [16] J. Y. Yin, J. Ren, and Q. Zhang, “Frequency-controlled broad-angle beam scanning of patch array fed by spoof surface plasmon polaritons,” *IEEE Transactions on Antennas and Propagation*, vol. 64, pp. 5181-5189, Nov. 2016.
- [17] D. F. Guan, P. You, and Q. Zhang, “A wide angle and circularly polarized beam scanning antenna based on microstrip spoof surface plasmon polariton transmission line,” *IEEE Antennas and Wireless Propagation Letters*, vol. 16, pp. 2538-2541, July 2017.
- [18] M. Ettorre, R. Sauleau, L. Le Coq, and F. Bodereau, “Single-folded leaky-wave antennas for automotive radars at 77 GHz,” *IEEE Antennas and Wireless Propagation Letters*, vol. 9, pp. 859-862, Sep. 2010.
- [19] F. Kozak, V. Jenik, J. Machac, and P. Hudec, “Microwave radar sensor based on CRLH siw leaky-wave antennas,” *European Radar Conference*, pp. 53-56, Dec. 2014.
- [20] M. Wang, H. F. Ma, H. C. Zhang, W. X. Tang, X. R. Zhang, and T. J. Cui, “Frequency-fixed beam-scanning leaky-wave antenna using electronically controllable corrugated microstrip line,” *IEEE Transactions on Antennas and Propagation*, vol. 66, pp. 4449-4457, June 2018.
- [21] M. Wang, H. F. Ma, W. X. Tang, H. C. Zhang, W. X. Jiang, and T. J. Cui, “A dual-band electronic-scanning leaky-wave antenna based on a corrugated microstrip line,” *IEEE Transactions on Antennas and Propagation*, vol. 67, pp. 3433-3438, Mar. 2019.
- [22] S. Chen, D. K. Karmokar, Z. Li, P. Qin, R. W. Ziolkowski, and Y. J. Guo, “Continuous beam scanning at a fixed frequency with a composite right-/left-handed leaky-wave antenna operating over a wide frequency band,” *IEEE Transactions on Antennas and Propagation*, vol. 67, pp. 7272-7284, Aug. 2019.
- [23] R. Shaw and M. K. Mandal, “Broadside scanning fixed frequency LWA with simultaneous electronic control of beam angle and beamwidth,” *IEEE Transactions on Antennas and Propagation*, vol. 68, pp. 3504-3514, Feb. 2020.
- [24] I. Serhsouh, M. Himdi, H. Lebbar, and H. Vettikalladi, “Reconfigurable SIW antenna for fixed frequency beam scanning and 5G applications,” *IEEE Access*, vol. 8, pp. 60084-60089, Mar. 2020.
- [25] H. Wang, “Capacity improvement through selection diversity for dual-polarized antenna systems,” *International Journal of Communication Systems*, vol. 33, pp. 1074-5351, Jan. 2020.
- [26] L. Xu and Y. J. Zhou, “Low profile high-gain antenna for broadband indoor distributed antenna system,” vol. 35, no. 7, pp. 791-796, July 2020.



Hao Xiang Li was born in Xian, Shanxi, China, in 1996. He is currently pursuing the Master's degree of Electronic and Communications Engineering in Shanghai University, Shanghai 200444, China. His research interests include broadband antenna, beaming scanning antenna and metamaterials.



Yong Jin Zhou was born in Shandong, China, in 1982. His current research interests include microwave and millimeter antenna, plasmonic metamaterials and applications, millimeter wave and THz functional devices, wireless energy transmission. He received the B.S. degree in Communication Engineering from Shandong University, Jinan, China, in 2006, and Ph.D. degree in Electromagnetic Field and Microwave Technology from Southeast University, Nanjing, China, in 2011, respectively. From 2009 to 2010, he was a Visiting Scholar of University of Houston. From 2011 to 2012, he was a Software Engineer with EEBU of Marvell Technology (Shanghai) Ltd. From 2012 to 2015, he was an Assistant Professor and from 2015 to 2020, he was an Associate Professor with School of Communication & Information Engineering, Shanghai University, Shanghai, China. Currently, he is a Professor with School of Communication & Information Engineering, Shanghai University, Shanghai, China. He has authored and coauthored over 90 papers in peer-reviewed journals and conference proceedings. He is IEEE Member, OSA Member, and Senior Member of Chinese Institute of Electronics. He is serving as a Reviewer for over 20 peer-reviewed journals, such as Nature electronics, Photonic Research, Optics Letter, Optics Express, Appl. Phys. Express, IEEE Access, IEEE MTT, IEEE MWCL, etc. He was serving as a Session Chair for several International Symposiums.

Miniaturized Wideband Bandpass Filter based on Capacitor-loaded One-eighth Wavelength Coupled Line

Jin Shi^{1,2,3}, Jiancheng Dong¹, Kai Xu^{1,2,3}, and Lingyan Zhang^{1,2,3}

¹ School of Information Science and Technology
Nantong University, Nantong, 226019, China

jinshi0601@hotmail.com, Dongjiancheng2019@outlook.com, xukaihopeness@hotmail.com, zhangly@ntu.edu.cn

² Nantong Research Institute for Advanced Communication Technologies
Nantong, 226019, China

³ Research Center for Intelligent Information Technology
Nantong University, Nantong, 226019, China

Abstract — A novel miniaturized wideband bandpass filter (BPF) using capacitor-loaded microstrip coupled line is proposed. The capacitors are loaded in parallel and series to the coupled line, which makes the filter just require one one-eighth wavelength coupled line and achieve filtering response with multiple transmission poles (TPs) and transmission zeros (TZs). Compared with the state-of-the-art microstrip wideband BPFs, the proposed filter has the advantages of compact size and simple structure. A prototype centered at 1.47 GHz with the 3-dB fractional bandwidth of 86.5% is demonstrated, which exhibits the compact size of $0.003\lambda_g^2$ (λ_g is the guided wavelength at the center frequency) and the minimum insertion loss of 0.37 dB.

Index Terms — Bandpass filter, capacitors, coupled line, miniaturized, wideband.

I. INTRODUCTION

Miniaturized wideband bandpass filter (BPF) is one essential component in the modern wireless communication system owing to the advantages of compact size and high data-rate transmissions. So far, numerous microstrip wideband BPFs have been proposed based on various structure, including stub-loaded multiple-mode resonator [1]-[6], stub-loaded coupled line [7]-[9], cross-coupled multiple-mode resonator [10], ring resonator associated with open stubs [11]-[12], and stub-loaded stepped impedance resonator (SIR) [13]-[16]. However, the filter utilizing the above structures suffers from the large circuit size (e.g., $0.271\lambda_g^2$), which is mainly derived from the large size of the resonator or extra loaded stubs.

In order to reduce the size of microstrip wideband

BPF, quarter-wavelength three-line coupled structure [17], high-impedance microstrip line with folded stepped impedance stubs and radial stubs [18], and quarter-wavelength interdigital coupled SIR [19] are utilized. The circuit size can be reduced to $0.013\lambda_g^2$, $0.009\lambda_g^2$, and $0.006\lambda_g^2$, respectively, but with a complex structure.

Loading lumped elements can also help reduce the circuit size of microstrip BPF. For instance, capacitors are loaded in parallel on the half-wavelength microstrip coupled line so that a miniaturized differential wideband BPF [20] can be achieved.

In this letter, four capacitors are loaded in parallel and series to just one one-eighth wavelength microstrip coupled line. The filter size can be further reduced, and the filter structure becomes much simpler. Wideband filtering response and out-of-band suppression are ensured by three transmission poles (TPs) and four transmission zeros (TZs), which are produced and controlled by capacitances and loading positions of capacitors as well as the even-odd-mode impedance of the coupled line. Odd- and even-mode analysis is utilized for theoretical analysis. One prototype is designed for demonstration.

II. PROPOSED WIDEBAND BANDPASS FILTER

The circuit model of the proposed wideband BPF is exhibited in Fig. 1 (a), which is composed of four capacitors (C_1 , C_2 , and C_3), one one-eighth wavelength coupled line with its one end shorted (Z_e and Z_o , $\theta_1 + \theta_2 = 45^\circ$), and two ports (Port 1 and Port 2). C_1 is loaded in series to the coupled line. C_2 and C_3 are loaded in parallel to the coupled line. C_1 and C_2 are located at the open end of the coupled line. The electrical distance between C_2 and C_3 is θ_1 .

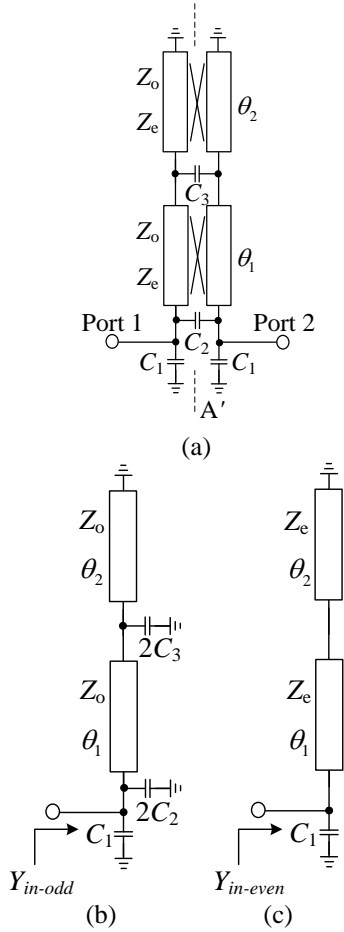


Fig. 1. Circuit model and even- and odd-mode equivalent circuits of the proposed wideband BPF. (a) Circuit model; (b) even-mode equivalent circuit; (c) odd-mode equivalent circuit.

The whole circuit is symmetrical to the A-A' plane, so odd- and even-mode analysis can be utilized. A virtual open/short appear along the symmetrical plane A-A' under the condition of even/odd-mode operation. Thus, the even- and odd-mode equivalent circuits are shown in Figs. 1 (b) and 1 (c), respectively. The input admittance of even-/odd-mode equivalent circuits can be extracted as:

$$Y_{in-even} = C_1 \omega j - \frac{\cot(\theta_1 + \theta_2) j}{Z_e}, \quad (1a)$$

$$Y_{in-odd} = C_1 \omega j + 2C_2 \omega j + \frac{2Z_o C_3 \omega j + j \tan \theta_1 - j \cot \theta_2}{Z_o + (Z_o \cot \theta_2 - 2Z_o^2 C_3 \omega j) \tan \theta_1}, \quad (1b)$$

respectively, where $\omega = 2\pi f$,

$$\theta_1 + \theta_2 = \frac{\pi f}{4 f_0}, \quad (2)$$

where f_0 is the center frequency. The reflection coefficients (S_{11} and S_{22}) and transmission coefficients (S_{21} and S_{12}) of the proposed design can be derived as:

$$S_{11} = S_{22} = \frac{Y_0^2 - Y_{in-odd} Y_{in-even}}{(Y_0 + Y_{in-odd})(Y_0 + Y_{in-even})}, \quad (3a)$$

$$S_{21} = S_{12} = \frac{Y_0(Y_{in-odd} - Y_{in-even})}{(Y_0 + Y_{in-odd})(Y_0 + Y_{in-even})}, \quad (3b)$$

where $Y_0 = 1/50 \Omega^{-1}$ is the port admittance. According to Equations (1)-(3), the curves of $|S_{11}|$ and $|S_{21}|$ can be obtained in MATLAB by setting a certain initial value for C_1 , C_2 , C_3 , θ_1/θ_2 , and Z_e/Z_o . The frequency corresponding to the extreme point of $|S_{11}|$ curve is the frequency of the TPs, and the frequency corresponding to the extreme point $|S_{21}|$ curve is the frequency of the TZs. Then, TPs and TZs can be obtained.

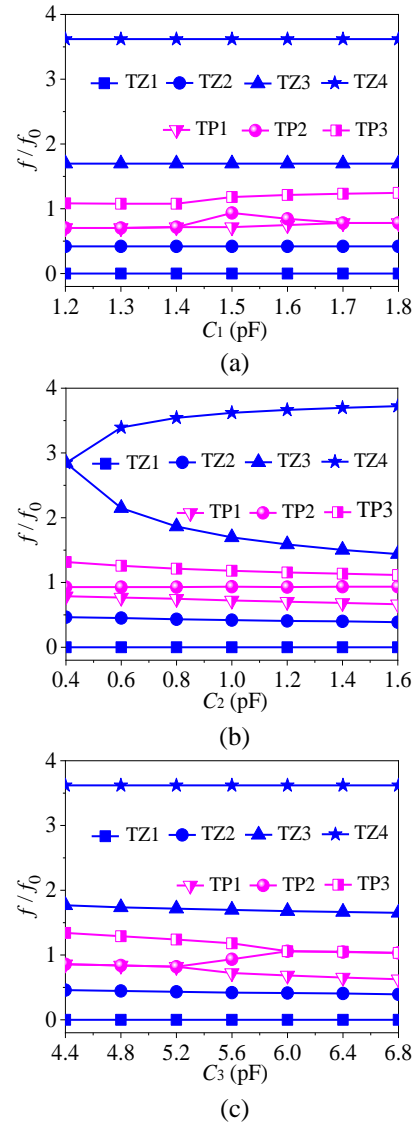


Fig. 2. Effect of capacitance values on theoretical variations of TPs and TZs. (a) C_1 changes; (b) C_2 changes; (c) C_3 changes. ($C_1 = 1.5$ pF, $C_2 = 1.0$ pF, $C_3 = 5.6$ pF, $\theta_1/\theta_2 = 1$ and $Z_e/Z_o = 1.6$).

A. Analysis of TPs and TZs

Figure 2 shows how C_1 , C_2 , C_3 affect theoretic TPs and TZs. Figure 3 exhibits how θ_1/θ_2 and Z_e/Z_o affect theoretic TPs and TZs. It can be found from Figs. 2 and 3 that TP1 moves upwards when C_1 , θ_1/θ_2 , or Z_e/Z_o is increased, or C_2 or C_3 is decreased. TP2 moves downwards with the decrease of C_3 or the increase of Z_e/Z_o , while TP2 moves upwards first then moves downwards with C_1 . TP3 moves upwards with the increase of C_1 or Z_e/Z_o , or the decrease of C_2 , C_3 , or θ_1/θ_2 . TZ3 moves downwards when C_2 or θ_1/θ_2 increases, or Z_e/Z_o decreases. TZ4 moves upwards with C_2 .

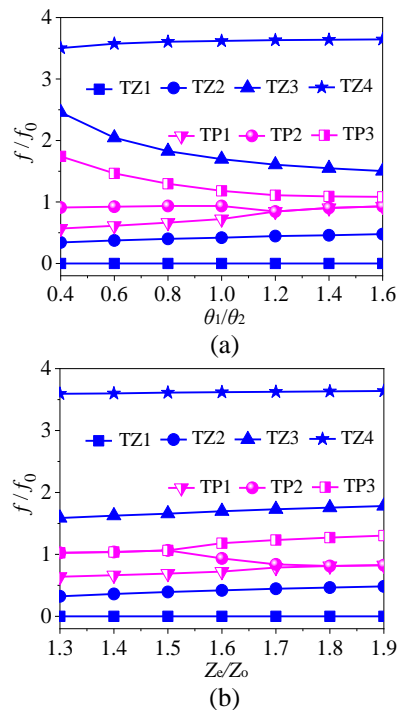


Fig. 3. Effect of loading position of capacitor and impedance of coupled line on theoretical variations of TPs and TZs. (a) θ_1/θ_2 changes; (b) Z_e/Z_o changes. ($C_1 = 1.5$ pF, $C_2 = 1.0$ pF, $C_3 = 5.6$ pF, $\theta_1/\theta_2 = 1$ and $Z_e/Z_o = 1.6$).

In addition, the number of TPs changes from three to two when C_1 , C_3 , θ_1/θ_2 , or Z_e/Z_o is outside a special range, while the number of TZs changes from four to three when C_2 is outside a special range. It can be found from Figs. 2 and 3 that three TPs and four TZs can be obtained when selecting appropriate parameters, which ensures wideband filtering response and enough out-of-band suppression for the proposed filter.

It is found that TZs will be affected by C_2 and C_3 but not by C_1 . This is because C_2 and C_3 could provide additional transmission paths beside the transmission path of the coupled line, and the signals on the paths will be cancelled each other when the phase difference is $(2n+1)180$ degrees ($n = 0, 1, 2, \dots$). However, C_1 doesn't provide an additional path so that it will not affect TZs.

B. Analysis of bandwidth and center frequency

The bandwidth and center frequency can also be obtained from $|S_{11}|$ and $|S_{21}|$ curves in MATLAB. By this way, the effect of C_1 , C_2 , C_3 , θ_1/θ_2 , and Z_e/Z_o on bandwidth and center frequency are exhibited in Figs. 4 and 5, respectively. It can be seen from Figs. 4 and 5 that the bandwidth and center frequency are mainly controlled by C_2 , C_3 , θ_1/θ_2 , and Z_e/Z_o . The 3-dB fractional bandwidth (FBW) increases when C_2 , θ_1/θ_2 , or Z_e/Z_o is decreased, or C_3 is increased. The center frequency moves upwards when C_2 , C_3 , or θ_1/θ_2 is decreased, or Z_e/Z_o is increased. In addition, the variations of bandwidth and center frequency in Figs. 4 and 5 are consistent with those of the space between the TPs and the position of TPs in Figs. 2 and 3, respectively.

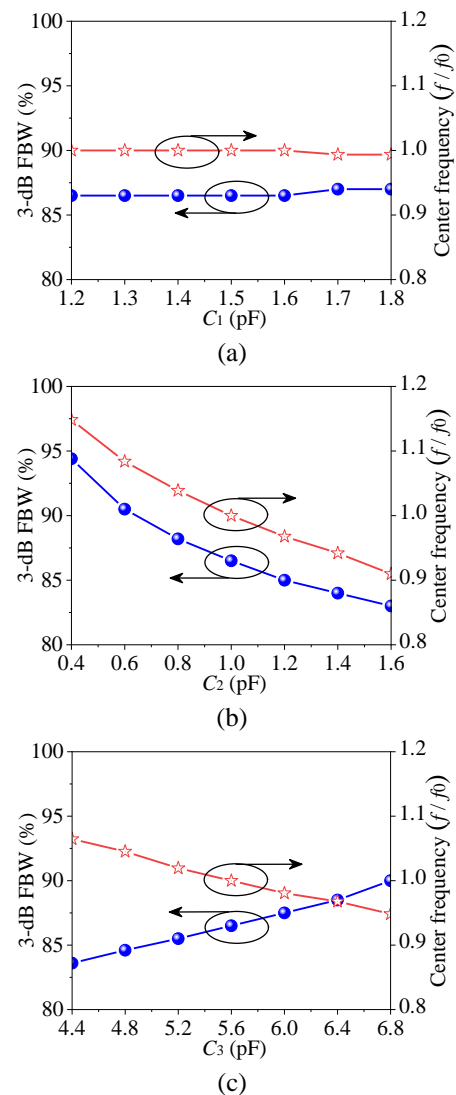


Fig. 4. Effect of capacitance values on theoretical variations of bandwidth and center frequency. (a) C_1 changes; (b) C_2 changes; (c) C_3 changes. ($C_1 = 1.5$ pF, $C_2 = 1.0$ pF, $C_3 = 5.6$ pF, $\theta_1/\theta_2 = 1$ and $Z_e/Z_o = 1.6$).

It is found that the bandwidth and center frequency are affected by C_2 and C_3 , but not by C_1 . This is because C_2 and C_3 change the coupling of the coupled line. However, C_1 will affect impedance matching because it will affect the intensity of the electric field at the feed point.

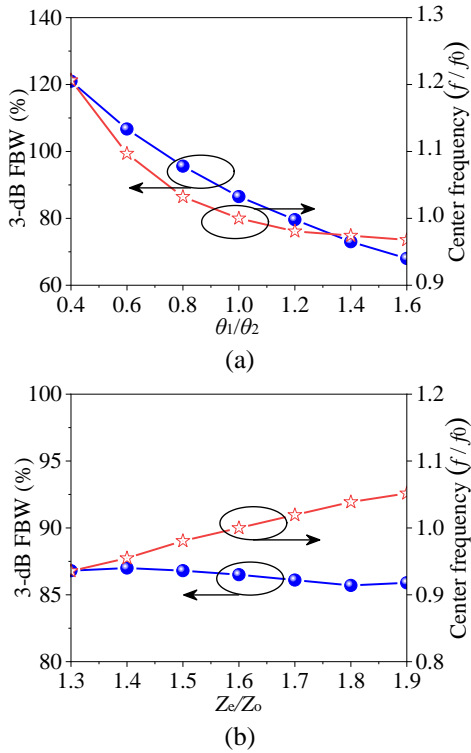


Fig. 5. Effect of the loading position of capacitor and the impedance of coupled line on theoretical variations of bandwidth and center frequency. (a) θ_1/θ_2 changes; (b) Z_c/Z_0 changes. ($C_1 = 1.5$ pF, $C_2 = 1.0$ pF, $C_3 = 5.6$ pF, $\theta_1/\theta_2 = 1$ and $Z_c/Z_0 = 1.6$).

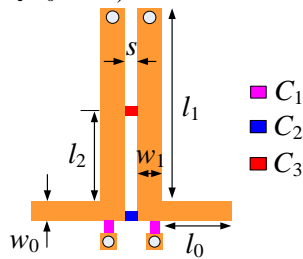


Fig. 6. Layout of the proposed wideband BPF.

C. Parametric study

The layout of the proposed wideband bandpass filter is exhibited in Fig. 6, where the substrate is RO4003C ($\epsilon_r = 3.38$, $h = 0.813$ mm, $\tan \delta = 0.0027$). In order to further study the performance variation, the parametric study on C_1 , C_2 , C_3 are displayed in Figs. 7 (a), 7 (b) and

7 (c), respectively. Meanwhile, the parametric study on l_2 , w_1 , and s_1 are depicted in Figs. 8 (a), 8 (b) and 8 (c), respectively. It can be found from Figs. 7 and 8 that the bandwidth and center frequency are mainly affected by C_2 , C_3 , l_2 , and s , and the out-of-band suppression is mainly changed by C_1 , C_2 , and s . The bandwidth increases when C_2 , l_2 , or s is decreased, or C_3 is increased. The center frequency moves upwards with the decrease of C_2 , C_3 , l_2 , or s . The out-of-band suppression becomes better when C_1 is increased, or C_2 or s is decreased.

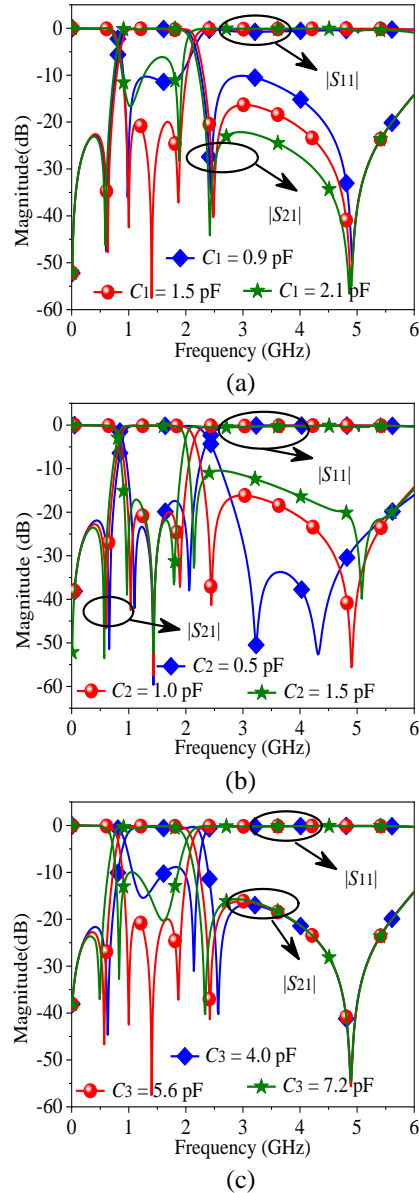


Fig. 7. Simulated responses of the proposed wideband BPF with (a) C_1 , (b) C_2 , and (c) C_3 . ($C_1 = 1.5$ pF, $C_2 = 1.0$ pF, $C_3 = 5.6$ pF, $l_2 = 6.7$ mm, $w_1 = 0.9$ mm, and $s = 0.58$ mm).

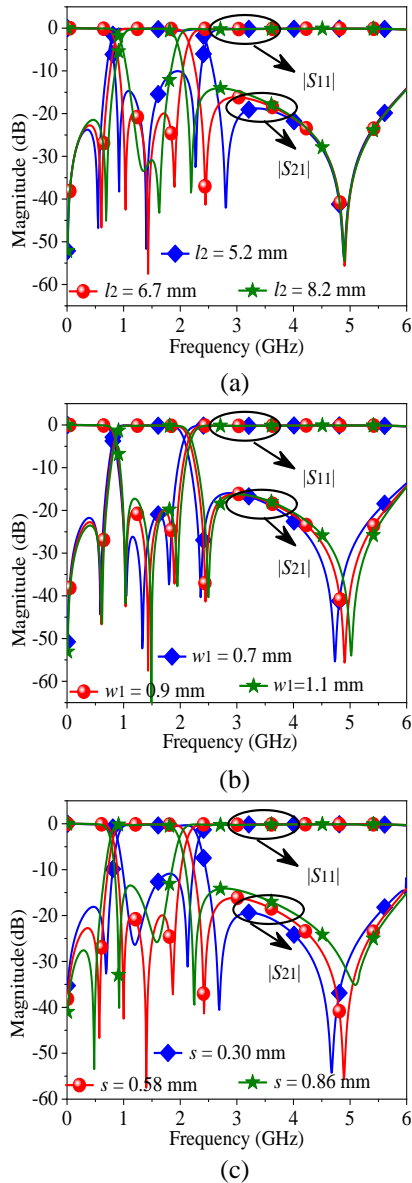


Fig. 8. Simulated responses of the proposed wideband BPF with (a) l_2 , (b) w_1 , and (c) s . ($C_1 = 1.5$ pF, $C_2 = 1.0$ pF, $C_3 = 5.6$ pF, $l_2 = 6.7$ mm, $w_1 = 0.9$ mm, and $s = 0.58$ mm).

D. Design procedure

According to the above analysis, the design procedure of the proposed wideband BPF is summarized as follows:

Step 1: Get initial C_1 , C_2 , C_3 , θ_1/θ_2 , and Z_e/Z_o according to the variation of TPs and TZs in Figs. 2 and 3, and the variation of bandwidth and center frequency in Figs. 4 and 5.

Step 2: Convert the theoretical θ_1/θ_2 and Z_e/Z_o to the dimensions of the coupled line.

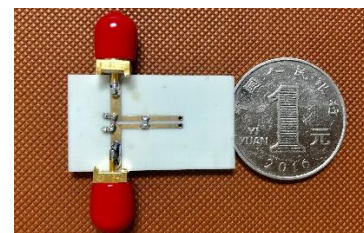
Step 3: Obtain final C_1 , C_2 , C_3 , l_2 , w_1 , and s in Ansoft High Frequency Structure Simulator (HFSS) by slightly tuning them according to their variation in Figs. 7 and 8.

III. PROTOTYPES AND RESULTS

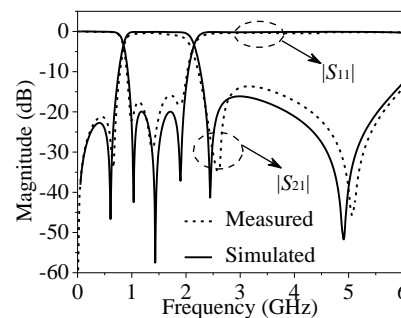
Based on the above analysis, a prototype is implemented with the target of 3-dB FBW of 87% and the center frequency of 1.5 GHz. The final parameters can be obtained from the design procedure and are shown as follows: $C_1 = 1.5$ pF, $C_2 = 1.0$ pF, $C_3 = 5.6$ pF, $w_0 = 1.85$ mm, $w_1 = 0.9$ mm, $l_0 = 8.0$ mm, $l_1 = 13.7$ mm, $l_2 = 4.85$ mm, and $s = 0.58$ mm. The photograph of the proposed wideband BPF is exhibited in Fig. 9 (a).

Figure 9 (b) demonstrates the simulated and measured results of the proposed wideband BPF. The fabricated filter works at the center frequency of 1.47 GHz, which exhibits the 3-dB FBW of 86.5% with a minimum insertion loss of 0.37 dB. Four TZs are loaded at 0 GHz, 0.65 GHz, 2.52 GHz, and 5.09 GHz, while three TPs are loaded at 0.98 GHz, 1.37 GHz, and 1.89 GHz. The overall size of the proposed design is 15.3 mm \times 2.38 mm ($0.139\lambda_g \times 0.022\lambda_g = 0.003\lambda_g^2$).

Table 1 lists the performance of this work and the state-of-the-art designs. Compared with the reported microstrip wideband BPF, the proposed design has the advantages of compact size and simple structure.



(a)



(b)

Fig. 9. Photograph and simulation and measured results of the proposed wideband BPF. (a) Photograph and (b) simulation and measured results.

Table 1: Performance comparison between previous state-of-the-art wideband bandpass filters and the proposed design

Ref.	f_0 (GHz)	3-dB FBW (%)	Number of TPs/TZs	Insertion Loss (dB)	Size (λ_g^2)
[1]	2.88	79.33	5/5	0.94	0.271
[7]	3.0	70	5/6	0.49	0.217
[9]	6.0	67.8	5/6	1.3	0.084
[10]	6.85	79.1	6/7	0.81	0.238
[12]	1.91	52.4	2/3	0.3	0.021
[13]	6.9	115.9	7/6	N.A.	0.256
[16]	3.0	80	2/3	0.5	0.013
[17]	0.885	87	3/8	0.66	0.009
[18]	1.0	59.19	4/2	0.64	0.006
This work	1.47	86.5	3/4	0.37	0.003

V. CONCLUSION

A wideband BPF based on capacitor-loaded one-eighth wavelength coupled line is proposed. A compact size of only $0.003\lambda_g^2$ and simple structure can be achieved. Theoretic analysis and parametric study are introduced to guide the practical design. It is believed that the proposed wideband BPF is able to promote the development of the miniaturized wideband wireless communication systems.

ACKNOWLEDGMENT

This work was partially supported by the Nantong Science and Technology Plan Project under Grant JC2018130, Natural Science Foundation of Jiangsu Province, China, under Grant BK20200962, and Natural Science Research Project of Jiangsu Higher Education Institutions under Grant 20KJB510004.

REFERENCES

- [1] Y. Wu, L. Cui, W. Zhang, L. Jiao, Z. Zhuang, and Y. Liu, "High performance single-ended wideband and balanced bandpass filters loaded with stepped-impedance stubs," *IEEE Access*, vol. 5, pp. 5972-5981, May 2017.
- [2] F. Wei, Z. D. Wang, F. Yang, and X. W. Shi, "Compact UWB BPF with triple-notched bands based on stub loaded resonator," *Electronics Letters*, vol. 49, no. 2, pp. 124-126, Jan. 2013.
- [3] R. Li and L. Zhu, "Compact UWB bandpass filter using stub-loaded multiple-mode resonator," *IEEE Microwave and Wireless Components Letters*, vol. 17, no. 1, pp. 40-42, Jan. 2007.
- [4] Q. X. Chu, X. H. Wu, and X. K. Tian, "Novel UWB bandpass filters using stub-loaded multiple-mode resonator," *IEEE Microwave and Wireless Components Letters*, vol. 21, no. 8, pp. 403-405, Aug. 2011.
- [5] X. Y. Zhang, Y.-W. Zhang, and Q. Xue, "Compact band-notched UWB filter using parallel resonators with a dielectric overlay," *IEEE Microwave and Wireless Components Letters*, vol. 23, no. 5, pp. 252-254, May 2013.
- [6] L. Gao, X. Y. Zhang, and Q. Xue, "Compact tri-band bandpass filter using novel eight-mode resonator for 5G WiFi application," *IEEE Microwave and Wireless Components Letters*, vol. 25, no. 10, pp. 660-662, Oct. 2015.
- [7] B. Zhang, Y. Wu, and Y. Liu, "Wideband single-ended and differential bandpass filters based on terminated coupled line structures," *IEEE Transactions on Microwave Theory and Techniques*, vol. 65, no. 3, pp. 761-774, Mar. 2017.
- [8] X. Xia, X. Cheng, F. Chen, and X. Deng, "Compact UWB bandpass filter with sharp roll-off using APCL structure," *Electronics Letters*, vol. 54, no. 4, pp. 223-225, May 2018.
- [9] X. Y. Zhang, X. Dai, H.-L. Kao, B.-H. Wei, Z. Y. Cai, and Q. Xue, "Compact LTCC bandpass filter with wide stopband using discriminating coupling," *IEEE Transactions on Components Packaging and Manufacturing Technology*, vol. 4, no. 4, pp. 656-663, Apr. 2014.
- [10] S. W. Ren, H. L. Peng, J. F. Mao, and A. M. Gao, "Compact quasi-elliptic wideband bandpass filter using cross-coupled multiple-mode resonator," *IEEE Microwave and Wireless Components Letters*, vol. 22, no. 8, pp. 397-399, Aug. 2012.
- [11] J. Zhou, Y. Chiang, and W. Che, "Wideband bandpass filter based on ring resonator with high selectivity and multiple transmission zeros," *Electronics Letters*, vol. 50, no. 5, pp. 384-386, Feb. 2014.
- [12] W. Feng, X. Gao, W. Che, and Q. Xue, "Bandpass filter loaded with open stubs using dual-mode ring resonator," *IEEE Microwave and Wireless Components Letters*, vol. 25, no. 5, pp. 295-297, May 2015.
- [13] J. Xu, Y.X. Ji, C. Miao, and W. Wu, "Compact single-/dual-wideband BPF using stubs loaded SIR (SsLSIR)," *IEEE Microwave and Wireless Components Letters*, vol. 23, pp. 338-340, July 2013.
- [14] Q. X. Chu and X. K. Tian, "Design of UWB bandpass filter using stepped-impedance stub-loaded resonator," *IEEE Microwave and Wireless Components Letters*, vol. 20, no. 9, pp. 501-503, Sep. 2010.
- [15] F. Li, W. Che, L. Gu, and Q. Xue, "Broadband bandpass filter with wide upper stopband using stub-loaded multiple-mode resonators," *Electronics Letters*, vol. 49, no. 13, pp. 818-820, June 2013.
- [16] F. Wei, W. T. Li, X. W. Shi, and Q. L. Huang, "Compact UWB bandpass filter with triple-notched bands using triple-mode stepped impedance

resonator,” *IEEE Microwave and Wireless Components Letters*, vol. 22, no. 10, pp. 512-514, Oct. 2012.

- [17] L. Li and Z. Li, “Side-coupled shorted microstrip line for compact quasi-elliptic wideband bandpass filter design,” *IEEE Microwave and Wireless Components Letters*, vol. 20, no. 6, pp. 322-324, June 2010.
- [18] J. Xu, Y.-X. Ji, W. Wu, and C. Miao, “Design of miniaturized microstrip LPF and wideband BPF with ultra-wide stopband,” *IEEE Microwave and Wireless Components Letters*, vol. 23, no. 8, pp. 397-399, Aug. 2013.
- [19] C.-H. Liang and C.-Y. Chang, “Compact wideband bandpass filters using stepped-impedance resonators and interdigital coupling structures,” *IEEE Microwave and Wireless Components Letters*, vol. 19, no. 9, pp. 551-553, Sep. 2009.
- [20] J. Dong, J. Shi, and K. Xu, “Compact wideband differential bandpass filter using coupled microstrip lines and capacitors,” *IEEE Microwave and Wireless Components Letters*, vol. 29, no. 7, pp. 444-446, June 2019.



Jin Shi (M'14) received the B.S. degree from HuaiYin Teachers College, Huai'an City, Jiangsu Province, China, in 2001, the M.S. degree from the University of Electronic Science and Technology of China (UESTC), Chengdu, China, in 2004, and the Ph.D. degree from City University of Hong Kong, in 2011, respectively.

From 2004 to 2006, he was a Research Engineer in Comba working on RF repeater system. During 2007–2008, he was a Research Assistant of the City University of Hong Kong. He joined the Institute for Infocomm Research, Singapore, as a Research Fellow and later served as a Scientist from 2011 to 2013. In 2013, he joined the School of Electronics and Information, Nantong University, China, as a Professor. His current research interests are RF/microwave components and subsystems, differential circuit and antennas, LTCC circuits and antennas.

Shi is the recipient of the IES Prestigious Engineering Achievement Award 2013. He has served as the TPC member and session chair for a number of conferences and a regular reviewer for the *IEEE Transactions on Microwave Theory and Techniques*, the *MWCL*, the *AWPL*, and *Electronics Letters*, and other publications.



Jiancheng Dong was born in Lianyungang, Jiangsu Province, China, in 1994. He received the B.Sc. degree from Nantong University, Nantong, Jiangsu Province, China, in 2018, where he is currently pursuing the M.S. degree in Electromagnetic Field and Microwave

Technology.

His current research interests include RF/microwave components, differential microwave circuits, and tunable circuits.



Kai Xu (M'19) was born in Hai'an, Jiangsu Province, China, in 1991. He received the B.Sc. degree from Taizhou Institute of Sci. and Tech., Jiangsu Province, China, in 2013, the M.S. degree from the Nantong University, Nantong, Jiangsu Province, China, in 2016, and the Ph.D. degree from the Nantong University, Nantong, Jiangsu Province, China, in 2019, respectively.

From 2015 to 2016, he was a Research Assistant of the Institute for Infocomm Research, Singapore. His current research interests include microwave components, balanced microwave circuits, antennas, and integrated designs.

He has served as a Reviewer for the *IEEE access*, *IEEE MWCL*, and *IET Electronic Letters*, and other publications.



Lingyan Zhang was born in Jiangsu, China in 1991. She received her B.Sc. degree in Applied Physics from Jiangsu University in 2014 and Ph.D. degree in Materials Science and Engineering from Nanjing University of Science and Technology in 2019.

Her research focuses on the microwave transmission system, interaction of ultrafast intense laser with semiconductors and the surface modification of materials.

A Wideband and Wide Scanning Tightly Coupled Dipole Array with Meta-Surface Wide-Angle Impedance Matching

Yuan Ye¹, Zhao Yu Huang¹, Yun Jiang^{1*}, Li-an Bian², Chang Zhu¹, Jing Jian Huang¹, and Nai Chang Yuan¹

¹College of Electronic Science and Engineering
National University of Defense Technology, Changsha, 410073, China
*867581306@qq.com

²Hunan Provincial Key Laboratory of Flexible Electronic Materials Genome Engineering
Changsha University of Science & Technology, Changsha, 410114, China

Abstract — A low profile ultra-wideband tightly coupled dipole array is studied. The antenna elements are fed by Marchand baluns of small size and low cost. A meta-surface based wide-angle impedance matching (MS-WAIM) layer is introduced to replace the traditional dielectric WAIM, improving the beam scan performance and reducing the antenna profile. The simulation shows that the proposed antenna array can operate over 2.4-12.4 GHz, approximately 5:1 bandwidth with maximum scanning angle of 50° for both E plane and 45° for H plane. The antenna profile above the ground is only 0.578 λ_H at the highest operating frequency. This antenna array can find its application in the forthcoming massive MIMO beamforming systems for 5G.

Index Terms — Meta-surface, phased array, tightly coupled dipole array, ultra-wide band, wide angle scanning.

I. INTRODUCTION

Wide-band antenna array has received extensive research over decades due to their important roles in military use, including remote, radar and electronic warfare [1],[2]. With scan ability, they make it possible to real time track object quickly; By producing multi-beams, multi-object task could be carried out simultaneously. For another side, to attain high data rates and large capacity, the next generation system (5G) plans to exploit frequency band below 6GHz (so called sub 6GHz band), which can provide spectrum covering 2.5 to 2.7 GHz, 3.3 to 3.8 GHz and additional frequencies between 4.4 to 5GHz [3]. The 5G also intent to use phase array technology to overcome interference problem, improving the signal transmission direction. However, the application of conventional phase array, such as slots array and microstrips array is confined by some shortcomings, including narrow bandwidth, limited

scanning angle etc. [4].

Vivaldi antenna has been regarded as good candidate for ultra-wideband (UWB) antenna. Numerous studies were made during the past three decades, leading to Vivaldi array that achieve bandwidths over 10:1 at wide scans [5]. With excellent performance, Vivaldi antennas array has already been put into practice. However, this taper slot array suffers from some drawbacks such as high profile and high cross-polarization, which limit its further application requiring compact structure and low cross-polarization [6].

Mutual coupling is always a major concern in the design of traditional array antenna since it can degrade the efficiency as well as radiation patterns of the antennas, therefore many efforts have been made to reduce the undesirable coupling between array elements [7],[8]. On the other hand, tightly coupled dipole array (TCDA) has drawn more and more attention since Munk *et al* published the first prototype in 2003 [9]. In contrast to the traditional antenna array, the elements of TCDA are placed so closely, that the resulting strong capacity can compensate the inductance introduced by ground at the low frequency band [10]. TCDA is proved to be feature with low profile and low cross-polarization level comparing with Vivaldi antenna array [11]-[13], hence they are believed to have promising application of the future UWB antenna. One major challenge for the realization of TCDA is the design of an equally wideband feed network, which not only provide impedance transformation but also transition from unbalance to balance feeding [14]-[18][15]. Another challenge faces the designers is that the bulky dielectric WAIM, which is usually $\lambda_H/4$ [10][13], rising both the profile and the cost of the antenna array.

In this paper, a low profile ultra-wideband tightly coupled dipole array is studied. The antenna elements are fed by Marchand baluns of small size and low cost. A

meta-surface based wide-angle impedance matching (MS-WAIM) layer is introduced to replace the traditional dielectric WAIM, improving the beam scan performance and reducing the antenna profile. The simulation shows that the proposed antenna array can operate over 2.4-12.4 GHz, approximately 5:1 bandwidth with maximum scanning angle of 50° for both E plane and 45° for H plane. The antenna profile above the ground is only $0.578\lambda_H$ at the highest operating frequency. This antenna array can find its application in the forthcoming massive MIMO beamforming systems for 5G.

II. EQUIVALENT CIRCUIT ANALYSIS

The concept of TCDA could be traced back to current sheet array (CSA). As shown in Fig. 1 (a), horizontal dipoles are placed periodically in array, where the distance between the adjacent elements is very small [14]. With the resulting strong capacitance, the array supports currents at wavelengths which significantly exceed the scale of individual element. To achieve uni-directional radiation, ground is introduced beneath the array. In the view of circuit, inter-element capacitance in associate with dipole inductance can counteract the reactance brought by the ground, thus broaden the bandwidth.

Figure 1 (b) presents the equivalent circuit for TCDA. In this schematic diagram, we denote dipole inductance by L_{dipole} , the inter-element capacitance by $C_{coupling}$. The substrate, superstrate, and free space layers are indicated by transmission line sections. Generally, the input impedance of TCDA is $100\text{-}200\Omega$, which brings a great challenge to the design of impedance matching network (conventional source is 50Ω).

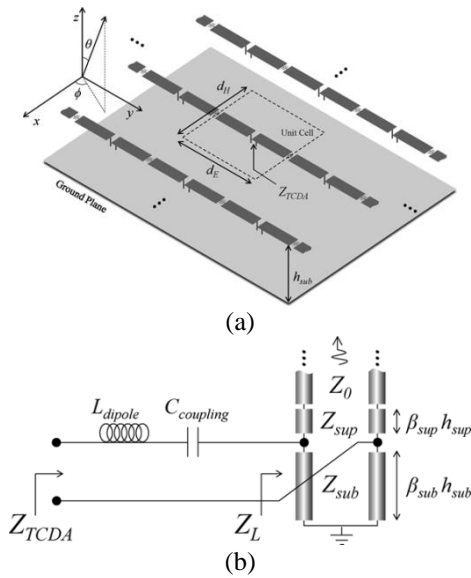


Fig. 1. (a) TCDA consisting of capacitively coupled dipole elements, placed above a conducting ground plane, and (b) equivalent circuit for the TCDA.

III. STRUCTURE DESIGN

A unit cell of the TCDA fed by a 150Ω lumped gap source is placed at distance of h above the ground, as shown in Fig. 2 (a), where the dipole is printed on the bottom of Rogers RT5880 dielectric slab ($\epsilon_r=2.2$) thickness of 0.5mm. There is small gap between the ends of the dipole arms (presented by dash line in the caption), bringing in strong coupling of adjacent elements, while the patch on the top of the dielectric slab is used to reinforce the capacitance. An electronically thick ($t=\lambda_H/4$) layer with low permittivity is placed above the antenna for wide band tuning, though at the expense of increasing the weight and cost of the antenna array.

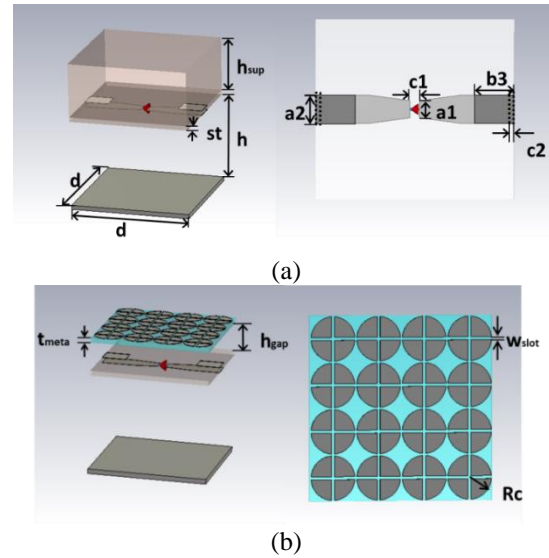


Fig. 2. (a) TCDA with dielectric MAIM, and (b) TCDA with Meta-surface MAIM.

An adaptation is introduced to improve the situation, the bulky superstrate is substituted by a thin dielectric slab (Rogers RO3033, $\epsilon_r=3$) with meta surface, as show in Fig. 2 (b). The meta-surface is comprised of small circular patches with cross slots in the center. It is worth noting that the lattice spacing of meta-surface is considerably smaller than that of the dipole array [16]. Thereby the meta-surface can be regarded as homogenized, in other words, a single relative permittivity in the case of a dielectric WAIM slab [19]. Similar to FSS, meta-surface could be treated on a Floquet mode by mode basis during analysis with multimode equivalent network, and when the array is fed, a sequence of Floquet modes will be excited. Accordingly, the Z_{sup} in the equivalent circuit of Fig. 1 (b) should be replaced by meta-surface impedance Z_W , comprising a series Floquet impedances,

$$Z_W = \sum_m \sum_n Z_{W_{mn}}$$

All impedances are function of polarization, scan

angle (θ, φ) . To prevent surface wave, there is an air layer between the superstrate and the dipole slab. In practice, foam plate is usually used to realize such suspension structure.

The proposed meta-surface WAIM is simulated in associated with TCDA, as shown in Fig. 2 (b). To focus on meta-surface WAIM and give a concise analysis, feeding system is not included in the model in the primary design. For comparison of the performance, the same TCDA is also simulated with conventional dielectric superstrate. Full-wave simulations are carried out with commercial software CST, and to ensure accuracy of the simulation, we adopt frequency domain solver as tetrahedral mesh can provide better fitting for realistic model. The boundaries are set as periodic for x and y direction, open space for z direction, the dimension of the unit cell, the ground plane height and the dipole scale are set the same and kept constant for both arrays. It's noted that the TCDA with the proposed meta_surface WAIM could provide better frequency/ angular response.

Figure 3 presents the simulated input impedance for both TCDAs, including broadside, 45° scan in E and H plane. It manifests that the impedance curves of array with meta-surface are more confined to the center of the smith chart, comparing with that of array with dielectric-loaded array, indicating better matching and wider bandwidth during scanning. Specially impedance matching is more difficult for beam scanning in the H plane than in other planes, because increasing Floquet modes are excited, leading to detune of the array [20]. It's observed that the introduction of meta_surface WAIM alleviates this detuning (see blue line in the chart). Nevertheless, it should be noted that vertically oriented feed-lines, which will be introduced in the following section, also have different response to Floquet modes, therefore they can provide additional degrees of freedom to the design of the TCDA, and improve the performance.

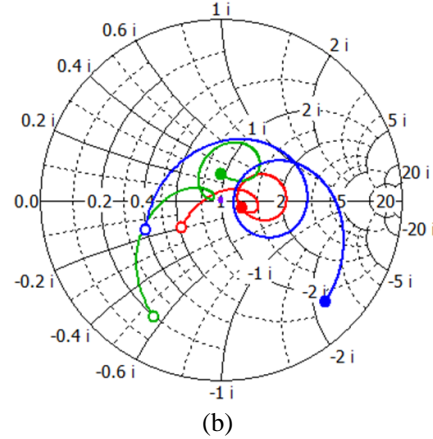
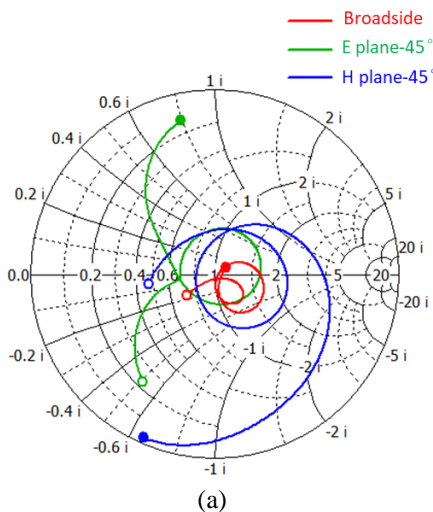


Fig. 3. S_{11} of the TCDAs with: (a) conventional dielectric superstrate, and (b) meta-surface WAIM, for broadside, E plane 45° and H plane 45° scan.

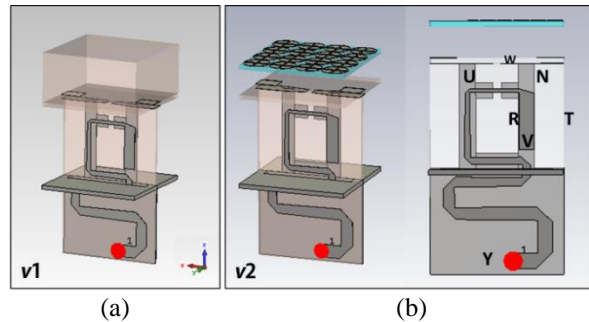


Fig. 4. Illustration of the TCDA with: (a) conventional dielectric MAIW and Marchand balun, and (b) meta-surface MAIW and Marchand balun

Feed and matching network for TCDA should carry out two jobs: impedance transformer and unbalanced to balanced feeding. As mentioned before, the input impedance of the TCDA is 150Ω , which is much larger than conventional 50Ω excitation. For another side, dipoles must be fed differentially, whereas practical feed networks, such as 50Ω coaxial line, fall into unbalanced transmission line category. Marchand Balun with taper feeding line is suggested to serve as feeding system for the TCDA, as shown in Fig. 4. The Marchand balun is composed of coupled quarter-wave transmission lines printed on one side of the dielectric slab (Rogers RT5880, $\epsilon_r=2.2$, thickness=0.5mm), while the taper feeding line together with a short circuit line printed on the other side of the slab [21]. To realize more compact structure, the straight feeding line is adapted to meandered line and by doing so the profile of the TCDA will be reduced.

Similarly, two models are studied: $v1$ is the combination of conventional dielectric loaded TCDA and the feeding balun mentioned above, as shown in Fig. 4 (a). $v2$ is similar with $v1$, only that the dielectric

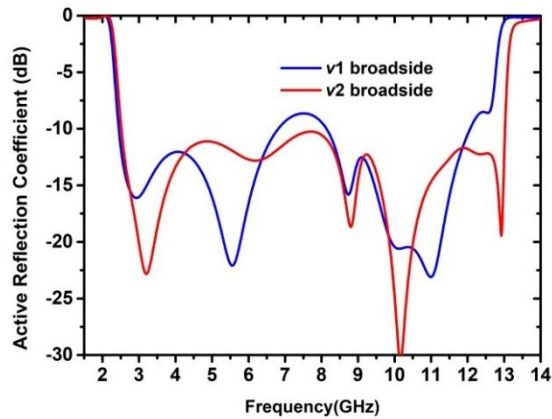
superstrate is replaced by meta_surface MAIW, as shown in Figs. 4 (b) and (c).

All the scheme parameters mentioned above are given in Table 1.

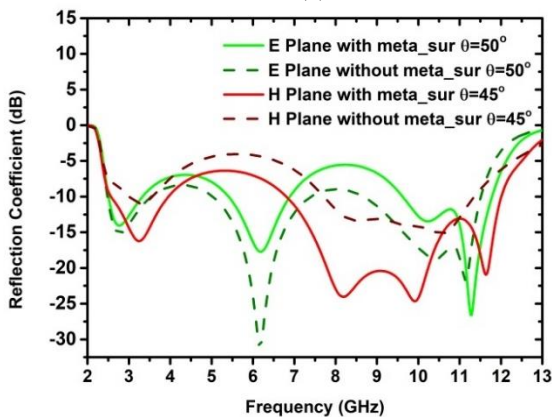
Table 1: Parameters of the antenna (mm)

Parameter	Value	Parameter	Value	Parameter	Value
h_{sup}	6.3	c_1	0.8	N	1.8
st	0.5	t_{meta}	0.5	R	4
h	10	h_{gap}	3	V	1.4
d	12.5	w_{slot}	0.2	T	5.6
a1	0.6	Rc	1.5	Y	1.55
a2	1	U	1.5	c_2	0.01
b	2.5	W	0.4		

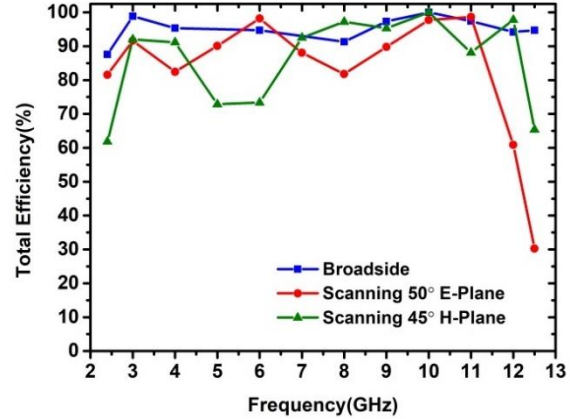
The simulated active reflection coefficients of the two models are presented in Fig. 5 (a), indicating that at broadside model v_2 achieves approximately 5.42:1 impedance bandwidth (2.4–13 GHz) for active $S_{11} < -10$, which is better than that of v_1 (2.3–12GHz), meaning meta-surface WAIM with lighter and thinner substrate, is totally competent to counteract the reactance of TCDA, broadening band width effectively. What's more, comparing with v_1 , v_2 enjoys more compact structure ($0.578\lambda_H$ above the ground), reducing the profile of the TCDA.



(a)



(b)



(c)

Fig. 5. Simulated active S_{11} of v_1 and v_2 : (a) for broadside, (b) different scan angles for E/H plane, and (c) total efficiency for v_2 while scanning into the E, H plane.

Modern phase array theory suggests that, the array suffers from impedance mismatch as the beam scans off the broadside direction. Specially, the element resistance alters with $\cos\theta$ and $1/\cos\theta$ in the E plane (TM polarization) and H plane (TE polarization), leading to the degradation of transmitted power [22]. As Fig. 4 (b) shows, when the beam goes in the E plane and scans up to 50° , there is very limit difference between the two models, though the impedance width for v_2 is a little wider than that of v_1 , being 2.4–12.4GHz with active $S_{11} < -6$. However, when it comes to scanning in the H plane, meta-surface MAIW manifests itself in improving impedance match. It can be observed that as the scan proceeds in H plane, and reaches $\theta=45^\circ$, active S_{11} for v_1 surges dramatically, exceeding -6 dB over the majority of the operating frequency band. In contrast, active S_{11} for v_2 is significantly lower and less than -6 dB within the whole operating frequency band, this is because the meta-surface WAIM provides capacitive reactance, which compensates inductive reactance introduced by dipole array backed by a ground plane, hence broaden the TCDA impedance width efficiently. The efficiency of model v_2 for both broadside and scanning cases are presented in Fig. 5 (c) The efficiency was showed to be no less than 60% while taking into account mismatch losses.

An 8×8 array of proposed unit cell v_2 is also simulated. Figure 6 presents theoretical aperture limit ($4\pi D/\lambda^2$) calculation as well as the full-wave simulation with CST. It can be observed that the theoretical aperture limits ($4\pi D/\lambda^2$) calculated of the array of theoretical gain limit is almost in consistent with the gain of the array from CST prediction. 3D radiation pattern of the array for 3GHz, 6GHz and 8GHz are showed in Fig. 7. It can be seen, as the length of the dipoles at high frequencies is approaching to half wavelength, the side lobes level at these frequencies is high.

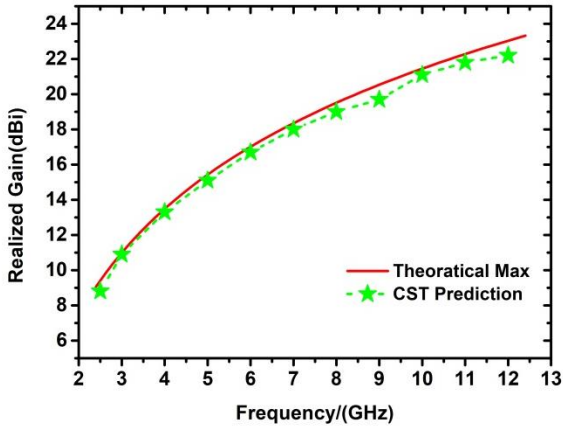


Fig. 6. Theoretical aperture limits calculation and CST prediction of the array for 8×8 of v2.

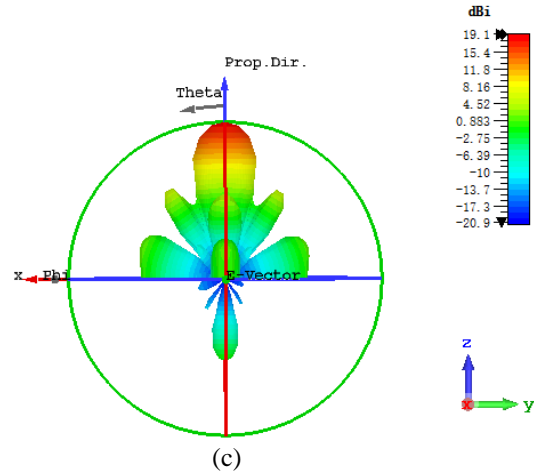
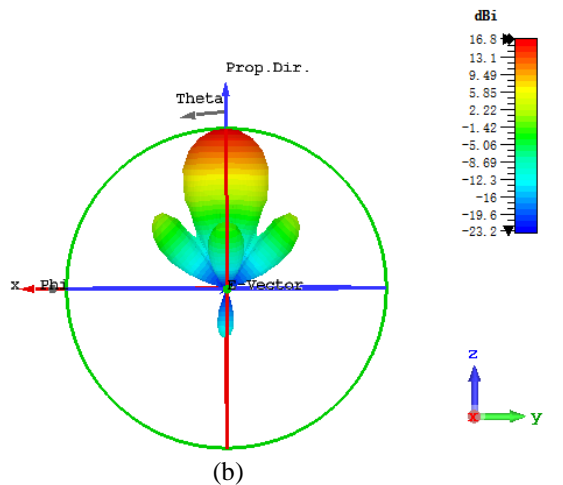
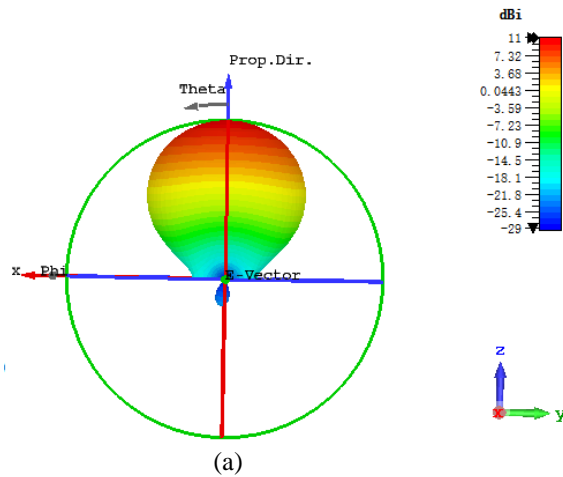


Fig. 7. Radiation pattern of the 8×8 array of proposed unit cell v2 working at: (a) 3 GHz; (b) 6 GHz; (c) 8GHz.



IV. CONCLUSION

A low profile ultra-wideband tightly coupled dipole array is studied. The antenna elements are fed by Marchand baluns of small size and low cost. A meta-surface based wide-angle impedance matching (MS-WAIM) layer is introduced to replace the traditional dielectric WAIM, improving the beam scan performance and reducing the antenna profile. The simulation shows that the proposed antenna array can operate over 2.4-12.4 GHz, approximately 5:1 bandwidth with maximum scanning angle of 50° for both E plane and 45° for H plane. The antenna profile above the ground is only 0.578λ_H at the highest operating frequency. This antenna array can find its application in the forthcoming massive MIMO beamforming systems for 5G.

ACKNOWLEDGMENT

This work was supported by the Equipment Pre-Research Area Foundation of China (Grant No. 61402090118).

REFERENCES

- [1] G. C. Tavakoli, ID Olin, “The advanced multifunction RF concept,” *IEEE Trans. Microw. Theory Techn.*, vol. 53, no. 3, pp. 1009-1020, Mar. 2005.
- [2] M. N. Shakib, M. Moghavvemi, and W. N. L. Mahadi, “Design of a compact planar antenna for ultra-wideband operation,” *Applied Computational Electromagnetics Society Journal*, vol. 30, no. 2, pp. 222-229, July 2015.

- [3] Q. C. Li, H. Niu, A. T. Papathanassiou, and G. Wu, "5g network capacity: Key elements and technologies," *IEEE Vehicular Technology Magazine*, vol. 9, no. 1, pp. 71-78, Jan. 2014.
- [4] J. J. Lee, S. Livingston, R. Koenig, D. Nagata, and L. L. Lai, "Compact light weight UHF arrays using long slot apertures," *IEEE Trans. Antennas Propag.*, vol. 54, no. 7, pp. 2009-2015, July 2006.
- [5] W. Elsallal, J. B. West, J. Wolf, R. Freeman, and P. E. Buxa, "Characteristics of decade bandwidth, balanced antipodal Vivaldi antenna (BAVA) phased arrays with time-delay beamformer systems," in *Proc. IEEE Int. Symp. Phased Array Syst. Technol.*, pp. 111-116, Oct. 2013.
- [6] M. Elsallal, J. Hood, and R. Kindt, "Development of substrate-free frequency-scaled ultra-wide spectrum element (FUSE) phased array," in *Proc. IEEE Int. Symp. PAST*, pp. 1-5, Oct. 2016.
- [7] K.-D. Xu, H. Luyen, and N. Behdad, "A decoupling and matching network design for single- and dual-band two-element antenna arrays," *IEEE Trans. Microw. Theory Techn.*, vol. 68, no. 9, pp. 3986-3999, Sep. 2020.
- [8] T. Jiang, T. Q. Jiao, and Y. S. Li, "A low mutual coupling MIMO antenna using periodic multilayered electromagnetic band gap structures," *Applied Computational Electromagnetics Society Journal*, vol. 33, no. 3, pp. 305-311, Mar. 2018.
- [9] B. Munk, R. Taylor, T. Durharn, W. Crosswell, B. Pignon, R. Boozer, S. Brown, M. Jones, J. Pryor, S. Ortiz, J. Rawnick, K. Krebs, M. Vanstrum, G. Gothard, and D. Wiebelt, "A low-profile broadband phased array antenna," in *Proc. IEEE Antennas Propag. Soc. Int. Symp.*, vol. 2, pp. 448-451, June 2003.
- [10] B. A. Munk, "Broadband wire arrays," in *Finite Antenna Arrays and FSS*, 1st ed., New York, NY, USA: Wiley-IEEE Press, ch. 6, pp. 181-213, July 2003.
- [11] H. Zhang, S. Yang, S. Xiao, Y. Chen, and S. Qu, "Low-profile, lightweight, ultrawideband tightly coupled dipole arrays loaded with split rings," *IEEE Trans. Antennas Propag.*, vol. 67, no. 6, pp. 4257-4262, Mar. 2019.
- [12] E. Yetisir, N. Ghalichechian, and J. L. Volakis, "Ultrawideband array with 70° scanning using FSS superstrate," *IEEE Trans. Antennas Propag.*, vol. 64, no. 10, pp. 4256-4265, Oct. 2016.
- [13] S. S. Holland and M. N. Vouvakis, "The planar ultrawideband modular antenna (PUMA) array," *IEEE Trans. Antennas Propag.*, vol. 60, no. 1, pp. 130-140, Jan. 2012.
- [14] J. P. Doane, K. Sertel, and J. L. Volakis, "A wideband, wide scanning tightly coupled dipole array with integrated balun (TCDA-IB)," *IEEE Trans. Antennas Propag.*, vol. 68, no. 9, pp. 4538-4548, Sep. 2013.
- [15] Y. Ma, S. Yang, Y. Chen, S.-W. Qu, and J. Hu, "Sparsely excited tightly coupled dipole arrays based on irregular array techniques," *IEEE Transactions on Antennas and Propagation*, vol. 68, no. 8, pp. 6098-6108, Aug. 2020.
- [16] B. J. Wang, S. W. Yang, Y. K. Chen, S. W. Qu, and J. Hu, "Low cross-polarization ultra-wideband tightly coupled balanced antipodal dipole array," *IEEE Trans. Antennas Propag.*, vol. 68, no. 6, pp. 4479-4488, Feb. 2020.
- [17] J. Zhong, E. A. Alwan, and J. L. Volakis, "2 to 18 GHz ultra-wideband dual-linear polarized phased array with 60° scanning," *2018 International Applied Computational Electromagnetics Society Symposium (ACES)*, Denver, CO, USA, pp. 1-2, Mar. 2018.
- [18] W. Zhou, Y. Chen, and S. Yang, "Efficient design of tightly coupled dipole array using an equivalent circuit-based approach," *IEEE Access*, vol. 8, pp. 14013-14023, Jan. 2020.
- [19] R. T. Cameron and V. G. Eleftheriades, "Analysis and characterization of a wide-angle impedance matching metasurface for dipole phased arrays," *IEEE Trans. Antennas Propag.*, vol. 63, no. 9, pp. 3928-3938, Sep. 2019.
- [20] H. A. Wheeler, "Simple relations derived from a phased-array antenna made of an infinite current sheet," *IEEE Trans. Antennas Propag.*, vol. AP-13, no. 4, pp. 506-514, July 1965.
- [21] D. M. L. Bartholomew, "Optimum design for a broadband microstrip balun," *Electron. Lett.*, vol. 13, no. 17, pp. 510-511, Aug. 1977.
- [22] J. Allen, "Gain and impedance variation in scanned dipole arrays," *IRE Trans. Antennas Propag.*, vol. 10, no. 5, pp. 566-572, Sep. 1962.



Yuan Ye was born in Guangxi, China. She received the M.S. degree in Sun Yat-sen University, Guangzhou, China, in 2012, and currently she is working toward the Ph.D. degree in National University of Defense Technology. Her current research interests include ultrawideband antenna arrays and reconfigurable antenna.



Huang Zhanyu was born in 1992. He received the M.S. degree in Electronics and Communication Engineering from the University of Electronic Science and Technology of China, Chengdu, China in 2018, where he is currently pursuing Ph.D. degree with the College of Electronic Science and Engineering, National University of Defense Technology, Changsha, China. His current research interests include passive RF/microwave circuits, microstrip antennas and wireless communication.



Yun Jiang was born in Hunnan Province, China. He received the M.S. degrees in Electronic Engineering from the University of Electronic Science and Technology of China (UESTC), Chengdu, China, in 2017, and currently he is working toward the Ph.D. degree in National University of Defense Technology. His research interests include RF/millimeter-wave components and circuits.



Li-an Bian is now working in the Changsha University of Science & Technology. He received the Ph.D. degree of Electronics Science and Technology from National University of Defense Technology, Changsha, China in 2018. His research interests include graphene devices, photonic crystals and antenna design etc. So far, he has published nearly fifty academic papers.



Jinjian Huang is now working in National University of Defense Technology. He received the Ph.D. degree of Electronics Science and Technology from National University of Defense Technology, Changsha, China in 2014. His research interests include ultra-wide band antenna and phase array antenna.



Chang Zhu was born in Anhui, China, in 1977. He received the M.S. and Ph.D. degrees in Electronic Science and Technology from National University of Defense Technology in 2001 and 2005 respectively. He is currently an Associate Professor with the National University of Defense Technology. His research interests include microwave and millimeter wave technology.



Naichang Yuan was born in Anhui, China, in 1965. He received the M.S. and Ph.D. degrees in Electronic Science and Technology from the University of Electronic Science and Technology of China in 1991 and 1994, respectively. He is currently a Professor with the National University of Defense Technology. His research interests include array signal processing, radar system design, SAR/ISAR imaging and electronic countermeasures.

Train-mounted Broadband Monopole Antenna for 5G Communication

Hao Xiang Li¹, Lu Xu¹, Feng Qian^{1,*}, and Yong Jin Zhou^{1,2,*}

¹ Key Laboratory of Specialty Fiber Optics and Optical Access Networks
Shanghai University, Shanghai 200444, China

² State Key Laboratory of Millimeter Waves, School of Information Science and Engineering
Southeast University, Nanjing 210096, China
*yjzhou@shu.edu.cn, *hayiji2015@shu.edu.cn

Abstract — As a convenient and efficient public transport system, high speed railway (HSR) was rapidly deployed in China. Since the fifth generation (5G) mobile communication system is commercially applied, it is necessary for mobile terminals antennas to cover multiple operating bands to be compatible with various communication systems. Here a HSR-mounted broadband and high-gain monopole antenna is proposed. By using the meander technology and introducing the tapered structure, the proposed antenna operates over a bandwidth of 694-960 MHz and 1350-5975 MHz (VSWR<1.8), which covers both 2G-5G mobile communication and WiFi frequency bands. The dimensions of the proposed antenna are 400 mm × 330 mm × 78 mm. The measured average gain is 6.11 dBi over the entire bandwidth.

Index Terms — 5G, antennas, broadband, high-gain, High Speed Railway (HSR).

I. INTRODUCTION

As a fast and convenient public transportation means, high-speed railway (HSR) has attracted a lot of attention in recent years [1]. On the one hand, the surrounding environment of HSR is much more complicated than other scenarios [2]. On the other hand, communication interruption caused by handover failures could seriously degrade the users' quality of service because of frequent handovers in wireless communication system for high-speed trains [3].

At third generation (3G) era, existing railway broadband communication systems were mainly suitable for low mobility environment and low data rate transmissions [3]. The railway network coverage mostly depends on both urban and rural base stations, which can meet the needs of users when the train runs with low speed and the data rate is low. However, there would be increasing handovers and drop-offs due to high mobility of 350-500 km/h [4]. Besides, the signals could suffer severe penetration loss when coming through the carriage body made of aluminum and

stainless steel [5]. Traditional mobile communication networks could not fulfill the increasing users' requirements at 4G era [6]. Hence, massive multiple-input multiple-output (MIMO) beam forming and distributed antenna system were used to solve the above problems [7-9]. A dual-antenna in distributed antenna system [2], MIMO antennas system [4], efficient multiple-group multiple-antenna (MGMA) scheme [10], and linearly located distributed antenna system [11] are presented for HSR. However, multiple antennas increase the complexity of the system. One kind of potential solution was proposed by using a relay station mounted outside the train to communicate with base stations [1]. The relay station consists of a train-mounted relay antenna communicating with the base station and a WiFi AP where the mobile station signal can be converted into WiFi signal. The communication system is shown in Fig. 1, where radio signal penetration loss and the coverage problem can be avoided, because radio signals do not need to penetrate into/from the carriages. The 5G mobile communication system is a good choice for huge traffic volume of wireless data service. The train-mounted antennas of the relay station need cover wide frequency band or multiple operating bands to be compatible with various communication systems, to cover both 2G-5G mobile communication and WiFi frequency bands. Besides, wide beam width of the antenna is also necessary to keep the stable link between the relay station and the base station.

The most widely used 2G-5G frequency spectrum in the world today is 700 MHz, 800-900 MHz, 1800-1900 MHz, 2100 MHz, 2600 MHz, 3.5 GHz and 4.9 GHz. Recently, 700 MHz was allocated to China Broadcasting Network Corporation Ltd. (CBN). By using 700 MHz, the investment of 5G network deployment would be saved, because it will use fewer base stations for its large-area network coverage. In addition, the 700 MHz frequency also offers good signal penetration through buildings, basements and elevators. Hence broadband antennas which can simultaneously

cover multiple service bands are in great demands [1], especially covering 700 MHz. Furthermore, to extend the radio transmission distance, the use of high-gain antennas is important [12, 13]. Vehicle mounted antennas for vehicle-mounted VHF/UHF communication system [14], vehicle-to-everything (V2X) communication [15], and car-to-car (C2C) communication [16, 17] have been designed. However, antenna in Ref. 14 operates from 80 MHz to 600 MHz, the gain of the antenna in Ref. 16 is very low, and Ref. 17 needs two antennas to realize broadband. A top-mounted train antenna operating in the bands of 825-960 MHz, 1.7-2.7 GHz, and 5.7-5.9 GHz by loading an asymmetrically folded branch was proposed [18], but it cannot cover 700 MHz. Dedicated antennas for HSR applications are rarely presented [19].

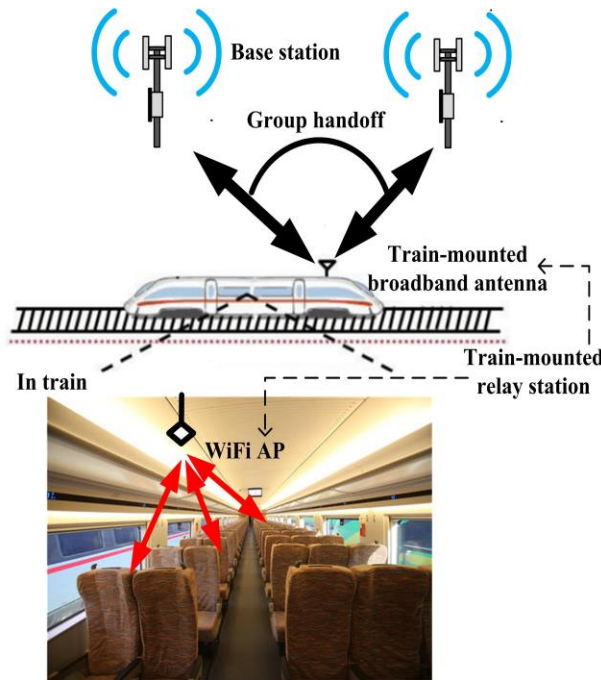


Fig. 1. Communication system by using a relay station mounted outside the train.

In this paper, we propose a train-mounted broadband and high-gain monopole antenna. The dimensions of the proposed antenna are 400 mm × 330 mm × 78 mm. By using the meander technology and introducing the tapered structure, the simulated results of the antenna achieved the desired performances. This antenna can operate over a bandwidth of 694 - 960 MHz and 1350 - 5975 MHz (VSWR < 1.8), which cover the 2G-5G and Wi-Fi communication bands. The measured average gain is 6.11 dBi over the entire bandwidth.

II. ANTENNA DESIGN

The original structure is a monopole antenna placed on the ground plane, which is illustrated in Fig. 2 (a). The monopole antenna includes a vertical radiating part, a horizontal metal strip, and a vertical metal strip shorted to the ground plane. The main radiating part is a tapered structure which can implement wideband characteristics. The final structure is Antenna D which can be seen in Fig. 2 (d).

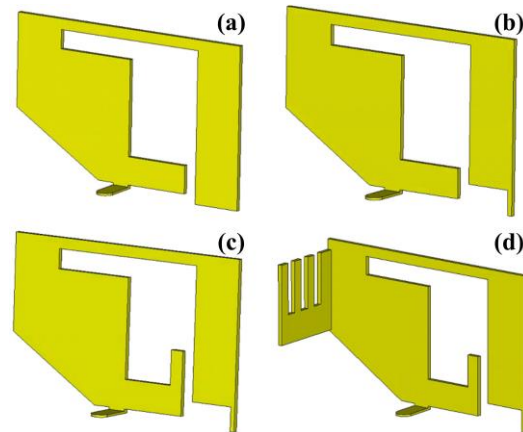


Fig. 2. (a) initial antenna A, (b) antenna B, (c) antenna C, and (d) antenna D.

Figure 3 shows the simulated VSWR of the initial antenna A and antenna B. It can be seen that the initial antenna A can operate at wideband frequencies, not including the frequency band from 1.69 GHz to 2.8 GHz. By loading a rectangle slot (shown in antenna B), the impedance matching over the band from 1.69 GHz to 2.8 GHz was obviously improved, which can be verified by the current distributions at 2.0 GHz, illustrated in Figs. 3 (b) and 3 (c). However, the VSWR is still larger than 2.0 at the frequency band.

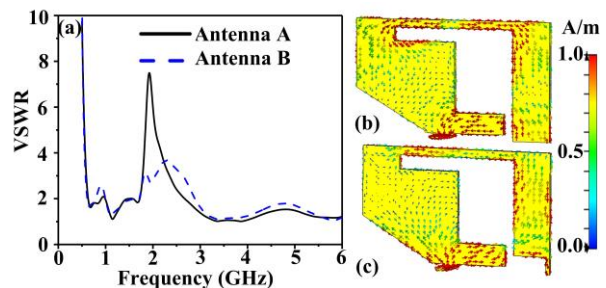


Fig. 3. (a) Simulated VSWR of the initial antenna A and antenna B, (b) the current distribution of initial antenna A at 2.0 GHz, and (c) the current distribution of antenna B at 2.0 GHz.

By loading a rectangular branch (shown in antenna C), the impedance matching around 2.0 GHz was further improved, as shown in Fig. 4 (a), where it can be seen that VSWR is smaller than 2.0 at the frequency band from 1.69 GHz to 2.8 GHz, which has been verified by the current distributions shown in Figs. 4 (b) and 4 (c). Furthermore, the VSWR at the lower stop-band was increased.

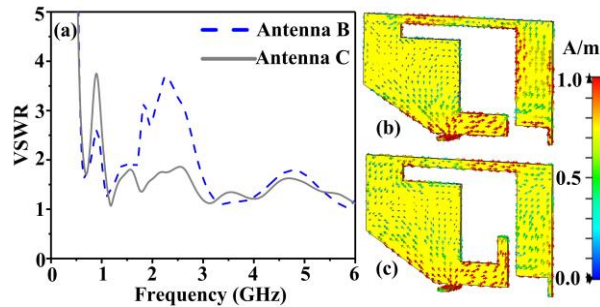


Fig. 4. (a) Simulated VSWR of antenna B and antenna C. (b) and (c) Current distributions of antenna B and antenna C at 2.0 GHz.

However, the central frequency of antenna C at the lower stop-band needs further adjustment. Antenna D shown in Fig. 2 (d) can operate at lower stop-band by loading a comb-like structure. The lower stop-band is from 960 to 1350 MHz, as shown in Fig. 5 (a). It can be seen that the operating frequency of Antenna D is from 694 to 960 MHz and from 1350 to 5975 MHz when $VSWR < 1.8$, which has been verified by the current distributions at 900 MHz illustrated in Fig. 5 (b) and Fig. 5 (c). From the surface current shown in Fig. 5(c), it can be seen that the comb-like structure reduces the effect of attenuating current cancellation. And the simulation setting for solving dispersion curves of comb-like structure is shown in Fig. 5 (d), where periodic boundary condition (PBC) is used in x direction and perfect electric conductor condition (PEC) is used in the other directions.

The detailed structure of Antenna D is illustrated in Fig. 6. And the dimensions of Antenna D shown in Table 1. The fabricated antenna is shown in Fig. 6 (d) (the material is copper), whose thickness is 2 mm.

III. RESULTS AND DISCUSSION

The simulated VSWR and gain are obtained by using CST. The measured VSWR and gain are shown in Fig. 7. From Fig. 7 (a), it can be seen that the simulated operating frequency is from 694 to 960 MHz and from 1350 to 5975 MHz ($VSWR < 1.8$) and the measurement results agree well with the simulation results. From Fig. 7 (b), we can see that the measured gain is a little lower than the simulation results. The simulated average gain is 7.67 dBi over the entire

bandwidth. The measured average gain is 6.11 dBi over the entire bandwidth.

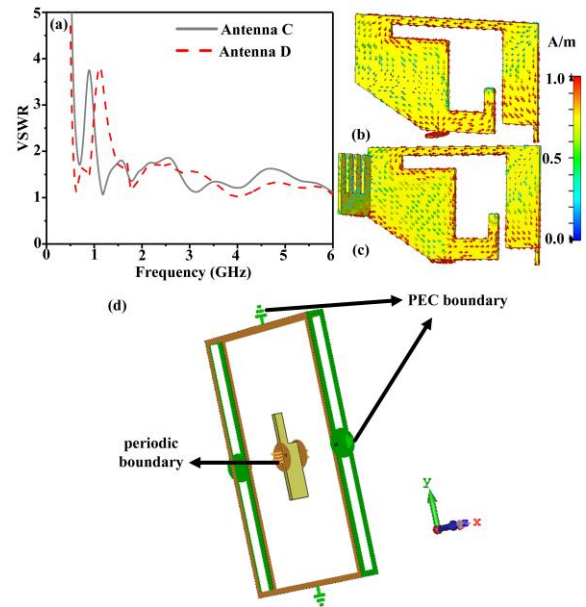


Fig. 5. (a) Simulated VSWR of antenna C and antenna D, (b) and (c) current distributions of antenna C and antenna D at 900 MHz, and (d) the details on simulation of comb-like structure.

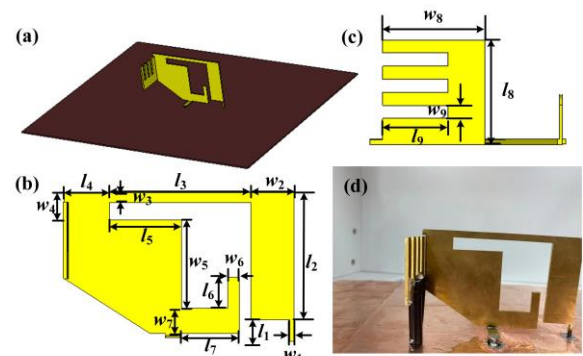


Fig. 6. (a) 3D perspective view, (b) side view, (c) side view, and (d) the sample of the fabricated antenna.

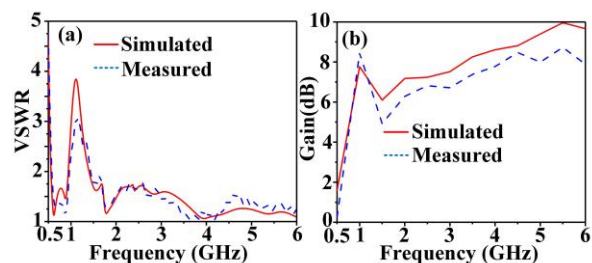


Fig. 7. Simulated and measured (a) VSWR and (b) Gain of Antenna D.

Table 1: Dimensions of the antenna D

Parameters	l_1	l_2	l_3	l_4	l_5	l_6	l_7	l_8	l_9
Unit (mm)	17	65	72	23	36.6	15.7	29.6	38	25
Parameters	w_1	w_2	w_3	w_4	w_5	w_6	w_7	w_8	w_9
Unit(mm)	2	22	5	14	45	6	13	39	5

The simulated and measured far-field radiation patterns of Antenna D at 1.0 GHz and 5.0 GHz are shown in Fig. 8 (a), Fig. 8 (b), respectively. It can be seen that the measured results agree well with the simulated results.

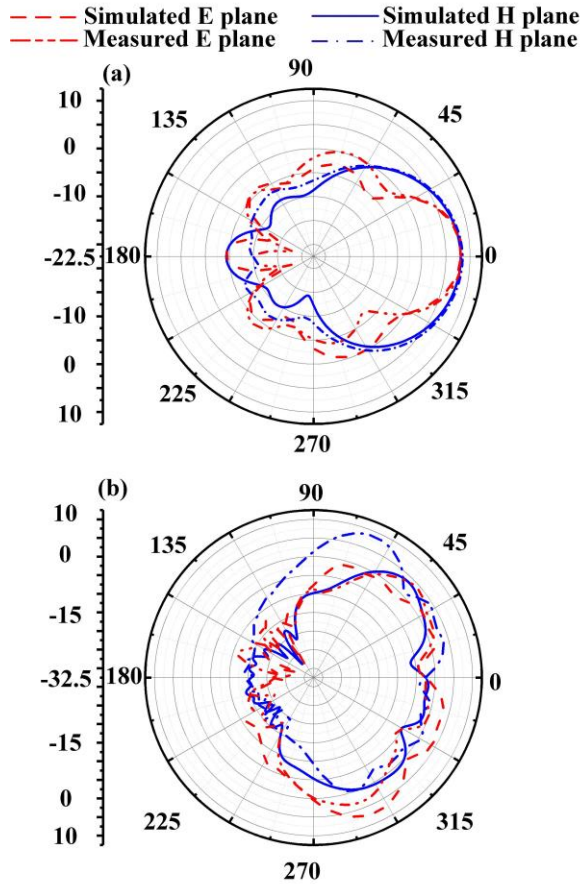


Fig. 8. The simulated and measured far-field radiation patterns at (a) 1.0 GHz and (b) 5.0 GHz.

The simulated and measured efficiencies of Antenna D are shown in Fig. 9. It can be seen that the measured results agree well with the simulation results above 1.35 GHz. The measure efficiency above 1 GHz is larger than 80%. However, the efficiency from 694 to 960 MHz is a little low, which is larger than 43.5%.

The performances of the proposed antenna are compared with other antennas in Table 2. Compared other works, Antenna D can realize broadband (cover 700 MHz) and high gain simultaneously.

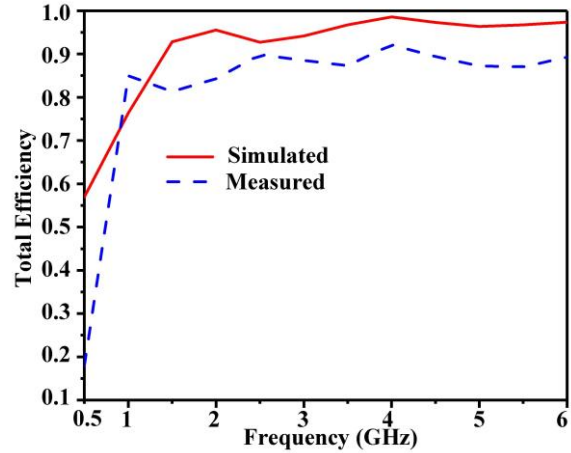


Fig. 9. Simulated and measured efficiencies of antenna D.

Table 2: Comparison of the related researches

Ref.	Dimensions (mm)	Bandwidth (MHz)	Gain
[14]	630 × 630 × 220	80 - 600	/
[15]	87 × 60	690 - 7000	/
[16]	120 × 52	698 - 2700 5000 - 6000	1.5 dBi - 4.4 dBi
[17]	40 × 40 × 60	698 - 960 1700 - 2700 5100 - 6000	/
[18]	116 × 40 × 1.6	825 - 960 1700 - 2700 5700 - 5900	4.27 dBi - 9.82 dBi
[20]	/	698 - 960 1710 - 2170 2400 - 2700 3400 - 3700 4900 - 5935	5 dBi - 8 dBi
This work	117 × 82 × 38	694 - 960 1350 - 5975	Average: 7.67 dBi

IV. CONCLUSION

Here a broadband, low-frequency, high-gain monopole antenna for HSR is proposed. The measured average gain is 6.11 dBi over the entire working bandwidth. By using the meander technology and introducing the tapered structure, the proposed antenna operates over a bandwidth of 694-960 MHz and 1350-5975 MHz (VSWR<1.8) covering 700 MHz, GSM, LTE, and Wi-Fi communication systems, which can be

mounted on the top of the train for 5G communication.

ACKNOWLEDGMENT

This work was supported in part by the National Natural Science Foundation of China under Grant No. 61971469, and in part by Science and Technology Commission Shanghai Municipality (STCSM) under Grant No. 18ZR1413500, and in part by the Open Project Program of the State Key Laboratory of Millimeter Waves under Grant No. K202109.

REFERENCES

- [1] J. Wang, H. Zhu, and N. J. Gomes, "Distributed antenna systems for mobile communications in high speed trains," *IEEE Journal on Selected Areas in Communications*, vol. 30, pp. 675-683, May 2012.
- [2] X. Qian, H. Wu, and J. Meng, "A dual-antenna and mobile relay station based handover in distributed antenna system for high-speed railway," *Seventh International Conference on Innovative Mobile and Internet Services in Ubiquitous Computing*, pp. 585-590, July 2013.
- [3] S. Pu and J. H. Wang, "Research on the receiving and radiating characteristics of antennas on high-speed train using integrative modeling technique," *Asia Pacific Microwave Conference*, pp. 1072-1075, Dec. 2009.
- [4] Y. Zhao, X. Li, and H. Ji, "Radio admission control scheme for high-speed railway communication with MIMO antennas," *IEEE International Conference on Communications*, pp. 5005-5009, June 2012.
- [5] L. Liu, C. Tao, J. Qiu, H. Chen, L. Yu, W. Dong, and Y. Yuan, "Position-based modeling for wireless channel on high-speed railway under a viaduct at 2.35 GHz," *IEEE Journal on Selected Areas in Communications*, vol. 30, pp. 834-845, May 2012.
- [6] F. Abrishamkar and J. Irvine, "Comparison of current solutions for the provision of voice services to passengers on high speed trains," *IEEE 52nd Vehicular Technology Conference Fall 2000. VTS*, vol. 4, pp. 1498-1505, Sep. 2000.
- [7] L. C. Godara, "Application of antenna arrays to mobile communications. II. Beam-forming and direction-of-arrival considerations," *Proceedings of the IEEE*, vol. 85, pp. 1195-1245, Aug. 1997.
- [8] W. Choi and J. G. Andrews, "Downlink performance and capacity of distributed antenna systems in a multicell environment," *IEEE Transactions on Wireless Communications*, vol. 6, no. 1, pp. 69-73, Feb. 2007.
- [9] X. Chen, J. Lu, P. Fan, and K. B. Letaief, "Massive MIMO beamforming with transmit diversity for high mobility wireless communications," *IEEE Access*, vol. 5, pp. 23032-23045, Oct. 2017.
- [10] J. H. Susanto, H. Miyazaki, K. Temma, T. Yamamoto, T. Obara and F. Adachi, "Linearly distributed antenna diversity using single frequency network for high-speed railway communications," *19th Asia-Pacific Conference on Communications*, pp. 299-303, Aug. 2013.
- [11] W. Luo, X. Fang, M. Cheng, and Y. Zhao, "Efficient multiple-group multiple-antenna (MGMA) scheme for high-speed railway viaducts," *IEEE Transactions on Vehicular Technology*, vol. 62, pp. 2558-2569, July 2013.
- [12] K. Abe, T. Hattori, A. Ishiwata, and H. Koizumi, "A study on antennas for railway millimeter-wave radio communication system," *IEEE International Conference on Personal Wireless Communications*, pp. 201-205, Dec. 1997.
- [13] P. T. Dat, A. Kanno, N. Yamamoto, and T. Kawanishi, "WDM RoF-MMW and linearly located distributed antenna system for future high-speed railway communications," *IEEE Communications Magazine*, vol. 53, pp. 86-94, Oct. 2015.
- [14] S. Y. Xu, J. Liu and H. C. Gen, "Design of a composite loaded UWB miniaturized vehicle-mounted antenna," *IEEE 18th International Conference on Communication Technology*, pp. 582-585, Oct. 2018.
- [15] Y. Hua, L. Huang, and Y. Lu, "A compact 3-port multiband antenna for V2X communication," *IEEE International Symposium on Antennas and Propagation & USNC/URSI National Radio Science Meeting*, pp. 639-640, July 2017.
- [16] Q. Wu, Y. Zhou, and S. Guo, "An L-sleeve L-monopole antenna fitting a shark-fin module for vehicular LTE, WLAN, and car-to-car communications," *IEEE Transactions on Vehicular Technology*, vol. 67, pp. 7170-7180, Apr. 2018.
- [17] D. V. Navarro-Méndez, L. F. Carrera-Suárez, D. Sánchez-Escuderos, M. Cabedo-Fabrés, M. Aquero-Escudero, M. Gallo, and D. Zamberlan, "Wideband double monopole for mobile, WLAN, and C2C services in vehicular applications," *IEEE Antennas and Wireless Propagation Letters*, vol. 16, pp. 16-19, Apr. 2016.
- [18] J. Cui, A. Zhang, and X. Chen, "An omnidirectional multiband antenna for railway application," *IEEE Antennas and Wireless Propagation Letters*, vol. 19, pp. 54-58, Jan. 2020.
- [19] L. Xu and Y. J. Zhou, "Low profile high-gain antenna for broadband indoor distributed antenna system," vol. 35, no. 7, pp. 791-796, July 2020.
- [20] J. N. Huang, Z. X. Chen, Y. T. Zhang, and F. Huang, "Broadband high-gain MIMO antenna for high-speed railway," *CN109411871A*, Mar. 2019.



Hao Xiang Li was born in Xian, Shanxi, China, in 1996. He is currently pursuing the Master's degree of Electronic and Communications Engineering in Shanghai University, Shanghai 200444, China. His research interests include broadband antenna, beaming scanning antenna and metamaterials.



Lu Xu was born in Yangzhou, Jiangsu, China, in 1996. She received the Master's degree of Electronic and Communications Engineering in Shanghai University, Shanghai 200444, China in 2020. Her research interests include small antenna, broadband antenna and metamaterials.



Feng Qian was born in Nantong, Jiangsu, China, in 1982. His current research interests include RF circuit and signal processing. He received the B.S. degree in Communication Engineering Xidian University, Shaanxi, China, in 2004, and M.S. degree in Communication and Information System from Xidian University, Shaanxi, China, in 2007, respectively. From 2015, he was a Senior Engineer with School of Communication & Information Engineering, Shanghai University, Shanghai, China.



Yong Jin Zhou was born in Shandong, China, in 1982. His current research interests include microwave and millimeter antenna, plasmonic metamaterials and applications, millimeter wave and THz functional devices, wireless energy transmission. He received the B.S. degree in Communication Engineering from Shandong University, Jinan, China, in 2006, and Ph.D. degree in Electromagnetic Field and Microwave Technology from Southeast University, Nanjing, China, in 2011, respectively. From 2009 to 2010, he was a Visiting Scholar of University of Houston. From 2011 to 2012, he was a Software Engineer with EEBU of Marvell Technology (Shanghai) Ltd. From 2012 to 2015, he was an Assistant Professor and from 2015 to 2020, he was an Associate Professor with School of Communication & Information Engineering, Shanghai University, Shanghai, China. Currently, he is a Professor with School of Communication & Information Engineering, Shanghai University, Shanghai, China. He has authored and coauthored over 90 papers in peer-reviewed journals and conference proceedings. He is IEEE Member, OSA Member, and Senior Member of Chinese Institute of Electronics. He is serving as a Reviewer for over 20 peer-reviewed journals, such as Nature electronics, Photonic Research, Optics Letter, Optics Express, Appl. Phys. Express, IEEE Access, IEEE MTT, IEEE MWCL, etc. He was serving as a Session Chair for several International Symposiums.

Single-Chip Two Antennas for MM-Wave Self-Powering and Implantable Biomedical Devices

D. Elshaekh¹, S. Kayed², and H. Shawkey³

¹Electrical Dept., Faculty of Engineering-Badr University, Badr University in Cairo
dalia-mohamed@buc.edu.eg

²Head of Electrical Dept., Obour High Institute for Engineering and Technology, 31 Elasmalia - Desert Road
dr.somayaismail@ohie.edu.eg

³Microelectronics Dept., Electronics Research Institute, 12622, El Dokki, Giza, Egypt
heba_shawkey@eri.sci.eg

Abstract — Implantable biomedical applications arise the need for multi-band sensors with a wideband frequency channel for RF energy harvesting operation. Using a separate antenna for energy harvesting can simplify device circuit complexity and reduces operation frequency bands interference. This paper demonstrates the design of single chip with two separate integrated antennas for implantable biomedical applications. The two antennas have different structures with orthogonal polarization to achieve low mutual coupling and negligible interaction between them. The first antenna is a multi-band meander line (MBML) designed for multiple channels data communication, with quad operating bands in the MM-wave range from 22-64 GHz with area $1150 \times 200 \mu\text{m}^2$. The second antenna is a wideband dipole antenna (WBDA) for RF energy harvesting, operates in the frequency range extend from 28 GHz to 36 GHz with area $1300 \times 250 \mu\text{m}^2$. The proposed antennas are designed by using high frequency structure simulator (HFSS) and fabricated by using UMC180nm CMOS technology with total area 0.55 mm². The MBML frequency bands operating bandwidths can reach 2 GHz at impedance bandwidth ≤ -10 dB. While, the WBDA antenna has gain -2 dB over the operating band extend from 28 GHz up to 36 GHz. The antenna performance is simulated separately and using the human-body phantom model that describes layers of fats inside body, and shows their compatibility for in body operation. Die measurements is performed using on wafer-probing RF PICOBROBES and shows the matching between simulation and measurement values.

Index Terms — Implantable antenna, Multi-Band Meander-Line (MBML), on-chip antenna, radio frequency energy harvesting and UMC 180 μm CMOS, Wideband Dipole Antenna (WBDA).

I. INTRODUCTION

Currently, promising implantable systems have been proposed for healthcare monitoring and remote sensing to improve the lifestyle of the patients. UWB frequency bands are applied for implantable devices as it enables high data rate and multiple frequency channels for multimode operation [1-5]. Recently, MMW range is described as a complementary imaging technique instead of exposure of patient to radiations as magnetic resonance, X-Ray or Ultrasound [6-8]. The antennas depend on 5G technology to meet the capacity, latency and the bandwidth requirements to support the request of the growing number of wireless communication users [9-10]. Besides, antenna and associated electronics could be designed to support multiple frequency channels for data communications of a group of implantable sensors simultaneously, with the need for a wideband frequency channel for RF energy harvesting to obtain a suitable power level for device operation [11-14]. Figure 1 shows the energy/power required for device operation can be obtained using energy harvester/wireless powering transfer from external source to be applied to the implantable devices in different locations in-body. Different types of on-chip implantable antennas are described in the sub GHz range and MMW range [15-20].

Simultaneous data communication mode and RF wireless powering mode using same antenna and matching network [21-22] where the antenna toggles between the two communication modes, the data mode and power mode, but this needs special control technique to fulfil continuous switching between both modes. To reduce circuit complexity, the modes of operation can be split up by using two separate antennas, one is used for data communication (for multiple sensors) while the other operates for RF energy harvesting. In this paper,

two separate integrated antennas on the same chip are proposed to be used for self-powering implantable biomedical devices. The antennas are designed for data communication and energy harvesting simultaneously, with two different structures are designed, a multiband meander line antenna (MBML) and a wide-band dipole antenna (WBDA), with no radiation coupling occurs. The MBML resonates at the 22, 36, 48, 60 GHz, such that it is suitable for multiple sensing applications, while the WBDA operates from 28 GHz-36 GHz to perform the wideband required for energy harvesting. The 3D configuration of the proposed antennas shown in Fig. 2, is fabricated using UMC 0.18 μm CMOS technology with 6-Metal layers. As implantable devices are affected by the permittivity of human tissues which causes signal losses, antenna design should consider the human-body effect during antenna design as wireless transfer between the on-body device and the external electronic circuits. For human activity monitoring, the implant is set to be below the human scalp or embedded in the muscle [23].

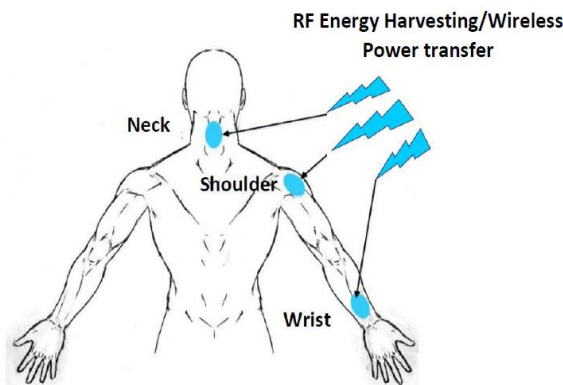


Fig. 1. RF wireless powering for different implantable devices.

In this paper, the chip is assumed for implantation in the fat layer of the human body. Phantom model is used to investigate the antenna signal transmission in the human body layers even in the presence of perturbations such as embedded muscle layers and blood vessels. Different sensor antenna are implemented in a chip 180 nm CMOS technology for radio frequency (RF) energy harvesting to increase the lifetime of the internal batteries or feed another system [30].

The paper sections are organized as follows; Section 2 shows detailed explanation of the proposed antennas configuration. In Section 3 the simulation and measurement performance of both antennas. In Section 4, the proposed antenna simulation using human-phantom is performed to investigate antenna compatibility with implantable applications. Finally, conclusions of the

paper are shown in Section 5.

II. ANTENNA CONFIGURATION AND DESIGN

Different shapes of on-chip integrated antennas are shown, as dipole [17], [24], [25], loop [18-20], zigzag [26], [27], and bowtie antennas [28], [29]. This is due to their circuits have differential input / output. The design of the two balanced antennas are utilized to obtain the benefits of the on-chip ground plane used to improve antenna radiation efficiency. Two different shapes of antennas are used to seeking different wireless applications, one for the data communication antenna and the second for wireless powering antenna integrated on the same chip with separate connecting PADS as shown in Fig. 3. The polarization of both antenna are linear polarized and there are orthogonal located to each other to reduced coupling between them. The chip is fabricated by using UMC 180nm CMOS process with silicon substrate and six metal layers. In this section, design and simulation for each antenna is demonstrated.

A. Data communication antenna

It is a multi-band meander line (MBML) implemented at 2 stacked layers to increase antenna total length-located at metal layers M6 and M4 as shown in Fig. 3. A layer of metal M1 is set as a ground plane to enlarge bandwidth with area of $1525\mu\text{m} \times 250\mu\text{m}$ with four connections to the four ground PADS. Each meander layer – whether at M4 and M6 – has a finger line width $15\mu\text{m}$, length $1150\mu\text{m}$ and line spacing $20\mu\text{m}$ between each two fingers. The meander structure at M6 layer has five fingers while the meander structure at M4 layer has only four fingers as shown in Fig. 2. The two layers have the same alignment but shifted $17.5\mu\text{m}$, to increase number of resonance frequency bands. Five PADS are used with area $80\mu\text{m} \times 60\mu\text{m}$ for each and separated by $150\mu\text{m}$. One of the PADS is connected to the upper meander layer M6 to be used as signal PAD and the others are used as ground PADS. The MBML has a 50Ω line connection with signal PAD. The two meander layers are connected through via 1.

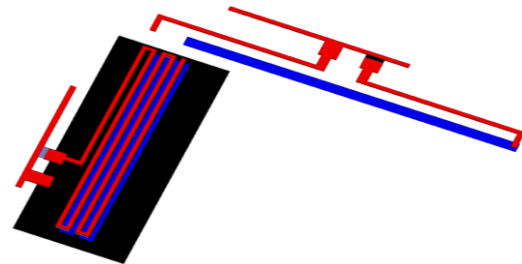


Fig. 2. The 3D configuration of MIMO.

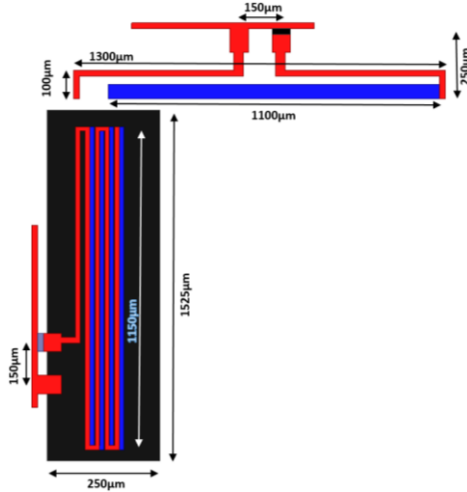


Fig. 3. Data communication of system multi-band meander line and dipole antenna.

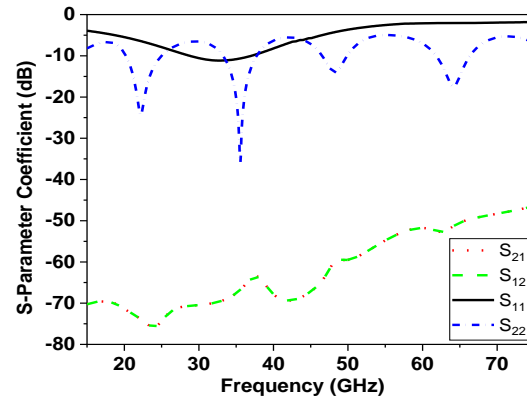
B. RF energy harvester antenna

Figure 3 shows the structure of the wideband dipole antenna used for RF energy harvesting. It is composed of three layers, a dipole layer, a patch layer, and a ground plane. The dipole consisting of a half wavelength radiating dipole implemented at the upper metal layer M_6 with total area $1300\mu\text{m}\times 250\mu\text{m}$. The patch layer is carried out in the intermediate metal layer M_4 with area $1100\mu\text{m}\times 50\mu\text{m}$. This middle patch layer acts as a parasitic element to broaden the antenna bandwidth. A ground layer is set at the M_1 layer with area $1300\mu\text{m}\times 250\mu\text{m}$. The patch layer is stacked to the dipole by VIA1. The signal and ground PADS (with area $80\mu\text{m}\times 60\mu\text{m}$) are separated by $150\mu\text{m}$. The ground M_1 layer is connected to the Ground PAD by VIA2. The proposed dipole antenna with patch layer is set to reduce the resonant frequency and increase the antenna bandwidth. The corresponding reflection coefficient response for both antennas is shown in Fig. 4 (a), where $|S_{22}|$ (as dashed blue line) represents the MBML response while $|S_{11}|$ (as black line) represents the WBDA. The green line explains the neglected coupling between both antennas. Current distribution at different tuning frequencies on both antennas' surfaces are shown in Fig. 5. The highest magnitude of current represents the corresponding element of radiation.

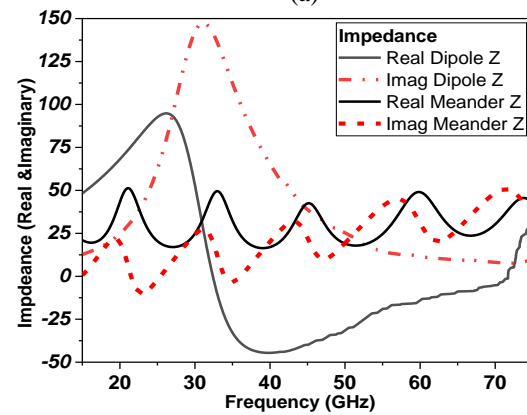
III. ANTENNA MEASUREMENTS RESULTS

The measured antenna S-parameters are carried out by using cascade probe station on top with Anritsu Vector Network as shown in Fig. 6. The measured reflection coefficient is achieved by using on-wafer probing. The measurements setup shown in Fig. 6, composed of one GSG 70 GHz PicoProbe-RF probe (pitch: $150\mu\text{m}$) and Anritsu Vector Network analyzer up to 70 GHz. The UMC180nm setup die (miniasic $1.525\text{ mm}\times 1.525\text{ mm}$)

is fabricated and fixed at PM5 KarlSuss manual probe-station.



(a)



(b)

Fig. 4. (a) Scattering parameters versus frequency of the proposed antennas, and (b) input impedance real and imaginary.

The fabricated photo of the proposed antennas are shown in Fig. 6 with four ground PADS connected to the ground metal layer M_1 , the extra PADS have no effect on antenna performance but are added due to measurements concerns. To ensure the reliability and accuracy of measurements; the proper fixture is applied. The die is fixed on the probe-station holder using vacuum pump while the GSG probe and the positioner are held by a manipulator that has magnetic fixture to ensure accurate contact between the die and the GSG probe. The other measurement problems that could be cause uncertainty of measurements [29] which is avoided by using a calibration substrate at the beginning of the measurements to ensure accurate calibration for the complete setup (network analyzer, cabling and probe) whenever it produces a reading different than the standard. Besides, before each measurement experiment the VNA was calibrated using (the open short, through calibration kit). Figure 7 (a) shows the comparison between the simulated and measured reflection coefficients $|S_{11}|$ of the double

meander antenna. However, the $|S_{11}|$ of the different dipole length is shown in Fig. 7 (b). The comparison between simulated and measured results showed that there are a good agreement between the lower and the upper of the operating frequencies' antenna bands. There are some ripples in the measured results and there are about -3 dB shift in the measured reflection coefficient results. These errors could be attributed to metal holder, which are not considered and many factors as the thickness of the layer, metal holder was not considered. In addition, uncertainty in the dielectric material properties are specified up to 15 GHz while the simulated dielectric material properties of the layer were identified up to 70 GHz. As well as the influence of larger wafer with the chuck and the uncertainty in the dielectric material properties. In the simulations, these values have been used for the characterization of the structure at 70 GHz. Table 1 shows the radiation pattern of the MBMA at different resonant frequencies. While table 2 shows the simulated polar radiation pattern for the WBDA antenna at three resonant frequencies 28 GHz, 32 GHz and 32 GHz, respectively.

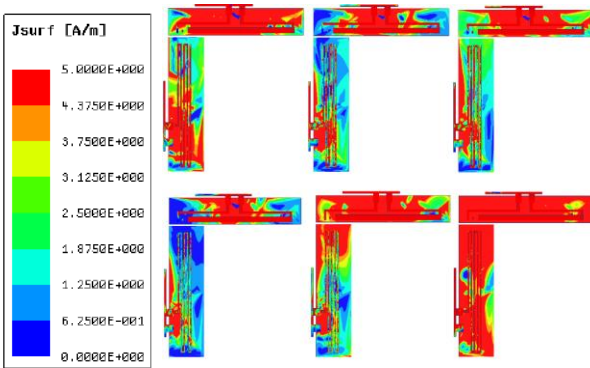


Fig. 5. Current distribution of the two antennas at different tuning frequency: (a) 22 GHz, (b) 28 GHz, (c) 30GHz, (d) 34 GHz, (e) 44 GHz, and (e) 62 GHz.

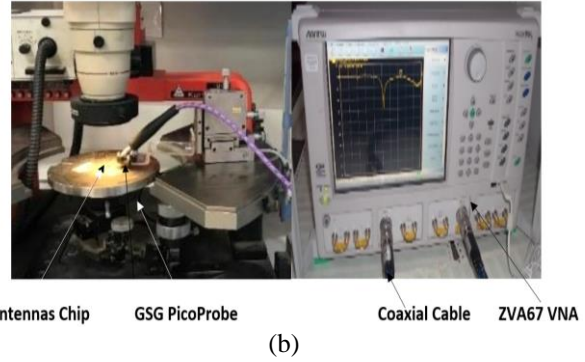
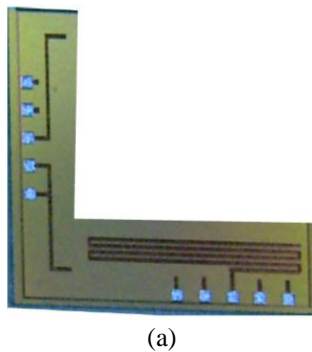


Fig. 6. (a) Photo of the fabricated antennas, and (b) the reflection coefficient measurement setup.

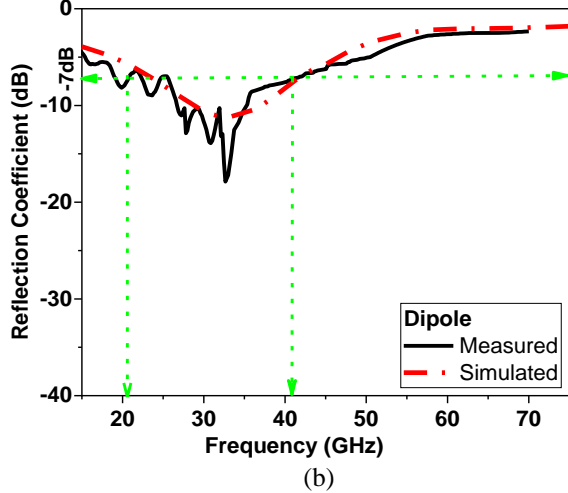
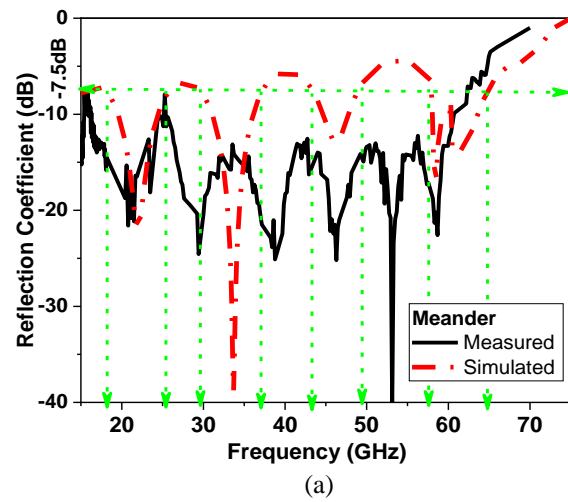
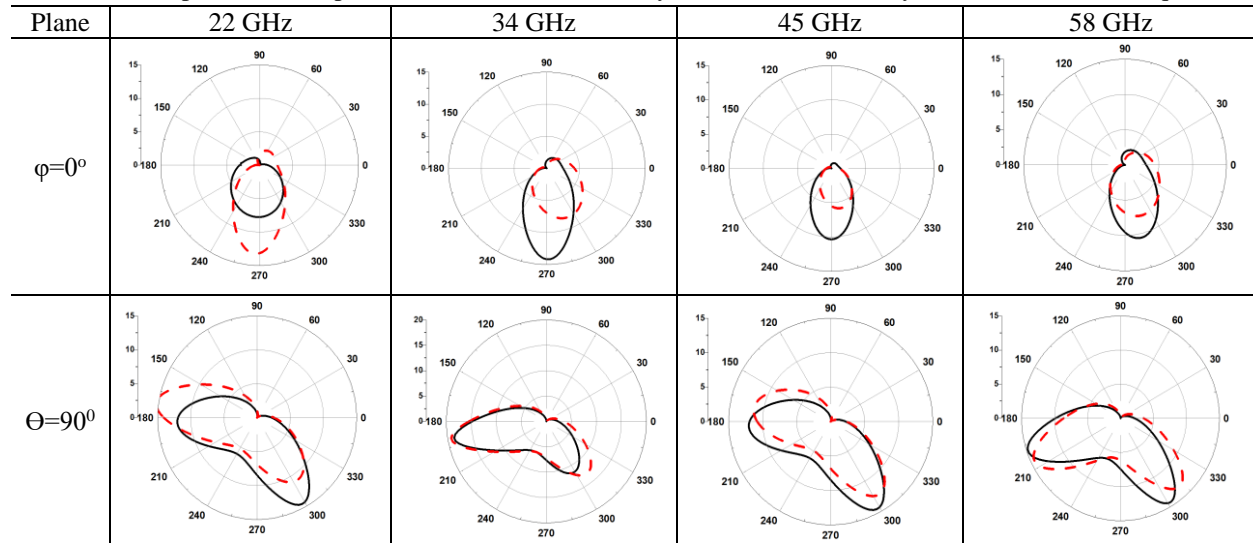
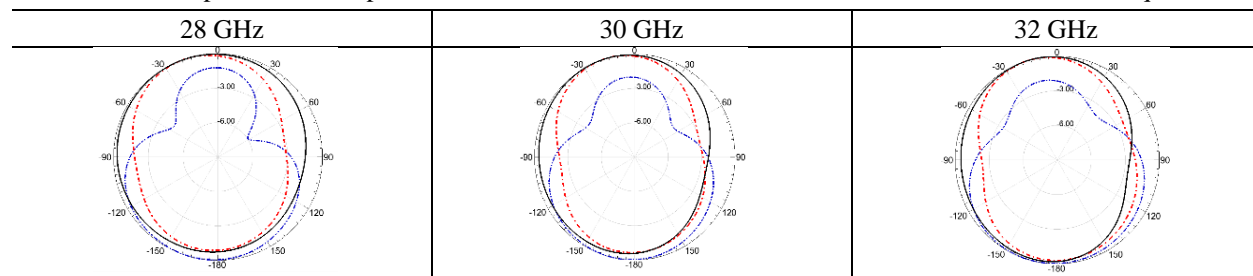


Fig. 7. Comparison of the proposed antennas measured and simulated of $|S_{11}|$: (a) DBMA and (b) WBDA antenna.

Table 1: The 2D polar radiation pattern — without human-body, - - - with human-body at different resonant frequencies

Table 2: THE 2D polar radiation pattern — $\Phi=0^\circ$, - - - $\Phi=90^\circ$, and - - - $\theta=90^\circ$ at different resonant frequencies

IV. HUMAN-BODY PHANTOM MODELING

To validate the performance of the proposed antennas for implantable applications, phantom model is used to simulate the implanted antenna and evaluate its performance to be used in-body environment. The specific absorption rate (SAR) is important factor that show that if these antennas are safe or not on the human body. SAR factor depend of the electrical field radiation and conductivity of the human tissues. According to IEEE standard it should be the SAR over 1g and 10 g of tissue of less than 1.6W/Kg and 2 W/Kg, respectively. Figure 8 shows the homogeneous multilayered model with a dimension of $80 \times 40 \times 63 \text{ mm}^3$ used to model human tissue [30]. The values of electrical properties are tuned around 40 GHz, the implanted depth in skin layer is 2 mm. inside the human body. The resonant frequencies are reduced and the operating bandwidths are broaden. The results as shown in Fig. 9 for both proposed antennas showed that when the human body effect is included in the simulation, the antenna impedance matching is more significant for the chip implanted. Moreover, the phase of the reflection coefficient was slightly changed when

the chip is placed outside a human body, and it was abruptly changed when the antenna was implanted in the human body. The changed results of the antenna performance are due to the conductivity of the human body, which adds extra load on the antenna surface and changes in the electrical properties of the substrate. However, when the chip is implanted in the human body, it became more dispersive and the operating bandwidths at -10dB ($\text{VSWR} \leq 2$) were extended from 20 GHz to 45 GHz and from 57 GHz up to 65 GHz as shown in Fig. 9. However, in both simulation scenarios, the antenna bandwidth still operated in the selected bands of operations. The packaging proposed antenna are done by light-weight polymer-based materials that are biocompatible, RF-transparent, easy-to-process, and low-cost. On the other side the embedded antennas have a peak broadside power density of -60 dBW/m^2 at a distance of 1 m. For an isotropic radiator with a transmit power of 1 W, the power density at a distance of 1 m is equal to -11 dB W/m^2 , and for the embedded patch with a gain of -50 dB the power density would be equal to -61 dB W/m^2 .

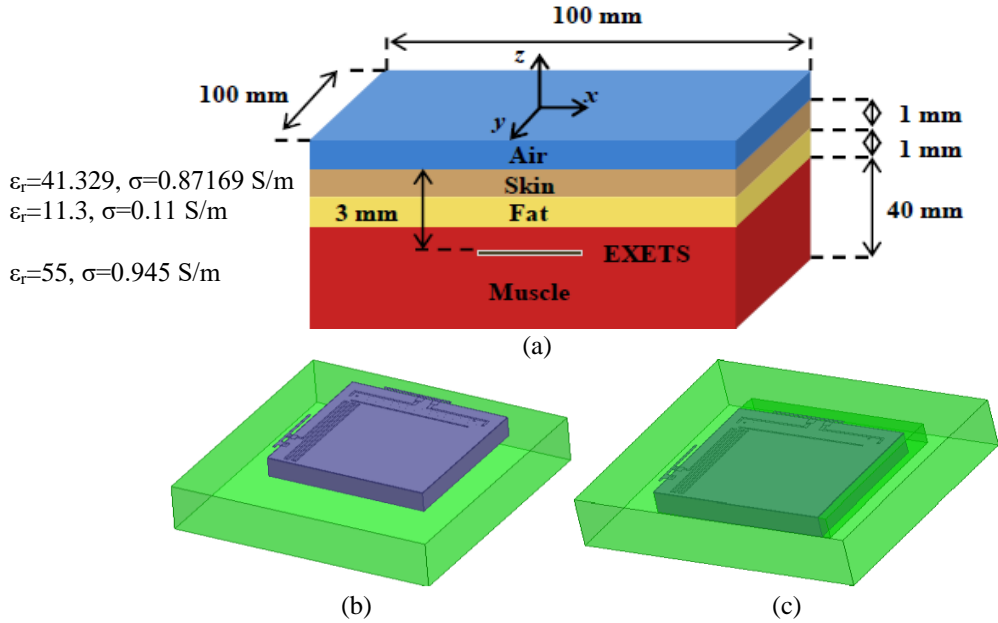


Fig. 8. (a) Simulation model of proposed antennas system, (b) outside the human phantom, and (c) inside the human phantom.

Table 3: Comparison of the proposed antenna with other on-chip antennas

Ref.	[15]	[16]	[17]	[18]	[19]	[20]	This work
Type	Dipole		Spiral Slot	Loop	Loop	Loop	Meander/Dipole
Freq	915 MHz	24/60 GHz	0.9 Ghz	60 Ghz	434 MHz	67GHz	22/ 34/ 44/58GHz. 26-34 GHz
Gain	-56 dB	-9/-1dB	-90dB	-3.2 dBi	16.45 dB	8dBi	-20/-15/-10/-1dBi
BW	26MHz	180/700MHZ	53%	5.5GHz	--	4GHz	5/6/4/8GHz
Area	2.52 mm ²	0.794 mm ²	0.385 mm ²	2.25 mm ²	2.56 mm ²	0.875mm ²	0.55 mm ²
Tech.	0.13μm CMOS	0.13μm CMOS	0.18 μm CMOS	0.18 μm CMOS	0.18 μm CMOS	0.18-μm CMOS	0.18-μm CMOS

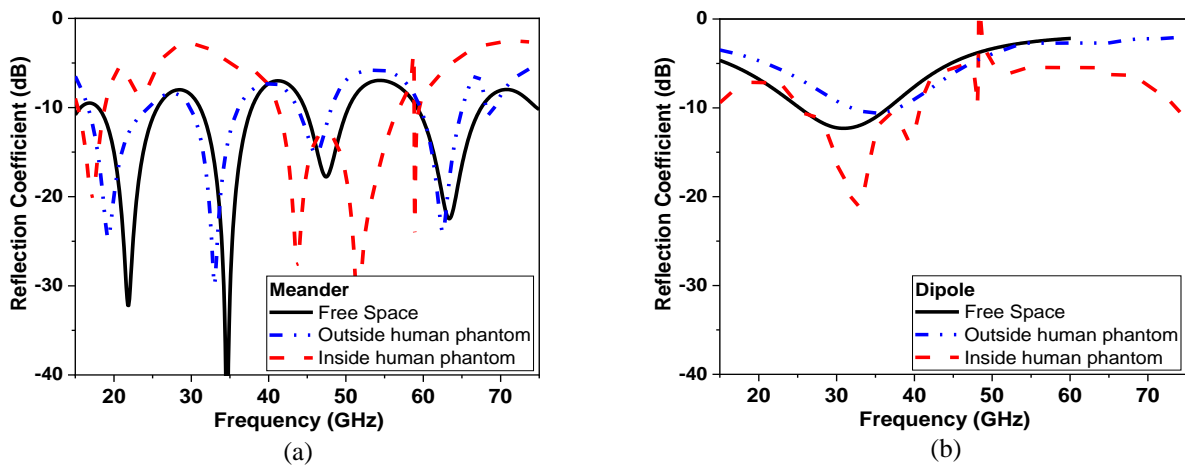


Fig. 9. Reflection coefficient versus frequency: (a) of the meander antenna and (b) of the dipole antenna.

The main drawback of such antennas design is the short communication range, which makes very hard reading process for the patient. As well as it is effect on the radiation efficiency due to the strong coupling of the near field components to the encapsulation of the antenna and electromagnetic absorption in the body tissues [30]. Which it could not to maintain a continuous communication link between the capsule and the external receiver. Table 3 tabulates different types of CMOS antennas operated at different frequencies; at high frequencies the gain is almost about -2 dB.

VI. CONCLUSION

This paper described two antennas integrated on the same- chip for implantable biomedical applications. Two separate antennas are designed with orthogonal polarization to ensure neglected mutual coupling between them. The first antenna (MBML) is used for data communication with multiple resonance frequencies at 22 GHz, 34 GHz, 44 GHz and 62 GHz.

The other antenna (WBDA) has a wideband from 28 GHz up to 36 GHz and used for RF Energy Harvesting. The antennas are fabricated using UMC 180nm CMOS technology with total area 0.55 mm². Measurements for both antennas - gain and bandwidth - are matched with design and simulation results. The proposed antennas are simulated using phantom model to check their compatibility for implantable devices.

REFERENCES

- [1] D. Elsheakh, H. Shawkey, and S. Saleh, "A 9 - 10.6 GHz microstrip antenna-UWB low noise with differential noise canceling technique for IoT applications," *Int. Journal of Communications, Network and System Sciences*, vol. 12, pp. 189, 2019.
- [2] R. Elyassi and G. Moradi, "Flexible and moon-shaped slot UWB implantable antenna design for head implants," *International Journal of Microwave and Wireless Technologies*, vol. 9, pp. 1559-1567, 2017.
- [3] A. Priya, S. K. Mohideen, and P. Thirumaraiselvanm, "Propagation losses of UWB antenna for on-body to in-body Signal Propagation," *Progress in Electromagnetics Research M*, vol. 73, pp. 101-109, 2018.
- [4] H. Shawkey and S. Saleh, "Low-power fully monolithic MICS band receiver for 402-405 MHz implantable devices," *International Journal of Electronics*, vol. 107, no. 1, pp. 28-45, 2020.
- [5] H. Shawkey and D. Elsheakh, "Multiband dual-meander line antenna for body-centric networks biomedical applications by using UMC 180 nm," *Electronics*, vol. 9, 1350, 2020.
- [6] T. Wu, T. S. Rappaport, and C. M. Collins, "The human body and millimeter-wave wireless communication systems: Interactions and implications," *IEEE International Conference on Communications (ICC)*, 2015.
- [7] M. Ali, H. Shawkey, A. Zekry, and M. Sawan, "One Mbps 1 nJ/b 3.5–4 GHz fully integrated FM-UWB transmitter for WBAN applications," *IEEE Trans. Circuits Syst. I: Regul.*, vol. 65, pp. 2005-2014, 2018.
- [8] C. Liu, Y. Guo, X. Liu, and S. Xiao "An integrated on-chip implantable antenna in 0.18 μ m CMOS technology for biomedical applications," *IEEE Transactions on Antennas and Propagation*, vol. 64, no. 3, Mar. 2016.
- [9] F. Gutierrez, Jr., S. Agarwal, K. Parrish, and T. S. Rappaport, "On-chip integrated antenna structures in CMOS for 60 GHz WPAN systems," *IEEE Journal on Selected Areas in Communications*, vol. 27, no. 8, Oct. 2009.
- [10] R. Yuwono and I. Mujahidin, "Rectifier using UWB microstrip antenna as electromagnetic energy harvester for GSM, CCTV and Wi-Fi transmitter," *Journal of Communications*, vol. 14, no. 11, Nov. 2019.
- [11] K. Celik and E. Kurt, "A novel super wideband circular fractal antenna for energy harvesting applications," *International Symposium on Advanced Electrical and Communication Technologies (ISAECT)*, 2019.
- [12] M. G. Tampouratzis, D. Vouyioukas, D. Stratakis, and T. Yioultsis "Use ultra-wideband discone rectenna for broadband RF energy harvesting applications," *Technologies Journal (MDPI)*, 2020.
- [13] V. Kuhn, C. Lahuec, F. Seguin, and C. Person, "A multi-band stacked RF energy harvester with RF-to-DC efficiency up to 84%," *IEEE Transaction on Microwave Theory and Techniques*, vol. 63, no. 5, May 2015.
- [14] J. Huang, J. Wu, Y. Chiou, and C. Jou, "A 24/60 GHz dual-band millimeter-wave on-chip monopole antenna fabricated with a 0.13- μ m CMOS technology," *In Proceedings of the IEEE International Workshop on Antenna Technology*, Santa Monica, CA, USA, Mar. 2-4, 2009.
- [15] A. A. Masius and Y. C. Wong, "On-chip miniaturized antenna in CMOS technology for biomedical implant," *International Journal of Electronics and Communications*, vol. 115, Feb. 2020.
- [16] Y. Song, Q. Xu, Y. Tian, J. Yang, Y. Wu, X. Tang, and K. Kang, "An on chip frequency-reconfigurable antenna for Q-band broadband applications," *IEEE Antennas Wireless Propagation Letters*, 2017.
- [17] H. Rahmani and A. Babakhani, "A dual-mode RF power harvesting system with an on-chip coil in 180-nm SOI CMOS for millimeter-sized

- biomedical implants,” *IEEE Transactions on Microwave Theory and Techniques*, vol. 67, no. 1, 2018.
- [18] Y. Song, Y. Wu, J. Yang, and K. Kang, “The design of a high gain on-chip antenna for SoC application,” *Advanced Materials and Processes for RF and THz Applications (IMWS-AMP), 2015 IEEE MTT-S International Microwave Workshop Series on*, Suzhou, pp. 1-3, 2015.
- [19] T. D. P. Perera, D. N. K. Jayakody, S. K. Sharma, S. Chatzinotas, and J. Li, “Simultaneous wireless information and power transfer (SWIPT): Recent advances and future challenges,” *IEEE Communications Surveys & Tutorials*, vol. 20, no. 1, 2018.
- [20] X. Peng and J. Li, “Harvested energy maximization of SWIPT system with popularity cache scheme in dense small cell networks,” *Hindawi Wireless Communications and Mobile Computing*, vol. 2019, 2019.
- [21] J. M. Felício, C. A. Fernandes, and J. R. Costa, “Wideband implantable antenna for body-area high data rate impulse radio communication,” *IEEE Transactions on Antennas and Propagation*, vol. 64, no. 5, May 2016.
- [22] I. El Masri, T. L. Gouguec, P. Martin, R. Allanic, and C. Quendo, “Integrated dipole antennas and propagation channel on silicon in Ka band for WiNoC applications,” *IEEE 22nd Workshop on Signal and Power Integrity (SPI)*, May 2018.
- [23] M. Nafe, A. Syed, and A. Shamim, “Gain-enhanced on-chip folded dipole antenna utilizing artificial magnetic conductor at 94 GHz,” *IEEE Antennas and Wireless Propagation Letters*, vol. 16, Sep. 2017.
- [24] R. S. Narde, J. Venkataraman, A. Ganguly, and I. Puchades, “Antenna arrays as millimeter-wave wireless interconnects in multi-chip systems,” *IEEE Antennas and Wireless Propagation Letters*, vol. 19, no. 11, Nov. 2020.
- [25] R. S. Narde, N. Mansoor, A. Gangul, and J. Venkataraman, “On-chip antennas for inter-chip wireless interconnections: Challenges and opportunities,” *12th European Conference on Antennas and Propagation (EuCAP)*, Apr. 2018.
- [26] M. S. Khan, F. A. Tahir, and H. M. Cheema, “Design of bowtie-slot on-chip antenna backed with E-shaped FSS at 94 GHz,” *10th European Conference on Antennas and Propagation*, June 2016.
- [27] S. Pan, L. Gilreath, P. Heydari, and F. Capolino, “An on-chip W-band bowtie slot antenna in silicon,” *Proceedings of the 2012 IEEE Int. Symposium on Antennas and Propagation*, Nov. 2012.
- [28] M. R. Karim, X. Yang, and M. F. Shafique, “On-chip antenna measurement: A survey of challenges and recent trends,” in *IEEE Access*, vol. 6, pp. 20320-20333, 2018.
- [29] Y. Zhang, C. Liu, X. Liu, and K. Zhang, “A miniaturized circularly polarized implantable RFID antenna for biomedical applications,” *International Journal of RF and Microwave Computer Aided Engineering*, Wiley Periodicals, Inc., Dec. 2019.
- [30] M. Caselli, M. Ronchi, and A. Boni, “Power management circuits for low-power RF energy harvesters,” *Journal of Low Power Electronics and Applications*, vol. 10, no. 29, pp. 1-17, 2020.



Dalia M. Elsheakh received the B.Sc., M.Sc. and Ph.D. degrees from Ain Shams University in 1998, 2005 and 2010, respectively. M.S. Thesis is on the Design of Microstrip PIFA for Mobile Handsets. Ph.D. Thesis is in Electromagnetic Band-Gap Structure. From 2010 to 2015, she was Assistant Prof. and from 2016 until 2019 she is Associate Prof. in Microstrip Dept., Electronics Research Institute. From 2019 until now she is the Head of Electronics and Communication Program in Faculty of Engineering and Technology, Badr University in Cairo. She was Assistant Researcher at Hawaii Center for advanced Communication (HCAC), College of Engineering, Hawaii University, USA at 2008 and Assistant Prof. at 2014 and 2018. Elsheakh has authored/co-authored four chapters in books. She has published 59 papers in peer-refereed journals and 50 papers in International Conferences. She is a member in many contracted projects (13 research and development project) funded from many funding agencies such as ASRT, NTRA, NSF, STDF, etc. She has three patents. She is an IEEE senior member from 2019.



Somaya I. Kayed is an Associate Professor and Head of the Electrical Dept. (Electronics, Communication, Computer and Control Engineering) at Oubor Higher Institute for Engineering and Technology. She graduated in 1987 from Ain Shams University with a B.Sc. in Electronics and Communications Department, with general grade (very Good). She finished her Masters of Science (M.Sc.) and Ph.D. from Ain Shams University at 1995 and 2000 respectively. She was an Acting Dean for the 2019 first term at Oubor Higher Institute for Engineering and Technology. Her related research interests (Analog

and digital VLSI design, current conveyor, nano-electronics).



Heba A. Shawkey received her B.Sc. and M.Sc. in Electrical Engineering, in 1993 and 2000, respectively, with honor degree from Ain Shams University-Egypt and her Ph.D. degree in 2005 from the Cairo University-Egypt. Heba has been working in Electronics Research

Institute since 1994 and her main research interests are wireless communication systems design, analog/mixed-signal/RF circuits, especially high speed PLL and frequency synthesizers. She also has many publications in low power digital circuit design, biomedical sensors read-out circuits, interconnect modeling and low power networks on chip (NoC). Now Heba is a member in nanotechnology lab and working in the field of nanomaterial electronics applications as graphene and CNT.

A Low-Profile and Beam-tilted Continuous Transverse Stub Array Antenna at W-band

Demiao Chu, Yujun Xiong, and Ping Li

School of Optical-Electrical and Computer Engineering
University of Shanghai for Science and Technology, Shanghai, 200093, China
liping@usst.edu.cn

Abstract — This paper presents a low-profile, high gain, beam-tilted continuous transverse stub (CTS) array antenna at W-band. The antenna comprises 32 radiating slots and is fed by a parallel plate waveguide (PPW) network with a linear source generator. To deflect the outgoing beam, the principle of linear array scanning is adopted to design inverted T-type structure in each stub to introduce wave path difference. PPW network allows the antenna to obtain lower profile compared to other transmission lines. The design procedure, and the antenna characterization are described. The main beam of the antenna is tilted 12 degree in H-plane. The simulation and measured results show that this antenna achieves peak gain of 32.4 dB and a 12 degree beam tilt angle at 99GHz. S11 parameters of the antenna is less than -10 dB in a broadband from 96 GHz to 103 GHz. This antenna has an advantage of miniaturization over other high-gain antenna solutions. The promising performance of this proposed CTS antenna reveals the possible candidate for Millimeter wave (MMW) telecommunication applications.

Index Terms — CTS array antenna, pillbox, W band.

I. INTRODUCTION

Millimeter wave (MMW) technology is becoming increasingly attractive in the future of telecommunications. Stringent requirements are imposed on the antennas which not only need high gain but also require a tilted beam. We can refer to several solutions to try to satisfy these previous requirements such as classical parabolic systems and electromechanical scanning planar antenna arrays [1]. However, the parabolic systems are bulky, and its size is too big to flexibly move on the platform, while the high requirements manufacturing precision of electromechanical scanning planar antenna arrays leads to high cost [2,3]. Therefore, it is necessary to study a miniaturized, low-cost MMW antenna with high gain and tilted beam.

Due to the attractive performance and manufacturing stability, Continuous Transverse Stub (CTS) array antennas can be considered as good candidates for

advanced antenna systems. The profile of CTS array antennas can be reduced at lower cost and radiation performance could be improved [4]. The CTS array antenna was first proposed in the early 1990s [5-8], which is evolved from the parallel-plate waveguide. In 1998, Chu of EMS Lab used the Floquet mode method [9] to analyze the radiation theory of CTS array antenna and perfect its basic theories. The main structure of a CTS array antenna is a one-dimensional (1-D) array of parallel-plate waveguide with parallel lateral openings. The electromagnetic waves are radiated from the parallel-plate waveguide and the impedance can be optimized by adding series of stubs. Over the past two decades, the CTS array antenna has evolved many types and been applied in various fields, such as True-Time-Delay (TTD) CTS and Multi-channel Video and Data Distribution Service (MVDDS), etc. [10]. Moreover, the increasing number of stubs can enlarge the antenna gain. In such a way, CTS array antennas have the ability to improve performance in high gain and broadband conditions. On the other hand, the increasing demand for satellite telecommunications and radar applications stimulate the increasing development of waveguide-based CTS array antenna, such as coaxial-waveguide type [11,12], coplanar-waveguide type [13,14] and rectangular-waveguide type [15]. However, those CTS antennas in conventional configurations adopt normal radiation. That is, when there needs an azimuth angle-between the antenna's normal direction and the target, a tilted beam that deviates from the normal direction of the antenna plane would be required.

Motivated to design a low-profile and beam-tilted CTS array antenna at W-band, a 32-slot CTS array antenna and 12 degree beam deflection angle working in the frequency band of 96-103 GHz is proposed. The antenna is fed by a pillbox, whose structure has a lower profile compared to the multiplexed power split structure. The impedance transformers in the design are introduced not only for the feeding network, but also for the radiation stubs. This method can optimize the return loss, reduce the size of the entire antenna and improve the antenna efficiency through structure and parameter

optimization. The radiating stubs of 32 slots are adjusted which are based on the principle of linear array scanning to contain an inverted T-type structure for realizing an azimuth-angle inclination. The final thickness of the antenna is 30 mm and can be further reduced by dielectric filled (parallel plate waveguide) PPW feeding network. Measurements of antenna performance are very promising and reveal the possibilities of CTS array offers for MMW communication applications.

II. ANTENNA DESIGN

Among all antenna structures, CTS array antennas are very different from other types of planar array antennas in the field of radiating realization, coupling mechanism, transmission-line properties, and feeding network [15]. Figure 1 illustrates a typical CTS array antenna structure, realized by a wide and continuous array of short transverse radiating stubs. CTS array antenna is of limited height, extending from the upper conductive plate of an open parallel plate transmission structure, internally excited by a linear source. These stubs interrupt the longitudinal current component within the parallel plate transmission structure and effectively couple and radiate propagating energy from the parallel plate structure into free space as a linearly polarized wave.

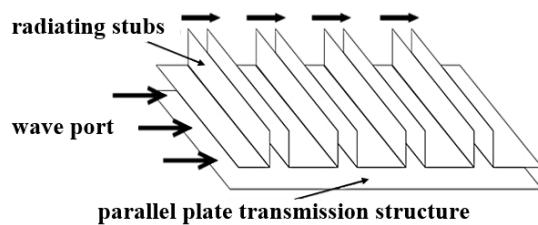


Fig. 1. Typical cross-sectional view of a CTS array.

In order to achieve a low-profile and high-gain CTS array antenna with an angle of beam inclination, the number of radiating stubs required is significant, all parts of the antenna need to be simulated and tolerance analysis according to principle of phased array beam control [16]. As shown in Fig. 2 (a), the CTS array antenna proposed in this paper consists of two main parts: The CTS array (CTS radiation stubs and parallel plate waveguide network) and a linear source generator. The CTS array contains 32 radiating stubs which are connected to the end of the power divider, the pillbox structure effectively reduces the overall height of the antenna by using an embedded two-dimensional (2-D) parabolic reflector. The beam emitted by the CTS array antenna is at a fixed declination to the antenna's normal direction, the application scenario rendering of the CTS antenna proposed in this paper is shown in Fig. 2 (b). Details of the CTS array antenna proposed in this paper are shown in Fig. 2 (a), inverted T-type structure is the

reason for the tilted beam of the antenna. The overall size of the CTS array antenna is 60mm * 60mm * 30mm, which mainly comprises the CTS array and the linear source generator.

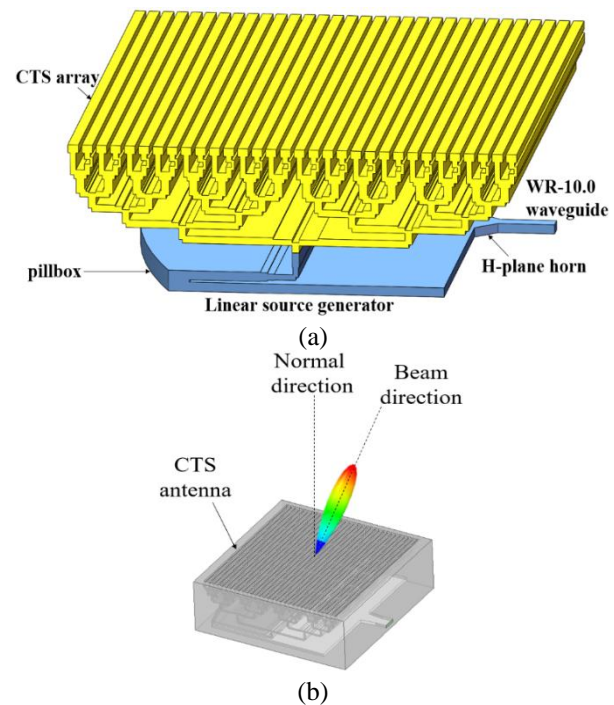


Fig. 2. Perspective view of the CTS array antenna: (a) Front view and (b) application scenario rendering.

A. The CTS array

As shown in Fig. 3, the CTS radiating stubs which are composed of 32 sections attach to the parallel plate waveguide network. The reflection coefficient of the radiation stubs depends on the width of stub (a), the array spacing (d) and dielectric constant of filled material within an operational frequency range. In order to achieve a good impedance match for broadband transmission, the radiating stubs are fed with the same amplitude and phase by the parallel plate waveguide network which consists of a parallel 1-to-32 power divider [17].

The beam inclination angle can be achieved by using an inverted T-type structure [18]. In such a way, the inverted T-type structure in this paper has been designed to steer the antenna beam to 12 degree in the azimuth plane. Phased array scanning and positioning are used here. For phase-controlled scanning of the beam in space, each radial array element is connected to a variable phase shifter. Inverted T-structure creates a wave path-difference between adjacent radiating stubs.

In the direction of deviation from the antenna normal to θ degree, the phase difference between the two adjacent array elements:

$$\Phi_B = 2\pi d \sin\theta / \lambda, \quad (1)$$

where d is the width of two adjacent periodic stubs, λ is the wavelength at the center frequency. It is caused by the wave path-difference of the target echo. Due to the nonzero phase difference between the array elements, the antenna normal direction of each array element of the radiation field strength cannot be summed, such that the antenna normal direction is no longer the direction of the largest field strength. In the direction of deviation from the antenna normal to θ degree, the maximum value is obtained by adding the field strengths in the same phase, and the beam direction changes from the array normal to the direction of deviation from the antenna normal to θ degree. By changing the phase difference Φ_B between neighboring cells in the array, we can have a titled beam at θ , which can change the direction of the antenna beam. Then, the wave path-difference can be calculated as:

$$d\tau = d\sin\theta. \tag{2}$$

This will give the wave path-difference as needed.

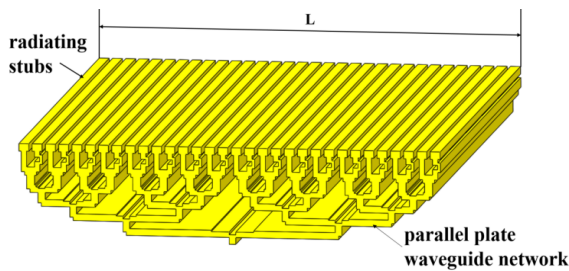


Fig. 3. Perspective view of the CTS array.

As shown in Fig. 4, every node of the parallel plate waveguide network is composed of an E-plane T-section and a multi-stage matching step. A multi-stage matching step based on Chebyshev impedance transformation theory [19] is designed, and the final size is determined in accordance with simulation and optimization.

The final array consists of 32 radiating stubs, and the original array spacing is set as $\lambda/2$ (λ is the wavelength at the center frequency). The center frequency of the design is 99 GHz (corresponds to a wavelength of 3mm in vacuum). The dimensions of stubs is illustrated in Fig. 5 (a). By setting $f_c=99$ GHz, the stub width $a < a_{max} = \lambda/2 = 1.502$ mm. On the other hand, as discussed in [19], for a given width of two adjacent periodic stubs d , the real part of the active slot impedance Z_{act} in the H-plane of a CTS array increases when a decreases. The active slot impedance of an infinite CTS array with this value for $(d+a)$ has been computed for different slot widths, approaching its upper bound of $(d+a_{max})$, by using the numerical model presented in [19]. Each active impedance is normalized with respect to the characteristic impedance $Z_0 = \eta a/\omega$ of a PPW line having its height equal to the slot width a and a unitary length ω , where η is the free-space impedance. Bringing back to the numerical model presented in [19], calculation results demonstrate that for $(d+a) = 1.5$ mm, the imaginary part

of the slot active impedance experiences limited variations and in low resistance. Therefore, the stub width a is set as $0.66a_{max} = 1$ mm and $d = 0.5$ mm. According to the mathematical model used to calculate d , the wavelength difference between two adjacent radiating stubs $d\tau$ is set to 0.104mm. As shown in Fig. 5 (a), after analysis of the simulation results, the best impedance matching is achieved when the inverted T-type structure is set at 0.76mm from the top of the radiating stubs and the length is 0.64mm. The equivalent circuit diagram of the end of the radiating branch with the inverted T-type structure added is shown in Fig. 5 (b). Phase difference between adjacent radiating stubs at the Y-port due to the difference in signal transmission distance

As shown in Fig. 5 (c), the E-plane T-section is a classical power divider in PPW technology associating to a quarter wavelength transformer, so the input and output ports have the same characteristic impedance and width (0.7 mm). The quarter-wavelength transformer of width 0.5 mm is used to halve the impedance value at the output ports before joining the section with width 0.36 mm.

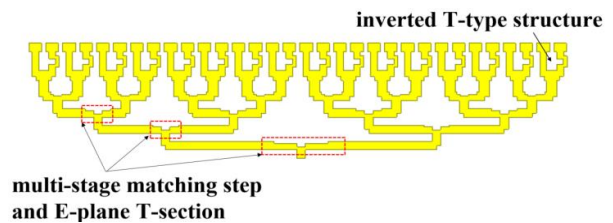


Fig. 4. Cross-section view of the CTS array.

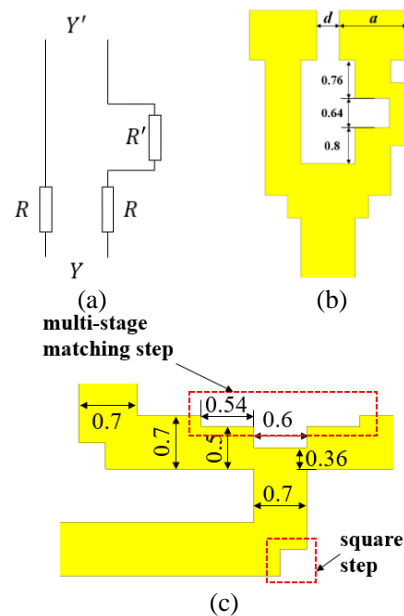


Fig. 5. E-plane cross-sectional view: (a) inverted T-type structure; (b) inverted T-type structure's equivalent circuit; (c) E-plane T-section. All dimensions are given in millimeters.

B. Linear source generator

The selection of feeding network is crucial. Existing feeding network contains a combination of a power divider and a radiator, pillbox, lens array, etc. [20]. There are two combinations (vertical and horizontal methods) to connect a power divider to a radiator. The horizontal method allows for lower profile compared with the vertical one, but both approaches are difficult to be used in a broadband application for the complexity and bandwidth limitation of the power divider. The attractive characteristics of pillbox are low-cost, compactness and miniaturization [21]. In order to achieve low profile and low cost, a pillbox is used in this paper. In the pillbox, various modes exist between the two plates according to the distance between parallel plates [22]. The pillbox supports free propagation of a principal wave (TEM-mode) in which the electric vector is normal to the plates, and the velocity of propagation and the wavelength are the same as in free space. TE and TM modes are also possible in a pillbox, which correspond to the modes in a rectangular waveguide [23].

As shown in Fig. 6, the linear source generator consists of a pillbox and an H-plane horn. The pillbox generates a linear source to excite the parallel plate waveguide network. The H-plane horn is fed by a standard WR-10.0 waveguide. The horn is located in the focal plane of the 2-D parabolic reflector. The H-plane horn and the pillbox are placed in the parallel plate waveguides and are same in height. Figure 7 shows a top view and a cross-sectional view of the linear source generator. It is made by two stacked PPW lines and a long slot with a width of 2.3 mm coupled through a spherical crown. The 2-D parabolic reflector in the common metal plate is contoured between the two PPW lines with the distance of 0.51 mm. As Fig. 7 (a) shows, the pillbox couplers designed here have the following parameters: the diameter of the pillbox length, denoted as D , the focal length of the parabola, denoted as F , the focal horn aperture as shown in Fig. 6. To match the parallel plate waveguide network, the diameter D is equal to length L (shown in Fig. 3) of the CTS radiating stubs. Once the parabola diameter has been selected, the focal length F and the focal horn aperture are to be chosen together [24]. In this work, we set the diameter $D=19.8\lambda=60\text{mm}$ and the focal length $F=15.2\lambda=46\text{mm}$ together with a horn width of 10.32 mm. Finally, a 90 degree bend with a stair-step height of 0.46mm connects the pillbox transition to the input port of the corporate-feed network after a three-layer decreasing rectangular waveguide structure. The three-layer decreasing rectangular waveguide structure can filter out high sub-modes in the structure.

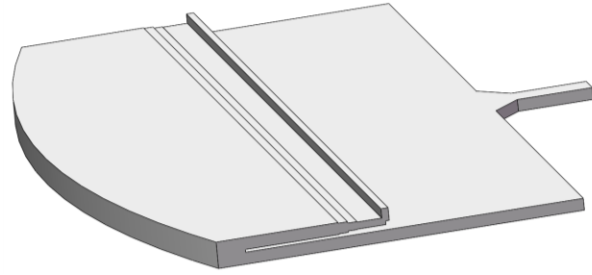


Fig. 6. 3-D view of the linear source generator.

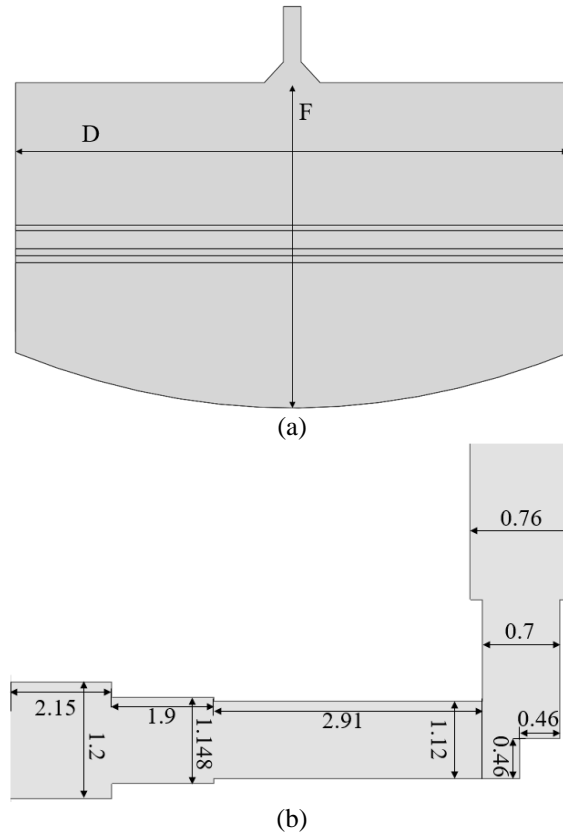


Fig. 7. (a) Top view and (b) cross-sectional view of the linear source generator. All dimensions are given in millimeters.

III. RESULT

The designed CTS array antenna was simulated by ANSYS Electronics Desktop HFSS 19.0. Based on the parameter optimization of CTS radiation stubs and waveguide feeding network, the results meet the design requirement of antenna.

The antenna in this paper is realized by gold-plated copper. An efficient method based on separate module

fabrication and screw assembly is used to simplify the fabrication process. The standard method of manufacturing hollow the CTS array and the pillbox relies on an expensive joining or brazing process and connecting the pillbox to the CTS array. The processed antenna is shown in the Fig. 8.

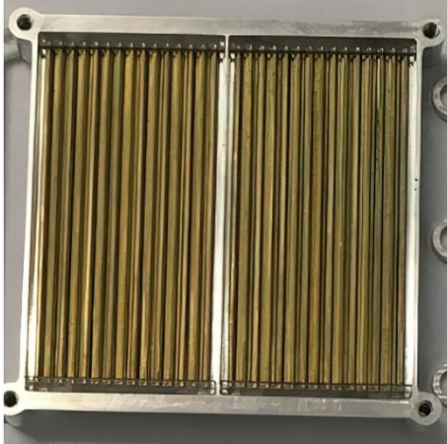


Fig. 8. Top view of antenna prototype.

The S-parameters and directional maps of the processed antenna are measured and also are compared with the simulation results. We use the Agilent N5227A PNA network analyzer and a set of WR-10 (75–110 GHz) VNA extenders to characterize the device transmission and using the method of rotating the antenna to test antenna pattern. The good agreement between the simulation and measurement is shown as following. Figure 9 (a) shows the simulation and measured results of the antenna reflection coefficient. The operating frequency band is 96 GHz to 103 GHz (relative working bandwidth: 7%), and the reflection coefficient is less than -10 dB in available frequency band. Fig. 9 (b) shows the simulation and measured results of the gain in E-plane at 99 GHz. The pattern shows that the gain is 32.5 dB at 99 GHz and normalized side lobe level is less than -12dB. The azimuth of the beam is 12 degree and the HPBW is 2.56 degree. We can see from the measured result that there is a peak gain of 31.6 dB at the center frequency of 99 GHz, the normalized side lobe level is less than -12dB. The gain of this antenna is over than 30 dB in the frequency range of 96-103 GHz. The beam has a deflection angle of approximately 12 degree. HPBW of this antenna is about 2.4degree. The measured peak gain is slightly lower than that in the simulation. The small difference may be attributed by the assembly error and the fabrication tolerance.

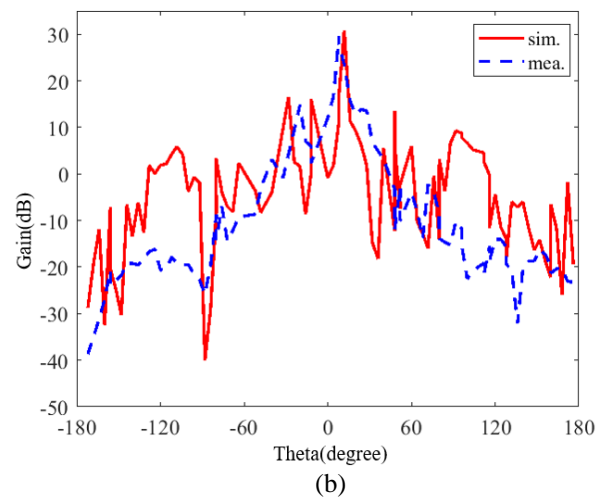
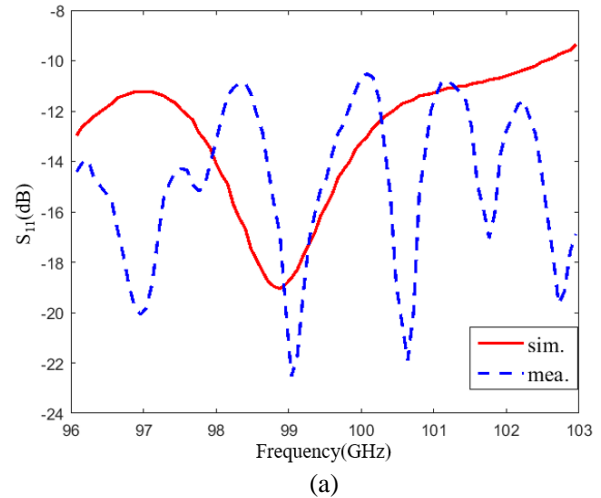


Fig. 9. (a) Simulated and measured S_{11} parameters of the CTS antenna. (b) Simulated and measured radiation patterns at the frequency of 99 GHz.

IV. CONCLUSION

This paper presents a CTS array antenna with low profile, high gain, high efficiency and 12 degree beam deflection angle. This antenna consists of CTS array (CTS radiation stubs and parallel plate waveguide network) and a linear source generator, which can be independently designed and optimized. We change the radiating stubs by the inverted T-type structure to realize an azimuth angle of inclination. This CTS antenna utilizes multistage impedance converter to increase radiation efficiency and achieve a higher gain and lower side lobe in feeding network and radiation components compared with other CTS antennas. And the pillbox structure of the linear source generator is also used to

implement this low-profile CTS array antennas. It has been demonstrated that the structure can be an attractive candidate for the through-the-wall detection system based on terahertz technology.

ACKNOWLEDGMENT

This work was supported in part by the National Key R&D Program of China (2018YFF01013003), in part by the National Natural Science Foundation of China (61731020, 61722111).

REFERENCES

- [1] Y. Asci, E. Curuk, K. Yegin, and C. Ozdemir, "Improved splash-plate feed parabolic reflector antenna for Ka-band VSAT applications," *2016 46th European Microwave Conference (EuMC)*, London, pp. 1283-1286, 2016.
- [2] M. Tripodi, F. Dimarca, T. Cadili, C. Mollura, F. Dimaggio, and M. Russo, "Ka-band active phased array antenna system for satellite communication on the move terminal," *2012 IEEE First AESS European Conference on Satellite Telecommunications (ESTEL)*, Rome, pp. 1-4, 2012.
- [3] M. Shelley, J. Vazquez, and D. Moore, "X- and Ka-band low profile antennas for aeronautical and land mobile satcom," *The 8th European Conference on Antennas and Propagation (EuCAP 2014)*, New York, pp. 2619-2622, 2014.
- [4] W. W. Milroy, "Continuous transverse stub element devices and methods of making same," U.S. Patent No. 5,266,961, Nov. 30, 1993.
- [5] W. W. Milroy, "Antenna array configurations employing continuous transverse stub elements," U.S. Patent No. 5,349,363, Sep. 20, 1994.
- [6] W. W. Milroy, "Continuous transverse stub element device antenna array configurations," U.S. Patent No. 5,412,394, May 2, 1995.
- [7] W. W. Milroy, "Continuous transverse stub element devices for flat plate antenna arrays," U.S. Patent No. 5,483,248, Jan. 9, 1996.
- [8] W. W. Milroy, "Radar and electronic warfare systems employing continuous transverse stub array antennas," U.S. Patent No. 5,469,165, Nov. 21, 1995.
- [9] R.-S. Chu, "Analysis of continuous transverse stub (CTS) array by floquet mode method," *IEEE Antennas and Propagation Society International Symposium*, Atlanta, pp. 1012-1015, 1998.
- [10] W. H. Henderson and W. W. Milroy, "Wireless communication applications of the continuous transverse stub (CTS) array at microwave and millimeter wave frequencies," *IEEE/ACES International Conference on Wireless Communications and Applied Computational Electromagnetics*, Honolulu, pp. 253-256, 2005.
- [11] M. F. Iskander, Z. Zhang, Z. Yun, and R. Isom, "Coaxial continuous transverse stub (CTS) array," *IEEE Microwave and Wireless Components Letters*, vol. 11, no. 12, pp. 489-491, Dec. 2001.
- [12] J. Qiu, X. Xing, and L. Zhong, "A novel coaxial CTS antenna design," *2007 6th International Conference on Antenna Theory and Techniques*, Sevastopol, pp. 323-325, 2007.
- [13] W. Kim and M. F. Iskander, "A new coplanar waveguide continuous transverse stub (CPW-CTS) antenna for wireless communications," *IEEE Antennas and Wireless Propagation Letters*, vol. 4, pp. 172-174, 2005.
- [14] L. Yue, M. F. Iskander, Z. Zhang, and Z. Feng, "A phased CPW-CTS array with reconfigurable NRI phase shifter for beam steering application," *2013 IEEE International Wireless Symposium (IWS)*, Beijing, pp. 1-3, 2013.
- [15] X. Pan, F. Yang, S. Xu, and M. Li, "W-band electronic focus-scanning by a reconfigurable transmitarray for millimeter-wave imaging applications," *Applied Computational Electromagnetics Society Journal*, vol. 35, no. 5, pp. 580-586, May 2020.
- [16] N. Seman, K. H. Yusof, and M. H. Jamaluddin, "Ultra-wideband six-port network constructed by 90° and in-phase power dividers," *Applied Computational Electromagnetics Society Journal*, vol. 34, no. 5, pp. 689-695, May 2019.
- [17] S. X. Ta, C. D. Bui, and T. K. Nguyen, "Wideband Quasi-Yagi antenna with broad-beam dual-polarized radiation for indoor access points," *Applied Computational Electromagnetics Society Journal*, vol. 34, no. 5, pp. 654-660, May 2019.
- [18] T. Potelon, M. Ettorre, L. L. Coq, T. Bateman, J. Francey, D. Lelaidier, E. Seguenot, F. Devillers, and R. Sauleau, "A low-profile broadband 32-slot continuous transverse stub array for backhaul applications in E-Band," *IEEE Transactions on Antennas and Propagation*, vol. 65, no. 12, pp. 6307-6316, Dec. 2017.
- [19] F. F. Manzillo, M. Ettorre, M. Casaletti, N. Capet, and R. Sauleau, "Active impedance of infinite parallel-fed continuous transverse stub arrays," *IEEE Trans. Antennas Propag.*, vol. 63, no. 7, pp. 3291-3297, July 2015.
- [20] P. Zhang, R. Mittra, and S. Gong, "Compact line source generator for low profile continuous transverse stub array antenna," *2016 International Workshop on Antenna Technology (iWAT)*, Cocoa Beach, pp. 77-79, 2016.
- [21] K. Tekkouk, M. Ettorre, E. Gandini, and R. Sauleau, "Multibeam pillbox antenna with low sidelobe level and high-beam crossover in SIW technology using the split aperture decoupling method," *IEEE Transactions on Antennas & Propagation*, vol. 63, no. 11, pp. 5209-5215, Nov.

- 2015.
- [22] E. L. Holzman, "Pillbox antenna design for millimeter-wave basestation applications," *IEEE Antennas and Propagation Magazine*, vol. 45, no. 1, pp. 27-37, Mar. 2003.
- [23] K. S. Feng, H. T. Qin, L. Na, Z. X. Liu, and J. Li, "A novel bow-tie feed for dual-layer pillbox antenna," *2014 IEEE International Conference on Signal Processing, Communications and Computing (ICSPCC)*, Guilin, pp. 663-666, 2014.
- [24] L. Chen, D. Liao, X. Guo, J. Zhao, Y. Zhu, and S. Zhuang, "Terahertz time-domain spectroscopy and micro-cavity components for probing samples: A review," *Frontiers of Information Technology & Electronic Engineering*, vol. 20, no. 5, pp. 591-607, May 2019.



Demiao Chu received the B.S. degree in Optoelectronic Information Science and Engineering from the Chizhou University, Chizhou, China, in 2019. He is currently working toward the M.S. degree in Optical Engineering at the University of Shanghai for Science and Technology, Shanghai, China. His research interests include millimeterwave and THz imaging technology, especially THz synthetic-aperture radar (SAR) and Cylinder imaging algorithm.



Yujun Xiong is currently working toward the M.S. degree in Optical Engineering at the University of Shanghai for Science and Technology, Shanghai, China. His research interests include microwave transmission line and antenna, especially front-end transmission network for MIMO imaging systems and high gain antenna design in terahertz non-destructive testing.



Ping Li received the Ph.D. degree from the Northwestern Polytechnical University, Xi'an, China, in 2006. She is currently a Researcher with the University of Shanghai for Science and Technology, Shanghai, China. Her research interests include millimeter-wave and terahertz-wave technology, especially with the Terahertz imaging system.

Design of W-band PIN Diode SPDT Switch with Low Loss

Yun Jiang¹, Yuan Ye¹, Daotong Li², Zhaoyu Huang¹, Chao Wang^{1,*}, Jingjian Huang¹,
and Naichang Yuan¹

¹ State Key Laboratory of Complex Electromagnetic Environment Effects on Electronics and Information System
College of Electronic Science, National University of Defense Technology, Changsha, 410073, China

² Center of Communication and Tracking Telemetry Command, Chongqing University, Chongqing, 400000, China
*sywangc@163.com

Abstract — A W-band PIN diode single pole double throw (SPDT) switch with low insertion loss (IL) was successfully developed using a hybrid integration circuit (HIC) of microstrip and coplanar waveguide (CPW) in this paper. In order to achieve low loss of the SPDT switch, the beam-lead PIN diode 3D simulation model was accurately established in Ansys High Frequency Structure Simulator (HFSS) and the W-band H-plane waveguide-microstrip transition was realized based on the principle of the magnetic field coupling. The key of the proposed method is to design the H-plane waveguide-microstrip transition, it not only realizes the low IL of the SPDT switch, but also the direct current (DC) bias of the PIN diode can be better grounded. In order to validate the proposed design method, a W-band PIN diode SPDT switch is fabricated and measured. The measurement results show that the IL of the SPDT switch is less than 2 dB in the frequency range of 85 to 95 GHz, while the isolation of the SPDT switch is greater than 15 dB in the frequency range of 89.5 to 94 GHz. In the frequency range of 92 to 93 GHz, the IL of the SPDT switch is less than 1.65 dB, and its isolation is higher than 22 dB. Switch rise time and switch fall time of the SPDT switch are smaller than 29ns and 19ns, respectively. Good agreement between the simulations and measurements validates the design method.

Index Terms — Insertion loss, isolation, PIN diode, SPDT switch, switch fall time, switch rise time, W-band, waveguide-microstrip transition.

I. INTRODUCTION

Driven by wide applications, such as the radio astronomy, radar system, 5G and 6G communication, there has been an increasing interest in developing the SPDT switch working at W-band (75-110 GHz) or high frequency band [1-5]. According to different design processes, the commonly used switches in the W-band include HIC switches [6-8], monolithic microwave integrated circuit (MMIC) switches [9-12], and micro-electromechanical system (MEMS) switches [13-17]. The W-band MMIC switches and MEMS switches technology

can realize wide bandwidth and good consistency, but the high loss, low power capacity, difficult processing and complex manufactures are inevitable. The HIC switches were considered as an expedient choice, which is suitable for low ILs, high power capacity, low-cost and mass production. However, the traditional hybrid integrated PIN diode switches are designed based on the principle of the electric field coupling. There are two commonly used methods, one is to use the fin line structure combined with the accurate PIN diode 3D simulation model to design the W-band switch [6], and the other is to use a microstrip line structure [8]. The switch of the fin line structure can achieve good DC bias grounding, but the relatively larger size, high ILs and difficult integrated with other devices are inevitable [7]. At the same time, the switch of the traditional microstrip line structure is easy to integrate with other millimeter wave devices. However, an external DC bias grounding structure is required, which will increase the ILs and size of the switch [8].

With the development of millimeter wave communication, the W-band SPDT switch with high power handling capability, low ILs and low-cost becomes indispensable. In this paper, an accurate PIN diode simulation model is established in Ansys HFSS. A W-band SPDT switch with compact structure, low loss and easy DC bias grounding was designed by using microstrip and CPW structure combined with accurate PIN diode simulation model. The W-band SPDT switch is fabricated, whose simulated and measured results are in good agreement. In the frequency range of 85 to 95 GHz, the IL of the SPDT switch is less than 2 dB, and its isolation is higher than 13 dB.

II. SWITCH STRUCTURE AND DESIGN

Figure 1 shows the schematic diagram of the proposed W-band SPDT switch, which can be seen as composing of two single pole single throw (SPST) circuits. The switches are divided into parallel switch and series switch according to the connection mode of the PIN diode. In this paper, in order to reduce the IL of the SPDT switch, the two PIN diodes are connected in

parallel with the microstrip line at the expense of the switch isolation. As shown in Fig. 1, the D_1 and D_2 are the PIN diode. At the same time, the lengths of L_1 and L_2 equal to quarter wavelength are adopted. As we all know, when the PIN diode is turned on, it exhibits low resistance characteristics, which can be equivalent to a short circuit. The PIN diode is reverse biased, it exhibits high resistance characteristics, which can be equivalent to an open circuit. The impedance characteristics of the PIN diode under different DC biases are used to design the SPDT switch, and then it is matched or mismatched at the millimeter wave input to control the signal on or off [18]. Considering the application of the SPDT switch, the port 1 is adopted the standard wave port WR10, and both of the port 2 and port 3 are matched to 50Ω .

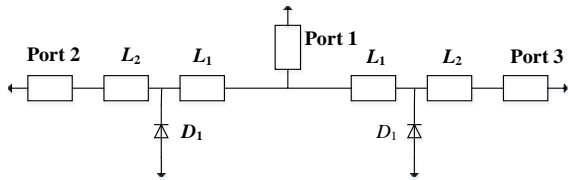


Fig. 1. Schematic of the W-band SPDT switch.

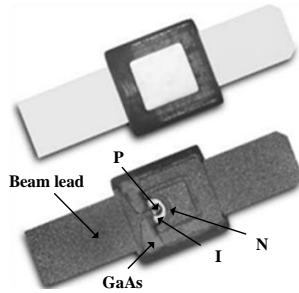


Fig. 2. The physical photo of the PIN diode.

In order to satisfy the needs of different frequencies and designs, the PIN diodes are available in various packaging forms. According to the W-band radar front-end requirements for SPDT switch IL, power capacity, isolation, volume, etc., the selected beam-led PIN diode was fabricated by Skyworks using GaAs technology. The physical photo of the PIN diode is shown in Fig. 2. The PIN diode size is $0.31\text{ mm} \times 0.28\text{ mm} \times 0.05\text{ mm}$ (length \times width \times thickness), which is not include the size of the beam lead. The basic parameters of the diode given by the manufacturer are shown in Table 1.

Table 1: The basic parameters of the diode

Reverse Voltage (V)	Max Total Capacitance (10V, 1MHz) (pF)	Max Series Resistance (10mA, 100MHz) (Ω)	Switch Time ($I_F=10\text{mA}$) (ns)
60	0.025	3.5	25

From the SPICE provided by the manufacturer, it is impossible to know the accurate forward and reverse bias impedance parameters of the PIN diode in the W band (85-100 GHz). On the basis of the PIN diode simulation model proposed in [6], the accurate diode model is established in Ansys HFSS. The PIN diode simulation model is shown in Fig. 3. As shown in Fig. 3, the P-region and N-region are equivalent to an ideal electrical conductor. At the same time, the I-region is simulated as the impedance boundary, whose value is $6+j30$ in the forward bias state and $130-j570$ in the reverse bias state. The package of the PIN diode contains an oxide-nitride passivation layer, copper and GaAs. Finally, the forward and reverse bias impedance parameters of the diode are extracted according to the SPICE provided by the manufacturer and the simulation model of the PIN diode in HFSS.

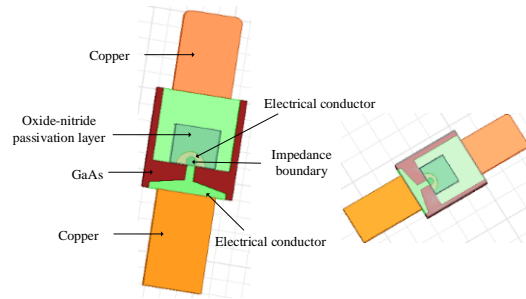


Fig. 3. The simulation model of the PIN diode.

In this section, the W-band H-plane waveguide-microstrip transition will be designed and analyzed based on the principle of the magnetic field coupling. The simulation model and results of the W-band (85-100 GHz) waveguide-microstrip transition are shown in Fig. 4. The metal strips (thickness = 0.017 mm) with different patterns are designed on a Duriod 5880 substrate (thickness = 0.127 mm and $\epsilon_r = 2.2$) and then inserted into the H-plane of a standard WR10 waveguide cavity. In order to achieve good matching of the H-plane transition structure in the frequency range of 85-100 GHz, two high-impedance lines are added between the probe and the 50Ω microstrip line. Meanwhile, for good grounding efficiency, the metal strip of the probe at the end must make good contact with the cavity, and the two ground vias must be filled with conductive glue. Finally, the H-plane transition structure can achieve good grounding by the cavity. In the frequency range of 85 to 100 GHz, the simulation results show that the return loss of the H-plane waveguide-microstrip transition is greater than 20 dB, and their IL is less than 0.09 dB. Therefore, the H-plane waveguide-microstrip transition structure not only has a transition effect, but also can achieve a good grounding effect. According to the above

discussion, in the subsequent design of the W-band SPDT switch, the H-plane waveguide-microstrip transition structure can reduce the size and IL of the switch.

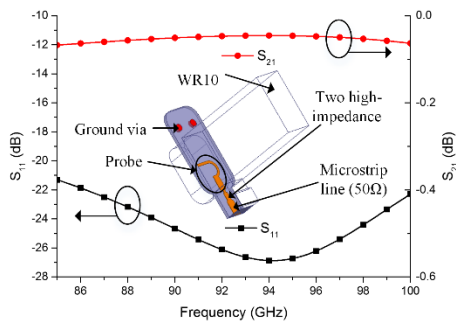


Fig. 4. The simulation model and results of the H-plane waveguide-microstrip transition.

In order to facilitate the measurement of the SPDT switch, an E-plane waveguide-CPW transition is designed. The simulation model and results are shown in Fig. 5. The used substrate is Duriod 5880 substrate with thickness of 0.127 mm and its top includes metal strips having different shapes with thickness of 0.017 mm. The substrate inserted into the central E-plane of a standard WR10 waveguide cavity.

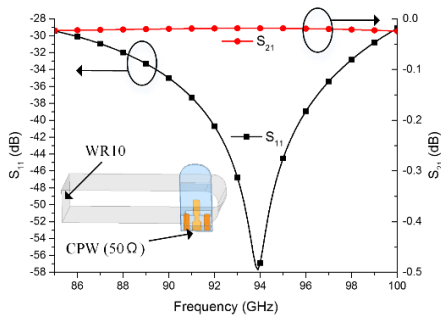


Fig. 5. The simulation model and results of the E-plane waveguide-CPW transition.

In the design of the W-band SPDT switch, in order to avoid the leakage of radio frequency signals due to the addition of a DC bias to the PIN diode, the low pass filter (LPF) in the W-band is designed. The LPF is used to power the diode, and its simulation results and model are shown in Fig. 6. The simulation results show that the LPF has high rejection in the frequency range of 85 to 100 GHz.

In the section, combining all the above designs, the W-band SPDT switch without waveguide-CPW transition is designed, and its simulation results and model are shown in Fig. 7. The substrate size of the SPDT switch without waveguide-CPW transition is $7.47 \times 3.44 \times 0.16$

mm³.

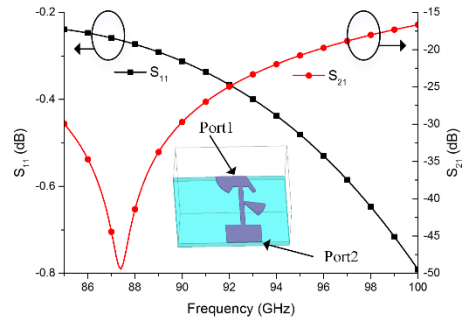


Fig. 6. The simulation model and results of the LPF.

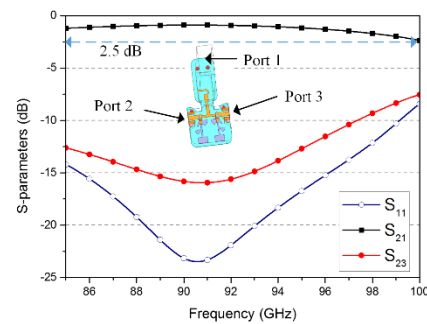


Fig. 7. The simulation model and results of the W-band SPDT switch without waveguide-CPW transition.

In order to facilitate the measurement of W-band SPDT switches, the ports 2 and 3 achieve standard wave port WR10 output through the waveguide-CPW transition. At the same time, a DC power supply board for PIN diodes is designed. The simulation model and results of the W-band SPDT switch with waveguide-CPW transition are shown in Fig. 8. It can be seen from the simulation results that the IL of the SPDT switch is less than 2dB, and its reflection and isolation are greater than 10 dB in the frequency range of 85 to 97 GHz.

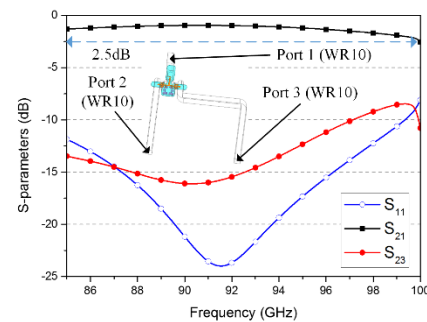


Fig. 8. The simulation model and results of the W-band SPDT switch with waveguide-CPW transition.

III. EXPERIMENTAL RESULTS

According to the analysis and discussion above, a W-band SPDT switch with waveguide-CPW transition is designed, and it is shown in Fig. 9. As shown in Fig. 9 (a), The PIN diode DC bias without the external grounding structure can achieve a good grounding effect only through the H-plane waveguide-microstrip transition. The assembly drawing of the W-band SPDT switch with the waveguide-CPW transition under the microscope is shown in Fig. 9 (b), and its physical photo is shown in Fig. 9 (c).

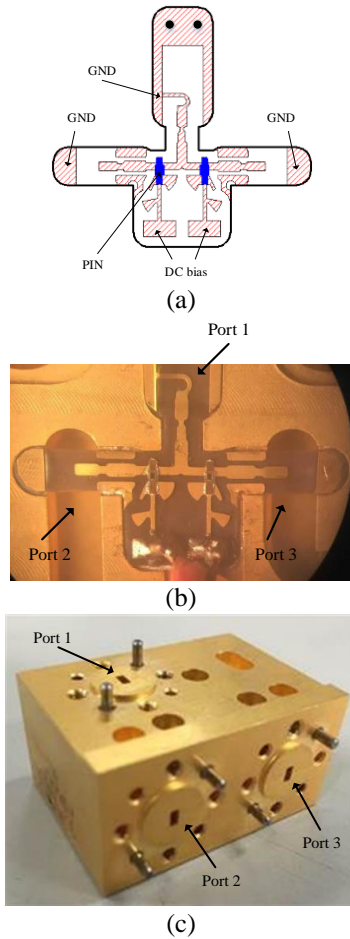


Fig. 9. (a) Fabricated substrate of the SPDT switch, (b) assembly drawing of the SPDT switch, and (c) physical photo of the SPDT switch.

An Agilent 83623B signal source along with Agilent W-band frequency extension modules 8355B and an Agilent 8757D scalar network analyzer were used for S-parameters measurement. In the measurement of the SPDT switch, port 1, port 2, and port 3 correspond to the ports in the simulation model in Fig. 8. The measured results of Fig. 9 (c) are shown in Fig. 10. When port 2 is on and port 3 is isolated, the measurement results of the

W-band SPDT switch with waveguide-CPW transition are shown in the Fig. 10 (a). Moreover, when port 3 is on, the measurement results are shown in the Fig. 10 (b). In the frequency range 85 to 95 GHz, the measured ILs of the port 2 is less than 2 dB and its isolation is greater than 12 dB under on-state, as seen in Fig. 10 (a). As shown in Fig. 10 (b), in the frequency range 85 to 96.5 GHz, the measured ILs of the port 3 is less than 2 dB and its isolation is greater than 10 dB under on-state. In the frequency range of 89.5 to 94 GHz, the measured results that the ILs of the SPDT switch are less than 2 dB, while its isolation is greater than 15 dB. In the frequency range of 92 to 93 GHz, the measured ILs of the SPDT switch are less than 1.65 dB, its return losses are greater than 15 dB, and its isolation is greater than 22 dB.

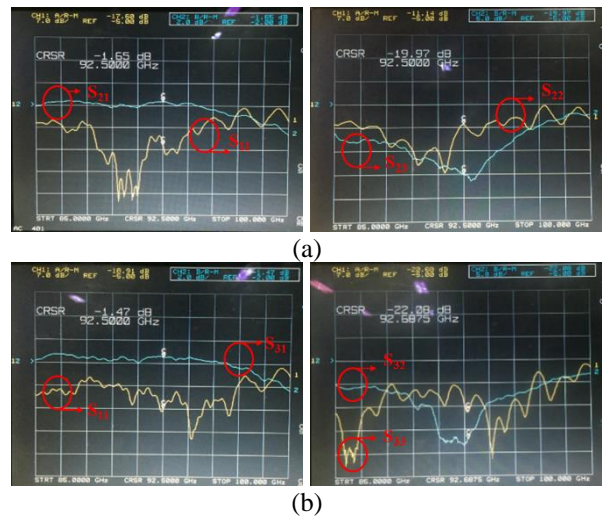


Fig. 10. (a) Measured results of the fabricated SPDT switch port 2, and (b) measured results of the fabricated SPDT switch port 3.

In the test of the SPDT switching time, the radio frequency signal after passing the detector is measured through an oscilloscope. The measured results of the SPDT switching times are shown in Fig. 11. As seen in Fig. 11, switch rise time and switch fall time of the SPDT switch are lower than 29ns and 19ns, respectively.

Table 2 tabulates the performance comparisons of the proposed W-band SPDT switches with some previous works. Compared with the designs in [6] and [14], our proposed one has lower ILs. At the same time, the design in [6] only provides simulation results. Note that the works in [9, 11-12] were used by MMIC technology and tested by GSG probing. Therefore, the ILs of [9, 11-12] in Table 2 were presented without losses of the waveguide-CPW transition. For our design, the IL in Table 2 has included the loss of the waveguide-CPW transition back to back, which is about 0.7 dB at the frequency range of 89.5-94 GHz.

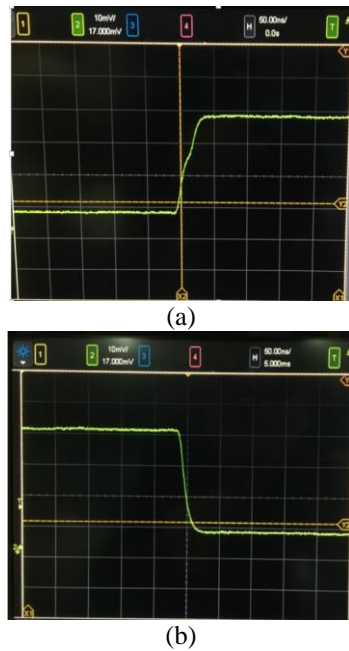


Fig. 11. (a) Measured results of the SPDT switch rise time, and (b) measured results of the SPDT switch fall time.

Table 2: Performance comparisons with some previous W-band SPDT switches

	Technology	Frequency (GHz)	IL (dB)	Isolation (dB)	Ports
[6]	HIC	85-95	1.3-2.5	17.5-24	WR10
[9]	MMIC	75-110	1.4-2	19-22	CPW
[11]	MMIC	75-110	1.2-1.6	17.7-20	CPW
[12]	MMIC	75-110	1-1.6	28.5-31.6	CPW
[14]	MEMS	75-80	9.1-11	22-25	CPW
This work	HIC	89.5-94	1.47-2	15-22	WR10

IV. CONCLUSION

Based on the principle of the magnetic field coupling, a W-band PIN diode SPDT switch with low IL has been presented using the HIC of microstrip and CPW in this paper. By designing H-plane waveguide-microstrip transition and the accurate models of PIN diode, low ILs and compact structure can be achieved. Finally, the simulations and measurements of the demonstrative W-band SPDT switch are in good agreement. The measured ILs of the SPDT switch are less than 1.65 dB, its return losses are greater than 15 dB, and its isolation is greater than 22 dB, in the frequency range of 92 to 93 GHz.

REFERENCES

- [1] A. Morales, O. Gallardo, J. J. V. Olmos, and I. T. Monroy, "Beam steering application for W-band

data links with moving targets in 5G wireless networks," *Journal of Communications and Information Networks*, vol. 2, no. 2, pp. 91-100, June 2017.

- [2] Y. J. Guo, K. D. Xu, X. J. Deng, X. Cheng, and Q. Chen, "Millimeter-wave on-chip bandpass filter based on spoof surface plasmon polaritons," *IEEE Electron Device Letters*, vol. 41, no. 8, pp. 1165-1168, Aug. 2020.
- [3] K. D. Xu, X. Zhu, Y. Yang, and Q. Chen, "A broadband on-chip bandpass filter using shut dual-layer meander-line resonators," *IEEE Electron Device Letters*, vol. 41, no. 11, pp. 1617-1620, Oct. 2020.
- [4] D. Li and K. Xu, "Multifunctional switchable filter using coupled-line structure," *IEEE Microw. Wireless Compon. Lett.*, Early Access, 2021. DOI: 10.1109/LMWC.2021.3067893.
- [5] I. F. Akyildiz, A. Kak, and S. Nie, "6G and beyond: The future of wireless communications systems," *IEEE Access*, vol. 8, pp. 133995-134030, June 2020.
- [6] S. H. Jia and W. Xue, "Design of W-band SPDT switch by employing full-wave EM simulator," *2012 IEEE International Conference on Computational Problem-Solving (ICCP)*, Leshan, China, pp. 425-427, Oct. 2012.
- [7] S. H. Jia and Y. H. Zhang, "W-band finline SPST switch," *2012 IEEE International Conference on Computational Problem-Solving (ICCP)*, Leshan, China, pp. 248-250, Oct. 2012.
- [8] Z. B. Xu, J. Guo, C. Qian, and W. B. Dou, "Analysis and design of a novel W-band SPST switch by employing full-wave EM simulator," *Journal of Infrared. Millimeter. and Terahertz Waves*, vol. 32, no. 12, pp. 1434-1445, Dec. 2011.
- [9] P. Song, R. L. Schmid, A. C. Ulusoy, and J. D. Cressler, "A high-power, low-loss W-band SPDT switch using SiGe PIN diodes," *2014 IEEE Radio Frequency Integrated Circuits Symposium*, Tampa, FL, USA, pp. 195-198, June 2014.
- [10] X. J. Bi, M. Annamalai, Arasu, Y. Zhu, and M. Je, "A low switching-loss W-band radiometer utilizing a single-pole-double-throw distributed amplifier in 0.13- μm SiGe BiCMOS," *IEEE Trans. Microw. Theory Tech.*, vol. 64, no. 1, pp. 226-238, Jan. 2016.
- [11] F. Thome, E. Ture, P. Brückner, R. Quay, and O. Ambacher, "W-band SPDT switches in planar and tri-gate 100-nm gate-length GaN-HEMT technology," *2018 German Microwave Conference (GeMIC)*, Freiburg, Germany, pp. 331-334, Mar. 2018.
- [12] F. Thome, A. Leuther, and O. Ambacher, "Low-loss millimeter-wave SPDT switch MMICs in a metamorphic HEMT technology," *IEEE Microw. Wireless Compon. Lett.*, vol. 30, no. 2, pp. 197-200, Feb. 2020.
- [13] J. Rizk, G. L. Tan, J. B. , and G. M. Rebeiz, "High-

isolation W-band MEMS switches,” *IEEE Microw. Wireless Compon. Lett.*, vol. 11, no. 1, Jan. 2001.

- [14] S. M. Sim, Y. Lee, Y. H. Jang, Y. S. Lee, Y. K. Kim, I. L. Garro, and J. M. Kim, “A 50-110 GHz ohmic contact RF MEMS silicon switch with dual axis movement,” *Microelectronic Engineering*, vol. 162, pp. 69-74, May 2016.
- [15] A. Kapoor, P. K. Shrivastava, S. K. Koul, and A. Basu, “Back to back wide-band CPW-to-waveguide transition with RF MEMS shunt switch in W-band,” *2019 IEEE International Conference on Microwaves, Antennas, Communications and Electronic Systems (COMCOS)*, Tel-Aviv, Israel, pp. 1-6, Nov. 2019.
- [16] M. H. Koh and A. E. Grant, “High power amplifier design with RF-MEMS output switch using SonnetTM,” *2012 International Applied Computational Electromagnetics Society Symposium (ACES)*, Columbus, Ohio, USA, pp. 10-14, Apr. 2012.
- [17] S. Suganthi, K. Murugesan, and S. Raghavan, “CPW dependent loss analysis of capacitive shunt RF MEMS switch,” *Applied Computational Electromagnetics Society Journal*, vol. 31, no. 4, pp. 410-416, Apr. 2016.
- [18] A. Tang, T. Reck, R. Shu, L. Samoska, Y. Ye, Q. Gu, B. J. Drouin, J. Truettel, R. A. Hadi, Y. Xu, S. Sarkozy, R. Lai, M. C. F. Chang, and I. Mehdi, “A W-band 65nm CMOS/InP-hybrid radiometer & passive imager,” *2016 IEEE MTT-S International Micro-wave Symposium (IMS)*, San, Francisco, CA, USA, pp. 1-3, May 2016.



Yun Jiang was born in Hunnan Province, China. He received the M.S. degrees in Electronic Engineering from the University of Electronic Science and Technology of China (UESTC), Chengdu, China, in 2017, and currently he is working toward the Ph.D. degree in National University of Defense University. His research interests include RF/millimeter-wave components and circuits.



Yuan Ye was born in Guangxi, China. She received the M.S. degree in Sun Yat-sen University, Guangzhou, China, in 2012, and currently she is working toward the Ph.D. degree in National University of Defense Technology. Her current research interests include ultra-

wideband antenna Arrays and reconfigurable antenna.



Daotong Li (S'15-M'16) received the Ph.D. degree in Electromagnetic Field and Microwave Technology from the University of Electronic Science and Technology of China (UESTC), Chengdu, China, in 2016.

He is currently an Associate Professor with the Center of Communication and Tracking Telemetry Command, Chongqing University, Chongqing. Since 2015, he has been a Visiting Researcher with the Department of Electrical and Computer Engineering, University of Illinois at Urbana-Champaign, Urbana, IL, USA, with financial support from the China Scholarship Council. He has authored or coauthored over 70 peer-reviewed journal or conference papers.

His current research interests include RF, microwave and millimeter-wave technology and applications, microwave power transmission (MPT), antennas, devices, circuits and systems, and passive and active (sub-) millimeter-wave imaging and radiometer. Li was a recipient of the UESTC Outstanding Graduate Awards by the Sichuan province and UESTC in 2016. He was a recipient of the National Graduate Student Scholarship from the Ministry of Education, China, and “Tang Lixin” Scholarship. He is serving as a Reviewer for several IEEE and IET journals, and many international conferences as a TPC Member, a Session Organizer, and the Session Chair.



Zhanyu Huang was born in 1992. He received the M.S. degree in Electronics and Communication Engineering from the University of Electronic Science and Technology of China, Chengdu, China in 2018, where he is currently pursuing Ph.D. degree with the College of Electronic Science and Engineering, National University of Defense Technology, Changsha, China. His current research interests include passive RF/microwave circuits, microstrip antennas and wireless communication.



Chao Wang was born in 1977. He received the Ph.D. degree from the National University of Defense Technology, Changsha, in 2007. He is currently an Associate Professor with the National University of Defense Technology. His research interest is electronic system design.



Jinjian Huang is now working in National University of Defense Technology. He received the Ph.D. degree of Electronics Science and Technology from National University of Defense Technology, Changsha, China in 2014. His research interests include ultra-wide band antenna and phase array antenna.



Naichang Yuan was born in Anhui, China, in 1965. He received the M.S. and Ph.D. degrees in Electronic Science and Technology from the University of Electronic Science and Technology of China in 1991 and 1994, respectively. He is currently a Professor with the National University of Defense Technology. His research interests include array signal processing, radar system design, SAR/ISAR imaging and electronic countermeasures.

Robust Adaptive Beamforming based on Automatic Variable Loading in Array Antenna

Bin Yang¹, Wenxing Li¹, Yuanyuan Li², and Yunlong Mao³

¹ College of Information and Communication Engineering
Harbin Engineering University, Harbin, Heilongjiang 150001, China
yb_alonline@126.com, liwenxing@hrbeu.edu.cn

² The 54th Research Institute of China Electronics Technology Group Corporation
Shijiazhuang, Hebei 050081 China
lyy008@hotmail.com

³ School of Electronics and Information
Jiangsu University of Science and Technology, Zhenjiang, Jiangsu 212003, China
maoyunlong0511@just.edu.cn

Abstract — Diagonal loading technology is widely used in array antenna beamforming because of its simple method, low computational complexity and the ability to improve the robustness of beamformer. On this basis, this paper proposes a robust adaptive beamforming method based on automatic variable loading technology. The automatic variable loading matrix (AVLM) of the method is composed of two parts. The non-uniform loading matrix dominants when the input signal-to-noise ratio (SNR) is small, effectively control the influence of noise disturbance without affecting the ability of array antenna to suppress interference. The variable diagonal loading matrix dominants when the input SNR is high to improve the output performance of array antenna. Simulated results show that compared to other methods, the proposed method has better output performance for both low and high input SNR cases.

Index Terms — Array antenna, loading, robust adaptive beamforming.

I. INTRODUCTION

Adaptive beamforming technology is an important topic in array signal processing. It is widely used in radar, sonar, array antenna, wireless communication, medical imaging and other fields [1-3]. In numerous adaptive beamforming methods, Capon beamforming method is used extensively for its effective suppression of interference and noise and good output performance in ideal environment [4]. However, in practical application, various error environments have led to the serious degradation in output performance of traditional Capon beamforming method. How to improve the robustness of beamformer has become a hot topic in

recent years.

To increase robustness of array antenna, many beamformers based on interference plus noise covariance matrix (INCM) reconstruction are proposed [5-7]. This kind of method has good performance, but these methods are computationally complex and rely heavily on array manifold information. To make the method beamformer simple and easy to implement, we mainly study the beamformer based on loading technology in this paper. Carlson proposed a diagonal loading method (LSMI) [8], which is robust towards the mismatch of the steering vector (SV) of desired signal and the influence of the low number of snapshots, and it is easy to implement without increasing computation. The output performance of conventional LSMI method varies with the selection of diagonal loading factor, but there is no certain method to determine the value of optimal loading factor. For diagonal loading technology, the selection of optimal loading factor is still an unsolved problem, which worth further research and discussions [9]. A beamforming method based on worst case performance optimization was proposed in [10]. In this method, the upper limit of error is set between imaginary SV and the SV. By constraining the response of the beamformer when the error of the desired signal steering vector reaches the upper limit, the worst-case performance can be optimized.

Compared to these fixed diagonal loading beamforming methods, more variable loading beamforming methods have been widely studied [11-13]. Zhuang proposed a variable loading method, which can improve the robustness of the array antenna by preventing the weight vector from converging to the noise subspace and setting the loading factor in a special way [11]. Li proposed a diagonal loading method which

makes loading factor change with the input SNR, and corrects the steering vector of the desired signal, so as to improve the robustness of the array antenna [12]. In reference [13], according to the interval of diagonal loading value, an adaptive diagonal loading technology with diagonal loading factor varying with input signal power is proposed to further improve the robustness of array antenna. However, above methods have limited robustness improvement for beamformer, especially when the input SNR is large. The output performance of Capon beamformer decreases sharply, because of the cancellation of desired signals when array antenna receives data with small snapshots.

In view of the above problems, this paper proposes a novel robust adaptive beamforming method based on automatic variable loading technology (AVL-RAB), which constructs the non-uniform loading matrix and variable diagonal loading matrix without increasing the complexity of calculation firstly. In order to better integrate the above matrices, we construct a mixed factor to make non-uniform loading matrix play a leading role when SNR is low. In this way, the beamformer can restrain the influence of noise disturbance, and try to keep the ability to suppress interference. When the SNR is high, variable diagonal loading matrix play an important role. Although the ability of array antenna to suppress interference is reduced, the desired signal cancellation is avoided to ensure the output performance of the array antenna. To further improve the robustness of the array antenna, the method corrects SV of the desired signal in a way similar to reference [14]. Numerical results demonstrate the superior performance of the proposed beamformer relative to other existing beamformers.

II. SIGNAL MODEL AND DIAGONAL LOADING

A. Signal model of array antenna

Consider a uniform linear array (ULA), which is composed of N omnidirectional antennas spaced by half a wavelength, receiving uncorrelated far-field narrowband signals. The sample data of array antenna at the k th snapshot is modeled as:

$$\mathbf{X}(k) = \mathbf{A}\mathbf{S}(k) + \mathbf{N}(k), \quad (1)$$

Where $\mathbf{X}(k) = [x_1(k) \ x_2(k) \ \cdots \ x_N(k)]^T$ is a $N \times 1$ data vector, $(\bullet)^T$ indicates transpose of the matrix, $\mathbf{S}(k) = [s_0(k) \ s_1(k) \ \cdots \ s_M(k)]^T$ is a mixed signal vector containing M narrow band interference and a desired signal. $\mathbf{N}(k)$ is assumed to be the additive spatially Gaussian white noise with zero mean and variance σ_n^2 . $\mathbf{A} = [\mathbf{a}(\theta_0) \ \mathbf{a}(\theta_1) \ \cdots \ \mathbf{a}(\theta_M)]$ is array manifold matrix, $\mathbf{a}(\theta_p) = [1 \ e^{j\beta_p} \ \cdots \ e^{j(N-1)\beta_p}]^T$ denotes the SV of θ_p . $\beta_p = 2\pi d \sin(\theta_p)/\lambda$ is the phase difference.

The output of this array antenna is given as:

$$y(k) = \mathbf{w}^H \mathbf{x}(k), \quad (2)$$

where $\mathbf{w} = [w_1, w_2, \dots, w_N]^T$ is the weight vector of the array antenna, $(\bullet)^H$ is the conjugate transpose of matrix. The minimum variance distortionless response (MVDR) beamformer is obtained by minimizing the variance of the interference and noise at the output while constraining the target response to be unity, hence can be formulated as:

$$\min_{\mathbf{w}} \mathbf{w}^H \mathbf{R}_{i+n} \mathbf{w} \quad \text{s.t.} \quad \mathbf{w}^H \mathbf{a}(\theta_0) = 1, \quad (3)$$

where $\mathbf{a}(\theta_0)$ is the desired signal steering vector, \mathbf{R}_{i+n} is the interference plus noise covariance matrix (INCM) matrix. In practice, \mathbf{R}_{i+n} is unavailable, so replace it with the following data sample covariance matrix (SCM):

$$\hat{\mathbf{R}} = \frac{1}{K} \sum_{k=1}^K \mathbf{x}(k) \mathbf{x}^H(k), \quad (4)$$

where K is the number of snapshots. Therefore, by solving the above problems, the weighted vector of the beamformer can be obtained as:

$$\mathbf{w}_{\text{opt}} = \frac{\hat{\mathbf{R}}^{-1} \mathbf{a}(\theta_0)}{\mathbf{a}^H(\theta_0) \hat{\mathbf{R}}^{-1} \mathbf{a}(\theta_0)}. \quad (5)$$

In the ideal cases, Capon beamformer has good output performance. However, since the desired signal is contained in the training data, the standard Capon beamforming method is more sensitive to the steering vector error of the desired signal. When beamformer suffers from large input SNR, small snapshots and steering vector mismatches, the performance of beamformer decreases sharply.

B. Diagonal loading method

Diagonal loading method can solve the problem of noise disturbance effect well. The principle is as follows:

$$\min_{\mathbf{w}} \mathbf{w}^H (\hat{\mathbf{R}} + \lambda \mathbf{I}) \mathbf{w} \quad \text{s.t.} \quad \mathbf{w}^H \mathbf{a}(\theta_0) = 1, \quad (6)$$

where λ is the diagonal loading factor. \mathbf{I} is the identity matrix. According to the formula (5), it can be concluded that:

$$\mathbf{w}_{DL} = \frac{(\hat{\mathbf{R}} + \lambda \mathbf{I})^{-1} \mathbf{a}(\theta_0)}{\mathbf{a}^H(\theta_0) (\hat{\mathbf{R}} + \lambda \mathbf{I})^{-1} \mathbf{a}(\theta_0)}. \quad (7)$$

The beampattern can be expressed as:

$$\begin{aligned} \mathbf{G}(\mathbf{w}_{DL}, \theta) &= \mathbf{w}_{DL}^H \mathbf{a}(\theta) \\ &= \frac{\mu}{\lambda_N^2} \left[\mathbf{a}^H(\theta_0) \mathbf{a}(\theta) - \sum_{i=1}^{N-1} \frac{\lambda_i - \lambda_N}{\lambda_i + \lambda} \mathbf{a}^H(\theta_0) \mathbf{v}_i \mathbf{v}_i^H \mathbf{a}(\theta) \right] \\ &= \mathbf{G}(\mathbf{a}(\theta_0), \theta) - \sum_{i=1}^M \frac{\lambda_i - \lambda_N}{\lambda_i + \lambda} \mathbf{a}^H(\theta_0) \mathbf{v}_i \mathbf{G}(\mathbf{v}_i, \theta) \\ &\quad - \sum_{i=M+1}^{N-1} \frac{\lambda_i - \lambda_N}{\lambda_i + \lambda} \mathbf{a}^H(\theta_0) \mathbf{v}_i \mathbf{G}(\mathbf{v}_i, \theta), \end{aligned} \quad (8)$$

where $\mu = 1/\mathbf{a}^H(\theta_0)(\hat{\mathbf{R}} + \lambda\mathbf{I})^{-1}\mathbf{a}(\theta_0)$. λ_i and \mathbf{v}_i are eigenvalues and eigenvectors of $\hat{\mathbf{R}}$, respectively, $\lambda_1 \geq \lambda_2 \geq \dots \geq \lambda_N$. The three terms on the right side of formula (8) are respectively the static array response, the weighted sum of interference beam response and the weighted sum of noise beam response. It can be seen that for the diagonal loading technology, the increase of the loading factor is conducive to reducing the impact of noise on the beam quality, while the large loading factor will reduce the interference suppression ability of the array antenna.

III. THE PROPOSED METHOD

In this section, a robust adaptive beamforming method based on automatic variable loading in array antenna is proposed.

A. The construction of non-uniform loading matrix

In this section, the SCM is preprocessed by forward and backward spatial smoothing technique. Define a transformation matrix \mathbf{J} :

$$\mathbf{J} = \begin{bmatrix} 0 & \dots & 0 & 1 \\ 0 & \dots & 1 & 0 \\ \vdots & \ddots & \vdots & 0 \\ 1 & \dots & 0 & 0 \end{bmatrix}, \quad (9)$$

A new covariance matrix $\bar{\mathbf{R}}$ is obtained by using forward and backward spatial smoothing technique. This technique can be considered as regularizing the unstructured SCM into a more structured one, which leads to a higher convergence rate. The proof, which uses this reconstructed SCM to improve the performance of the beamformer, is shown in [15]. $\bar{\mathbf{R}}$ can be expressed as:

$$\bar{\mathbf{R}} = \frac{\hat{\mathbf{R}} + \mathbf{J}\hat{\mathbf{R}}^*\mathbf{J}}{2}, \quad (10)$$

where $(\bullet)^*$ is conjugate operation of matrix.

According to formula (3), a constraint is imposed on Capon beamformer to make the weighting vector approximately orthogonal to the noise space. It can be expressed as:

$$\min_{\mathbf{w}} \mathbf{w}^H \bar{\mathbf{R}} \mathbf{w} \text{ subject to } \mathbf{w}^H \tilde{\mathbf{a}}(\theta_0) = 1, \mathbf{w}^H \bar{\mathbf{R}}^{-m} \mathbf{w} \leq T, \quad (11)$$

where T is a minimum value, $\tilde{\mathbf{a}}(\theta_0)$ is assumed desired signal SV. The above formula can be resolved into:

$$\min_{\mathbf{w}} \mathbf{w}^H (\bar{\mathbf{R}} + \gamma \bar{\mathbf{R}}^{-m}) \mathbf{w} \text{ subject to } \mathbf{w}^H \tilde{\mathbf{a}}(\theta_0) = 1. \quad (12)$$

The non-uniform loading matrix is as follows:

$$\lambda_u = \gamma \bar{\mathbf{R}}^{-m}. \quad (13)$$

Through the non-uniform diagonal loading matrix, the weighted vector can be avoided to converge to the noise space, which is conducive to the array antenna to

suppress small eigenvalue disturbance and ensure the interference suppression ability of the array antenna.

B. The construction of variable diagonal loading factor

In this section, the variable diagonal loading factor (VDLF) is constructed. Process the $\bar{\mathbf{R}}$ in formula (10) via eigen-decomposition:

$$\begin{aligned} \bar{\mathbf{R}} &= \bar{\mathbf{U}} \bar{\mathbf{\Lambda}} \bar{\mathbf{U}}^H \\ &= \sum_{i=1}^N \bar{\lambda}_i \bar{\mathbf{v}}_i \bar{\mathbf{v}}_i^H, \end{aligned} \quad (14)$$

where $\bar{\mathbf{U}} = [\bar{\mathbf{v}}_1, \bar{\mathbf{v}}_2, \dots, \bar{\mathbf{v}}_N]$. $\bar{\mathbf{\Lambda}} = \text{diag}(\bar{\lambda}_1, \bar{\lambda}_2, \dots, \bar{\lambda}_N)$ is a diagonal matrix, $\bar{\lambda}_1 \geq \bar{\lambda}_2 \geq \dots \geq \bar{\lambda}_N$. The desired signal SV falls in the signal subspace formed by large eigenvalues. Because the difference between the assumed desired signal SV $\tilde{\mathbf{a}}(\theta_0)$ and the real value is little. Project $\tilde{\mathbf{a}}(\theta_0)$ to each eigenvector to get the following result:

$$p(i) = |\bar{\mathbf{v}}_i^H \tilde{\mathbf{a}}(\theta_0)|^2, \quad i = 1, 2, \dots, N, \quad (15)$$

when $p(i)$ is the maximum, the eigenvalue of the corresponding eigenvector is $\hat{\lambda}_{1N1}$. It is the eigenvalue of the desired signal. The small eigenvalues are added and averaged to estimate the noise power:

$$\sigma_n^2 = \frac{\sum_{i=M+2}^N \bar{\lambda}_i}{N - M - 1}. \quad (16)$$

The VDLF can be set as:

$$\lambda_v = \frac{\hat{\lambda}_{1N1} - \sigma_n^2}{N \sigma_n^2}. \quad (17)$$

C. Construction of automatic variable loading matrix

In this section, we construct the mixed factor, which can change the parameters according to the change of the input SNR and has obvious allocation ability whether SNR is large or small. The mixed factor can be constructed as follows:

$$\alpha = \frac{\hat{\lambda}_{1N1}}{\hat{\lambda}_{1N1} + N \sigma_n^2}, \quad (18)$$

$$\kappa = 1 - \alpha = \frac{N \sigma_n^2}{\hat{\lambda}_{1N1} + N \sigma_n^2}, \quad (19)$$

where α and κ are the mixed factors constructed in this paper, which can effectively reflect the low input SNR and the high input SNR.

Based on the above research, the automatic variable loading matrix can be constructed as follows:

$$\begin{aligned} \lambda_m &= \alpha \lambda_u + \kappa \lambda_v \mathbf{I} \\ &= \alpha \gamma \bar{\mathbf{R}}^{-m} + \kappa \frac{\hat{\lambda}_{1N1}}{\sigma_n^2} \mathbf{I}. \end{aligned} \quad (20)$$

D. Desired signal SV estimation

This section estimates the SV of the desired signal with the method similar to that in reference [14]. We assume that the Θ is the angular sector in which the desired signal is located. Define the correlation matrix of the SV:

$$\mathbf{G} = \sum_i^N \bar{\mathbf{a}}(\theta_i) \bar{\mathbf{a}}^H(\theta_i) \Theta / N. \quad (21)$$

Process the \mathbf{G} via eigen-decomposition. The eigenvectors corresponding to the first L large eigenvalues are extracted as orthogonal matrices $\mathbf{U} = [\bar{\mathbf{v}}_1, \bar{\mathbf{v}}_2 \cdots \bar{\mathbf{v}}_L]$. So the actual SV of the desired signal can be estimated as:

$$\hat{\mathbf{a}}(\theta_0) = \mathbf{U} \mathbf{y}, \quad (22)$$

where \mathbf{y} is defined as a rotating vector. By maximizing the output power of the desired signal, take \mathbf{y} into the norm constraint. The optimization problem can be expressed as:

$$\min_{\mathbf{y}} \mathbf{y}^H \mathbf{U}^H \bar{\mathbf{R}}^{-1} \mathbf{U} \mathbf{y} \text{ s.t. } \mathbf{y}^H \mathbf{y} = N. \quad (23)$$

The problem (23) can be solved by Lagrange multiplier methodology. We can get:

$$\mathbf{U}^H \bar{\mathbf{R}}^{-1} \mathbf{U} \mathbf{y} = \mu \mathbf{y}. \quad (24)$$

Define \mathbf{y}_U as the eigenvector corresponding to the minimum eigenvalue of matrix $\mathbf{U}^H \bar{\mathbf{R}}^{-1} \mathbf{U}$ and $\mathbf{y}_U^H \mathbf{y}_U = N$. Then, the estimated SV of the desired signal can be obtained by substituting this solution into (22):

$$\hat{\mathbf{a}}(\theta_0) = \frac{\sqrt{N}}{\|\mathbf{y}_U\|} \mathbf{U} \mathbf{y}_U. \quad (25)$$

E. Calculation of weighted vector

The mixed loading matrix of formula (20) and the desired signal steering vector estimated by formula (25) are introduced into formula (12):

$$\min_{\mathbf{w}} \mathbf{w}^H (\bar{\mathbf{R}} + \alpha \gamma \bar{\mathbf{R}}^{-m} + \kappa \lambda_v \mathbf{I}) \mathbf{w} \text{ s.t. } \mathbf{w}^H \hat{\mathbf{a}}(\theta_0) = 1. \quad (26)$$

By solving the above equation, it can be concluded that:

$$\mathbf{w}_{al} = (\bar{\mathbf{R}} + \alpha \gamma \bar{\mathbf{R}}^{-m} + \kappa \lambda_v \mathbf{I})^{-1} \hat{\mathbf{a}}(\theta_0). \quad (27)$$

Substitute formula (14) into the above formula, we can get:

$$\mathbf{w}_{al} = \sum_{i=1}^N \frac{(\bar{\mathbf{v}}_i^H \hat{\mathbf{a}}(\theta_0))}{\tilde{\lambda}_i + (\alpha \gamma / \tilde{\lambda}_i^m) + \kappa \lambda_v} \bar{\mathbf{v}}_i. \quad (28)$$

In order to further suppress the influence of small eigenvalue disturbance, we take the noise power estimation as the threshold of small eigenvalue, which is defined as $\tilde{\lambda}_i = \max(\bar{\lambda}_i, \sigma_n^2)$, $i = 1, 2, \dots, N$. Through the formula (28), we can find that when $m = 0$, the non-uniform loading technology becomes uniform diagonal loading technology. When m becomes larger, the non-

uniform loading corresponding to large eigenvalue and the influence on the interference suppression will be smaller. Larger m will result with smaller non-uniform loading which corresponds to large eigenvalue, hence leading to smaller influences on interference suppression of array antenna. However, if m is overlarge, the beam sidelobe will be enhanced. In this paper, we define $m = 2$, $\gamma = 10\sigma_n^{2+m}$. Thus, the weight vector can be expressed as:

$$\mathbf{w}_{al} = \sum_{i=1}^N \frac{(\bar{\mathbf{v}}_i^H \hat{\mathbf{a}}(\theta_0))}{\tilde{\lambda}_i + (\alpha \gamma / \tilde{\lambda}_i^2) + \kappa \lambda_v} \bar{\mathbf{v}}_i. \quad (29)$$

The main computational complexity of the AVL-RAB is the eigen-decomposition operation. Its overall computational complexity is of $\mathcal{O}(N^3)$. Compared to the methods using optimization algorithms to estimate diagonal loading value, the computational complexity is relatively low. Table 1 shows the computational complexity of several methods.

Table 1: Comparison of computational complexity

Beamformer	Computational Complexity
INCM-RAB [5]	$\mathcal{O}(N^{3.5})$
INCM-NVM [6]	$\mathcal{O}(MN^3)$
LSMI [8] LC-RAB [11] LCHP-RAB [12] ADL-SMI [13] AVDL-RAB	$\mathcal{O}(N^3)$

IV. SIMULATIONS AND COMPARISONS

Consider a ULA with 10 antennas spaced half-wavelength. The desired signal direction is 0° . Two sidelobe interferences impinge on the ULA from -30° and 50° with interference-to-noise ratio (INR) 30dB. The signal and interference are statistically independent, and the added noise is Gaussian white noise. The snapshots of received data is 100. All experimental results are from 100 independent Monte Carlo experiments. The AVL-RAB in this paper is compared to IPNM-NVM [6], LSMI [8] with the loading factor $\gamma = 10\sigma_n^2$, LC-RAB [11], LCHP-RAB [12], ADL-SMI [13].

A. The simulation of VHDL and mixed factor

In this simulation, the snapshots number is 100 and the input SNR changes from -10dB to 30dB uniformly. Fig. 1. shows the VDLF versus the input SNR. From the simulation results, the proposed VDLF can estimate the input SNR of the received signal, and the estimation result is accurate. This factor can make the array antenna avoid the desired signal cancellation when the input SNR is large and snapshots are small, so as to ensure the

output performance of the array antenna. Figure 2 shows the curve of mixed factor changing with input SNR. It can reasonably allocate the proportion of two loading matrices according to the value of SNR.

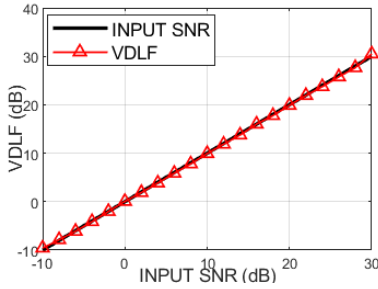


Fig. 1. VDLF versus the input SNR.

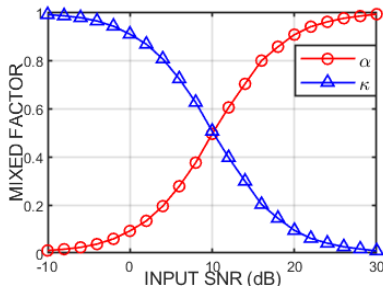


Fig. 2. Mixed factors versus the input SNR.

B. Ideal condition

In this simulation, the performance comparison of the above methods is made. Figure 3 shows the curves of the output signal to interference and noise ratio (SINR) with the input SNR when the number of snapshots is 100. The input SNR changes from -10dB to 30dB uniformly. Figure 4 shows the curves of the output SINR of each method changing with the number of snapshots. The input SNR is 15dB and the range of snapshots number changes from 20 to 100.

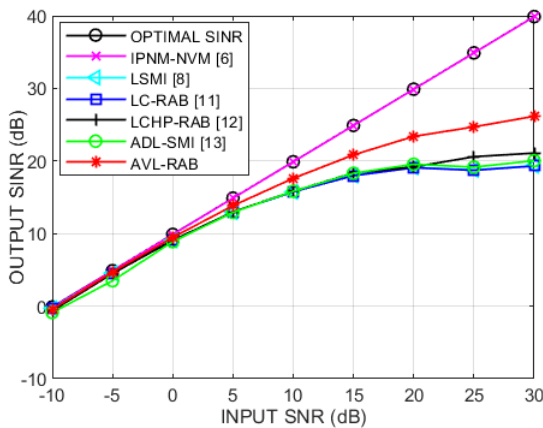


Fig. 3. Output SINR versus the SNR in ideal condition.

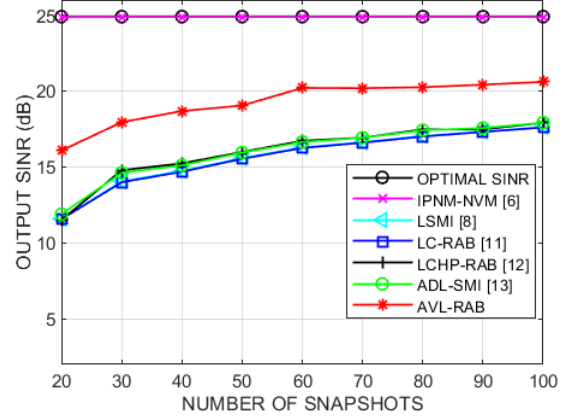


Fig. 4. Output SINR versus the number of snapshots in ideal condition.

From Fig. 3 and Fig. 4, the IPNM-NVM has excellent performance, but it is very complex and needs more prior information. For the methods based on loading technology, the proposed method has higher output SINR and fast convergence speed. Thus, the proposed method outperforms other similar methods in ideal condition.

C. Desired signal steering vector mismatch

In this simulation, the look direction error of the desired signal is randomly distributed in $[-5^\circ, 5^\circ]$. The true steering vector is formed by five signal paths and is given by $\mathbf{a} = \mathbf{a}(\theta_0) + \sum_{i=1}^4 e^{j\phi_i} \mathbf{a}_i(\theta_i)$, where $\mathbf{a}_i(\theta_i)$ corresponds to the coherently scattered paths. θ_i is random value in $[-5^\circ, 5^\circ]$, ϕ_i is the phase of the independent path and randomly distributed in $[0, 2\pi]$. Other simulation conditions remain unchanged, the performance of each method is simulated.

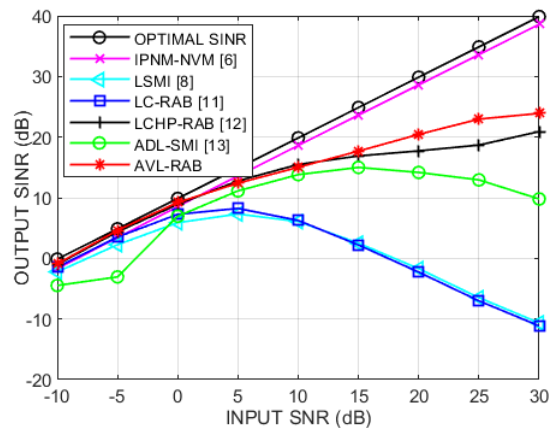


Fig. 5. Output SINR versus the SNR with desired signal SV mismatches.

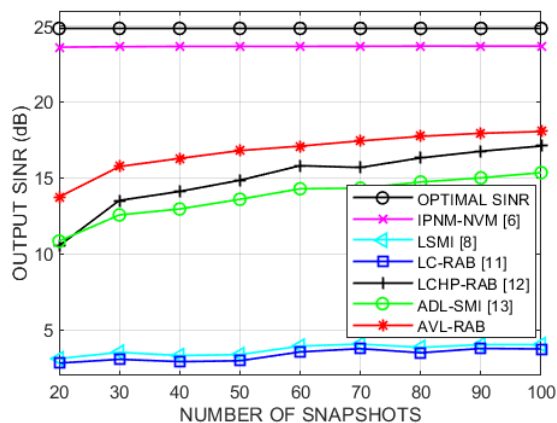


Fig. 6. Output SINR versus the number of snapshots with desired signal SV mismatches.

From above simulation results, the output SINR of all methods decreases significantly in this condition. The beamformer based on INCM reconstruction still perform well. The output performance of the method in this paper is better than other existing similar methods.

V. CONCLUSION

In this paper, a novel robust adaptive beamforming method based on automatic variable loading technology is proposed for array antenna. The method constructs the automatic variable loading matrix by mixing the non-uniform loading matrix and variable diagonal loading matrix so as to ensure that the array antenna has better output performance whether SNR is large or small. The computational complexity of the matrix is relatively low. Simulation results show that the proposed method has better robustness in the error environment of small number of data snapshots and mismatch of SV. The proposed method outperform other existing similar methods obviously.

ACKNOWLEDGMENT

This paper is supported by the Natural Science Foundation of Jiangsu province of China (BK20190956).

REFERENCES

- [1] W. Shi, Y. Li, S. Luo, and Ieee, "Adaptive antenna array beamforming based on norm penalized NLMS algorithm," *IEEE Antennas and Propagation Society International Symposium*, pp. 2207-2208, 2018.
- [2] W. Shi and Y. Li, "A p-norm-like constraint LMS algorithm for sparse adaptive beamforming," *Applied Computational Electromagnetics Society Journal*, vol. 34, no. 12, pp. 1797-1803, Dec. 2019.
- [3] S. Mohammadzadeh and O. Kukrer, "Robust adaptive beamforming based on covariance matrix and new steering vector estimation," *Signal Image and Video Processing*, 2019.
- [4] J. W. Jia, W. Jin, S. Zhou, and M. Yao, "Robust adaptive beamforming based on a new steering vector estimation algorithm," *Signal Process*, vol. 93, no. 9, pp. 2539-2542, Sep. 2013.
- [5] Y. Gu and A. Leshem, "Robust adaptive beamforming based on interference covariance matrix reconstruction and steering vector estimation," *IEEE Transactions on Signal Processing*, vol. 60, no. 7, pp. 3881-3885, 2012.
- [6] X. Yuan and L. Gan, "Robust adaptive beamforming via a novel subspace method for interference covariance matrix reconstruction," *Signal Processing*, 2017.
- [7] P. Zhang, Z. Yang, G. Jing, and T. Ma, "Adaptive beamforming via desired signal robust removal for interference-plus-noise covariance matrix reconstruction," *Circuits Systems and Signal Processing*, vol. 40, no. 1, pp. 401-417, Jan. 2021.
- [8] B. D. Carlson, "Covariance matrix estimation errors and diagonal loading in adaptive arrays," *IEEE Transactions on Aerospace Electronic Systems*, vol. 24, no. 4, pp. 397-401, 1988.
- [9] Y. L. Chen and J. H. Lee, "Finite data performance analysis of Mvdr antenna array beamformers with diagonal loading," vol. 134, pp. 475-507, 2013.
- [10] S. A. Vorobyov, A. B. Gershman, and Z. Q. Luo, "Robust adaptive beamforming using worst-case performance optimization: A solution to the signal mismatch problem," *IEEE Transactions on Signal Processing*, vol. 51, no. 2, pp. 313-324, 2003.
- [11] J. Zhuang, Q. Ye, Q. Tan, and A. H. Ali, "Low-complexity variable loading for robust adaptive beamforming," *Electronics Letters*, vol. 52, no. 5, pp. 338-340, 2016.
- [12] W. Li, X. Mao, Z. Zhai, and Y. Li, "A low complexity high performance robust adaptive beamforming," *Applied Computational Electromagnetics Society Journal*, vol. 32, no. 5, pp. 441-448, 2017.
- [13] J. Gao, J. Zhen, Y. Lv, and B. Guo, "Beamforming technique based on adaptive diagonal loading in wireless access networks," *Ad Hoc Networks*, vol. 107, p. 102249, 2020.
- [14] W. Zhang, J. Wang, and S. Wu, "Robust Capon beamforming against large DOA mismatch," *Signal Processing*, 2013.
- [15] L. Zhang, W. Liu, and L. Yu, "Performance analysis for finite sample MVDR beamformer with forward backward processing," *IEEE Transactions on Signal Processing*, vol. 59, no. 5, pp. 2427-2431, 2011.

Ultra-wideband Transmissive Linear Polarization Device Based on Graphene

Liwei Guo¹, Simin Li^{1,2,*}, Xing Jiang¹, Xin Liao¹, and Lin Peng¹

¹ School of Information and Communication
Guilin University of Electronic Technology, Guilin 541004, China

² School of Electrical and Information Engineering
Guangxi University of Science and Technology, Liuzhou 545006, China
siminl_guet@163.com

Abstract — In order to achieve both adjustable wideband and high Polarization Conversion Rate (PCR) of the transmitted waves, a novelty tri-layered structure is proposed for terahertz applications. The Rhombus Hollow Square (RHS) is built up by top and bottom gold gratings on Silicon Dioxide and Polyamide substrate with graphene strips. The proposed polarizer broadens the bandwidth and has well performance. As chemical potential increases, the bandwidth is also broadened by adjusting the graphene. From 0.5 THz to 3 THz, the PCR is greater than 90%, and the relative bandwidth up to 142.9%. The transmission and absorption of polarizer are analyzed at the oblique incidence with chemical potential 0.1eV. By simulating and analyzing the performance, a new result of maintaining broadband and high transmittance in oblique incidence is obtained.

Index Terms — Graphene, Terahertz, transmitting polarizer, ultra-wideband.

I. INTRODUCTION

Usually, terahertz (THz) wave is a length of 3000 to 30 μm , and the frequency is 0.1 to 10 THz. The application of terahertz technology in the field of electromagnetics is a hot topic now [1-2]. Terahertz is used in fields such as high-temperature superconducting materials, semiconductor materials properties research, and broadband communication [3], microwave device [4-6] and so on. Currently, there are mainly three types of polarizers used in the terahertz band liquid crystal polarizers [7], carbon nanotube polarizers [8], and metal wire grid polarizers [9]. Metal wire grid polarizers can be obtained mainly through precision machining, laser direct writing technology, photolithography and other processing methods. This is also the most widely used terahertz polarizer.

Generally, metal is fine material to design metamaterials and which is designed for reflective [10-12] and transmitting polarization converters [13-18]. For some non-adjustable materials, such as dielectric

materials and metal materials, which dynamic control becomes more inconvenient, and its application is limited. However, there are many advanced technologies for terahertz/mid-infrared tunable polarizer. In particular, the transmittance of the polarization control is adjustable. The bandwidth is broadened by adjusting the parameters of graphene to design the structure. This research provides a unique idea for the controllable polarization conversion rate in the research [18].

At the same time, the graphene has high electron mobility, the electrical grating or doping level of graphene can be adjusted to make it conductive [19-30]. For example, the absorbers [19] are tunable graphene based with polarization insensitive [20]. Light efficiently into graphene surface plasmon can be captured by the graphene sheet [21]. The graphene frequency selective surface achieves tunable polarization rotation of the transmitted wave and controllable bandpass response [23]. Graphene can be combined with other materials, which performance and bandwidth will enhance [24].

The conductivity of graphene is used to control by voltage [25]. According to design the polarization converter, the electron scattering time characteristic of graphene ranges from *ps* to *sub-ps*, which can vary in a wide range of frequency. MMW/IR beam synthesizer based on graphene infrared window, used for MMW/IR compound Compact Antenna Test Range (CATR), solves the infrared transmittance in the MMW/IR compound target simulation system [26].

We propose an original cross-polarized tri-layered structure metamaterial converter, which is a new transmission type, based on graphene to optimize the conversion rate and widened the operating frequency. We validated transmitting rate and high polarization conversion rate by full-wave numerical simulations. The physical mechanisms of the device are also discussed.

II. DESIGN OF TRANSMITTING POLARIZER BASED ON GRAPHENE

A schematic diagram of the unit structure of a

metamaterial cross-polarized transmission converter based on graphene strip, in which a vertically incident x -polarized waves are transformed to cross-polarized waves. The RHS patch, which arranged at a diagonal of 45° in Fig. 1 (a). The dielectric spacers are silicon dioxide and polyamide, with the RHS and graphene strip between them. The top and bottom of the polarizer are gratings. The gold grating wire width and periodicity both are w , and the thickness of the grating is $0.1\mu\text{m}$. The gratings are respectively covered on the substrates.

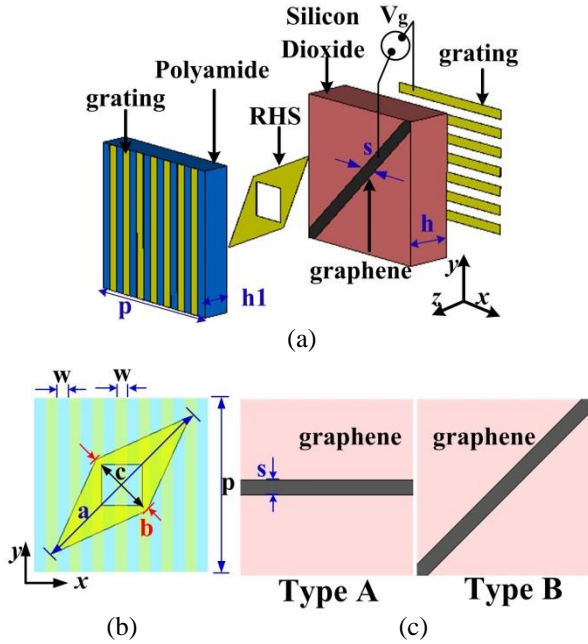


Fig. 1. (a) Schematic and geometric dimensions of transmissive polarizer unit cell by graphene, (b) the RHS of polarizer, and (c) type of the graphene strips in the structure.

The middle part of the transmitting polarizer is composed of graphene strip and a metal resonator layer RHS in Fig. 1 (b), which is located on the bottom $20\mu\text{m}$ -thick substrates. The unit is arranged in a periodic array structure of constant p . The structural parameters of the graphene strips are p and s , respectively. The two types of graphene strips are along the x -axis and rotated 45 degree with the unit diagonally, respectively. The thickness of the graphene strips and RHS are 100 nm . And the tri-layered structure substrate uses Silicon Dioxide thickness of h and Polyamide thickness of $h1$ respectively. Table 1 shows the optimized parameters of the structure. In order to excite the metal resonator RHS, the polarization field is applied along the $-z$ -direction when the terahertz waves are normally incident. Simultaneously, graphene strips are located under the RHS transmitting polarizer to proactively modulate the near-field coupling effect of terahertz waves.

Table 1: The optimal parameters of the polarizer

Parameters	p	c	s	b	w	h	h1	a
Value(μm)	60	20	5	25	4	20	12	67

In the research, the structures were numerically investigated through frequency domain solver by CST Studio Suite 2020 of commercially available full-wave electromagnetic simulator software. The unit calculation is shown in the Fig. 2. The periodic boundary structure is unit cell and floquet ports on the top and bottom. In the terahertz band, the three-layer metal-graphene-metal layers realize the controllable characteristics of linear transmission and perfect polarization conversion.

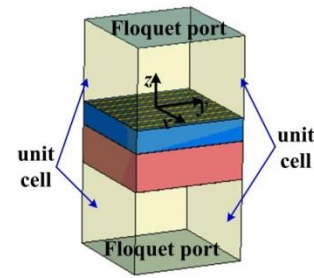


Fig. 2. The model of numerically investigates.

Two polarizers in the form of graphene are analyzed. Type A is a horizontal graphene strip and Type B which graphene with 45° angle in the horizontal direction. The graphene layer is shown in Fig. 1 (c), which is isolated by Silicon Dioxide with a dielectric constant $\epsilon_r=3.9$ and Polyamide with a dielectric constant of 3.5 . Introduce the conductivity of the graphene strip according to the Kubo formula, which is mainly intra/inter-band [27]:

$$\sigma_s = \sigma_{intra}(\omega, \mu_c, \Gamma, T) + \sigma_{inter}(\omega, \mu_c, \Gamma, T), \quad (1)$$

$$\sigma_{intra}(\omega, \mu_c, \Gamma, T) = \frac{-je^2kBT}{\pi\hbar^2(\omega - j2\Gamma)} \left(\frac{\mu_c}{kBT} + 2\ln(e^{-\mu_c/kBT} + 1) \right), \quad (2)$$

$$\sigma_{inter}(\omega, \mu_c, \Gamma, T) = -j \frac{e^2}{4\pi\hbar} \ln \left(\frac{2|\mu_c| - (\omega - j2\Gamma)\hbar}{2|\mu_c| + (\omega - j2\Gamma)\hbar} \right), \quad (3)$$

where the kB and T represent Boltzmann's constant and temperature. Parameters e and σ are the electron charge and Planck's constant, respectively. In addition, τ and μ_c refer to the relaxation time and chemical potential, namely Fermi energy E_F . The $\tau=1\text{ps}$, meanwhile $T=300\text{K}$. Therefore, $\sigma=1/2\tau$ represents the frequency of collision.

Before analyzing the design, it is necessary to consider the selectivity structure of the polarizer. In the first design, use graphene strips instead of whole graphene sheets. Then, the polarization of the transmitted wave with the applied voltage between the graphene strip and the gold grating is investigated. The permittivity of graphene [2] can be obtained by $\epsilon = 1 + (i\delta_s)/(\epsilon_0\omega\Delta t)$ in

the CST Studio Suite 2020. The carrier density and the position of the μ_c among the strips can be restrained with the bias voltage, and the phenomenon is dynamically. Formula (4) gives an approximate expression related to μ_c and V_g :

$$E_F = \mu_c \approx \hbar v_f \sqrt{\frac{\pi \epsilon_r \epsilon_0 V_g}{et}}, \quad (4)$$

The parameters ϵ_0 and ϵ_r respectively represent the dielectric constant of vacuum and silicon dioxide. The parameter V_g is bias voltage. The parameters e and V_f are the electronic charge and the Fermi velocity at 1.1×10^6 m/s in graphene, respectively. The $t=20$ nm is the thickness of the insulating layer between the graphene and the electrode. Novel polarizer we designed, the maximum bias voltage of 100V is adopted. Calculated by the formula, as the external load voltage increases, the chemical formula gradually increases. The adjustment range of the E_F is between 0eV-1eV, which requires range 5V to 75V bias voltage.

III. SIMULATION RESULTS AND DISCUSSIONS

The original unit structure of we proposed in Fig. 1 with the Cartesian coordinates of x - y - z axis. The periodic unit can be designed as a polarizer. If the incident and transmitted wave are E^i and E^t , respectively. The both forward and backward propagation of the transmission polarizer can be used as a four-port transmission system with the two ends as input and output. Then the positive propagation and opposite propagation can be indicated as the equation of electric field [28].

The superscript p indicate positive propagation along the $-z$ direction of forward, and the o indicate opposite propagation along the $+z$ of backward:

$$\begin{cases} \vec{E}^i = \begin{pmatrix} E_x^i \hat{x} \\ E_y^i \hat{y} \end{pmatrix} e^{jkz} \\ \vec{E}^t = \begin{pmatrix} E_x^t \hat{x} \\ E_y^t \hat{y} \end{pmatrix} e^{jkz} \end{cases}, \quad (5)$$

$$\begin{pmatrix} E_x^{io} \\ E_y^{io} \\ E_x^{ip} \\ E_y^{ip} \end{pmatrix} \cdot T = \begin{pmatrix} E_x^{ro} & E_x^{rp} \\ E_y^{ro} & E_y^{rp} \\ E_x^{ro} & E_x^{rp} \\ E_y^{ro} & E_y^{rp} \end{pmatrix}. \quad (6)$$

In that way, the transmission coefficients and reflection coefficients of the positive (forward) and opposite (backward) propagation in two componential arrays are expressed by the 4×4 scattering matrix as:

$$T = \begin{pmatrix} t_{xx}^o & t_{xy}^o & t_{xx}^p & t_{xy}^p \\ t_{yx}^o & t_{yy}^o & t_{yx}^p & t_{yy}^p \\ t_{xx}^o & t_{xy}^o & t_{xx}^p & t_{xy}^p \\ t_{yx}^o & t_{yy}^o & t_{yx}^p & t_{yy}^p \end{pmatrix}. \quad (7)$$

The subscripts x and y denote the electromagnetic waves state of polarization, meanwhile mark down i and t denote incident and transmit terahertz waves respectively. The t_{yx} indicate y -polarization transmitting from x -polarization incidence. The r_{xx} indicate x -polarization co-polarized reflection amplitude from x -polarization incidence. We propose a transmitting metamaterial linear polarizer, which transform the incident x -polarized terahertz wave to y -polarized, which is pure cross-polarized wave. The Stokes method is introduced to accurately describe transmitted waves. Four parameters with the same physical dimensions are used to determine the polarization state:

$$Tr_{-0} = t_{xx}^2 + t_{yx}^2, \quad (8)$$

$$Tr_{-1} = t_{xx}^2 - t_{yx}^2, \quad (9)$$

$$Tr_{-2} = 2t_{xx}t_{yx} \cos \Delta\varphi, \quad (10)$$

$$Tr_{-3} = 2t_{xx}t_{yx} \sin \Delta\varphi. \quad (11)$$

The formula $\Delta\varphi = \phi_{yx} - \phi_{xx} = \arg(t_{yx}) - \arg(t_{xx})$ is the difference of phase between the cross-polarized transmission coefficient t_{yx} and opposite propagation coefficient t_{xx} . The polarization conversion rate (PCR) of a tunable transmitting polarizer is usually expressed in terms of conversion efficiency. The calculation formula is:

$$PCR = t_{yx}^2 / (t_{yx}^2 + t_{xx}^2). \quad (12)$$

Since electromagnetic energy may be lost, the absorption rate of the conversion rate is calculated. The absorption rate of transmission (A_t) designs formula:

$$A_t = 1 - t_{yx}^2 - r_{xx}^2. \quad (13)$$

The graphene-based transmitting polarizer is designed to perform linear polarization conversion in the transmitting mode, so the metal layer of the traditional reflective polarizer is replaced by gratings. The double-layered grating is shown in Fig. 1 (a). The tri-layered structure shown plays an important role in transmitting pure linear polarized waves. With the double-layer orthogonal metal gratings design, the upper grating layer will not block the incident wave, and the cross-polarized waves can be transmitted by bottom gratings, which reflect the co-polarized waves as the metal layer. In this way, a pure cross-polarized wave can be transmitted, while its reflection is prohibited, and the polarization conversion is improved.

In addition, vertical gratings are added in front of the RHS. The cross-polarized and the co-polarized transmittance obtained by numerical simulations and the phase difference with the x -polarization normal incidence are shown in Fig. 3. The transmission simulation result of the Type-A graphene polarizer is shown in Fig. 3 (a). The plots give information about the condition of loading 0dB incident power, the transmitted cross-polarized wave exceeds -3dB, which is equivalent to half of the energy transmitted. The opposite propagation t_{xx}^o can be

lower than -10dB from 1.25 THz to 2.0 THz. Between 2.0 THz and 2.7 THz, the decrease of the cross-polarization transmittance is due to the sharp increase of the opposite propagation. The co-polarization transmission t_{xx} (or t_{yy}) and t_{xy} are all below -30dB.

The Fig. 3 (b) plots the performance of another device Type B. Among 1.125 THz and 2.375 THz, the power of cross-polarization transmission exceeds -3dB, and from 2.0 THz to 2.375 THz, it exceeds -1dB. The opposite propagation t_{xx}^o in the same frequency band is less than -10dB, at some frequency points close to -20dB. It shows that the transmission mode linear polarization converter of Type B has a high-performance over a broad-band.

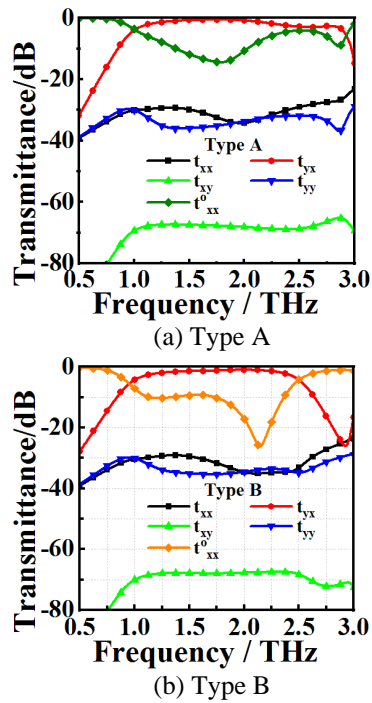


Fig. 3. Cross-polarized transmittance t_{yx} and opposite propagation t_{xx}^o are obtained through numerical simulations with x -polarization normal incidence. (a) Type A of graphene layout, and (b) Type B of graphene layout.

As shown in Fig. 4. (a), the PCR and the Absorption with x -polarized at normal incidence. First, we analyze the conversion rate of the Type A device. Between 0.5 THz and 2.75 THz the absorption ratio is kept below 20%. Between 0.75 THz and 2.8 THz the PCR is above 90%. In comparison, the performance of the Type B polarizer is analyzed in Fig. 4 (b). Between 0.5 THz and 2.75 THz the PCR is greater than 90%. At 2.9 THz, the PCR sudden decrease is due to the increase in opposite propagation t_{xx}^o and absorption of metasurfaces. The

parameter phase difference $\Delta\phi$ demonstrates the ability to transform the linear incoming wave by 90° of polarization. The absorption ratio of Type B decreases with the change of the chemical potential.

By comparison from Fig. 3 and Fig. 4, the Type B polarizer has better performance than the Type A. The device of Type B has a high-performance of 90% over a broad-band. Next, the performance of the graphene-loaded Type B polarizer was analyzed in detail.

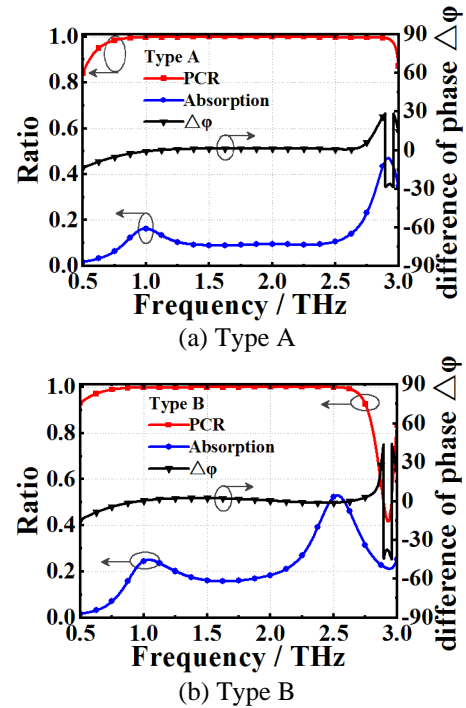


Fig. 4. The PCR and the Absorption and the phase difference with x -polarized normal incidence. (a) Type A of graphene layout, and (b) Type B of graphene layout.

IV. PERFORMANCE ANALYSIS

The principle of graphene-based double-layer transmission polarizer is F-P-like cavity. The schematic diagram of F-P-like cavity is shown in Fig. 5. In the multi-transmission process, the interference of polarization couplings may change total transmitted field about cross- and co-polarized. Analyze the interference process of waves to obtain the calculation method of transmittance. According to the formula definition, t_{xy}^h (r_{xy}^h) represent the y -polarized transmission (or reflection) coefficient of x -polarized incident on the h interface. The parameter h is 1 and 2, which represent the top and bottom of the F-P cavity, respectively. It should be noted that the transmittance (or reflectance) defined is equal to its square root, and it has nothing to do with the refractive index of the dielectric material near the interfaces.

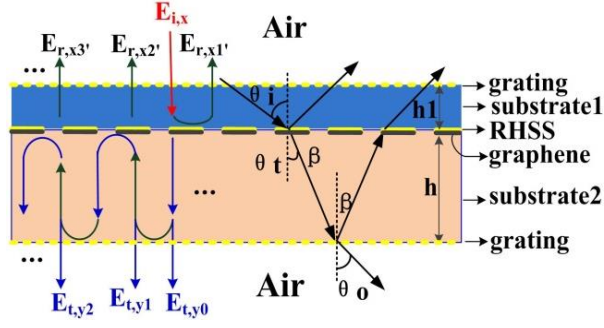


Fig. 5. Schematic diagram of a graphene-based double-layer dielectric F-P-like cavity.

According to the definition of light vector field in electromagnetic theory, the normal incident wave of x -polarized and the transmitted wave of y -polarized are $E_{i,x}$ and $E_{t,y}$. The letter n refers to the sequence round trip in the cavity. Generally, the grating layer is considered an ideal polarizer, and it can be easily calculated. Therefore, the y -polarized transmitting phase will be calculated, which ideal state is marked with a red line via Fig. 5. Under ideal conditions, since the y -polarized wave is transmitted round trip between the double-layer gratings, the electric field after the n th round trip is E_m , and the polarization transmission usually consists of several parts. Therefore, $E_{m,ym}$ ($m = 1, 2, \dots, 2n$) is defined to explanation each transmission part of $E_{m,y}$. The amplitude of $E_{m,ym}$ decreases exponentially with the increase of n . The loss caused by the absorbing of the structure is directly proportional to n . From the above analysis, the transmitting energy will be acquired via superimposing principal of n terms, formula is:

$$\vec{E}_{t,n} \approx \vec{E}_{t,y1} + \vec{E}_{t1,y2} + \vec{E}_{t2,y3} + \vec{E}_{t3,y4}. \quad (14)$$

Next, the principle of the polarizer is discussed from the electric field and surface current, which are shown in Fig. 5 and Fig. 6 at 1.47THz, 1.95 THz, and 2.6 THz when $E_F = \mu_c = 0.1\text{eV}$. It is important to establish the electromagnetic coupling effect between the multilayer transmitting polarizer in detail from the physical principle of the F-P-like cavity.

While the terahertz wave is incoming the polarizer, Fig. 6 (a) and Fig. 6 (b) show the surface currents on the patch and graphene strip, respectively, where the chemical potential $E_F = 0.1\text{eV}$ at 1.95 THz. The surface current along the RHS in Fig. 6 (a) is the same as the induced current on the graphene strips in Fig. 6 (b) at 1.47 THz, 1.95 THz and 2.6 THz. The graphs show that the surface current is mainly distributed on the RHS patch. At 1.47 THz and 2.6 THz, the surface current and RHS are vertically downward and upward respectively. At 1.95 THz, the surface current is downward in the RHS direction. The direction of the surface current is different at different frequencies, so the equivalent wavelength is different.

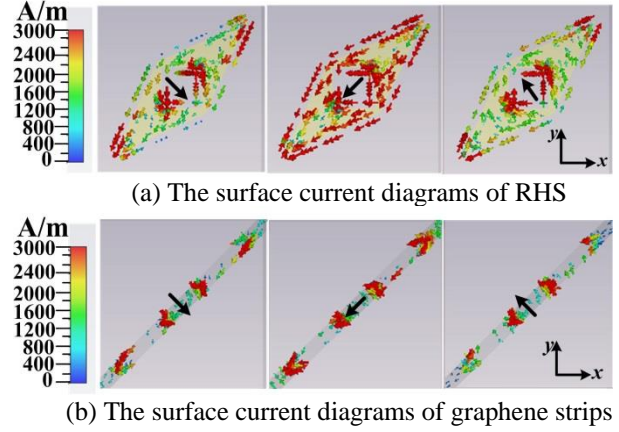


Fig. 6. The surface current diagrams of RHS and graphene strips at 1.47THz (left) 1.95 THz (middle) and 2.6 THz (right) when $E_F = \mu_c = 0.1\text{eV}$.

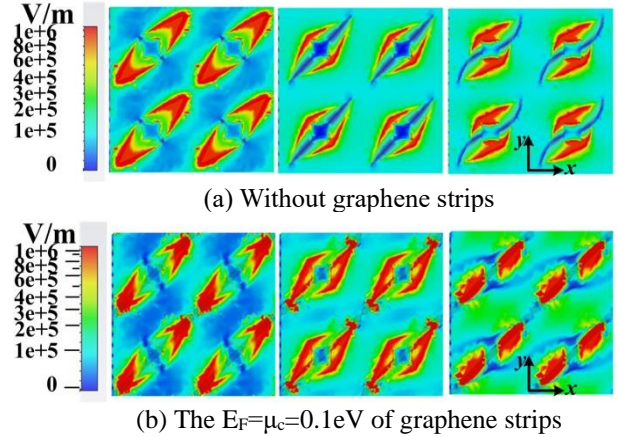


Fig. 7. The electric field diagrams of polarizer at 1.47THz (left) 1.95 THz (middle) and 2.6 THz (right).

When the x -polarized incident wave is proposed for RHS, the electric field diagrams of transmitted polarizer are shown in Fig. 7. The electric field diagrams of the polarizer without graphene strips in Fig. 7 (a). The area where the field strength is enhanced varies with different frequencies. When a graphene strip at E_F of 0.1 eV is loaded in Fig. 7 (b), the field strength focusing phenomenon at the corresponding frequency point is more obvious. The electromagnetic field accumulation in space among the tips of RHS resonator patches showing the capacitance characteristic. Via changing the Fermi energy, the impedance of the graphene strip is adjusted, and the metasurface structure parameters are adjusted. With the Fermi level of raise the permittivity of graphene gets closer and closer to the characteristics of gold. By optimizing various parameters, the proposed RHS of the original structure satisfies the condition of linear polarization conversion, that is, the amplitude of the transmitted y -polarized component equivalent to

the incident wave. Meanwhile, the phase difference is $\pm\pi+2k\pi$ approximately.

In order to analyze the performance of the RHS with graphene polarizer we designed, the transmittance of cross-polarization was simulated with x -polarized normal incidence are given in Fig. 8, while $E_F=\mu_c$ covers among 0.05eV and 1.0eV. It can be obtained that the transmitted terahertz waves are linearly polarized waves, when its phase difference $\Delta\varphi$ is given in Fig. 8 (a). The Figs. 8 (b), and (c) present the transmittance cross-polarized waves, the opposite propagation t_{xx} and absorption of the polarizer at different chemical potential μ_c . We plot the curve with the gradual increase of μ_c , the absorption rate of the transmitting polarizer continues to decrease, while the transmission cross-polarized wave gradually increases. When μ_c keeps increasing, the opposite propagation t_{xx} increases by a resonance point, so the frequency of the PCR is also broadened.

Figure 8 (d) shows the PCR simulation curves of graphene polarizer with different fermi energies. It can be seen from the figure $E_F=\mu_c=0.05\text{eV}$, 0.1V, 0.15eV, 0.2V, 0.25eV, 0.3eV, 0.5eV and 1 eV. The PCR of the proposed RHS are greater than 90% from 0.5 THz to 2.75THz. With the increase of E_F , the bandwidth is broadened, especially when $E_F=\mu_c=0.5\text{eV}$ and 1.0eV, the conversion rate reaches up to 99%. While it's transmitting polarization conversion efficiency maintains high performance. Therefore, it is concluded that the characteristics of the graphene strip are the key factor for the enhancement of the bandwidth of the proposed RHS polarizer.

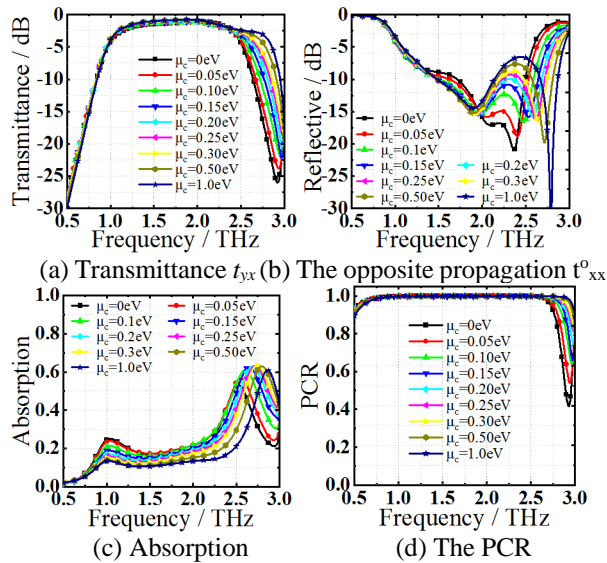


Fig. 8. The transmittance of cross-polarization was simulated vertical incidence with varying chemical potential $E_F=\mu_c$. (a) Transmittance cross-polarized waves t_{yx} , (b) transmissive co-polarized waves t_{xx} , (c) absorption, and (d) the PCR.

Finally, the transmittance of cross-polarization was simulated with x -polarized incidence at oblique incidence θ . As shown in Fig. 9 (a) with chemical potential $E_F=\mu_c=0.1\text{eV}$. From 1THz to 2THz, the high transmission performance can be maintained in the range of 0° - 60° with oblique incidence. The cross-polarization transmission performance in the high frequency range (2.1THz to 2.5THz) decreases when the oblique incidence is 60 degrees. In Fig. 9 (b), the opposite propagation t_{xx} gradually deteriorates and is greater than -10dB with the increase of oblique incident. In Fig. 9 (c), that it is mainly caused by the loss of absorption. The cross-polarized waves can transmit through the back of gratings, which still equivalent to a metal ground blocking the opposite propagation t_{xx} . The absorption rate of the polarizer is kept below 30% as the angle of incidence increases from 0.5 THz to 2 THz. Due to the metasurface structure of the device and graphene, as the incident angle increases, the absorption rate increases sharply from 2THz to 3THz. In Fig. 9 (d), from 0.5THz to 2.75 THz, the conversion rate is greater than 90%. The widening of the frequency is caused by the peaks in the PCR curve near 2.25, 2.75 and 2.9 THz. At these peaks, the efficiency is mainly limited by the dielectric loss.

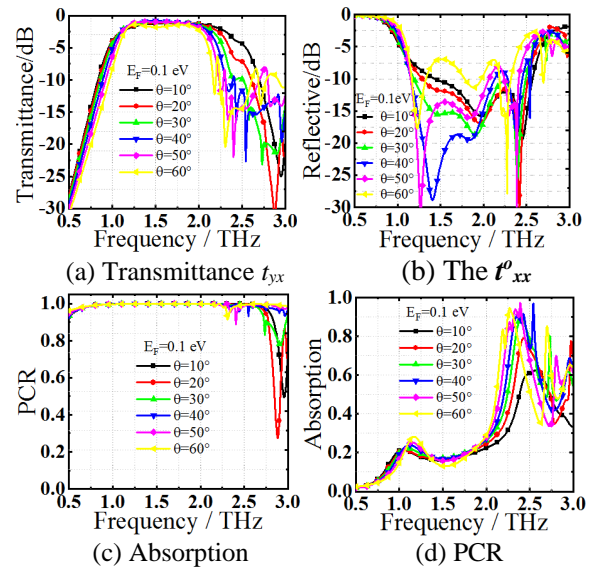


Fig. 9. The transmittance of cross-polarization was simulated or x -polarized incidence at oblique incidence θ with chemical potential $E_F=\mu_c=0.1\text{eV}$. (a) Transmittance cross-polarized wave's t_{yx} , (b) the opposite propagation t_{xx} , (c) absorption, and (d) PCR.

Compared with the other references in Table 2, the tri-layered resonant structure transmitting polarizer loaded with graphene is very competitive. The device achieves tunable ultra-wideband transmission performance. It is important that the PCR is still above 90% at large incident angles.

Table 2: Comparison of transmission polarizer performance

Ref.	OB (THz)	RB (PCR≥90%)	Tunable	OI
[17]	0.55-1.37	85.4%	No	0-45°
[18]	0.22-1.22	133%	No	No
[28]	0.23-1.17	134.3%	No	No
[29]	1.3-1.63	22.5%	Yes	0-90°
[30]	0.2-1.97	163.3	No	0-30°
This work	0.5-3	142.9%	Yes	0-60°

OB: Operator Bandwidth; RB: Relative Bandwidth; OI: Oblique incidence.

V. CONCLUSION

Our transmitting polarizers of graphene-based are wide incidence angle which achieved broadband and almost perfect polarization conversion transmission. In this study, two polarizers in the form of graphene strips are analyzed. The graphene strip of type B is on the diagonal of the unit structure, which has a high-performance over a broadband. Next, the performance of the graphene-based Type B polarizer was analyzed in detail, when E_F spans from 0.05eV to 1.0 eV. As the E_F increase, the bandwidth is also broadened, while its transmittance maintains high performance. Between 0.5 THz and 3 THz the PCR is greater than 90%, and the relative bandwidth up to 142.9%. Finally, the transmittance of cross-polarization was simulated at oblique incidence θ with chemical potential 0.1eV. The proposed novel tunable polarizer has high transmittance among in 0°-60°. The future research is the composite electromagnetic target simulation of the CATR, which is applied to the RF/THz composite scene simulation to cope with the complex and changing detection condition.

ACKNOWLEDGMENT

This research was supported by National Natural Science Foundation of China (Grant No. 61761012, 61661011), by Innovation Project of Guangxi Graduate Education (Grant No. YCBZ2019051), and by Guangxi Innovation Driven Development Special Fund Project (Grant No. GUIKEAA19254012).

REFERENCES

- [1] N. K. Grady, J. E. Heyes, D. R. Chowdhury, Y. Zeng, M. T. Reiten, A. K. Azad, A. J. Taylor, D. A. R. Dalvit, and H.-T. Chen, "Terahertz metamaterials for linear polarization conversion and anomalous refraction," *Science*, vol. 340, pp. 1304-1307, 2013.
- [2] A. Vakil and N. Engheta, "Transformation optics using graphene," *Science*, vol. 332, pp. 1291-1294, 2011.
- [3] L. Zakrajsek, E. Einarsson, N. Thawdar, M. Medley, and J. M. Jornet, "Lithographically defined plasmonic graphene antennas for terahertz-band communication," *IEEE Antennas and Wireless Propagation Letters*, vol. 15, pp. 1553-1556, 2016.
- [4] M. I. Shalaev, J. Sun, A. Tsukernik, A. Pandey, and K. Nikolskiy, "High-efficiency all-dielectric metasurfaces for ultracompact beam manipulation in transmission mode," *Nano Letters*, vol. 15, pp. 6261-6266, 2015.
- [5] M. Camacho, M. Camacho, R. R. Boix, S. A. Kuznetsov, M. Beruete, and M. Navarro-Cía, "Far-field and near-field physics of extraordinary THz transmitting hole-array antennas," *IEEE Transactions on Antennas and Propagation*, vol. 67, pp. 6029-6038, 2019.
- [6] M. Chen, L. Chang, X. Gao, H. Chen, C. Wang, X. Xiao, and D. Zhao, "Wideband tunable cross polarization converter based on a graphene metasurface with a hollow-carved "H" array," *IEEE Photon. J.*, vol. 9, pp. 1-11, 2017.
- [7] B. Vasic, D. C. Zografopoulos, and G. Isic, "Electrically tunable terahertz polarization converter based on overcoupled metal-isolator-metal metamaterials infiltrated with liquid crystals," *Nanotechnology*, vol. 28, p. 124002, 2017.
- [8] A. Zubair, D. Tsentalovich, C. Young, M. Heimbeck, and J. Kono, "Carbon nanotube fiber terahertz polarizer," *Applied Physics Letters*, vol. 108, no. 14, p. 141107, 2016.
- [9] D. J. Liu, Z. Y. Xiao, X. L. Ma, K. K. Xu, J. Y. Tang, and Z. H. Wang, "Broadband asymmetric transmission and polarization conversion of a linearly polarized wave based on chiral metamaterial in terahertz region," *Wave Motion*, vol. 66, pp. 1-9, 2016.
- [10] X. Yu, X. Gao, W. Qiao, L. Wen, and W. Yang, "Broadband tunable polarization converter realized by graphene-based metamaterial," *IEEE Photonics Technology Letters*, vol. 28, 1-1, 2016.
- [11] X. Gao, W. Yang, W. Cao, M. Chen, and H. Li, "Bandwidth broadening of a graphene-based circular polarization converter by phase compensation," *Opt. Express*, vol. 25, pp. 23945-23954, 2017.
- [12] L. Peng, X. Li, X. Jiang, and S. Li, "A novel THz half-wave polarization converter for cross-polarization conversions of both linear and circular polarizations and polarization conversion ratio regulating by graphene," *Journal of Lightwave Technology*, vol. 36, pp. 4250-4258, 2018.
- [13] F. Fan, S. Xu, X. Wang, and S. Chang, "Terahertz polarization converter and one-way transmission based on double-layer magneto-plasmonics of magnetized InSb," *Optics Express*, vol. 24, no. 23, pp. 26431-26443, 2016.
- [14] J. Woo, S. Hussain, and J. Jang, "A terahertz in-line polarization converter based on through-via connected double layer slot structures," *Scientific Reports*, vol. 7, p. 42952, 2017.

- [15] H. Mao, L. Xia, X. Rao, H. Cui, S. Wang, Y. Deng, D. Wei, J. Shen, H. Xu, and C. Du, "A terahertz polarizer based on multilayer metal grating filled in polyimide film," *IEEE Photonics Journal*, vol. 8, pp. 1-6, 2017.
- [16] J. Su, Z. Li, Z. Li, Q. Guo, and Y. Yang, "Ku-band phase-gradient metasurface for broadband high-gain circularly polarized lens antenna," *Applied Computational Electromagnetics Society Journal*, vol. 34, no. 5, pp. 669-675, 2019.
- [17] X. Jing, X. Gui, P. Zhou, and Z. Hong, "Physical explanation of Fabry-Pérot cavity for broadband bilayer metamaterials polarization converter," *Journal of Lightwave Technology*, vol. 36, pp. 2322-2327, 2018.
- [18] R. T. Ako, W. S. L. Lee, S. Atakaramians, M. Bhaskaran, and W. Withayachumnankul, "Ultra-wideband tri-layer transmissive linear polarization converter for terahertz waves," *APL Photonics*, vol. 5, no. 4, pp. 0461011-0461017, 2020.
- [19] S. Masuminia, C. Ghobadi, J. Nourinia, M. Karamirad, and B. Mohammadi, "A novel tunable graphene based terahertz absorber with polarization insensitive," *Applied Computational Electromagnetics Society Journal*, vol. 31, no. 12, 1439-1444, 2016.
- [20] K. Xu, J. Li, A. Zhang, and Q. Chen, "Tunable multi-band terahertz absorber using single-layer square graphene ring structure with T-shaped graphene strips," *Optics Express*, vol. 28, no. 8, 2020.
- [21] S. Xia, Z. Xiang, H. Yu, J. Liu, L. Wang, and S. Wen, "Graphene surface plasmons with dielectric metasurfaces," *Journal of Lightwave Technology*, vol. 35, pp. 4553-4558, 2017.
- [22] Y. Gang, F. Ling, Y. Jin, and Y. Rao, "Dynamically tunable terahertz cross polarization amplitude based on graphene metamaterials," *Optoelectronic Devices & Integration*, 38, JW3A, 2015.
- [23] X. Li, L. Lin, L. Wu, W. Yin, and J. Mao, "A, bandpass graphene frequency selective surface with tunable polarization rotation for THz applications," *IEEE Transactions on Antennas and Propagation*, vol. 65, pp. 662-672, 2017.
- [24] X. He, A. Hu, and X. Guo, "In-fiber graphene-h-BN polarizer with enhanced performance and bandwidth," *IEEE Photonics Journal*, vol. 99, 1-1, 2019.
- [25] S. Amanatiadis, T. Ohtani, Y. Kanai, and N. Kantartzis, "Effective design of graphene patch arrays for adjustable plane-wave scattering," *Applied Computational Electromagnetics Society Journal*, vol. 35, no. 11, pp. 1310-1311, 2021.
- [26] D. Chen, Y. Li, and X. Pang, "MMW/IR beam combiner with graphene IR window for MMW/IR compact range compound test," *Appl. Phys. Lett.*, vol. 110, p. 251902, 2017.
- [27] G. W. Hanson, "Dyadic, Green's functions for an anisotropic, non-local model of biased graphene," *IEEE Trans. Antennas Propag.*, vol. 56, pp. 747-757, 2008.
- [28] Y. Cheng, R. Gong, and L. Wu, "Ultra-broadband linear polarization conversion via diode-like asymmetric transmission with composite metamaterial for terahertz waves," *Plasmonics*, vol. 12, pp. 1113-1120, 2017.
- [29] L. Dai, Y. Zhang, Y. Zhang, S. Liu, and H. Zhang, "Multifunction tunable broadband terahertz device for polarization rotation and linear asymmetric transmission based on Dirac semimetals," *Optics Communications*, vol. 468, p. 125802, 2020.
- [30] W. Pan, Q. Chen, Y. Ma, X. Wang, and X. Ren, "Design and analysis of a broadband terahertz polarization converter with significant asymmetric transmission enhancement," *Optics Communications*, vol. 459, p. 124901, 2019.

High-Q Active Microwave Sensor Based on Microstrip Complementary Split-Ring Resonator (MCSRR) Structure for Dielectric Characterization

Hong-Yi Gan, Wen-Sheng Zhao, Da-Wei Wang, Jing Wang, Qi Liu, and Gaofeng Wang

MOE Engineering Research Center of Smart Micro-sensors and Micro-systems
School of Electronics and Information, Hangzhou Dianzi University, Hangzhou, 310018, China
honyigan@163.com, {wshzhao, davidw.zoeq, wangjing, liuqi67, gaofeng}@hdu.edu.cn

Abstract — This paper presents an active microwave sensor for the characterization of dielectric materials. The sensor is consisted of a microstrip complementary split-ring resonator (MCSRR) structure and an active feedback loop. The loop uses an amplifier to generate negative resistance to compensate the resonator's loss and increase the loaded quality factor. The developed sensor possesses the advantages of high quality factor, ultra-small electrical size, and high sensitivity. A prototype of the sensor is fabricated and measured for validation.

Index Terms — Active feedback loop, Microstrip Complementary Split-Ring Resonator (MCSRR), quality factor, sensor.

I. INTRODUCTION

Accurate measurement of complex permittivity of dielectric materials plays a vital role in healthcare, food safety, and industrial manufacturing [1]-[6]. To this end, microwave resonance planar sensors have been widely explored in recent years due to their low cost and easy fabrication [7]-[10]. In microwave resonance sensors, the resonant frequency and quality factor are related to the relative permittivity and electrical loss of the material under test. This is, as the MUT sample is loaded, the resonant frequency would shift downwards due to the increased resonator capacitance, while the quality factor is degraded due to the dielectric loss.

According to the frequency response characteristics, the microwave resonance planar sensors can be divided into two types, i.e., band-pass response and band-stop response. In [7] and [8], the split-ring resonator (SRR) and complementary split-ring resonator (CSRR) coupled microstrip transmission lines were used in the sensor design, and the complex permittivity of the MUT were extracted through the transmission zero. These two sensors act as band-stop filters. On the contrary, the microstrip SRR and microstrip CSRR (MCSRR) structures developed in [9] and [10] behave like band-pass filters, i.e., the transmission is close to 1 at the resonant point. It is evident that the band-pass sensor is

more suitable than the band-stop sensor to characterize the dielectric loss. This is because that the dielectric loss is usually retrieved by the variation in the notch depth, which is difficult to discern in a band-stop resonator, thereby putting pressure on the design of peripheral circuit.

However, due to conductor loss and radiation, the resonant magnitude of band-pass sensor in the measurement is usually much smaller than theoretical value (i.e., 0 dB). To improve sensor resolution, it is necessary to increase the quality factor as much as possible. The active feedback loop with a microwave amplifier can generate negative resistance to compensate the resonator's loss, and therefore was utilized to enhance the sensor's quality factor [11], [12]. In this paper, an MCSRR-based sensor is presented for dielectric characterization. The active feedback loop is employed to improve the sensor resolution. The rest of this paper is organized as follows. Section II introduces the structure of the proposed active MCSRR-based sensor, with the operating principle discussed. Section III presents the experimental validation, and some conclusions are finally drawn in Section IV.

II. MCSRR-LOADED PLANAR SENSOR

Figure 1 shows the schematic of the proposed microwave resonance sensor, which is composed of an MCSRR and an active feedback loop. The MCSRR can be viewed as a band-pass resonator, where the transmitted energy reaches maximum at the resonant point. The active loop is formed by connecting two 1.5 mm wide L-shaped microstrip lines through the transistor, which is placed with 3.25 mm distance away from the feedline of MCSRR. The transistor is MRF947, which is a low-noise, high-gain amplifier with a unity-gain current frequency of 10 GHz. The bending points of two L-shaped microstrip lines are connected to VB and VC, respectively, through a 2.2 nH inductor to bring the DC bias voltage to the base and collector of the transistor at resonance (1.64 GHz). The electrode and the emitter of the transistor are grounded.

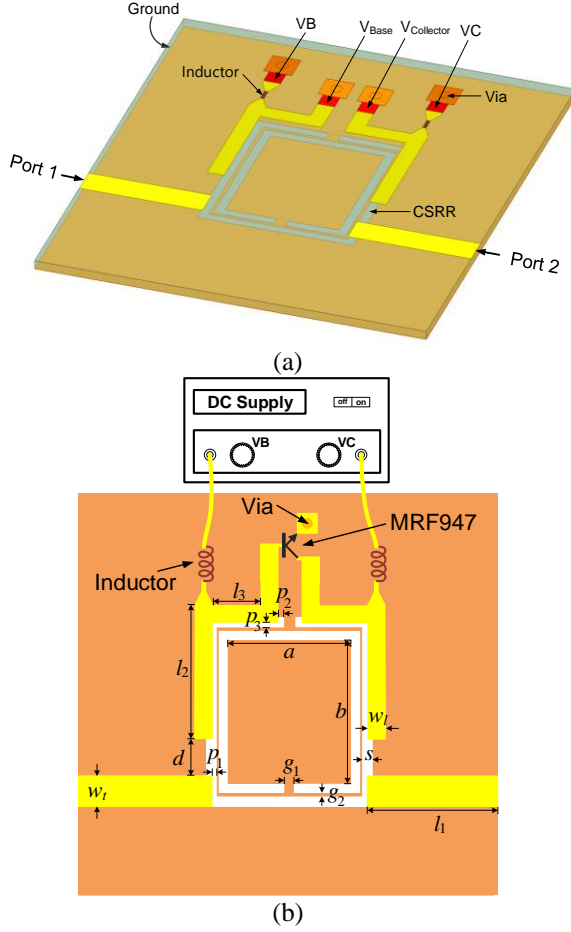


Fig. 1. (a) 3-D view and (b) planar view of the proposed MCSRR-based sensor.

The substrate is adopted as Rogers RO5880 with dielectric constant of 2.2 and loss tangent of 0.0009. The substrate dimension is $40\text{mm} \times 35\text{mm} \times 0.79\text{mm}$. As shown in Fig. 1 (b), the width of the microstrip line port is 2.5 mm, which is exactly matched to $50\ \Omega$ characteristic impedance. Detailed geometrical parameters are listed in Table 1. The MCSRR substrate occurs resonance when the resonant cavity stores an oscillating and balanced electric and magnetic energy. The resonant frequency changes when the distribution of the electromagnetic fields within the resonator perturbs. The change in the resonant frequency can be related to the MUT properties according to cavity perturbation theory:

$$\frac{\Delta f_r}{f_r} = \frac{\int_V (\Delta \epsilon |E_0|^2 + \Delta \mu |H_0|^2) dV}{\int_V (\epsilon_0 |E_0|^2 + \mu_0 |H_0|^2) dV}, \quad (1)$$

where Δf_r denotes the shift in the resonant frequency f_r , $\Delta \epsilon$ and $\Delta \mu$ are the variations in the permittivity and permeability, ϵ_0 and μ_0 are the permittivity and permeability in vacuum, E_0 and H_0 are the electric and magnetic fields, and v denotes the perturbed volume.

Table 1: Geometrical parameters (Unit: mm)

Parameter	Value	Parameter	Value
w_t	2.5	l_1	11
l_2	11.25	l_3	4
a	10.2	b	12.2
s	0.8	g_1	1
g_2	0.3	p_1	0.5
p_2	0.38	p_3	0.22
w_i	1.5	d	3.25

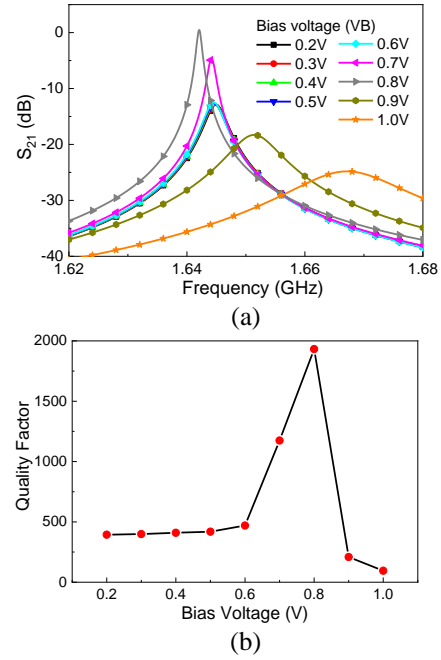


Fig. 2. (a) Transmission coefficient of the sensor with different bias voltages. (b) Quality factor versus bias voltage.

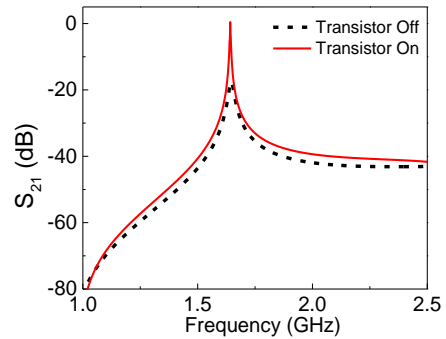


Fig. 3. Transmission coefficient of the sensor with different states of active loop. The bias voltage in the on state is 0.8 V.

To investigate the influence of active loop on the sensor quality factor, the frequency responses of the

designed sensor with active loop powered ON and OFF are captured and compared. Firstly, the sensor response of the original passive MCSRR-based sensor is simulated using commercial software ANSYS HFSS. HFSS is based on finite element method (FEM) that utilizes solutions of Maxwell's equations to compute the scattering parameters of each port. Then, the simulated scattering parameter matrix is input into the circuit simulator ADS. Since the physical parameters of the MCSRR structure, active loop, and lumped devices have been fixed, the only variable parameter is the gain controlled by the external voltage source (see Fig. 1 (b)). As shown in Fig. 2 (a), by tuning the bias voltage, the amplifier gain would be changed, thereby affecting the frequency response significantly. Here, the sensor quality factor is defined as the ratio of resonant frequency and 3 dB bandwidth, i.e., $Q = f_r/f_{3dB}$. It is calculated that the quality factor of passive MCSRR-based sensor is about 92.8. With the bias voltage increasing to 0.5V, the sensor response is almost unchanged, while the quality factor is slightly increased from 393.7 to 469.9. As the bias voltage exceeds 0.6 V, the transistor enters linear operating region and generates high gain, which greatly increases the sensor quality factor. It can be seen in Fig. 2 (b) that the quality factor reaches maximum value of 1931.9 as the bias voltage equals 0.8 V. Fig. 3 shows the simulated sensor responses with ON-state and OFF-state active loop (the bias voltage in the ON-state is 0.8 V). As transistor is turned on, the resonant frequency is reduced from 1.646 GHz to 1.642 GHz, implying the active loop has little influence on the resonant point and the measurement.

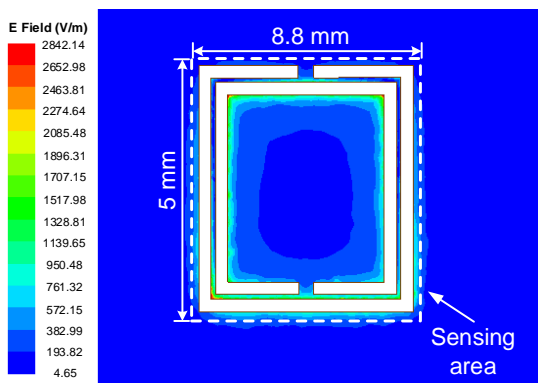


Fig. 4. Distribution of the electric field magnitude on the ground plane at the resonant frequency. The white dotted box in the middle represents the sensing area.

Further, the distribution of the electric field magnitude on the ground plane of the sensor is shown in Fig. 4. It is evident that the electric field intensity is mainly confined to the CSRR ring. The CSRR region, which is marked by the white dotted box in Fig. 4, is suitable to be used as sensing area to retrieve the

complex permittivity of the MUT sample. To validate the sensor function, an 8.5 mm×5 mm×1 mm-size MUT sample is placed onto the sensing area of the proposed sensor. The sensor responses to the MUT sample with different complex permittivity are shown in Fig. 5. In the simulation, the relative permittivity ϵ_r' and loss tangent $\tan \delta_e$ of the MUT sample are varied from 1 to 10 and from 0 to 0.1, respectively.

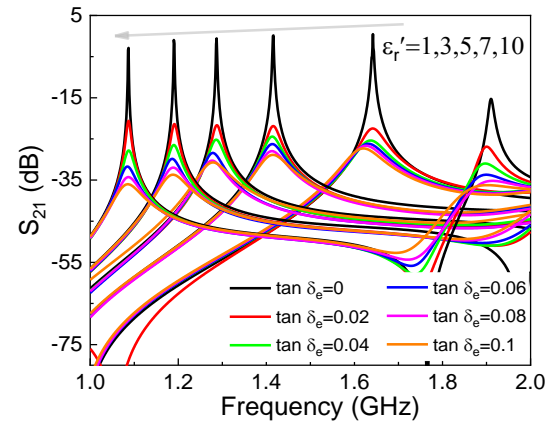


Fig. 5. Sensor responses for different values of (a) ϵ_r' and (b) $\tan \delta_e$ when an MUT sample is placed on the sensing area.

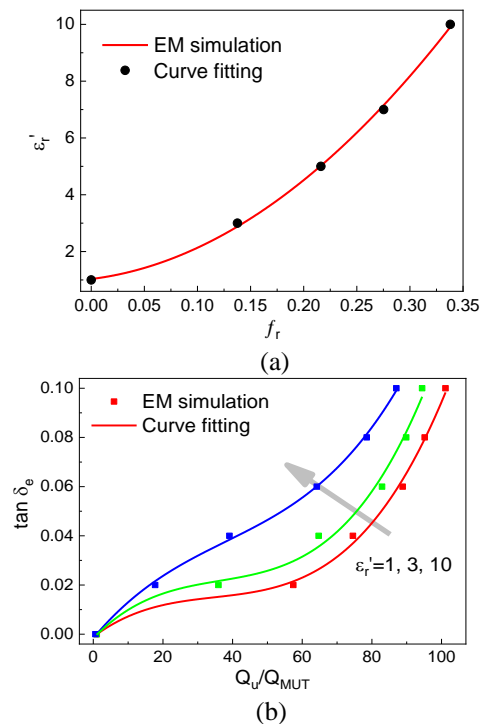


Fig. 6. Fitting curves for (a) ϵ_r' and (b) $\tan \delta_e$.

Owing to the effect of active loop, the proposed sensor possesses high quality factor, which is beneficial

to the extraction of resonant point as well as the design of peripheral circuit [13]. Moreover, as the loss tangent is usually retrieved by the variation in the quality factor, the sensor sensitivity in measuring the dielectric loss can be improved by employing the active loop [14]. With the help of curve fitting method, as shown in Fig. 6 (a), the function between relative permittivity ϵ_r' and resonant frequency shift Δf_r is given as:

$$\epsilon_r' = 1.0033 + 8.607\Delta f_r + 17.044\Delta f_r^2, \quad (2)$$

where $\Delta f_r = (f_u - f_{\text{MUT}})/f_u$, f_u denotes the resonant frequency of unloaded sensor, and f_{MUT} is the resonant frequency of the sensor with the MUT sample loaded.

When ϵ_r' is fixed, as shown in Fig. 5, the increase in the loss tangent $\tan \delta_e$ would result in a decrease in the quality factor. The loss tangent can be expressed as a function of inverse normalized quality factor, i.e., $Q_n = Q_u/Q_{\text{MUT}}$, where Q_u and Q_{MUT} represent the quality factors of the sensors unloaded and loaded, respectively. As shown in Fig. 6 (b), the loss tangent $\tan \delta_e$ increases monotonically with the increase of Q_n and the fitting function is given as:

$$\tan \delta_e = \sum_{i=0}^3 Q_n^i \cdot \sum_{j=0}^2 a_{ij} \epsilon_r'^j. \quad (3)$$

The fitting coefficient a_{ij} ($i, j = 0, 1, \text{ and } 2$) is listed in Table 2.

Table 2: Fitting coefficient a_{ij} for retrieving loss tangent

	$j = 0$	$j = 1$	$j = 2$
$i = 0$	-0.4796	-0.7459	-0.276
$i = 1$	5.316×10^{-2}	-8.891×10^{-2}	3.736×10^{-2}
$i = 2$	-3.745×10^{-2}	-0.2256	-4.297×10^{-3}
$i = 3$	5.923×10^{-6}	-3.28×10^{-5}	4.509×10^{-5}

III. RESULTS AND DISCUSSION

To validate the ability of the proposed MCSRR-based sensor in characterizing dielectric materials, a prototype of the sensor was processed, as shown in Fig. 7 (a). The input and output ports of the sensor are mounted with 50Ω SMA connectors for measuring the transmission data. The active loop is provided with 0.8 V bias voltage through the power supply. A number of dielectric materials are prepared and the transmission coefficients for testing these dielectric materials are recorded through the Keysight E5071C vector network analyzer (VNA).

Figure 7 (b) shows the measurement setup for the fabricated sensor. An $8.5 \text{ mm} \times 5 \text{ mm} \times 1 \text{ mm}$ -size sample of the MUT is placed on the sensing area, and the transmission coefficients are recorded with the VNA. The measured sensor responses are shown in Fig. 8. For unloaded sensor, the resonant frequency is 1.546 GHz, and the quality factor is about 1288. The measured data are deviated from the simulated values, which may be due to the dielectric loss of resonator, the noises of the

active loop, undesired signal at the frequency band, and the impact of the fluctuations in the environmental properties including temperature and humidity [15]. These deviations have little impact on the retrieval of the permittivity [16], and can be further suppressed by experimental calibration. For example, considering the deviations caused by manufacturing inaccuracies, the geometrical parameters of the fabricated sensor can be measured to correct the simulations [17]. Moreover, the measurement errors can be reduced by determining the fitting coefficients experimentally or adding error correction terms [18], [19]. Following the procedure described in [19], the fitting expressions are updated to increase the retrieval accuracy.

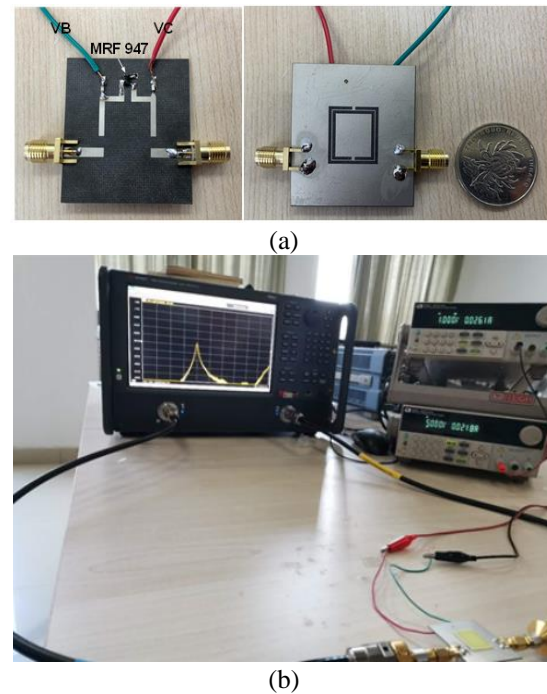


Fig. 7. (a) Photograph of the fabricated sensor and (b) experimental setup.

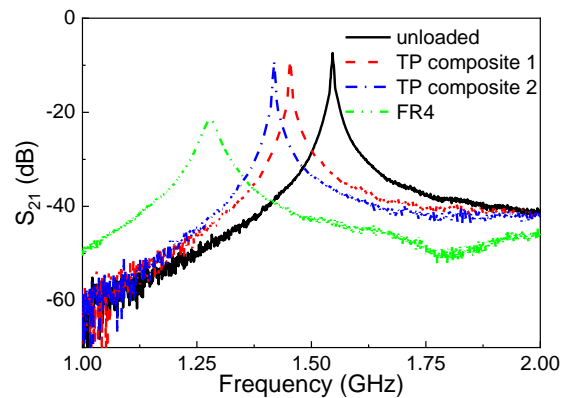


Fig. 8. Measured transmission coefficients.

Table 3: Comparison of the retrieved material parameters with reference values

	ϵ'_r		$\tan \delta_e$	
	Meas.	Ref.	Meas.	Ref.
TP composite 1	1.85	1.83	0	≤ 0.001
TP composite 2	2.23	2.2	0	≤ 0.001
FR4	4.51	4.4	0.018	0.02

Based on the measured data and fitting expressions, the complex permittivity of the MUT samples are calculated and compared with the reference values taken from manufacturer datasheets (see Table 3). The measured values are basically consistent with the reference values. Table 4 presents the comparison of the proposed sensor with previous designs. It is found that the proposed sensor has comparable performance but higher sensitivity and smaller electrical size than previous designs.

Table 4: Comparison of the proposed sensor with previous designs

	[11]	[12]	Proposed
Resonator	SRR	SRR	MCSRR
f_0 (GHz)	1.52	1.03/1.14	1.546
Q_0	1540	200	1288
Electrical size (λ_0^2)	0.132	0.121	0.052
S_{avg} ($\times 10^{-2}$)	0.17	0.36	4.67

III. CONCLUSION

In this paper, an MCSRR-based sensor was proposed for characterizing dielectric materials. The active feedback loop was employed to improve the quality factor, which is beneficial to the sensor resolution and the design of peripheral circuit. A prototype of the proposed sensor was fabricated and measured. It was demonstrated that the proposed sensor possesses high quality factor, small electrical size, and high sensor sensitivity, validating its potential for low-cost and precise characterization of dielectric materials.

ACKNOWLEDGMENT

This work was in part supported by NSFC under Grants 61874038, and the National Key R&D Program under Grant 2018YFE0120000.

REFERENCES

- [1] S. O. Nelson and S. Trabelsi, "Dielectric spectroscopy measurements on fruit, meat, and grain," *Trans. ASABE*, vol. 51, no. 5, pp. 1829-1834, Oct. 2013.
- [2] B. S. Cook, A. Shamim, and M. M. Tentzeris, "Passive low-cost inkjet-printed smart skin sensor for structural health monitoring," *IET Microw., Antennas Propag.*, vol. 6, no. 14, pp. 1536-1541, Nov. 2012.
- [3] G. Gennarelli, S. Romeo, M. R. Scarfi, and F. Soldovieri, "A microwave resonant sensor for concentration measurements of liquid solutions," *IEEE Sensors J.*, vol. 13, no. 5, pp. 1857-1864, May 2013.
- [4] J. Liu and P. B. Li, "Palladium decorated SWCNTs sensor for detecting methane at room temperature based on UWB-RFID," *Applied Computational Electromagnetics Society Journal*, vol. 31, no. 8, pp. 989-996, Aug. 2016.
- [5] M. H. Zarifi and M. Daneshmand, "Liquid sensing in aquatic environment using high quality planar microwave resonator," *Sens. Actuators B, Chem.*, vol. 225, pp. 517-521, Mar. 2016.
- [6] A. Ali, S. I. Jafri, A. Habib, Y. Amin, and H. Tenhunen, "RFID humidity sensor tag for low-cost applications," *Applied Computational Electromagnetics Society Journal*, vol. 32, no. 12, pp. 1083-1088, Dec. 2017.
- [7] L. Su, J. Mata-Contreras, P. Vélez, and F. Martín, "Splitter/combiner microstrip sections loaded with pairs of complementary split ring resonators (CSRRs): Modeling and optimization for differential sensing applications," *IEEE Trans. Microw. Theory Tech.*, vol. 64, no. 12, pp. 4362-4370, Dec. 2016.
- [8] A. Ebrahimi, J. Scott, and K. Ghorbani, "Differential sensors using microstrip lines loaded with two split-ring resonators," *IEEE Sensors J.*, vol. 18, no. 14, pp. 5786-5793, July 2018.
- [9] A. A. Abduljabar, D. J. Rowe, A. Porch, and D. A. Barrow, "Novel microwave microfluidic sensor using a microstrip split-ring resonator," *IEEE Trans. Microw. Theory Tech.*, vol. 62, no. 3, pp. 679-688, Mar. 2014.
- [10] H.-Y. Gan, W.-S. Zhao, Q. Liu, D.-W. Wang, L. Dong, G. Wang, and W.-Y. Yin, "Differential microwave microfluidic sensor based on microstrip complementary split-ring resonator (MCSRR) structure" *IEEE Sensors J.*, vol. 20, no. 11, pp. 41985-41999, Feb. 2020.
- [11] M. H. Zarifi, T. Thundat, and M. Daneshmand, "High resolution microwave microstrip resonator for sensing applications," *Sens. Actuators A, Phys.*, vol. 233, pp. 224-230, June 2015.
- [12] M. Abdolrazzagh and M. Daneshmand, "Dual active resonator for dispersion coefficient measurement of asphaltene nano-particles," *IEEE Sensors J.*, vol. 17, no. 22, pp. 7248-7256, Nov. 2017.
- [13] B. Yu, X. Ding, H. Yu, Y. Ye, X. Liu, and Q. J. Gu, "Ring-resonator-based sub-THz dielectric sensor," *IEEE Microw. Wireless Compon. Lett.*, vol. 28, no. 11, pp. 969-971, Nov. 2018.
- [14] W.-S. Zhao, H.-Y. Gan, Li. He, Q. Liu, D.-W. Wang, K. Xu, S. Chen, L. Dong, and G. Wang, "Microwave planar sensors for fully characterizing magneto-dielectric materials" *IEEE Access*, vol. 8,

pp. 41985-41999, Mar. 2020.

- [15] H. Saghlatoon, R. Mirzavand, and P. Mousavi, "Fixed-frequency low-loss dielectric material sensing transmitter," *IEEE Trans. Ind. Electron.*, available online in early access.
- [16] H.-Y. Gan, W.-S. Zhao, L. He, Y. Yu, K. Xu, F. Wen, L. Dong, and G. Wang, "A CSRR-loaded planar sensor for simultaneously measuring permittivity and permeability," *IEEE Microw. Wireless Compon. Lett.*, vol. 30, no. 2, pp. 219-221, Feb. 2020.
- [17] S. Sun and W. Menzel, "Novel dual-mode Balun bandpass filters using single cross-slotted patch resonator," *IEEE Microw. Wireless Compon. Lett.*, vol. 21, no. 8, pp. 415-417, Aug. 2011.
- [18] L.-C. Fan, W.-S. Zhao, D.-W. Wang, Q. Liu, S. Chen, and G. Wang, "An ultrahigh sensitivity microwave sensor for microfluidic applications," *IEEE Microw. Wireless Compon. Lett.*, vol. 30, no. 12, pp. 1201-1204, Dec. 2020.
- [19] A. Kapoor, P. K. Varshney, and M. J. Akhtar, "Inter-digital capacitor loaded electric-LC resonator for dielectric characterization," *Microw. Opt. Technol. Lett.*, vol. 62, no. 9, pp. 2835-2840, Sep. 2020.



H.-Y. Gan is currently pursuing the M.E. degree with Hangzhou Dianzi University, Hangzhou, China. His research interest is focused on the design of microwave sensors.



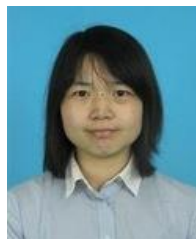
W.-S. Zhao received the B.E. degree from Harbin Institute of Technology, Harbin, China, in 2008, and the Ph.D. degree from Zhejiang University, Hangzhou, China, in 2013.

As a part of his Ph.D. program, he visited the National University of Singapore (17 months) from 2010 to 2013. After graduation, he joined Hangzhou Dianzi University, Hangzhou, China, where he has been a Full Professor since January 2020. He as a Visiting Scholar with Georgia Institute of Technology from 2017 to 2018. He has two books, three book chapters, and more than 80 journal articles (including more than 40 IEEE papers). His current research interests include IC interconnect and packaging, electromagnetic devices, and electronic design automation.

Zhao is a senior member of IEEE and CIE, and serves as an associate editor for IEEE Access and an editor for Microelectronics Journal.



D.-W. Wang is currently an Associate Professor with Hangzhou Dianzi University, Hangzhou, China. His research interests include computational electromagnetics, multiphysics simulation, and signal integrity analysis.



J. Wang is currently a faculty member with Hangzhou Dianzi University, Hangzhou, China. Her research interests include the design of tunnel transistors.



Q. Liu is currently a faculty member with Hangzhou Dianzi University, Hangzhou, China. Her research interests include the design and applications of microwave sensors.



G. Wang received the Ph.D. degree in Electrical Engineering from the University of Wisconsin-Milwaukee, WI, USA, in 1993, and the Ph.D. degree in Scientific Computing from Stanford University, Stanford, CA, USA, in 2001.

Wang is currently a Distinguished Professor with Hangzhou Dianzi University, Hangzhou, China. He has published more than 260 journal articles and held 48 patents. His current research interests include design, modeling, and simulation of IC and MEMS.

Fast Analysis of Broadband Electromagnetic Scattering Characteristics of Electrically Large Targets using Precorrected Fast Fourier Transform Algorithm based on Near Field Matrix Interpolation Method

Wei Bin Kong^{1,2}, Xiao Fang Yang¹, Feng Zhou¹, Jia Ye Xie³, Chuan Jie Chen¹, Na Li¹, and Wen Wen Yang⁴

¹ College of Information Engineering
Yancheng Optical Fiber Sensing and Application Engineering Technology Research Center
Yancheng Institute of Technology, Jiangsu Yancheng, 224051, China
kongweibin2007@sina.com,

² State Key Laboratory of Millimeter Waves
Southeast University, Jiangsu Nanjing, 210096, China

³ Industrial Center
Nanjing Institute of Technology, Jiangsu Nanjing, 211167, China

⁴ School of Information Science and Technology, Nantong University, Jiangsu Nantong, 226019, China

Abstract — In this paper, a new method is proposed to analyze the broadband electromagnetic characteristics of electrically large targets by combining the precorrected-FFT algorithm (P-FFT) with the near-field matrix interpolation technique. The proposed method uses the precorrected-FFT algorithm to reduce the storage and accelerate the matrix vector product of the far field. In order to make the precorrected-FFT algorithm can calculate the broadband characteristics of electrically large targets more quickly, the matrix interpolation method is used to interpolate the near-field matrix of the precorrected-FFT algorithm to improve the efficiency of calculation. The numerical results obtained validate the proposed method and its implementation in terms of accuracy and runtime performance.

Index Terms— Broadband electromagnetic scattering, interpolation technique, near matrix, P-FFT.

I. INTRODUCTION

As an accurate numerical method, method of moments (MoM) is widely used to analyze various complex electromagnetic problems [1]. However, the storage and calculation of MoM are very large, which limits the scale of solution to the problem. In order to expand the solution scale of MoM, many fast algorithms based on MoM are developed. It can be divided into two categories: one is the algorithm related to the integral kernel, such as FMM [2], MLFMA [3-4] and MLGFIM [5], and a class of methods based on fast Fourier

transform (FFT) (AIM, P-FFT, IE-FFT, etc. [6-14]). The other is matrix compression method, such as the adaptive cross approximation (ACA) algorithm [15-18], skeletonization [19], etc. The analysis of broadband electromagnetic scattering is very important for radar target stealth and identification engineering. However, it is necessary to obtain the broadband RCS data in radar target identification engineering. It will take a lot of time to solve the integral equation point by point at each frequency point in the whole frequency band by using MoM. In the process of obtaining the broadband electromagnetic characteristics of the target, the characteristics of these fast algorithms are different. The methods based on fast multipole mainly use the addition theorem of Green's function in free space, so it has the problem of "wavelet interruption". The methods based on fast Fourier transform (FFT) algorithm can be used in wide frequency band, but the calculation efficiency is not high if it is used directly. In the analysis of broadband electromagnetic problem, the grid of the highest frequency point is used to discretize the target surface, which saves the time of preprocessing. In addition, the electrical size of the target is constantly changing in the process of frequency sweeping calculation. Therefore, if the fast multipole method is adopted, the setting of the bottom box must be increased, which undoubtedly increases the storage capacity of the near-field matrix.

In this paper, the precorrected fast Fourier transform (FFT) algorithm combined with near-field matrix

interpolation technique is proposed to analyze the broadband electromagnetic characteristics of electrically large targets. The precorrected-FFT algorithm is used to speed up the solution of matrix vector multiplication. Moreover, the impedance matrix is stored sparsely, which reduces the memory requirement. At the same time, the matrix interpolation method is used to quickly fill the near matrix to improve the calculation speed.

II. METHOD OF MOMENTS OF ELECTROMANETIC FIELD

In order to solve the electric field integral equation (EFIE) and magnetic field integral equation (MFIE) numerically by the method of moments, firstly, the conductor surface is divided into triangles, and then the current density expressed by RWG basis function expansion is substituted:

$$\vec{E}^i(\vec{r})\Big|_{\text{tan}} = j\omega\mu\int_S[\vec{J}_s(\vec{r}') + \frac{1}{k^2}\nabla(\nabla\cdot\vec{J}_s)]G(\vec{r},\vec{r}')d\vec{r}'\Big|_{\text{tan}}, \quad (1)$$

$$n\times\vec{H}^i = \frac{\vec{J}_s(\vec{r}')}{2} - n\times P.V.\int_S\vec{J}_s(\vec{r}')\times\nabla G(\vec{r},\vec{r}')d\vec{r}', \quad (2)$$

where P.V. in (2) is Cauchy Principal value integral.

By using the Galerkin method, the RWG basis function $\vec{f}_m(\vec{r})$ is used as the testing basis function to test the equations (1) and (2):

$$Z_{mn}^{EFIE} = jk\eta\int_{S_m}ds\vec{J}_m(\vec{r})\cdot\int_{S_n}G(\vec{r},\vec{r}')\vec{J}_n(\vec{r}')ds' - j\frac{\eta}{k}\int_{S_m}ds[\nabla\cdot\vec{J}_m(\vec{r})]\cdot\int_{S_n}G(\vec{r},\vec{r}')[\nabla\cdot\vec{J}_n(\vec{r}')]ds', \quad (3)$$

$$Z_{mn}^{MFIE} = \frac{1}{2}\int_{S_m}\vec{J}_m(\vec{r})\cdot\vec{J}_n(\vec{r})ds + \int_{S_m}ds[\hat{n}\times\vec{J}_m(\vec{r})]\cdot\int_{S_n}\nabla G(\vec{r},\vec{r}')\times\vec{J}_n(\vec{r}')ds', \quad (4)$$

where, k and $\eta=\sqrt{\mu/\varepsilon}$ denote the wave number and wave impedance in free space. \vec{J}_m and \vec{J}_n are the test function and the basis function, respectively, S_m and S_n are their support sets.

Equations (3) and (4) are a series of linear equations, which are abbreviated as follows:

$$\sum_{n=1}^N Z_{mn} I_n = V_m, \quad m=1,2,\dots,N, \quad (5)$$

The expression (5) in the form of vector can be more succinctly written as the following matrix equation:

$$ZI=V, \quad (6)$$

which includes unknown current density I , elements of impedance matrix Z and excitation vector V .

The single electric field integral equation and the single magnetic field integral equation may encounter the phenomenon of internal resonance when dealing with the closed structure. That is to say, MoM matrix formed by the electric field integral equation and the magnetic field integral equation is almost singular or has a large condition number at some frequency points. However, the resonance frequency of the electric field integral equation is different from that of the magnetic field integral equation. Therefore, the combination field integral equation (CFIE) is derived by linear combination of electric field integral equation and magnetic field integral equation:

$$CFIE = \gamma EFIE + (1-\gamma)\eta MFIE, \quad (7)$$

where, the parameter $\gamma(\in[0,1])$ is generally selected as 0.5. CFIE not only guarantees high precision, but also has small matrix condition number.

III. P-FFT ALGORITHM

In P-FFT, the basis function is projected onto the corresponding grid, and the potential of the basis function is obtained by interpolating the potential of the grid. Before applying the P-FFT, it is necessary to construct a cube containing the whole solution domain. The cube is evenly divided into a series of grids, and the grid is further evenly divided into a series of meshes.

Generally speaking, the P-FFT can be divided into four steps: projection, convolution, interpolation and precorrection. Finally, the P-FFT approximate expression of Z_{mn} is obtained:

$$Z_{mn}^{P-FFT} = (Z_{mn} - Z_{mn}^{(P-FFT)-far}) + Z_{mn}^{(P-FFT)-far} \cong Z_{mn}^{(P-FFT)-near} + Z_{mn}^{(P-FFT)-far}, \quad (8)$$

where the calculation formula of $Z_{mn}^{(P-FFT)-far}$ is:

$$Z_{mn}^{(P-FFT)-far} = R_m^T H W_n. \quad (9)$$

The projection operator W projects the basis function to the regular grid, the convolution operator H calculates the potential of the regular grid, and the interpolation operator R calculates the potential on the basis function according to the potential on the regular grid.

IV. INTERPOLATION TECHNIQUE OF MOM MATRIX

Over the entire frequency band, the MoM matrix element $Z_{mn}(f)$ is a function of frequency. Set the frequency variation range as $[f_l, f_h]$, the scatterer is discretized at the highest frequency, and adopt triangular

mesh. The wavelength at the highest frequency is recorded as λ_h . In this case, the expressions of matrix elements of EFIE and MFIE are as follows:

$$Z_{mn}^E(f_r) = \int_{S_m(\lambda_h)} ds \int_{S_n(\lambda_h)} ds' \left[\vec{J}_m(\vec{r}) \cdot \vec{J}_n(\vec{r}') k_r - \nabla_h \cdot \vec{J}_m(\vec{r}) \nabla_h' \cdot \vec{J}_n(\vec{r}') \frac{1}{k_r} \right] \frac{e^{-jk_r R}}{R} \frac{j\eta\lambda_h^2}{4\pi}, \quad (10)$$

$$Z_{mn}^M(f_r) = \left[\int_{S_m(\lambda_h)} ds \vec{J}_m(\vec{r}) \cdot \vec{J}_n(\vec{r}) - \frac{1}{2\pi} \int_{S_m(\lambda_h)} ds \vec{J}_m(\vec{r}) \cdot \hat{n} \times \int_{S_n(\lambda_h)} ds' \nabla_h \frac{e^{-jk_r R}}{R} \times \vec{J}_n(\vec{r}') \right] \frac{\eta\lambda_h^2}{2}, \quad (11)$$

where, $k_r = 2\pi f_r$, the normalized frequency is $f_r = f / f_h$ in the interval $[f_l / f_h, 1]$. The following changes:

$$z_{mn}^S(f_r) := \frac{Z_{mn}^S(f_r)}{\lambda_h^2}, \quad (12)$$

where, the superscript S represents E, M, C .

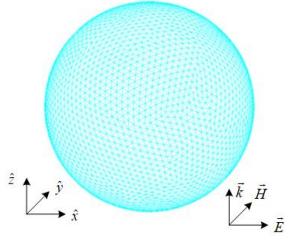


Fig. 1. A PEC sphere with radius $1.5\lambda_h$.

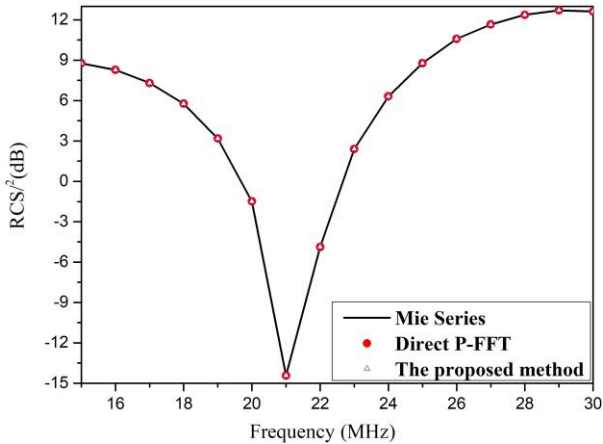


Fig. 2. Wide frequency band RCS curve of PEC sphere.

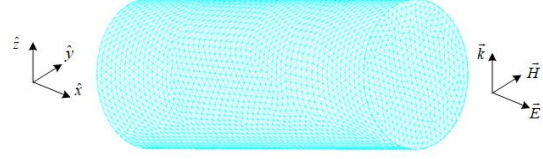


Fig. 3. A PEC cylinder with length $5\lambda_h$ and radius λ_h .

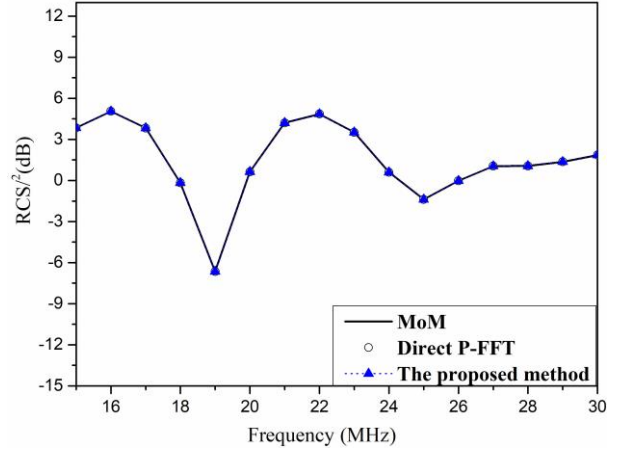


Fig. 4. Wide frequency band RCS curve of PEC cylinder.

Table 1: CPU time comparison of different algorithms for the three examples at 23 MHz (time: seconds)

Ex.	Method	Cartesian Grid Spacing	Filling Time of Z^{near}	Filling Time of the Near Part of Z^{far}
A	Direct P-FFT	$h = 0.2\lambda_h$	21.6	0.5
	The proposed method	$h = 0.2\lambda_h$	0.8	0.5
B	Direct P-FFT	$h = 0.2\lambda_h$	19.6	0.4
	Triangle-Triangle	$h = 0.2\lambda_h$	0.7	0.4
C	Direct P-FFT	$h = 0.2\lambda_h$	15.2	0.3
	The proposed method	$h = 0.2\lambda_h$	0.5	0.3
D	Direct P-FFT	$h = 0.2\lambda_h$	166.2	3.8
	The proposed method	$h = 0.2\lambda_h$	6.4	3.8
	AIM	$h = 0.1\lambda_h$	146.1	3.1

Considering the fluctuation caused by the phase term $e^{-jk_r R}$, the correction matrix elements can be constructed as follows:

$$\tilde{z}_{mn}^S(f_r) = \begin{cases} z_{mn}^S(f_r) f_r e^{jk_r R_{mn}} & S_m \cap S_n = 0 \\ z_{mn}^S(f_r) f_r & S_m \cap S_n \neq 0 \end{cases}, \quad (13)$$

where, the description of the relationship between S_m and S_n can be found in [20]. In this way, it becomes a quadratic polynomial about $\tilde{z}_{mn}^S(f_r)$.

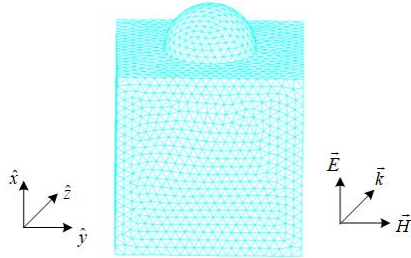


Fig. 5. A PEC combination of hemisphere and cube.

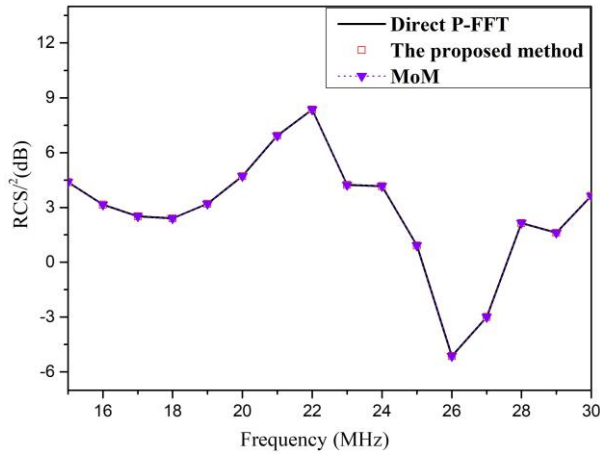


Fig. 6. Wide frequency band RCS curve of PEC combination of hemisphere and cube.

The modified matrices at $y_i = f_i / f_h$ ($i = 0, 1, 2, 3$; $f_i \in [f_l, f_h]$) which are optical frequency samples are generated primarily in the cubic polynomial inter/extrapolation method under investigation. The inter/extrapolation formula for each f_r is expressed as [21]:

$$\tilde{z}_{mn}^S(f_r) = \sum_{i=0}^3 \tilde{z}_{mn}^S(y_i) \varphi_i(f_r), \quad (14)$$

where

$$\varphi_i(f_r) = \prod_{j=0, j \neq i}^3 \left(\frac{f_r - y_j}{y_i - y_j} \right), \quad (15)$$

V. NUMERICAL RESULTS

In order to verify the correctness and efficiency of the proposed algorithm, some numerical examples are provided: a PEC sphere, a PEC cylinder, a PEC combination of hemisphere and cube and a PEC missile model. In all the examples, take the expansion order as $M = 2$. When the Cartesian grid spacing is at the highest frequency f_h , it is taken as $h_x = h_y = h_z = h$.

Example A: A PEC sphere

Consider a PEC sphere which's radius is $1.5\lambda_h$ with the incident angle of plane wave as shown in Fig. 1. The frequency range is [15 MHz, 30 MHz], and the frequency interval is $\Delta f = 1$ MHz. The surface of the sphere is discretized into triangular mesh with an edge length of about $\lambda_h / 10$. 10461 RWG basis functions are generated.

Figure 2 shows the broadband RCS curve with scattering angle $(\theta^s, \phi^s) = (40^\circ, 0^\circ)$ obtained by using the fast sweep frequency P-FFT algorithm. In the calculation, direct P-FFT with point-by-point calculation and the proposed method with interpolation technique are used. The results show that the two algorithms are in good agreement with the results of Mie series. Table 1 shows the time consumed by direct P-FFT and the proposed method at 23MHz. It can be seen that the latter significantly improves the computational efficiency. In this example, the proposed method takes 546.2 seconds to complete the full band calculation, while the direct with point-by-point calculation takes 810.1 seconds.

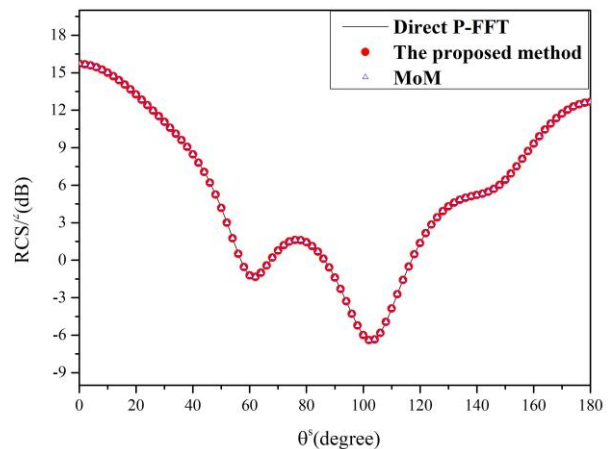


Fig. 7. Comparisons of the bistatic RCS of PEC combination of hemisphere and cube at 16MHz.

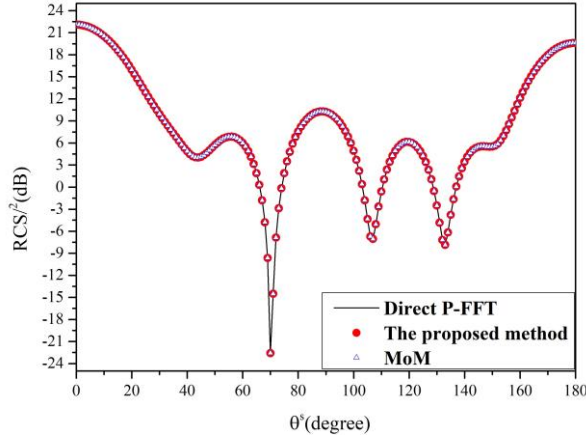


Fig. 8. Comparisons of the bistatic RCS of PEC combination of hemisphere and cube at 23MHz.

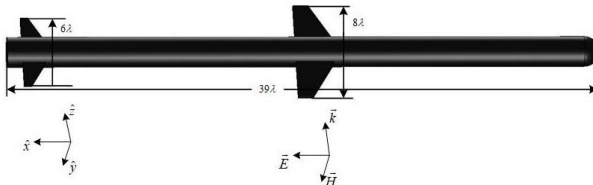


Fig. 9. A PEC missile model.

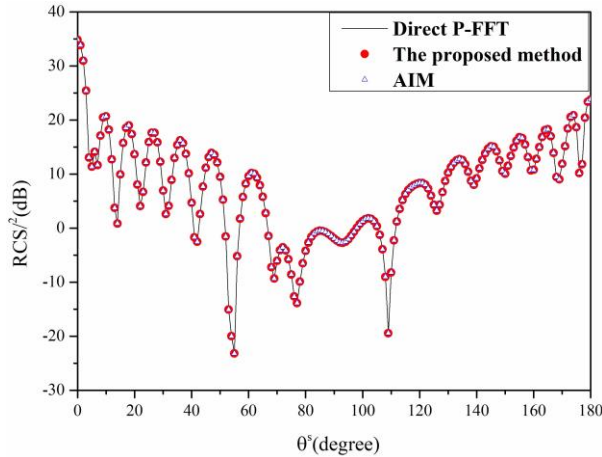


Fig. 10. Comparisons of the bistatic RCS of PEC missile model at 11MHz.

Example B: A PEC cylinder

A PEC cylinder of length $5\lambda_h$ and radius λ_h is shown in Fig. 3. The surface of the cylinder is discretized into triangular mesh with an edge length of $\lambda_h/10$ about 12675 RWG basis functions. The direction of incident plane wave and polarization direction of electric field are shown in Fig. 3. The frequency range is [15 MHz, 30 MHz], and the frequency interval is $\Delta f = 1$ MHz.

Figure 4 shows the broadband RCS curve with scattering angle $(\theta^s, \phi^s) = (70^\circ, 0^\circ)$ obtained by using the fast sweep frequency P-FFT algorithm. Direct P-FFT with point-by-point calculation, the proposed method with interpolation technique and MoM with point-by-point calculation are used in the calculation. By comparing the RCS obtained by the three algorithms, it shows that they are good agreement. Table 1 shows the time consumed by direct P-FFT and the proposed method with interpolation technique at 23 MHz. It can be seen that the latter significantly improves the computational efficiency. In this example, the proposed method with interpolation technique takes 695.2 second-ds to complete the full band calculation, while the direct P-FFT takes 956.4 seconds.

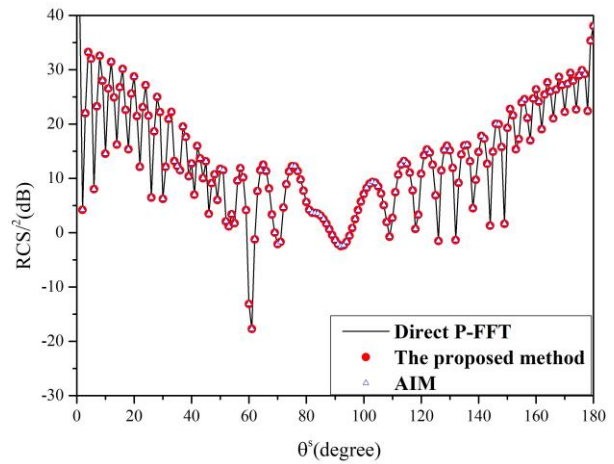


Fig. 11. Comparisons of the bistatic RCS of PEC missile model at 24MHz.

Example C: A PEC combination of hemisphere and cube

A combination model of a PEC hemisphere and a cube is considered. The surface of the combination model is discretized into triangular mesh, and its edge length is about $\lambda_h/10$. A total of 8471 RWG basis functions are generated, as shown in Fig. 5. The incident angle of incident plane wave is $(\theta^i, \phi^i) = (0^\circ, 0^\circ)$, and the polarization direction of electric field is shown in Fig. 5. The frequency range is [15 MHz, 30 MHz], and the frequency interval is $\Delta f = 1$ MHz.

Figure 6 shows the broadband RCS curve with scattering angle $(\theta^s, \phi^s) = (125^\circ, 0^\circ)$ obtained by using the fast sweep frequency P-FFT algorithm. Direct P-FFT with point-by-point calculation, the proposed method with interpolation technique and MoM with point-by-point calculation are used in the calculation. Figure 7 and Fig. 8 compare the bistatic RCS at 16 and 23MHz. It is observed that the results of the proposed

method agree very well with direct P-FFT and MoM. Table 1 shows the time consumed by direct P-FFT and the proposed method with interpolation technique at 23MHz. It can be seen that the latter significantly improves the computational efficiency. In this example, the proposed method with interpolation technique takes 710.1 seconds to complete the full band calculation, while the direct P-FFT takes 975.5 seconds.

Example D: A PEC missile

To examine the correctness of the proposed method, the broadband EM scattering from 5 to 30MHz of a PEC missile model shown in Fig. 9 is analyzed, and the frequency interval is $\Delta f = 1$ MHz. The model is discretized with 98475 RWG bases.

In Fig. 10 and Fig. 11, direct P-FFT with point-by-point calculation and AIM with point-by-point calculation are compared. Figure 10 and Fig. 11 illustrate the bistatic RCS curves at 11MHz and 24MHz, which differ from the interpolated nodes. The figure shows that the results of the proposed method are in good agreement with those of direct P-FFT point by point calculation and AIM. Related data of the three schemes are recorded in Table 1 at 23MHz. In this example, the proposed method with interpolation technique takes 4.1 hours to complete the full band calculation, while the direct P-FFT takes 5.2 hours. In this case, the proposed method with interpolation technique reduces the total CPU time by about 22% with almost no change in accuracy.

VI. CONCLUSION

In this paper, P-FFT and near-field matrix interpolation technique are combined to analyze the broadband scattering characteristics of targets. The matrix interpolation technique is introduced into P-FFT to improve the efficiency of near-field matrix filling, and avoid the problem that the traditional P-FFT takes too much time to calculate each frequency point. Finally, numerical results verify the correctness and effectiveness of the proposed method for calculating the broadband RCS of targets.

ACKNOWLEDGMENT

This work was supported partly by the National Natural Science Foundation of China under Grant 62071256, 11801492, The Natural Science Foundation of the Jiangsu Higher Education Institutions of China under Grant No. 18KJD510010, 19KJB120014, 19KJB510061, 19KJA110002, 20KJB140025.

REFERENCES

- [1] R. F. Harrington, *Field Computation by Moment Methods*. New York, NY, USA: MacMillan, 1968.
- [2] N. Engheta, W. D. Murphy, V. Rokhlin, and M. S. Vassiliou, "The fast multipole method (FMM) for electromagnetic scattering problems," *IEEE Trans. Antennas Propag.*, vol. 40, no. 6, pp. 634-641, June 1992.
- [3] J.-M. Song, C.-C. Lu, and W. C. Chew, "Multi-level fast multipole algorithm for electromagnetic scattering by large complex objects," *IEEE Trans. Antennas Propag.*, vol. 45, no. 10, pp. 1488-1493, Oct. 1997.
- [4] C. Delgado and F. Catedra, "Fast monostatic RCS computation using the near-field sparse approximate inverse and the multilevel fast multipole algorithm," *Applied Computational Electromagnetics Society*, vol. 35, no. 7, pp. 735-741, 2020.
- [5] L. Li, H. G. Wang, and C. H. Chan, "An improved multilevel Green's function interpolation method with adaptive phase compensation," *IEEE Trans. Antennas Propag.*, vol. 56, no. 6, pp. 1381-1393, 2008.
- [6] E. Bleszybski, M. Bleszynski, and T. Jaroszewicz, "AIM: Adaptive integral method for solving large-scale electromagnetic scattering and radiation problems," *Radio Science*, vol. 31, pp. 1225-1251, 1996.
- [7] J. R. Phillips and J. K. White, "A precorrected-FFT method for electrostatic analysis of complicated 3-D structures," *IEEE Trans. Computer-Aided Design of Integrated Circuits and Systems*, vol. 16, pp. 1059-1072, 1997.
- [8] W. J. Yu, C. H. Yan, and Z. Y. Wang, "Fast multi-frequency extraction of 3-D impedance based on boundary element method," *Microw. Opt. Tech. Lett.*, vol. 50, no. 8, pp. 2191-2197, 2008.
- [9] C. F. Wang, F. Ling, and J. M. Jin, "A fast full-wave analysis of scattering and radiation from large finite arrays of microstrip antennas," *IEEE Trans. Antennas Propag.*, vol. 46, no. 10, pp. 1467-1474, Oct. 1998.
- [10] S. Seung Mo and J. F. Lee, "A fast IE-FFT algorithm for solving PEC scattering problems," *IEEE Trans. Magn.*, vol. 41, no. 5, pp. 1476-1479, May 2005.
- [11] M. Li, R. S. Chen, H. Wang, Z. Fan, and Q. Hu, "A multilevel FFT method for the 3-D capacitance extraction," *IEEE Trans. Comput. Aided Design Integr.*, vol. 32, no. 2, pp. 318-322, Feb. 2013.
- [12] J. Y. Xie, H. X. Zhou, W. B. Kong, J. Hu, Z. Song, W. D. Li, and W. Hong, "A novel FG-FFT method for the EFIE," *Int. Conf. Comput. Problem-Solving (ICCP)*, 2012.
- [13] J. Y. Xie, H. X. Zhou, W. Hong, W. D. Li, and G. Hua, "A highly accurate FGG-FG-FFT for the combined field integral equation," *IEEE Trans. Antennas Propag.*, vol. 61, no. 9, pp. 4641-4652, 2013.
- [14] W. B. Kong, H. X. Zhou, K. L. Zheng, X. Mu, and W. Hong, "FFT-based method with near-matrix

- compression,” *IEEE Trans. Antennas Propag.*, vol. 65, no. 11, pp. 5975-5983, 2017.
- [15] M. Li, T. Su, and R. S. Chen, “Equivalence principle algorithm with body of revolution equivalence surface for the modeling of large multiscale structures,” *IEEE Trans. Antennas Propag.*, vol. 64, no. 5, pp. 1818-1828, 2016.
- [16] M. Li, M. A. Francavilla, R. S. Chen, and G. Vecchi, “Wideband fast kernel-independent modeling of large multiscale structures via nested equivalent source approximation,” *IEEE Trans. Antennas Propag.*, vol. 63, no. 5, pp. 2122-2134, 2015.
- [17] H. X. Zhou, G. Y. Zhu, W. B. Kong, and W. Hong, “An upgraded ACA algorithm in complex field and its statistical analysis,” *IEEE Trans. Antennas Propag.*, vol. 65, no. 5, pp. 2734-2739, 2017.
- [18] A. Heldring, E. Ubeda, and J. M. Rius, “Stochastic estimation of the frobenius norm in the ACA convergence criterion,” *IEEE Trans. Antennas Propag.*, vol. 63, no. 3, pp. 1155-1158, 2015.
- [19] H. Rasool, J. Chen, X. M. Pan, and X. Q. Sheng, “Skeletonization accelerated solution of Crank-Nicolson method for solving three-dimensional parabolic equation,” *Applied Computational Electromagnetics Society*, vol. 35, no. 9, pp. 1006-1011, 2020.
- [20] W. D. Li, H. X. Zhou, W. Hong, and T. Weiland, “An accurate interpolation scheme with derivative term for generating MoM matrices in frequency sweeps,” *IEEE Trans. Antennas Propag.*, vol. 57, no. 8, pp. 2376-2385, 2009.
- [21] W. D. Li, H. X. Zhou, J. Hu, Z. Song, and W. Hong, “Accuracy improvement of cubic polynomial inter/extrapolation of MoM matrices by optimizing frequency samples,” *IEEE Antennas Wireless Propag. Lett.*, vol. 10, pp. 888-891, 2011.

A Compact High Gain Multiband Bowtie Slot Antenna with Miniaturized Triangular Shaped Metallic Ground Plane

Zaheer A. Dayo¹, Qunsheng Cao^{1,*}, Yi Wang¹, Permanand Soothar², Imran A. Khoso¹, Gulab Shah¹, and Muhammad Aamir³

¹ College of Electronic and Information Engineering
Nanjing University of Aeronautics and Astronautics, Nanjing, 211106, Peoples Republic of China
zaheer.dayo, qunsheng, jflsjfls, shah_hussain @nuaa.edu.cn; imrankhoso2@gmail.com

² School of Electronic and Optical Engineering
Nanjing University of Science and Technology, Nanjing, 210094, Peoples Republic of China
permanand.soothar@njust.edu.cn

³ Department of Computer, Huanggang Normal University Huangzhou, Hubei, 438000, China, Peoples Republic of China
aamirshaikh86@hotmail.com

Abstract — This paper presents a new compact, high gain and multiband planar bowtie slot antenna. The antenna structure comprises of dielectric substrate, copper conducting sheet, fillet triangular-shaped slots, and a chamfered metallic ground plane. The proposed antenna model is fed with the 50 Ω standard grounded coplanar waveguide (GCPW) feedline. The designed antenna is low profile with compact dimensions of $0.379\lambda \times 0.186\lambda \times 0.012\lambda$ at 2.39 GHz frequency. Stable multi-resonant behavior of frequencies is obtained with the material selection, slots dimensions and position. Moreover, the parametric study has been carried out in order to validate the frequency tuning mechanism and impedance matching control. The novelty of designed antenna lies in high performance features which have been achieved with ultra-compact ($0.039\lambda \times 0.022\lambda$) modified triangular shaped metallic ground plane. The proposed antenna is fabricated and experimentally verified. The antenna key features in terms of return loss, surface current distribution, peak gain, radiation efficiency and radiation patterns have been analyzed and discussed. The designed radiator exhibits the excellent performance including strong current density, peak realized gain of 6.3 dBi, 95% radiation efficiency, wide fractional bandwidth of 39.5% and good radiation characteristics at in-band frequencies. The simulation and measured results are in good agreement and hence make the proposed antenna a favorable candidate for the advanced heterogeneous wireless communication applications.

Index Terms — Advanced Heterogeneous Wireless Communication Applications, Bow-tie Slot Antenna, Compact, High Gain, Triangular shaped Ground Plane.

I. INTRODUCTION

In past few decades, the demand to integrate multiple communication standards into a single device is increasing rapidly [1]. At present, different modern communication services are offered seamlessly by one device at the same time. Besides, there are multiple standards which can support wireless local area network (WLAN), wireless fidelity (WIFI), world-wide interoperability over microwave access (WiMAX), global positioning systems (GPS), radio detection and ranging (RADAR) and satellite communication applications. It is important to design a system which can support multiple service standards and covers advanced heterogeneous applications including the civil and military regime [2]. Therefore, it is still a challenging task for active researchers to design a compact, multiband and high gain antenna with miniaturized triangular shaped metallic ground plane (MGP) specific for advanced heterogeneous wireless communication applications.

In the last five years, the researchers proposed several approaches and modified designs of slot antennas to achieve the multiband features. These approaches mainly focused on the different feeding networks [3],[4],[5], etching out slots from the radiating patch [6],[7],[8], defected ground structure (DGS) [9]–[11], artificial magnetic conductor (AMC) loaded lattice [12], complementary split ring resonator (CSRR) loaded metamaterial cell geometry [13],[14],[15] and fractal structures [16]. A dual-band antenna with cavity backed substrate integrated waveguide (SIW) approach has been reported [17]. The authors proposed annular ring slot antenna, which exhibited narrowband features [18]. A reconfigurable slot antenna with gamma shaped slots and

PIN diodes for different applications has been suggested [19]. A tapered slot antenna (TSA) array reported the optimal performance with increased the number of radiating elements [20]. These antennas have the complex geometries and operated at a given range.

Furthermore, the planar antennas with different configurations including U shaped slots and butterfly shaped parasitic elements [21], omega shaped strips cut out from rectangular slot [22], slotted inverted omega shaped MGP [23] and the single layer multi-element approach planar antennas have been reported [24]. The antennas achieved the different functions and cover multiple wireless communication applications. In the literature, antennas exhibited the dual-band triple-band and quad-band response [25],[26],[27] with reasonable performance. However, the suggested methods were complex and time consuming.

Recently, modified designs of multiband antennas have also been found in the literature. The authors designed the simple antennas with embedded slots on the radiator and obtained the penta-band and hexa-band response [28]. A comb-shaped slot antenna with simple configuration for penta-band applications was reported [29]. A simple antenna with cut slots was fabricated on Taconic material and obtained the penta-band response [30]. A multiband antenna for wireless handset covered lowest 6 GHz sub-band of fifth generation (5G) spectrum [31]. A crossed line based rectangular ring shaped multiband antenna fabricated on the flexible Roggers substrate material [32]. A modified design of slot antenna achieved the penta-band response with 2.3 dBi peak gain [33]. The authors proposed a bowtie slot antenna (BTSA) over 2-16 GHz frequency range and intended radiator occupied 1800 mm² ample space [34]. Another multiband antenna resonated within 1-7 GHz exhibited the peak gain of 5.45 dBi [35]. A magneto-electric dipole antenna achieved the multiband response with 6.6 dBi gain operated within 1.5-7.5 GHz [36]. A planar antenna with the multi-circular shaped slotted substrate exhibited multiband response [37]. The antenna has larger size and the peak gain and radiation efficiency is not reported. It is worthy to note that the recent reported works on compact multiband radiators have complex geometries, larger dimensions and most of the designed antennas achieved optimal results over short frequency range. Also, it is well known fact that there is always a tradeoff between antenna performance characteristics with compact size, computational load and expensive material. Hence, it is hard to achieve optimal results with simple and compact geometry of radiators keeping in view with the tradeoff among the multiple features of the intended radiator.

The key contribution of this manuscript is explained as:

- ❖ The proposed structure validates a new geometrical structure of BTSA with compact

electrical size $0.379\lambda \times 0.186\lambda \times 0.012\lambda$, which constructs the more efficient model that not only accelerates the optimization process but also consumes less computational load.

- ❖ The defined variables have increased the flexibility in terms of frequency tuning and impedance matching controllability.
- ❖ The designed antenna operates over a broad frequency span of 2-18 GHz in contrast to most of the reported works which resonated at the short frequency range.
- ❖ For the first time, the modified ultra-compact triangular shaped metallic ground plane has been designed with the advantages of antenna miniaturized dimensions.
- ❖ The proposed antenna has the simple geometry and covers advanced heterogeneous wireless communication applications.
- ❖ Finally, antenna performance is examined and analyzed with recently published state-of-the-art existing works. The antenna exhibits broad fractional BW at required frequencies, peak realized gain of 6.3 dBi and excellent radiation efficiency performance of 95% which is higher than most of the previous investigated antenna designs.

In this paper, a new compact multiband BTSA structure with ultra-compact triangular shaped MGP and GCPW feedline is presented. The proposed antenna is realized on low cost FR4 epoxy thick substrate. The designed radiator exhibits penta-band response at 10 dB return loss. The antenna has achieved high-performance features including good fractional bandwidth (BW), high realized gain, excellent radiation efficiency, strong surface current distribution and stable far-field co-polarization and cross-polarization patterns across the standard planes. The design and simulation of the prototype have been carried out with high frequency structure simulator (HFSS) full wave electromagnetic solver based on the finite element method (FEM). The proposed antenna covers 5G spectrum, WLAN (2.3 - 3.4 GHz), H-band (6-7.35 GHz), X-band (8.4 - 12.5 GHz), military airborne, naval and land RADAR (9.8 - 10.8 GHz), Ku-band (14.9 - 5.59 GHz) and satellite (17.17 - 17.37 GHz) frequency standard bands. Results reveal that the proposed antenna is well suitable for advanced latest heterogeneous wireless communication applications.

II. PROPOSED RADIATOR METHODOLOGY

The antenna development stages are shown in Figs. 1 (a)-(e). The proposed antenna model comprises of dielectric substrate, copper conducting sheet (CCS), triangular shaped slots, MGP and 50 Ω GCPW feeding structure. These elements are engraved on the top and bottom side of the low cost FR4 epoxy printed circuit

board (PCB) laminate material with the constant values of relative permittivity $\epsilon_r = 4.4$ and dielectric loss tangent $\delta = 0.02$. The structure of proposed radiator from the top, bottom and lateral view perspective is shown in Figs. 1 (e)-(g). The methodology of intended radiator is mainly based on designing of triangular shaped slots and CPW feedline above the thick substrate. CCS is embedded on top of the substrate. The standard thickness value of the copper material is chosen as 0.035 mm.

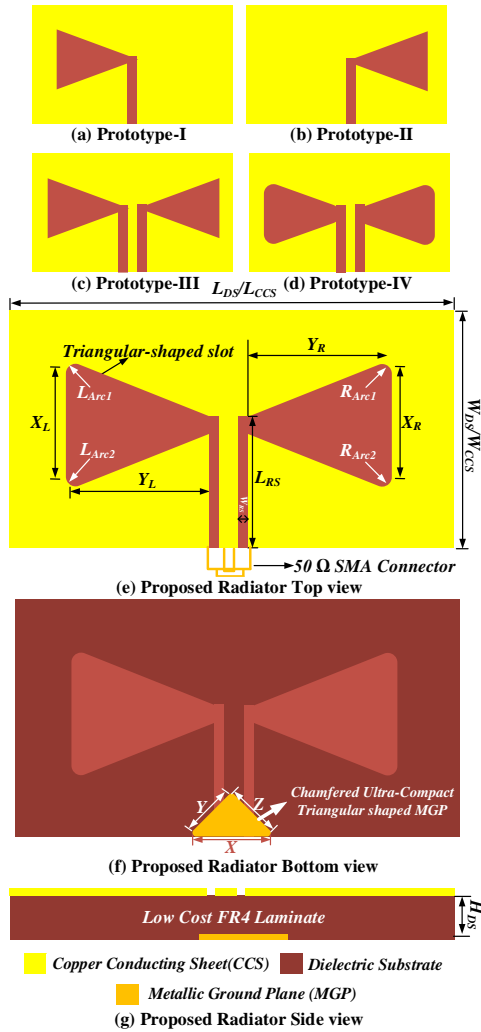


Fig. 1. Development stages of antenna and proposed radiator structure.

The triangular and rectangular slots are etched out from the upper CCS and form a left-side bowtie arm slot as depicted in Fig. 1 (a). Likewise, the right side triangular and rectangular slots are etched out from the upper CCS, which are exactly the mirror image of the left side bowtie arm slot and form right side bowtie arm slot as shown in Fig. 1 (b). The purpose of designing rectangular shaped slots is to realize the CPW feed line

as given in Fig. 1 (c). The dimensions of the feeding structure are carefully optimized to achieve the 50Ω input impedance. Fillet operation is performed at top and bottom edges of the left and right ($L_{Arc1,2} = R_{Arc1,2} = 0.0079\lambda$) triangular shaped bowtie arms. These two bowtie arm slots have fulfilled the symmetry property as illustrated in Fig. 1 (d). The miniaturized rectangular MGP with compact size of $0.039\lambda \times 0.022\lambda$ is engraved on the bottom side of the dielectric substrate and right below the CPW feedline. The chamfered operation of 0.0183λ is performed at the edges of MGP and thus forms ultra-compact triangular shaped MGP as shown in Fig. 1 (f). The proposed antenna possesses overall size of $0.379\lambda \times 0.186\lambda \times 0.012\lambda$ (where λ denote free space wavelength at lowest resonant frequency of 2.39 GHz). An approximated equations extracted from transmission line model are used to compute the dimensions of the triangular shaped bowtie arms and CPW feedline [38].

The return loss performance of developed antenna prototypes is elucidated in Fig. 2. It can be analyzed that designed antenna structure obtained the fractional BW of 39.5%, 36.7%, 19.35%, 4.25% and 1.16% at third, first, second, fourth and fifth frequency bands. Likewise, good matching performance and stable penta-band resonances at targeted frequencies are observed.

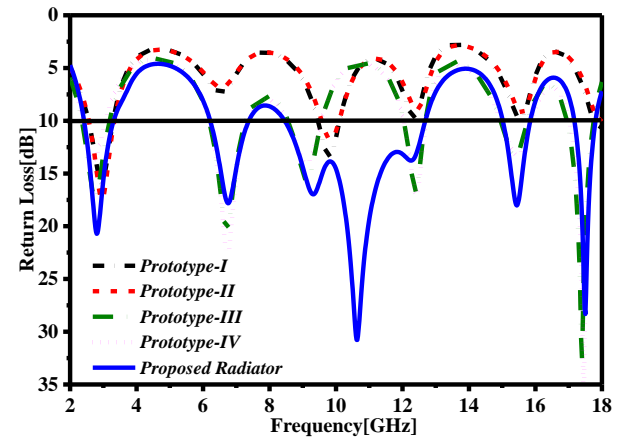


Fig. 2. Developed antenna model's return loss over specified frequency range.

Table 1: Antenna optimized values, unit: (mm)

Variable Symbol	Optimized Value	Variable Symbol	Optimized Value
L_{DS}	47.6	L_{CCS}	47.6
W_{DS}	23.4	W_{CCS}	23.4
H_{DS}	1.6	X	5
X_L	11.57	Y	2.3
Y_L	20	Z	2.3
X_R	11.57	Y_R	20
W_{RS}	1.2	L_{RS}	11.1

Further, the rectangular slots, dielectric substrate, CCS and MGP size (length and width) affects the proposed radiator performance. The chamfered and fillet operations are performed on the bowtie arm slots and MGP. This modification has the great impact on the multi-resonant performance and impedance matching control of the radiator. The proposed antenna exhibits overall optimum performance by carefully selecting defined variables values. The geometrical dimensions of the proposed antenna are listed in Table 1.

III. SIMULATION RESULTS ANALYSIS

This section explains and analyzes the multi-resonant frequency tuning, matching performance, and surface current distribution of the proposed antenna.

A. Influence of L_{RS} , W_{DS} and W_{CCS}

Tuning of three bands is observed with the variation of three important variables as shown in Fig. 3. The multiple resonant bands centered at 2.86 GHz, 15.5 GHz and 17.5 GHz (first, fourth and fifth resonances) are tuned with the rectangular slot (L_{RS}), dielectric substrate (W_{DS}) and copper conducting sheet (W_{CCS}) dimensions.

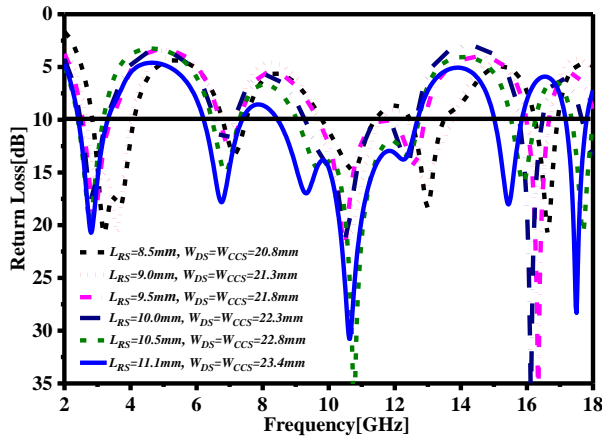


Fig. 3. Tuning and impedance matching control of multiple resonances across the operating frequency range.

It can be analyzed from Fig. 3 that the L_{RS} value varies from 8.5 mm to 11.1 mm with the step size of 0.5 mm and W_{DS} , W_{CCS} values vary from 20.8 mm to 23.4 mm to achieve perfect matching at the higher values.

B. Influence of rectangular slot width (W_{RS})

The influence of rectangular slot width (W_{RS}) variation with step size of 0.2 mm across frequency is displayed in Fig. 4. One can observe shifting of the two bands centered at 6.72 GHz and 10.6 GHz (second and third) towards the lower and upper frequency range. As displayed in Fig. 4, optimum results are obtained at 1.2

mm which shows stable and good impedance matching over specified frequency.

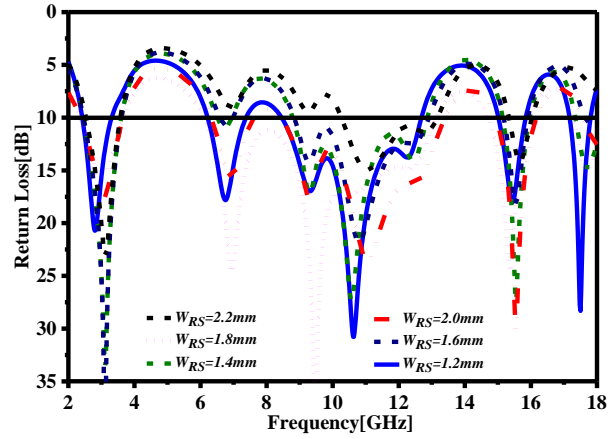


Fig. 4. Tuning and impedance matching control of resonances across the operating frequency range.

C. Influence of metallic ground plane (MGP)

The impact of MGP on overall performance of the proposed antenna is portrayed in Fig. 5. This impact is analyzed by simple MGP, chamfered MGP and absence of embedded MGP scenarios. One can observe that the antenna achieves required stable multiband response with chamfered MGP.

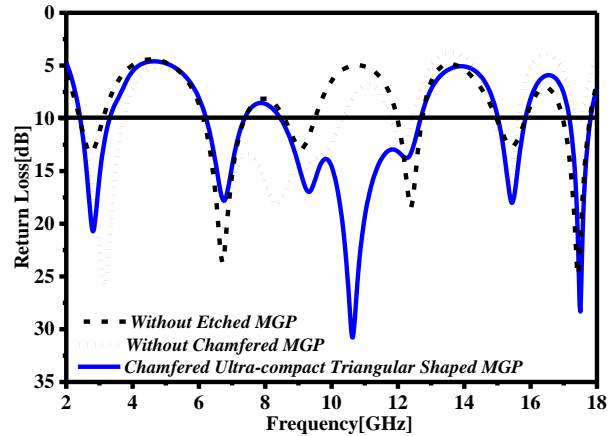


Fig. 5. Impact of chamfered MGP on the impedance matching across the frequency span.

D. Influence of different substrate material

In order to technically validate the stable multiband response, it is essential to verify the proposed radiator performance with different substrate material. The results of substrate materials are compared and depicted in Fig. 6. One can observe that the antenna achieves the perfect matching with stable desired resonances at 10 dB return loss by using the FR4 substrate material.

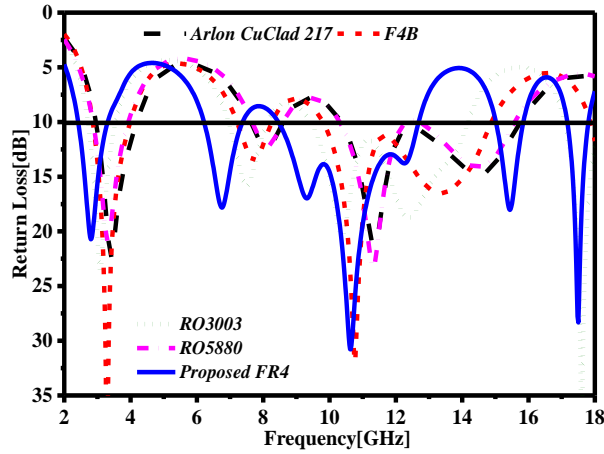


Fig. 6. Simulated results of different substrate material correspond to specified frequency.

E. Surface current distribution (Jsurf)

The concentration of current across the surface of radiator is analyzed and discussed in order to validate the effective working of proposed antenna. The current distributed density across the proposed antenna lattice at multiple resonant frequencies is depicted in Figs. 7 (a)-(e). It can be seen that at lower resonances i.e. 2.86 GHz and 6.72 GHz, the strong current is concentrated along the structure of the radiator and 50 Ω GCPW feedline. However, a diminutive variation in circulation of current at higher resonances for example, 10.6 GHz, 15.5 GHz and 17.5 GHz, can be noticed on the upper and lower front edges of radiator. The above analysis concludes that the current is equally distributed across the proposed antenna structure which confirms the cabinet’s optic principle for slot antennas.

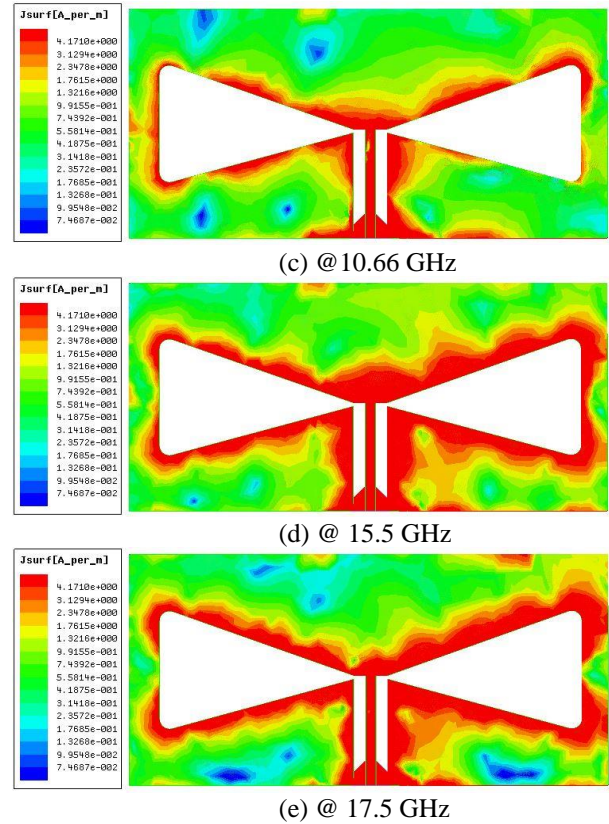
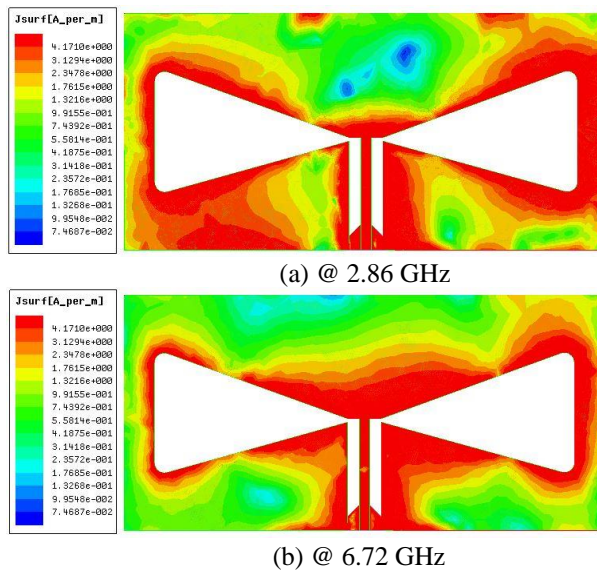


Fig. 7. Surface current distribution (Jsurf) across the proposed antenna lattice at multiple resonances.

IV. EXPERIMENTALLY VALIDATED RESULTS

This section mainly focuses on the experimental results of return loss, peak realized gain, radiation efficiency and co-polarization and cross-polarization far-field two dimensional (2D) radiation patterns. The fabricated antenna sample photograph along with top and bottom view is shown in Figs. 8 (a)-(b). The pin (inner conductor) of 50 Ω SMA connector is carefully soldered at middle of the GCPW feedline, which is engraved on top of the substrate. The outer conductor is connected to the chamfered ultra-compact triangular shaped MGP, which is embedded on the bottom of substrate as shown in Fig. 8 (b).

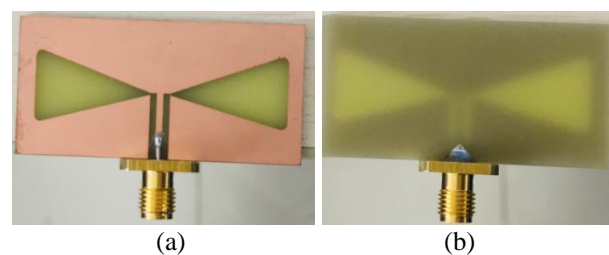


Fig. 8. Fabricated sample of the proposed radiator: (a) top view and (b) bottom view.

A. Return loss performance

The fabricated antenna model is tested to validate simulation results. The simulated (blue) and measured (dashed red) return loss results across the specified frequency range are compared in Fig. 9. The antenna model is connected to one port of calibrated keysight PNA-X N-5245B network analyzer.

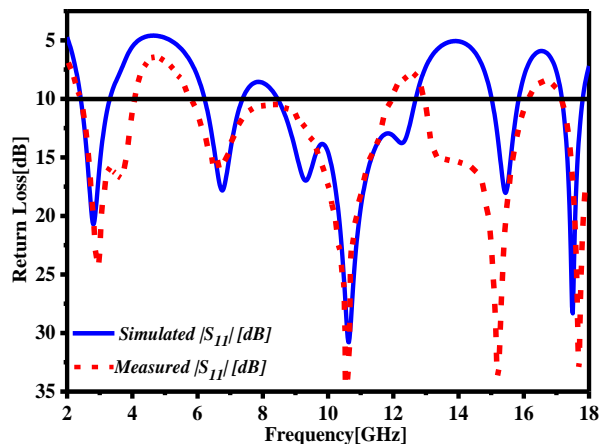


Fig. 9. Simulated and measured return loss performance across the operable frequency range.

It can be seen from Fig. 9 that the return loss performance of the designed and fabricated model is well coincides. One can observe a slight shift of the resonances in the measured result. A close agreement is clearly seen among the simulated and tested results. However, the deviation in experimental and simulation results is mainly due to the fabrication tolerances in the manufacturing of the substrate material, thickness, loss tangent or relative permittivity values, and imperfect soldering.

B. Peak realized gain and radiation efficiency

The simulated and measured results of peak realized gain and radiation efficiency against the given frequency range are plotted and compared in Fig. 10. The antenna model simulation result (blue) achieved the high gain of 6.3 dBi and 5.72 dBi at 15.5 GHz and 17.5 GHz. Similarly, fair and acceptable gain is observed at other resonances. The peak realized gain of fabricated sample of antenna was measured with two identical ridge horn antennas with known gain. It can be seen from Fig. 10 (dashed red streak) that about 1 dB deviation in measured and simulated gain results is observed which validates the performance of fabricated prototype. The radiation efficiency simulation result of the proposed antenna model (black curve) shows high performance of 95%, 90%, 88%, 75.4% and 74.9% at in-band frequencies. An effective pattern integration method was applied to measure the radiation efficiency. The proposed antenna radiation efficiency measurement

results are slightly deviated in comparison with the simulation results as can be seen from Fig. 10 (dashed pink streak). The results have revealed the practical performance of designed sample across the operational frequency span.

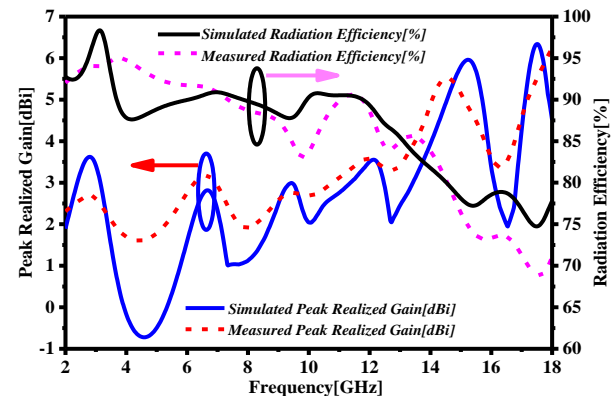


Fig. 10. Simulated and measured peak realized gain and radiation efficiency against the operable frequency range.

C. Co-polar and cross polar patterns

The radiation patterns in principal planes of the proposed antenna are measured inside the anechoic chamber under far-field condition. The placement of device under test (DUT) is shown in Figs. 11 (a)-(b). The fabricated antenna prototype co-polarization and cross-polarization radiation patterns in elevation (E-plane) and azimuth (H-plane) are measured inside the chamber room. The measurement indoor facility walls are covered with radio absorbing material. DUT was placed on the azimuth rotator and move around 360°. The rotary table has been controlled by the positioner controller and connected to the computer with ethernet cable. The standard ridge gap horn (transmitter) and the DUT (receiver) have been fixed in line of sight (LoS) at a certain distance which fulfilled the far-field condition. Besides, the microwave cables are connected to the antennas and with the ports of vector network analyzer (VNA). A computer has been installed to monitor the measurement results, execute the commands and save the measured data.

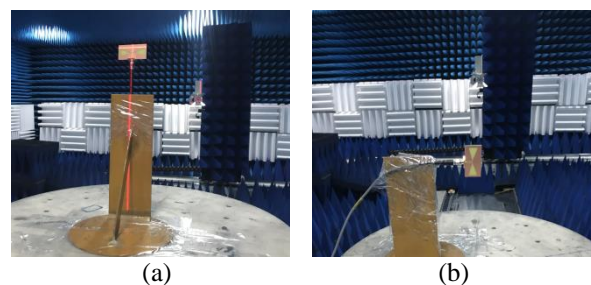


Fig. 11. DUT placement in anechoic chamber.

The simulation and measurement results of co-polarization and cross-polarization in principal planes at in-band resonances are displayed and compared in Figs. 12 (a)-(j). The co-polarization and cross-polarization pattern results of the proposed antenna in E-plane at multiple resonances are shown in Figs. 12 (a), (c), (e), (g) and (i). The antenna exhibits near omni-directional radiation pattern of co-polarization in E-plane at in-band resonances. One can see the simulation results at higher resonances are changing gradually. At higher resonances cross-polarization level is slightly increased. The cross-polarization level is almost -20 dB at targeted resonances. It is found that the measurement results of co-polarization and cross-polarization radiation patterns are slightly deteriorated as the frequency increases and nulls are observed at higher resonances. Further, the co-polarization and cross-polarization antenna results in H-plane at multiple resonances are portrayed in Figs. 12 (b), (d), (f), (h) and (j). The antenna exhibits nearly monopole like co-polarization and cross-polarization radiation pattern at lower resonances. A slight change in radiation patterns at higher resonances is observed. One can analyze that the simulation and measurement results show a diminutive shift and slightly deteriorated. The deviations in measured results at principal planes are mainly due to the fact of losses inside measurement chamber facility, rotation of the antenna model and SMA radiation. The overall measured radiation patterns at in-band resonant frequencies are well coincide with simulated results.

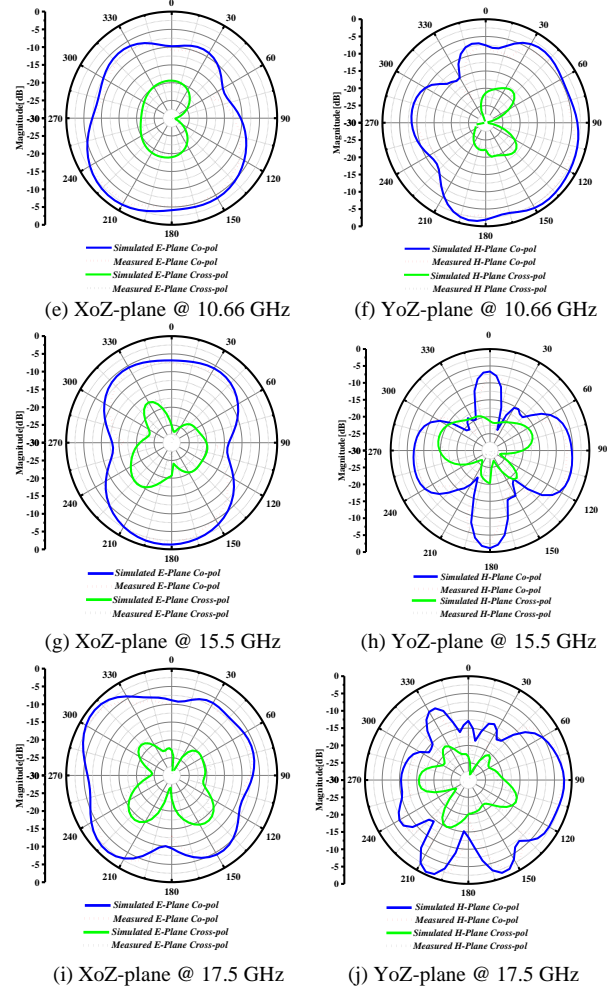
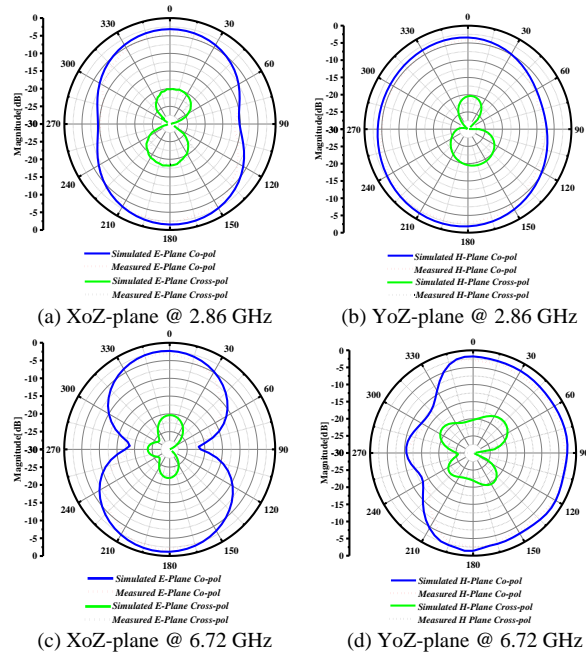


Fig. 12. Simulated and measured co-polar and cross-polar far-field patterns across the principal plane at multiple resonances.

V. LITERATURE COMPARISON

The performance comparison of the proposed antenna with state-of-the-art work is compared in Table II. It can be seen that the proposed antenna is miniaturized, low profile and exhibited the optimal performance in terms of peak gain and radiation efficiency. The proposed antenna is very smaller in size and decreases in overall occupied space of 84.5%, 38.1% and 36.34% in comparison to Refs. [29]-[31]. The antenna reported in [29] obtained a higher gain with compromised overall occupied space. It can be noticed that the radiation efficiency of the antennas were not focused in [5], [33] and [35]-[37]. From the comparison analyzed results, it is evident that most of the reported works on multiband antennas cover a small frequency

span as compared to the proposed multiband BTSA.

Table 2: Proposed radiator performance comparison with state-of-the-art investigated multiband antennas

Ref.	Electrical Size (λ) [$L_{DS} \times W_{DS}$] (mm ²)	Antenna Profile (λ) [H_{DS}] (mm)	Gain (dBi)	Efficiency (%)
Our work	0.379 λ ×0.186 λ	0.012 λ	6.3	95
[29]	0.694 λ ×0.484 λ	0.003 λ	6.46	79
[30]	0.53 λ ×0.48 λ	0.009 λ	5.37	94.8
[31]	0.966 λ ×0.485 λ	0.013 λ	2.86	77
[33]	0.966 λ ×0.485 λ	0.004 λ	2.5	Not Reported (NR)
[5]	0.099 λ ×0.165 λ	0.0135 λ	3.0	NR
[35]	0.35 λ ×0.22 λ	0.0079 λ	5.45	NR
[36]	0.4 λ ×0.13 λ	0.16 λ	6.6	NR
[37]	0.489 λ ×0.351 λ	0.024 λ	NR	NR

VI. CONCLUSION

In this article, a new compact high gain and multiband BTSA with miniaturized triangular shaped MGP has been proposed and investigated. The antenna is realized on the low-cost FR4 epoxy thick substrate. The antenna prototype has miniaturized dimensions of 0.379 λ ×0.186 λ ×0.012 λ . Influence of multiple variables have been analyzed and discussed. Analysis of surface current distribution at multiple resonances has been investigated. The proposed antenna model exhibited an excellent performance of return loss, peak realized gain, radiation efficiency and stable far-field co-polarization and cross-polarization radiation patterns. The designed antenna obtained the wide fractional bandwidths at in-band resonances. High gain of 6.3 dBi, 5.72 dBi, 3.64 dBi, 2.89 dBi and 2.58 dBi are achieved at 17.5 GHz, 15.5 GHz, 2.86 GHz, 6.72 GHz and 10.66 GHz resonances. The proposed antenna showed an excellent radiation efficiency performance of 95%, 90%, 88%, 75.5% and 74.9% at in-band frequencies. The designed antenna has been fabricated, tested and experimentally verified. The simulation and measured results are in close agreement and hence make the proposed antenna as an excellent choice for advanced heterogeneous wireless communication applications.

ACKNOWLEDGMENT

Authors Zaheer Ahmed Dayo, Qunsheng Cao, Yi Wang and Gulab Shah gratefully acknowledge the support from National Natural Science Foundation of China under grant No. 61871219.

REFERENCES

- [1] E. A. Soliman, S. Brebels, P. Delmotte, G. A. E. Vandenbosch, and E. Beyne, "Bow-tie slot antenna

fed by CPW," *Electron. Lett.*, vol. 35, no. 7, pp. 514-515, Apr. 1999.

- [2] Z. A. Dayo, Q. Cao, Y. Wang, S. Ur Rahman, and P. Soothar, "A compact broadband antenna for civil and military wireless communication applications," *Int. J. Adv. Comput. Sci. Appl.*, vol. 10, no. 9, pp. 39-44, Sep. 2019.
- [3] S. C. Basaran and K. Sertel, "Compact and planar monopole antenna for WLAN and WiMAX applications," *Appl. Comput. Electromagn. Soc. J.*, vol. 30, no. 5, pp. 546-550, May 2015.
- [4] P. Soothar, H. Wang, C. Xu, Z. A. Dayo, B. Muneer, and K. Kanwar, "A compact broadband and high gain tapered slot antenna with stripline feeding network for H, X, Ku and K band applications," *Int. J. Adv. Comput. Sci. Appl.*, vol. 11, no. 7, pp. 239-244, July 2020.
- [5] P. N. Vummadisetty and A. Kumar, "Multi feed multi band uniplanar ACS fed antenna with N shape and inverted L shape radiating branches for wireless applications," *Microsyst. Technol.*, vol. 24, no. 4, pp. 1863-1873, Apr. 2018.
- [6] K. Mondal, P. P. Sarkar, and D. Chanda Sarkar, "High gain triple band microstrip patch antenna for WLAN, Bluetooth and 5.8 GHz/ISM band applications," *Wirel. Pers. Commun.*, vol. 109, no. 4, pp. 2121-2131, Dec. 2019.
- [7] A. Ahmad, F. Arshad, S. I. Naqvi, Y. Amin, and H. Tenhunen, "Design, fabrication, and measurements of extended I-shaped multiband antenna for wireless applications," *Appl. Comput. Electromagn. Soc. J.*, vol. 33, no. 4, pp. 388-393, Apr. 2018.
- [8] M. R. Ahsan, M. T. Islam, and M. Habib Ullah, "A new meandered-stripline fed dual band patch antenna," *Appl. Comput. Electromagn. Soc. J.*, vol. 30, no. 2, pp. 213-221, Feb. 2015.
- [9] M. M. Fakharian, P. Rezaei, and A. A. Orouji, "A novel slot antenna with reconfigurable meander-slot DGS for cognitive radio applications," *Appl. Comput. Electromagn. Soc. J.*, vol. 30, no. 7, pp. 748-753, July 2015.
- [10] D. Behera, B. Dwivedy, D. Mishra, and S. K. Behera, "Design of a CPW fed compact bow-tie microstrip antenna with versatile frequency tunability," *IET Microwaves, Antennas Propag.*, vol. 12, no. 6, pp. 841-849, May 2018.
- [11] C. Zebiri, D. Sayad, I. Elfergani, A. Iqbal, W. F. A Mshwat, J. Kosha, J. Rodriguez, R. Abd-Alhameed, "A compact semi-circular and arc-shaped slot antenna for heterogeneous RF front-ends," *Electron.*, vol. 8, no. 10, Oct. 2019.
- [12] E. W. Coetzee, J. W. Odendaal, and J. Joubert, "A quad-band antenna with AMC reflector for WLAN and WiMAX applications," *Appl. Comput. Electromagn. Soc. J.*, vol. 33, no. 10, pp. 1123-1128, Oct. 2018.

- [13] R. Rajkumar and K. Usha Kiran, "A compact meta-material multiband antenna for WLAN/WiMAX/ITU band applications," *AEU - Int. J. Electron. Commun.*, vol. 70, no. 5, pp. 599-604, May 2016.
- [14] S. I. R. and S. Raghavan, "CSRR-based compact pentaband printed antenna for GPS/GSM/ WLAN/WiMAX applications," *Microw. Opt. Technol. Lett.*, vol. 57, no. 7, pp. 1538-1542, July 2015.
- [15] Z. A. Dayo, Q. Cao, P. Soothar, M. M. Lodro, and Y. Li, "A compact coplanar waveguide feed bow-tie slot antenna for WIMAX, C and X band applications," *2019 IEEE Intl. Conf. on Comput. Electromagn.*, (ICCEM), Shanghai, China, pp. 1-3, July 2019.
- [16] N. Kumar Mungaru, K. Yogaprasad, and V. R. Anitha, "A quad-band Sierpinski based fractal antenna fed by co-planar waveguide," *Microw. Opt. Technol. Lett.*, vol. 62, no. 2, pp. 1-6, Oct. 2019.
- [17] M. A. Belen, P. Mahouti, A. Çaliskan, and A. Belen, "Modeling and realization of cavity-backed dual band SIW antenna," *Appl. Comput. Electromagn. Soc. J.*, vol. 32, no. 11, pp. 974-978, Nov. 2017.
- [18] Y. F. Lin, Y. C. Kao, S. C. Pan, and H. M. Chen, "Bidirectional radiated circularly polarized annular-ring slot antenna for portable RFID reader," *Appl. Comput. Electromagn. Soc. J.*, vol. 25, no. 3, pp. 182-189, Mar. 2010.
- [19] B. Badamchi, A. Valizade, P. Rezaei, and Z. Badamchi, "A reconfigurable square slot antenna with switchable single band, UWB and UWB with band notch function performances," *Appl. Comput. Electromagn. Soc. J.*, vol. 29, no. 5, pp. 383-390, May 2014.
- [20] P. Soothar, H. Wang, B. Muneer, Z. A. Dayo, and B. S. Chowdhry, "A broadband high gain tapered slot antenna for underwater communication in microwave band," *Wirel. Pers. Commun.*, vol. 116, no. 2, pp. 1025-1042, Jan. 2021.
- [21] P. Beigi, J. Nourinia, B. Mohammadi, and A. Valizade, "Bandwidth enhancement of small square monopole antenna with dual band notch characteristics using U-shaped slot and butterfly shape parasitic element on backplane for UWB applications," *Appl. Comput. Electromagn. Soc. J.*, vol. 30, no. 1, pp. 78-85, Jan. 2015.
- [22] A. Valizade, C. Ghobadi, J. Nourinia, N. Ojaroudi, and M. Ojaroudi, "Band-notch slot antenna with enhanced bandwidth by using Ω -shaped strips protruded inside rectangular slots for UWB applications," *Appl. Comput. Electromagn. Soc. J.*, vol. 27, no. 10, pp. 816-822, Oct. 2012.
- [23] Z. A. Dayo, Q. Cao, Y. Wang, P. Soothar, B. Muneer, and B. S. Chowdhry, "A compact broadband high gain antenna using slotted inverted omega shape ground plane and tuning stub loaded radiator," *Wirel. Pers. Commun.*, vol. 113, no. 1, pp. 499-518, July 2020.
- [24] Z. A. Dayo, Q. Cao, Y. Wang, S. Pirbhulal, and A. H. Sodhro, "A compact high-gain coplanar waveguide-fed antenna for military RADAR applications," *Int. J. Antennas Propag.*, vol. 2020, no. 8024101, pp. 1-10, Aug. 2020.
- [25] D. Pathak, S. K. Sharma, and V. S. Kushwah, "Dual-band linearly polarized integrated dielectric resonator antenna for Wi-MAX applications," *Wirel. Pers. Commun.*, vol. 111, no. 1, pp. 235-243, Mar. 2020.
- [26] K. Yu, Y. Li, and W. Yu, "A compact triple band antenna for bluetooth, WLAN & WiMAX applications," *Appl. Comput. Electromagn. Soc. J.*, vol. 32, no. 5, pp. 424-429, May 2017.
- [27] S. S. Sran and J. S. Sivia, "Quad staircase shaped microstrip patch antenna for S, C and X band applications," *Procedia Comput. Sci.*, vol. 85, pp. 443-450, Feb. 2016.
- [28] K. Srivastava, A. Kumar, and B. K. Kanaujia, "Design of compact penta-band and hexa-band microstrip antennas," *Frequenz*, vol. 70, no. 3-4, pp. 101-111, Mar. 2016.
- [29] Y. J. Chen, T. W. Liu, and W. H. Tu, "CPW-fed penta-band slot dipole antenna based on comb-like metal sheets," *IEEE Antennas Wirel. Propag. Lett.*, vol. 16, pp. 202-205, May 2017.
- [30] N. H. Gad and M. Vidmar, "Design of a microstrip-fed printed-slot antenna using defected ground structures for multiband applications," *Appl. Comput. Electromagn. Soc. J.*, vol. 33, no. 8, pp. 854-860, Aug. 2018.
- [31] A. J. Khalilabadi and A. Zadehgo, "Multiband antenna for wireless applications including GSM/UMTS/LTE and 5G bands," *Appl. Comput. Electromagn. Soc. J.*, vol. 34, no. 2, pp. 270-271, Feb. 2019.
- [32] A. Javed, A. Ejaz, S. Mehak, Y. Amin, J. Loo, and H. Tenhunen, "Miniaturized cross-lines rectangular ring-shaped flexible multiband antenna," *Appl. Comput. Electromagn. Soc. J.*, vol. 34, no. 5, pp. 625-630, May 2019.
- [33] B. Bag, P. Biswas, S. Biswas, P. P. Sarkar, and D. Ghoshal, "Novel monopole microstrip antennas for GPS, WiMAX and WLAN applications," *J. Circuits, Syst. Comput.*, vol. 29, no. 3, pp. 1-15, May 2020.
- [34] Z. A. Dayo, Q. Cao, Y. Wang, and P. Soothar, "A compact high gain multiband bow-tie slot antenna," *2019 Int. Appl. Comput. Electromagn. Soc. Symp. - China (ACES)*, Nanjing, China, pp. 1-2, Apr. 2019.
- [35] M. A. Al-Mihrab, A. J. Salim, and J. K. Ali, "A compact multiband printed monopole antenna with hybrid polarization radiation for GPS, LTE, and satellite applications," *IEEE Access*, vol. 8, pp.

- 110371-110380, June 2020.
- [36] G. Yang, S. Zhang, J. Li, Y. Zhang, and G. F. Pedersen, "A multi-band magneto-electric dipole antenna with wide beam-width," *IEEE Access*, vol. 8, pp. 68820-68827, Apr. 2020.
- [37] A. E. Ahmed and W. A. E. Ali, "A Novel multiband antenna with 3D-printed multicircular substrate for wireless applications," *2nd Int. Conf. Electr. Commun. Comput. Eng. ICECCE 2020*, pp. 1-5, Aug. 2020.
- [38] R. Nayak and S. Maiti, "A review of bow-tie antennas for GPR applications," *IETE Tech. Rev. (Institution Electron. Telecommun. Eng. India)*, vol. 36, no. 4, pp. 382-397, July 2019.



Zaheer Ahmed Dayo was born in village Rustam, District Shikarpur Sindh, Pakistan. He received the M.E degree in Telecommunication Engineering & Management from Mehran University of Engineering & Technology (MUET) Jamshoro Sindh Pakistan in the year 2014.

He is currently pursuing the Ph.D. degree under the supervision of Professor Qunsheng Cao; with major in Communication Information System, at College of Electronic and Information Engineering (CEIE), Nanjing University of Aeronautics & Astronautics (NUAA), P.R China. Dayo has published several articles in international journals and conference proceedings. He served as a reviewer and TPC member in international journal and conference He has a vast academic and research experience of more than 5 years. He is currently working in the field of Electromagnetics particularly focused on Microwave & RF Engineering and Measurements areas. His current research interests include Designing of Compact, Broadband, High gain Antennas, Array topology and optimization Schemes, Multiband slot antennas, Reconfigurable, Metamaterial inspired antennas, Active and Passive Frequency Selective Surfaces.



Qunsheng Cao received the Ph.D. degree in Electrical Engineering from The Hong Kong Polytechnic University, Hong Kong, in 2000. From 2000 to 2005, He worked as a Research Associate with the Department of Electrical Engineering, University of Illinois at Urbana-Champaign and with the Army High Performance Computing Research Center, University of Minnesota, U.S.A. In 2006, he joined the Nanjing University of

Aeronautics and Astronautics, China, as a Professor for Electrical Engineering. He has authored more than 190 academic articles in refereed international journals and conference proceedings. His current research interests include computational electromagnetics, microwave, and antennas technologies and radar signal processing. His research team is also engaged in high-speed circuit signal integrity, antenna, microwave components, and new method in radar signal processing.



Yi Wang received the B.S. and Ph.D. degrees in Communication and Information System from the Nanjing University of Aeronautics and Astronautics (NUAA), Nanjing, China, in 2006 and 2012, respectively. In 2012, he joined the College of Electronic and

Information Engineering, NUAA, as an Assistant Professor, where he is currently working as an Associate Professor. His research interests include computational electromagnetics, especially the finite difference time-domain (FDTD) method, the FDTD modeling of the entire earth-ionosphere system, and the earthquake electromagnetics, and research focuses on the FDTD simulation of anisotropic media and earthquake phenomena.



Permanand Soothar was born in Sindh, Pakistan. He received the M.E. degree in Electronics and Telecom Engineering from the Mehran University of Engineering and Technology (MUET), Jamshoro, Sindh Pakistan, in 2012. Soothar is working as a Faculty Member in the

Department of Electronics Engineering, MUET Jamshoro Since 2015. Currently, He is pursuing the Ph.D. degree under the supervision of Professor Hao Wang at the School of Electronic and Optoelectronic Engineering, Nanjing University of Science and Technology (NJUST), Nanjing, P.R. China. His research interests include planar microstrip patch antennas, Ultra-wideband antennas, Millimeter-wave antennas, 5G communication antennas, Gap waveguide technology, satellite communication system, dual polarization slotted waveguide antennas and Arrays.



Imran A Khoso received the M.S. degree in Information and Communication Engineering from University of Science and Technology Beijing, Beijing in 2019. He is currently working toward the Ph.D. degree in Communication and Information Systems at Nanjing University of

Aeronautics and Astronautics, Nanjing, China. Khoso serves as a peer reviewer for IEEE Access, IET Communications, and several conferences. His research interests include random matrix theory, signal processing and wireless communications.



Gulab Shah received his M.Sc. and M.Phil. degrees in the field of Electronics from Quaid-e- Azam University (QAU), Islamabad, Pakistan in 2006 and 2008, respectively. Currently, Shah is pursuing Ph.D. degree from College of Electronic and Information

Engineering Nanjing University of Aeronautics and Astronautics, China. His research interests include radio frequency and microwave designing components, antennas, meta-material and frequency selective surface.



Muhammad Aamir received the Bachelor of Engineering degree in Computer Systems Engineering from Mehran University of Engineering & Technology Jamshoro, Sindh, Pakistan, in 2008, the Master of Engineering degree in Software Engineering from Chongqing University, China, in 2014, and the Ph.D. degree in Computer Science and Technology from Sichuan University, Chengdu, China, in 2019. He is currently an Associate Professor at the Department of Computer, Huanggang Normal University, Huanggang, China. His main research interests include pattern recognition, computer vision, image processing, deep learning, wireless communication and fractional calculus.